
4 Chemical Physics of Colloid Systems and Interfaces

Peter A. Kralchevsky and Krassimir D. Danov

CONTENTS

4.1	Introduction	248
4.2	Surface Tension of Surfactant Solutions	249
4.2.1	Static Surface Tension	249
4.2.1.1	Nonionic Surfactants	250
4.2.1.2	Ionic Surfactants	257
4.2.2	Dynamic Surface Tension	266
4.2.2.1	Adsorption under Diffusion Control	267
4.2.2.2	Small Initial Perturbation	268
4.2.2.3	Large Initial Perturbation	269
4.2.2.4	Generalization for Ionic Surfactants	271
4.2.2.5	Adsorption under Barrier Control	274
4.2.2.6	Dynamics of Adsorption from Micellar Surfactant Solutions	276
4.3	Capillary Hydrostatics and Thermodynamics	283
4.3.1	Shapes of Fluid Interfaces	283
4.3.1.1	Laplace and Young Equations	283
4.3.1.2	Solutions of Laplace Equations for Menisci of Different Geometry	285
4.3.1.3	Gibbs–Thomson Equation	289
4.3.1.4	Kinetics of Ostwald Ripening in Emulsions	291
4.3.2	Thin Liquid Films and Plateau Borders	293
4.3.2.1	Membrane and Detailed Models of a Thin Liquid Film	293
4.3.2.2	Thermodynamics of Thin Liquid Films	294
4.3.2.3	The Transition Zone between Thin Film and Plateau Border	297
4.3.2.4	Methods for Measuring Thin Film Contact Angles	301
4.3.3	Lateral Capillary Forces between Particles Attached to Interfaces	302
4.3.3.1	Particle–Particle Interactions	302
4.3.3.2	Particle–Wall Interactions	307
4.3.3.3	Electrically Charged Particles at Liquid Interfaces	308
4.4	Surface Forces	314
4.4.1	Derjaguin Approximation	314
4.4.2	van der Waals Surface Forces	315
4.4.3	Electrostatic Surface Forces	318
4.4.3.1	Two Identically Charged Planes	318
4.4.3.2	Two Nonidentically Charged Planes	321
4.4.3.3	Two Charged Spheres	322
4.4.4	DLVO Theory	323
4.4.5	Non-DLVO Surface Forces	324
4.4.5.1	Ion Correlation Forces	324
4.4.5.2	Steric Interaction	325

4.4.5.3	Oscillatory Structural Forces.....	328
4.4.5.4	Repulsive Hydration and Attractive Hydrophobic Forces	335
4.4.5.5	Fluctuation Wave Forces.....	340
4.5	Hydrodynamic Interactions in Dispersions	342
4.5.1	Basic Equations and Lubrication Approximation.....	342
4.5.2	Interaction between Particles of Tangentially Immobile Surfaces.....	346
4.5.2.1	Taylor and Reynolds Equations, and Influence of the Particle Shape	346
4.5.2.2	Interactions among Nondeformable Particles at Large Distances	348
4.5.2.3	Stages of Thinning of a Liquid Film	350
4.5.2.4	Dependence of Emulsion Stability on the Droplet Size.....	355
4.5.3	Effect of Surface Mobility.....	357
4.5.3.1	Diffusive and Convective Fluxes at an Interface—Marangoni Effect	357
4.5.3.2	Fluid Particles and Films of Tangentially Mobile Surfaces	360
4.5.3.3	Bancroft Rule for Emulsions.....	363
4.5.3.4	Demulsification	368
4.5.4	Interactions in Nonpreequilibrated Emulsions	369
4.5.4.1	Surfactant Transfer from Continuous to Disperse Phase	369
4.5.4.2	Surfactant Transfer from Disperse to Continuous Phase.....	371
4.5.4.3	Equilibration of Two Droplets across a Thin Film	372
4.5.5	Hydrodynamic Interaction of a Particle with an Interface	373
4.5.5.1	Particle of Immobile Surface Interacting with a Solid Wall	374
4.5.5.2	Fluid Particles of Mobile Surfaces.....	375
4.5.6	Bulk Rheology of Dispersions.....	379
4.6	Kinetics of Coagulation	384
4.6.1	Irreversible Coagulation	385
4.6.2	Reversible Coagulation	388
4.6.3	Kinetics of Simultaneous Flocculation and Coalescence in Emulsions.....	390
	Acknowledgments.....	392
	References.....	392

4.1 INTRODUCTION

A *colloidal system* represents a multiphase (heterogeneous) system in which at least one of the phases exists in the form of very small particles: typically smaller than 1 μm but still much larger than the molecules. Such particles are related to phenomena like Brownian motion, diffusion, and osmosis. The terms “microheterogeneous system” and “disperse system” (dispersion) are more general because they also include bicontinuous systems (in which none of the phases is split into separate particles) and systems containing larger, non-Brownian particles. The term dispersion is often used as a synonym of colloidal system.

A classification of the colloids with respect to the state of aggregation of the *disperse* and *continuous* phases is shown in [Table 4.1](#). Some examples are the following.

1. Examples for *gas-in-liquid* dispersions are the foams or the boiling liquids. *Gas-in-solid* dispersions are the various porous media like filtration membranes, sorbents, catalysts, isolation materials, etc.
2. Examples for *liquid-in-gas* dispersions are the mist, the clouds, and other aerosols. *Liquid-in-liquid* dispersions are the emulsions. At room temperature there are only four types of mutually immiscible liquids: water, hydrocarbon oils, fluorocarbon oils, and liquid metals (Hg and Ga). Many raw materials and products in food and petroleum industries exist in the form of oil-in-water or water-in-oil emulsions. The soil and some biological tissues can be considered as examples of *liquid-in-solid* dispersions.

TABLE 4.1
Types of Disperse Systems

Disperse Phase	Continuous Phase		
	Gas	Liquid	Solid
Gas	—	G in L	G in S
Liquid	L in G	L ₁ in L ₂	L in S
Solid	S in G	S in L	S ₁ in S ₂

3. Smoke, dust, and some other aerosols are examples for *solid-in-gas* dispersions. The *solid-in-liquid* dispersions are termed *suspensions* or *sols*. The pastes and some glues are highly concentrated suspensions. The *gels* represent *bicontinuous* structures of solid and liquid. The pastes and some glues are highly concentrated suspensions. Examples for *solid-in-solid* dispersions are some metal alloys, many kinds of rocks, some colored glasses, etc.

In the following section, we will consider mostly liquid dispersions, that is, dispersions with liquid continuous phase, like foams, emulsions and suspensions. Sometimes these are called “complex fluids.”

In general, the area of the interface between the disperse and continuous phases is rather large. For instance, 1 cm³ of dispersion phase with particles of radius 100 nm and volume fraction 30% contains interface of area about 10 m². This is the reason why the interfacial properties are of crucial importance for the properties and stability of colloids.

The *stabilizing* factors for dispersions are the repulsive surface forces, the particle thermal motion, the hydrodynamic resistance of the medium, and the high surface elasticity of fluid particles and films.

On the contrary, the factors *destabilizing* dispersions are the attractive surface forces, the factors suppressing the repulsive surface forces, the low surface elasticity, gravity, and other external forces tending to separate the phases.

In Sections 4.2 and 4.3 we consider effects related to the surface tension of surfactant solution and capillarity. In Section 4.4 we present a review on the surface forces due to intermolecular interactions. In Section 4.5 we describe the hydrodynamic interparticle forces originating from the effects of bulk and surface viscosity and related to surfactant diffusion. Finally, Section 4.6 is devoted to the kinetics of coagulation in dispersions.

4.2 SURFACE TENSION OF SURFACTANT SOLUTIONS

4.2.1 STATIC SURFACE TENSION

As a rule, the fluid dispersions (emulsions, foams) are stabilized by adsorption layers of amphiphilic molecules. These can be ionic [1,2] and nonionic [3] surfactants, lipids, proteins, etc. (see Chapter 4 of this Handbook). All of them have the property to lower the value of the surface (or interfacial) tension, σ , in accordance with the *Gibbs adsorption equation* [4–6],

$$d\sigma = - \sum_i \Gamma_i d\mu_i \quad (4.1)$$

where

Γ_i is the surface concentration (adsorption) of the i th component
 μ_i is its chemical potential

The summation in Equation 4.1 is carried out over all components. Usually an equimolecular dividing surface with respect to the solvent is introduced for which the adsorption of the solvent is set zero by definition [4,5]. Then the summation is carried out over all other components. Note that Γ_i is an excess surface concentration with respect to the bulk; Γ_i is positive for surfactants, which decreases σ in accordance with Equation 4.1. On the contrary, Γ_i is negative for aqueous solutions of electrolytes, whose ions are repelled from the surface by the electrostatic image forces [5]; consequently, the addition of electrolytes increases the surface tension of water [6]. For surfactant concentrations above the critical micellization concentration (CMC) $\mu_i = \text{constant}$ and, consequently, $\sigma = \text{constant}$ (see Equation 4.1).

4.2.1.1 Nonionic Surfactants

4.2.1.1.1 Types of Adsorption Isotherms

Consider the boundary between an aqueous solution of a nonionic surfactant and a hydrophobic phase, air or oil. The dividing surface is usually chosen to be the equimolecular surface with respect to water, that is $\Gamma_w = 0$. Then Equation 4.1 reduces to $d\sigma = -\Gamma_1 d\mu_1$, where the subscript “1” denotes the surfactant. Because the bulk surfactant concentration is usually not too high, we can use the expression for the chemical potential of a solute in an ideal solution: $\mu_1 = \mu_1^{(0)} + kT \ln c_1$, where k is the Boltzmann constant, T is the absolute temperature, c_1 is the concentration of nonionic surfactant, and $\mu_1^{(0)}$ is its standard chemical potential, which is independent of c_1 . Thus the Gibbs adsorption equation acquires the form

$$d\sigma = -kT\Gamma_1 d \ln c_1 \quad (4.2)$$

The surfactant adsorption isotherms, expressing the connection between Γ_1 and c_1 , are usually obtained by means of some molecular model of adsorption. Table 4.2 contains the six most popular surfactant adsorption isotherms, those of Henry, Freundlich [7], Langmuir [8], Volmer [9], Frumkin [10] and van der Waals [11]. For $c_1 \rightarrow 0$ all isotherms (except that of Freundlich) reduce to the Henry isotherm: $\Gamma_1/\Gamma_\infty = Kc_1$. The physical difference between the Langmuir and Volmer isotherms is that the former corresponds to a physical model of *localized* adsorption, whereas the latter to *nonlocalized* adsorption. The Frumkin and van der Waals isotherms generalize, respectively, the Langmuir and Volmer isotherms for case, in which the interaction between neighboring adsorbed molecules is not negligible. (If the interaction parameter β is set zero, the Frumkin and van der Waals isotherms reduce to the Langmuir and Volmer isotherms, correspondingly.) The comparison between theory and experiment shows that for air–water interfaces $\beta > 0$, whereas for oil–water interfaces we can set $\beta = 0$ [12,13]. The latter facts lead to the conclusion that for air–water interfaces β takes into account the van der Waals attraction between the hydrocarbon tails of the adsorbed surfactant molecules across air; such attraction is missing when the hydrophobic phase is oil. (Note that in the case of ionic surfactants it is possible to have $\beta < 0$, see the next section.) The adsorption parameter K in Table 4.2 characterizes the surface activity of the surfactant: the greater K , the higher the surface activity. K is related to the standard free energy of adsorption, $\Delta G^\circ = \mu_{1s}^{(0)} - \mu_1^{(0)}$, which is the energy gain for bringing a molecule from the bulk of the aqueous phase to a diluted adsorption layer [14,15]:

$$K = \frac{\delta_1}{\Gamma_\infty} \exp\left(\frac{\mu_1^{(0)} - \mu_{1s}^{(0)}}{kT}\right) \quad (4.3)$$

The parameter δ_1 characterizes the thickness of the adsorption layer; δ_1 can be set (approximately) equal to the length of the amphiphilic molecule. Γ_∞ represents the maximum possible value of the adsorption. In the case of localized adsorption (Langmuir and Frumkin isotherms), $1/\Gamma_\infty$ is the area

TABLE 4.2
Types of Adsorption and Surface Tension Isotherms

Type of Isotherm	Surfactant Adsorption Isotherms (for Nonionic Surfactants: $a_{1s} \equiv c_1$)
Henry	$Ka_{1s} = \frac{\Gamma_1}{\Gamma_\infty}$
Freundlich	$Ka_{1s} = \left(\frac{\Gamma_1}{\Gamma_\infty}\right)^{1/m}$
Langmuir	$Ka_{1s} = \frac{\Gamma_1}{\Gamma_\infty - \Gamma_1}$
Volmer	$Ka_{1s} = \frac{\Gamma_1}{\Gamma_\infty - \Gamma_1} \exp\left(\frac{\Gamma_1}{\Gamma_\infty - \Gamma_1}\right)$
Frumkin	$Ka_{1s} = \frac{\Gamma_1}{\Gamma_\infty - \Gamma_1} \exp\left(-\frac{2\beta\Gamma_1}{kT}\right)$
van der Waals	$Ka_{1s} = \frac{\Gamma_1}{\Gamma_\infty - \Gamma_1} \exp\left(\frac{\Gamma_1}{\Gamma_\infty - \Gamma_1} - \frac{2\beta\Gamma_1}{kT}\right)$
	Surface Tension Isotherm $\sigma = \sigma_0 - kTJ + \sigma_d$ (for Nonionic Surfactants: $\sigma_d \equiv 0$)
Henry	$J = \Gamma_1$
Freundlich	$J = \frac{\Gamma_1}{m}$
Langmuir	$J = -\Gamma_\infty \ln\left(1 - \frac{\Gamma_1}{\Gamma_\infty}\right)$
Volmer	$J = \frac{\Gamma_\infty\Gamma_1}{\Gamma_\infty - \Gamma_1}$
Frumkin	$J = -\Gamma_\infty \ln\left(1 - \frac{\Gamma_1}{\Gamma_\infty}\right) - \frac{\beta\Gamma_1^2}{kT}$
van der Waals	$J = \frac{\Gamma_\infty\Gamma_1}{\Gamma_\infty - \Gamma_1} - \frac{\beta\Gamma_1^2}{kT}$

Note: The surfactant adsorption isotherm and the surface tension isotherm, which are combined to fit experimental data, obligatorily must be of the same type.

per adsorption site. In the case of nonlocalized adsorption (Volmer and van der Waals isotherms), $1/\Gamma_\infty$ is the excluded area per molecule.

The standard free energy of surfactant adsorption, ΔG° , can be determined by nonlinear fits of surface tension isotherms with the help of a theoretical model of adsorption. The models of Frumkin, van der Waals, and Helfant–Frisch–Lebowitz have been applied, and the results have been compared [16]. Irrespective of the differences between these models, they give close values for the standard free energy because all of them reduce to the Henry isotherm for diluted adsorption layers. The results from the theoretical approach have been compared with those of the most popular empirical approach [17]. The latter gives values of the standard free energy, which are considerably different from the respective true values, with ca. 10 kJ/mol for nonionic surfactants, and 20 kJ/mol for ionic surfactants. These differences are due to contributions from interactions between the molecules in dense adsorption layers. The true values of the standard free energy can be determined with the help of an appropriate theoretical model. The van der Waals model was

found to give the best results, especially for the determination of the standard adsorption enthalpy ΔH° and entropy ΔS° from the temperature dependence of surface tension [16].

As already mentioned, the Freundlich adsorption isotherm, unlike the other ones in Table 4.2, does not become linear at low concentrations, but remains convex to the concentration axis. Moreover, it does not show saturation or limiting value. Hence, for the Freundlich adsorption isotherm in Table 4.2 Γ_∞ is a parameter scaling the adsorption (rather than saturation adsorption). This isotherm can be derived assuming that the surface (as a rule solid) is heterogeneous [18,19]. Consequently, if the data fit the Freundlich equation, this is an indication, but not a proof, that the surface is heterogeneous [6].

The *adsorption* isotherms in Table 4.2 can be applied to both fluid and solid interfaces. The *surface tension* isotherms in Table 4.2, which relate σ and Γ_1 , are usually applied to fluid interfaces, although they could also be used also for solid–liquid interfaces if σ is identified with the Gibbs [4] *superficial* tension. (The latter is defined as the force per unit length which opposes every increase of the wet area without any deformation of the solid.)

The surface tension isotherms in Table 4.2 are deduced from the respective adsorption isotherms in the following way. The integration of Equation 4.2 yields

$$\sigma = \sigma_0 - kTJ \quad (4.4)$$

where σ_0 is the interfacial tension of the pure solvent and

$$J \equiv \int_0^{c_1} \Gamma_1 \frac{dc_1}{c_1} = \int_0^{\Gamma_1} \frac{d \ln c_1}{d\Gamma_1} d\Gamma_1 \quad (4.5)$$

The derivative $d \ln c_1/d\Gamma_1$ is calculated for each adsorption isotherm, and then the integration in Equation 4.5 is carried out analytically. The obtained expressions for J are listed in Table 4.2. Each surface tension isotherm, $\sigma(\Gamma_1)$, has the meaning of a *2D equation of state* of the adsorption monolayer, which can be applied to both *soluble* and *insoluble* surfactants [6,20].

An important thermodynamic property of a surfactant adsorption monolayer is its Gibbs (surface) elasticity

$$E_G \equiv -\Gamma_1 \left(\frac{\partial \sigma}{\partial \Gamma_1} \right)_T \quad (4.6)$$

Expressions for E_G , corresponding to various adsorption isotherms, are shown in Table 4.3. The Gibbs elasticity characterizes the lateral fluidity of the surfactant adsorption monolayer. At high values of the Gibbs elasticity the adsorption monolayer behaves as tangentially immobile. In such case, if two emulsion droplets approach each other, the hydrodynamic flow pattern, and the hydrodynamic interaction as well, is almost the same as if the droplets were solid. For lower values of the surfactant adsorption the so-called “Marangoni effect” appears, which is equivalent to appearance of gradients of surface tension due to gradients of surfactant adsorption: $\nabla_s \sigma = -(E_G/\Gamma_1) \nabla_s \Gamma_1$ (here ∇_s denotes surface gradient operator). The Marangoni effect can considerably affect the hydrodynamic interactions of fluid particles (drops, bubbles), (see Section 4.5).

4.2.1.1.2 Derivation from First Principles

Each surfactant adsorption isotherm (that of Langmuir, Volmer, Frumkin, etc.), and the related expressions for the surface tension and surface chemical potential, can be derived from an expression for the surface free energy, F_s , which corresponds to a given physical model. This derivation helps us obtain (or identify) the self-consistent system of equations, referring to a given model,

TABLE 4.3
Elasticity of Adsorption Monolayers at a Fluid Interface

Type of Isotherm (cf. Table 4.2)	Gibbs Elasticity E_G
Henry	$E_G = kT\Gamma_1$
Freundlich	$E_G = kT \frac{\Gamma_1}{m}$
Langmuir	$E_G = kT\Gamma_1 \frac{\Gamma_\infty}{\Gamma_\infty - \Gamma_1}$
Volmer	$E_G = kT\Gamma_1 \frac{\Gamma_\infty^2}{(\Gamma_\infty - \Gamma_1)^2}$
Frumkin	$E_G = kT\Gamma_1 \left(\frac{\Gamma_\infty}{\Gamma_\infty - \Gamma_1} - \frac{2\beta\Gamma_1}{kT} \right)$
van der Waals	$E_G = kT\Gamma_1 \left[\frac{\Gamma_\infty^2}{(\Gamma_\infty - \Gamma_1)^2} - \frac{2\beta\Gamma_1}{kT} \right]$

Note: The above expressions are valid for both nonionic and ionic surfactants.

which is to be applied to interpret a set of experimental data. Combination of equations corresponding to different models (say Langmuir adsorption isotherm with Frumkin surface tension isotherm) is incorrect and must be avoided.

The general scheme for derivation of the adsorption isotherms is the following:

1. With the help of statistical mechanics an expression is obtained, say, for the canonical ensemble partition function, Q , from which the surface free energy F_s is determined [11]:

$$F_s(T, A, N_1) = -kT \ln Q(T, A, N_1) \quad (4.7)$$

where

A is the interfacial area

N_1 is the number of adsorbed surfactant molecules; see Table 4.4

2. Differentiating the expression for F_s , we derive expressions for the *surface pressure*, π_s , and the *surface chemical potential* of the adsorbed surfactant molecules, μ_{1s} [11]:

$$\pi_s \equiv \sigma_0 - \sigma = - \left(\frac{\partial F_s}{\partial A} \right)_{T, N_1}, \quad \mu_{1s} = \left(\frac{\partial F_s}{\partial N_1} \right)_{T, A} \quad (4.8)$$

Combining the obtained expressions for π_s and μ_{1s} , we can deduce the respective form of the Butler equation [21], see Equation 4.16.

3. The surfactant adsorption isotherm (Table 4.2) can be derived by setting the obtained expression for the surface chemical potential μ_{1s} equal to the bulk chemical potential of the surfactant molecules in the subsurface layer (i.e., equilibrium between surface and subsurface is assumed) [11]:

$$\mu_{1s} = \mu_1^{(0)} + kT \ln \left(\frac{a_{1s} \delta_1}{\Gamma_\infty} \right) \quad (4.9)$$

TABLE 4.4
Free Energy and Chemical Potential for Surfactant Adsorption Layers

Type of Isotherm	Surface Free Energy $F_s(T, A, N_1)$ ($M = \Gamma_\infty A$)	
	Henry	$F_s = N_1 \mu_{1s}^{(0)} + kT \left[N_1 \ln \left(\frac{N_1}{M} \right) - N_1 \right]$
Freundlich	$F_s = N_1 \mu_{1s}^{(0)} + \frac{kT}{m} \left[N_1 \ln \left(\frac{N_1}{M} \right) - N_1 \right]$	
Langmuir	$F_s = N_1 \mu_{1s}^{(0)} + kT [N_1 \ln N_1 + (M - N_1) \ln(M - N_1) - M \ln M]$	
Volmer	$F_s = N_1 \mu_{1s}^{(0)} + kT [N_1 \ln N_1 - N_1 - N_1 \ln(M - N_1)]$	
Frumkin	$F_s = N_1 \mu_{1s}^{(0)} + kT [N_1 \ln N_1 + (M - N_1) \ln(M - N_1) - M \ln M] + \frac{\beta \Gamma_\infty N_1^2}{2M}$	
van der Waals	$F_s = N_1 \mu_{1s}^{(0)} + kT [N_1 \ln N_1 - N_1 - N_1 \ln(M - N_1)] + \frac{\beta \Gamma_\infty N_1^2}{2M}$	
Surface Chemical Potential μ_{1s} ($\theta \equiv \Gamma_1 / \Gamma_\infty$)		
Henry	$\mu_{1s} = \mu_{1s}^{(0)} + kT \ln \theta$	
Freundlich	$\mu_{1s} = \mu_{1s}^{(0)} + \frac{kT}{m} \ln \theta$	
Langmuir	$\mu_{1s} = \mu_{1s}^{(0)} + kT \ln \frac{\theta}{1 - \theta}$	
Volmer	$\mu_{1s} = \mu_{1s}^{(0)} + kT \left(\frac{\theta}{1 - \theta} + \ln \frac{\theta}{1 - \theta} \right)$	
Frumkin	$\mu_{1s} = \mu_{1s}^{(0)} + kT \ln \frac{\theta}{1 - \theta} - 2\beta \Gamma_1$	
van der Waals	$\mu_{1s} = \mu_{1s}^{(0)} + kT \left(\frac{\theta}{1 - \theta} + \ln \frac{\theta}{1 - \theta} \right) - 2\beta \Gamma_1$	

Here a_{1s} is the activity of the surfactant molecule in the subsurface layer; a_{1s} is scaled with the volume per molecule in a dense (saturated) adsorption layer, $v_1 = \delta_1 / \Gamma_\infty$, where δ_1 is interpreted as the thickness of the adsorption layer, or the length of an adsorbed molecule. In terms of the subsurface activity, a_{1s} , Equation 4.9 can be applied to ionic surfactants and to dynamic processes. In the simplest case of nonionic surfactants and equilibrium processes we have $a_{1s} \approx c_1$, where c_1 is the bulk surfactant concentration.

First, let us apply the general scheme mentioned earlier to derive the *Frumkin isotherm*, which corresponds to *localized* adsorption of *interacting* molecules. (Expressions corresponding to the Langmuir isotherm can be obtained by setting $\beta = 0$ in the respective expressions for the Frumkin isotherm.) Let us consider the interface as a 2D lattice having M adsorption sites. The corresponding partition function is [11]

$$Q(T, M, N_1) = \frac{M!}{N_1! (M - N_1)!} [q(T)]^{N_1} \exp\left(-\frac{n_c w N_1^2}{2kTM}\right) \quad (4.10)$$

The first multiplier in the right-hand side of Equation 4.10 expresses the number of ways N_1 indistinguishable molecules can be distributed among M labeled sites; the partition function for a single

adsorbed molecule is $q = q_x q_y q_z$, where q_x , q_y , and q_z are 1D harmonic-oscillator partition functions. The exponent in Equation 4.10 accounts for the interaction between adsorbed molecules in the framework of the Bragg–Williams approximation [11]. w is the nearest-neighbor interaction energy of two molecules and n_c is the number of nearest-neighbor sites to a given site (for example $n_c = 4$ for a square lattice). Next, we substitute Equation 4.10 into Equation 4.7 and using the known Stirling approximation, $\ln M! = M \ln M - M$, we get the expression for the surface free energy corresponding to the Frumkin model:

$$F_s = kT[N_1 \ln N_1 + (M - N_1) \ln(M - N_1) - M \ln M - N_1 \ln q(T)] + \frac{n_c w N_1^2}{2M} \quad (4.11)$$

Note that

$$M = \Gamma_\infty A, \quad N_1 = \Gamma_1 A \quad (4.12)$$

where Γ_∞^{-1} is the area per one adsorption site in the lattice. Differentiating Equation 4.11 in accordance with Equation 4.8, we deduce expressions for the surface pressure and chemical potential [11]:

$$\pi_s = -\Gamma_\infty kT \ln(1 - \theta) - \beta \Gamma_1^2 \quad (4.13)$$

$$\mu_{1s} = \mu_{1s}^{(0)} + kT \ln \frac{\theta}{1 - \theta} \mp 2\beta \Gamma_1 \quad (4.14)$$

where we have introduced the notation

$$\theta = \frac{\Gamma_1}{\Gamma_\infty}, \quad \beta = -\frac{n_c w}{2\Gamma_\infty}, \quad \mu_{1s}^{(0)} = -kT \ln q(T) \quad (4.15)$$

We can check that Equation 4.13 is equivalent to the Frumkin's surface tension isotherm in Table 4.2 for a nonionic surfactant. Furthermore, eliminating $\ln(1 - \theta)$ between Equations 4.13 and 4.14, we obtain the Butler [21] equation in the form

$$\mu_{1s} = \mu_{1s}^{(0)} + \Gamma_\infty^{-1} \pi_s + kT \ln(\gamma_{1s} \theta) \quad \text{Butler equation} \quad (4.16)$$

where we have introduced the surface activity coefficient

$$\gamma_{1s} = \exp \left[-\frac{\beta \Gamma_\infty \theta (2 - \theta)}{kT} \right] \quad \text{\textcircled{f} (for Frumkin isotherm)} \quad (4.17)$$

(In the special case of Langmuir isotherm we have $\beta = 0$, and then $\gamma_{1s} = 1$.) The Butler equation is used by many authors [12,22–24] as a starting point for the development of thermodynamic adsorption models. It should be kept in mind that the specific form of the expressions for π_s and γ_{1s} , which are to be substituted in Equation 4.16, is not arbitrary, but must correspond to the *same* thermodynamic model (to the same expression for F_s —in our case Equation 4.11). At last, substituting Equation 4.16 into Equation 4.9, we derive the Frumkin adsorption isotherm in Table 4.2, where K is defined by Equation 4.3.

Now, let us apply the same general scheme, but this time to the derivation of the *van der Waals isotherm*, which corresponds to *nonlocalized* adsorption of *interacting* molecules. (Expressions corresponding to the Volmer isotherm can be obtained by setting $\beta = 0$ in the respective expressions

for the van der Waals isotherm.) Now the adsorbed N_1 molecules are considered as a 2D gas. The corresponding expression for the canonical ensemble partition function is

$$Q(T, M, N_1) = \frac{1}{N_1!} q^{N_1} \exp\left(-\frac{n_c w N_1^2}{2kTM}\right) \quad (4.18)$$

where the exponent accounts for the interaction between adsorbed molecules, again in the framework of the Bragg–Williams approximation. The partition function for a single adsorbed molecule is $q = q_{xy}q_z$, where q_z is 1D (normal to the interface) harmonic-oscillator partition function. On the other hand, the adsorbed molecules have free translational motion in the xy -plane (the interface); therefore we have [11]

$$q_{xy} = \frac{2\pi\tilde{m}kT}{h_p^2} \hat{A} \quad (4.19)$$

where

\tilde{m} is the molecular mass

h_p is the Planck constant

$\hat{A} = A - N_1\Gamma_\infty^{-1}$ is the area accessible to the moving molecules; the parameter Γ_∞^{-1} is the excluded area per molecule, which accounts for the molecular size

Having in mind that $M \equiv \Gamma_\infty A$, we can bring Equation 4.18 into the form

$$Q(T, M, N_1) = \frac{1}{N_1!} q_0^{N_1} (M - N_1)^{N_1} \exp\left(-\frac{n_c w N_1^2}{2kTM}\right) \quad (4.20)$$

where

$$q_0(T) \equiv \frac{2\pi\tilde{m}kT}{h_p^2\Gamma_\infty} q_z(T) \quad (4.21)$$

Further, we substitute Equation 4.20 into Equation 4.7 and, using the Stirling approximation, we determine the surface free energy corresponding to the van der Waals model [11,20,25]:

$$F_s = kT[N_1 \ln N_1 - N_1 - N_1 \ln q_0(T) - N_1 \ln(M - N_1)] + \frac{n_c w N_1^2}{2M} \quad (4.22)$$

Again, having in mind that $M \equiv \Gamma_\infty A$, we differentiate Equation 4.22 in accordance with Equation 4.8 to deduce expressions for the surface pressure and chemical potential:

$$\pi_s = \Gamma_\infty kT \frac{\theta}{1-\theta} - \beta\Gamma_1^2 \quad (4.23)$$

$$\mu_{1s} = \mu_{1s}^{(0)} + kT \left(\frac{\theta}{1-\theta} + \ln \frac{\theta}{1-\theta} \right) \mp 2\beta\Gamma_1 \quad (4.24)$$

where

$$\mu_{1s}^{(0)} = -kT \ln q_0(T)$$

β is defined by Equation 4.14

We can check that Equation 4.23 is equivalent to the van der Waals surface tension isotherm in Table 4.2 for a nonionic surfactant. Furthermore, combining Equations 4.23 and 4.24, we obtain the Butler Equation 4.16, but this time with another expression for the surface activity coefficient

$$\gamma_{1s} = \frac{1}{1-\theta} \exp \left[-\frac{\beta \Gamma_{\infty} \theta (2-\theta)}{kT} \right] \quad (\text{for van der Waals isotherm}) \quad (4.25)$$

[In the special case of Volmer isotherm we have $\beta = 0$, and then $\gamma_{1s} = 1/(1-\theta)$.] Finally, substituting Equation 4.24 into Equation 4.9, we derive the van der Waals adsorption isotherm in Table 4.2, with K defined by Equation 4.3.

In Table 4.4 we summarize the expressions for the surface free energy, F_s , and chemical potential μ_{1s} , for several thermodynamic models of adsorption. We recall that the parameter Γ_{∞} is defined in different ways for the different models. On the other hand, the parameter K is defined in the same way for all models, viz. by Equation 4.3. The expressions in Tables 4.2 through 4.4 can be generalized for multicomponent adsorption layers [20,26].

At the end of this section, let us consider a general expression, which allows us to obtain the surface activity coefficient γ_{1s} directly from the surface pressure isotherm $\pi_s(\theta)$. From the Gibbs adsorption isotherm, $d\pi_s = \Gamma_1 d\mu_{1s}$, it follows that

$$\left(\frac{\partial \mu_{1s}}{\partial \Gamma_1} \right)_T = \frac{1}{\Gamma_1} \left(\frac{\partial \pi_s}{\partial \Gamma_1} \right)_T \quad (4.26)$$

By substituting μ_{1s} from the Butler's Equation 4.16 into Equation 4.26 and integrating, we can derive the sought for expression:

$$\ln \gamma_{1s} = \int_0^{\theta} \left(\frac{(1-\theta)}{\Gamma_{\infty} kT} \frac{\partial \pi_s}{\partial \theta} - 1 \right) \frac{d\theta}{\theta} \quad (4.27)$$

We can check that a substitution of π_s from Equations 4.13 and 4.23 into Equation 4.27 yields, respectively, the Frumkin and van der Waals expressions for γ_{1s} , viz. Equations 4.17 and 4.24.

4.2.1.2 Ionic Surfactants

4.2.1.2.1 The Gouy Equation

The thermodynamics of adsorption of *ionic* surfactants [13,26–30] is more complicated (in comparison with that of nonionics) because of the presence of long-range electrostatic interactions and, in particular, electric double layer (EDL) in the system, see Figure 4.1. The electro-chemical potential of the ionic species can be expressed in the form [31]

$$\mu_i = \mu_i^{(0)} + kT \ln a_i + Z_i e \psi \quad (4.28)$$

where

e is the elementary electric charge

ψ is the electric potential

Z_i is the valence of the ionic component “ i ”

a_i is its activity

In the EDL (Figure 4.1), the electric potential and the activities of the ions are dependent on the distance z from the phase boundary: $\psi = \psi(z)$, $a_i = a_i(z)$. At equilibrium the electrochemical

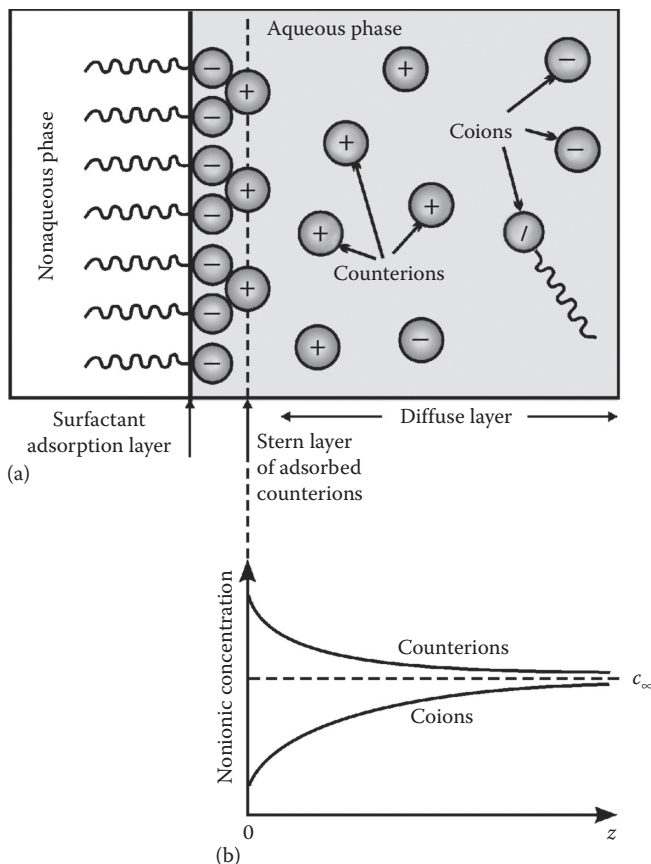


FIGURE 4.1 Electric double layer in the vicinity of an adsorption layer of ionic surfactant. (a) The diffuse layer contains free ions involved in Brownian motion, while the Stern layer consists of adsorbed (bound) counterions. (b) Near the charged surface there is an accumulation of counterions and a depletion of coions.

potential, μ_i , is uniform throughout the whole solution, including the EDL (otherwise diffusion fluxes would appear) [31]. In the bulk of solution ($z \rightarrow \infty$) the electric potential tends to a constant value, which is usually set equal to zero, that is $\psi \rightarrow 0$ and $\partial\psi/\partial z \rightarrow 0$ for $z \rightarrow \infty$. If the expression for μ_i at $z \rightarrow \infty$ and that for μ_i at some finite z are set equal, from Equation 4.28 we obtain a Boltzmann-type distribution for the activity across the EDL [31]:

$$a_i(z) = a_{i\infty} \exp \left[-\frac{Z_i e \psi(z)}{kT} \right] \quad (4.29)$$

where $a_{i\infty}$ denotes the value of the activity of ion “ i ” in the bulk of solution. If the activity in the bulk, $a_{i\infty}$, is known, then Equation 4.29 determines the activity $a_i(z)$ in each point of the EDL. A good agreement between theory and experiment can be achieved [12,13,26] using the following expression for $a_{i\infty}$:

$$a_{i\infty} = \gamma_{\pm} C_{i\infty} \quad (4.30)$$

where

$c_{i\infty}$ is the bulk concentration of the respective ion
the activity coefficient γ_{\pm} is calculated from the known formula [32]

$$\log \gamma_{\pm} = - \frac{A|Z_+Z_-|\sqrt{I}}{1 + Bd_i\sqrt{I}} + bI \quad (4.31)$$

which originates from the Debye–Hückel theory; I denotes the ionic strength of the solution:

$$I \equiv \frac{1}{2} \sum_i Z_i^2 c_{i\infty} \quad (4.32)$$

where the summation is carried out over all ionic species in the solution. When the solution contains a mixture of several electrolytes, then Equation 4.31 defines γ_{\pm} for each separate electrolyte, with Z_+ and Z_- being the valences of the cations and anions of *this* electrolyte, but with I being the *total* ionic strength of the solution, accounting for all dissolved electrolytes [32]. The log in Equation 4.31 is decimal, d_i is the ionic diameter, A , B , and b are parameters, whose values can be found in the book by Robinson and Stokes [32]. For example, if I is given in moles per liter (M), the parameters values are $A = 0.5115 \text{ M}^{-1/2}$, $Bd_i = 1.316 \text{ M}^{-1/2}$, and $b = 0.055 \text{ M}^{-1}$ for solutions of NaCl at 25°C.

The theory of EDL provides a connection between surface charge and surface potential (known as the Gouy equation [33,34] or Graham equation [35,36]), which can be presented in the form [26,37]

$$\sum_{i=1}^N z_i \Gamma_i = \frac{2}{\kappa_c} \left\{ \sum_{i=1}^N a_{iz} [\exp(-z_i \Phi_s) - 1] \right\}^{1/2} \quad (\text{Gouy equation}) \quad (4.33)$$

where

Γ_i ($i = 1, \dots, N$) are the adsorptions of the ionic species
 $z_i = Z_i/Z_1$

the index $i = 1$ corresponds to the surfactant ions

$$\kappa_c^2 \equiv \frac{2Z_1^2 e^2}{\epsilon_0 \epsilon kT}, \quad \Phi_s \equiv \frac{Z_1 e \psi_s}{kT} \quad (4.34)$$

ϵ is the dielectric permittivity of the medium (water)

$\psi_s = \psi(z = 0)$ is the surface potential

Note that the Debye parameter is $\kappa^2 = \kappa_c^2 I$.

For example, let us consider a solution of an ionic surfactant, which is a symmetric 1:1 electrolyte, in the presence of a symmetric, 1:1, inorganic electrolyte (salt). We assume that the counterions due to the surfactant and salt are identical. For example, this can be a solution of sodium dodecyl sulfate (SDS) in the presence of NaCl. We denote by $c_{1\infty}$, $c_{2\infty}$, and $c_{3\infty}$ the bulk concentrations of the surface-active ions, counterions, and coions, respectively (Figure 4.1). For the special system of SDS with NaCl $c_{1\infty}$, $c_{2\infty}$, and $c_{3\infty}$ are the bulk concentrations of the DS^- , Na^+ and Cl^- ions, respectively. The requirement for the bulk solution to be electroneutral implies $c_{2\infty} = c_{1\infty} + c_{3\infty}$. The multiplication of the last equation by γ_{\pm} yields

$$a_{2\infty} = a_{1\infty} + a_{3\infty} \quad (4.35)$$

The adsorption of the coions of the nonamphiphilic salt is expected to be equal to zero, $\Gamma_3 = 0$, because they are repelled by the similarly charged interface [26,38–40]. However, the adsorption of surfactant at the interface, Γ_1 , and the binding of counterions in the Stern layer, Γ_2 , are different from zero (Figure 4.1). For this system the Gouy Equation 4.33 acquires the form

$$\Gamma_1 - \Gamma_2 = \frac{4}{\kappa_c} \sqrt{a_{2\infty}} \sinh\left(\frac{\Phi_s}{2}\right) \quad (Z_1:Z_1 \text{ electrolyte}) \quad (4.36)$$

4.2.1.2.2 Contributions from the Adsorption and Diffuse Layers

In general, the *total* adsorption $\tilde{\Gamma}_i$ of an ionic species includes contributions from *both* the adsorption layer (surfactant adsorption layer + adsorbed counterions in the Stern layer), Γ_i , and the diffuse layer, Λ_i [13,26,27,29]:

$$\tilde{\Gamma}_i = \Gamma_i + \Lambda_i, \quad \text{where } \Lambda_i \equiv \int_0^\infty [a_i(z) - a_{i\infty}] dz \quad (4.37)$$

and $\tilde{\Gamma}_i$ represents a surface excess of component “*i*” with respect to the *uniform* bulk solution. Because the solution is electroneutral, we have $\sum_{i=1}^N z_i \tilde{\Gamma}_i = 0$. Note, however, that $\sum_{i=1}^N z_i \Gamma_i \neq 0$, see the Gouy Equation 4.33. Expressions for Λ_i can be obtained by using the theory of EDL. For example, because of the electroneutrality of the solution, the right-hand side of Equation 4.36 is equal to $\Lambda_2 - \Lambda_1 - \Lambda_3$, where

$$\Lambda_2 = 2a_{2\infty} \kappa^{-1} \left[\exp\left(\frac{\Phi_s}{2}\right) - 1 \right]; \quad \Lambda_j = 2a_{j\infty} \kappa^{-1} \left[\exp\left(\frac{-\Phi_s}{2}\right) - 1 \right], \quad j = 1, 3 \quad (4.38)$$

($\kappa^2 = \kappa_c^2 I$; $Z_1:Z_1$ electrolyte). In analogy with Equation 4.37, the interfacial tension of the solution, σ , can be expressed as a sum of contributions from the adsorption and diffuse layers [26,27,34]:

$$\sigma = \sigma_a + \sigma_d \quad (4.39)$$

where

$$\sigma_a = \sigma_0 - kTJ \quad \text{and} \quad \sigma_d = -\varepsilon_0 \varepsilon \int_0^\infty \left(\frac{d\psi}{dz} \right)^2 dz \quad (4.40)$$

Expressions for J are given in Table 4.2 for various types of isotherms. Note that Equations 4.39 and 4.40 are valid under both equilibrium and dynamic conditions. In the special case of SDS + NaCl solution (see the text explained earlier), *at equilibrium*, we can use the theory of EDL to express $d\psi/dz$; then from Equation 4.40 we derive [26,27,34]

$$\sigma_d = -\frac{8kT}{\kappa_c} \sqrt{a_{2\infty}} \left[\cosh\left(\frac{\Phi_s}{2}\right) - 1 \right] \quad (Z_1:Z_1 \text{ electrolyte, at equilibrium}) \quad (4.41)$$

Analytical expressions for σ_d for the cases of 2:1, 1:2, and 2:2 electrolytes can be found in Refs. [26,36].

In the case of ionic surfactants, Equation 4.1 can be presented in two alternative, but equivalent forms [26,37]:

$$d\sigma = -kT \sum_{i=1}^N \tilde{\Gamma}_i d \ln a_{i\infty} \quad (T = \text{const.}) \quad (4.42)$$

$$d\sigma_a = -kT \sum_{i=1}^N \Gamma_i d \ln a_{is} \quad (T = \text{const.}) \quad (4.43)$$

where $a_{is} = a_i (z = 0)$ is the “subsurface” value of activity a_i . From Equations 4.29 and 4.34, we obtain

$$a_{is} = a_{i\infty} \exp(-z_i \tilde{\Phi}_s) \quad (4.44)$$

The comparison between Equations 4.42 and 4.43 shows that the Gibbs adsorption equation can be expressed either in terms of σ , $\tilde{\Gamma}_i$, and $a_{i\infty}$, or in terms of σ_a , Γ_i , and a_{is} . Note that Equations 4.42 and 4.44 are valid under *equilibrium* conditions, whereas Equation 4.43 can also be used for the description of *dynamic* surface tension (Section 4.2.2) in the case of surfactant adsorption under diffusion control, assuming local equilibrium between adsorptions Γ_i and subsurface concentrations of the respective species.

The expression $\sigma_a = \sigma_0 - kTJ$, with J given in Table 4.2, can be used for description of both static and dynamic surface tension of ionic and nonionic surfactant solutions. The surfactant adsorption isotherms in this table can be used for both ionic and nonionic surfactants, with the only difference that in the case of ionic surfactant the adsorption constant K depends on the subsurface concentration of the inorganic counterions [26], see Equation 4.48.

4.2.1.2.3 The Effect of Counterion Binding

As an example, let us consider again the special case of SDS + NaCl solution. In this case, the Gibbs adsorption equation (4.1) takes the form

$$d\sigma_a = -kT(\Gamma_1 d \ln a_{1s} + \Gamma_2 d \ln a_{2s}) \quad (4.45)$$

where as before, the indices “1” and “2” refer to the DS⁻ and Na⁺ ions, respectively. The differentials in the right-hand side of Equation 4.45 are independent (we can vary independently the concentrations of surfactant and salt), and moreover, $d\sigma_a$ is an exact (total) differential. Then, according to the Euler condition, the cross derivatives must be equal [26]:

$$\frac{\partial \Gamma_1}{\partial \ln a_{2s}} = \frac{\partial \Gamma_2}{\partial \ln a_{1s}} \quad (4.46)$$

A surfactant adsorption isotherm, $\Gamma_1 = \Gamma_1(a_{1s}, a_{2s})$, and a counterion adsorption isotherm, $\Gamma_2 = \Gamma_2(a_{1s}, a_{2s})$, are *thermodynamically compatible* only if they satisfy Equation 4.46. The counterion adsorption isotherm is usually taken in the form

$$\frac{\Gamma_2}{\Gamma_1} = \frac{K_2 a_{2s}}{1 + K_2 a_{2s}} \quad (\text{Stern isotherm}) \quad (4.47)$$

where K_2 is a constant parameter. The latter equation, termed the *Stern isotherm* [41], describes Langmuirian adsorption (binding) of counterions in the Stern layer. It can be proven that a sufficient condition Γ_2 from Equation 4.47 to satisfy the Euler's condition 4.46, together with one of the surfactant adsorption isotherms for Γ_1 in Table 4.2, is [26]

$$K = K_1(1 + K_2 a_{2,s}) \quad (4.48)$$

where K_1 is another constant parameter. In other words, if K is expressed by Equation 4.48, the Stern isotherm 4.47 is thermodynamically compatible with each of the surfactant adsorption isotherms in Table 4.2. In analogy with Equation 4.3, the parameters K_1 and K_2 are related to the respective standard free energies of adsorption of surfactant ions and counterions $\Delta\mu_i^{(0)}$:

$$K_i = \frac{\delta_i}{\Gamma_\infty} \exp\left(\frac{\Delta\mu_i^{(0)}}{kT}\right) \quad (i = 1, 2) \quad (4.49)$$

where δ_i stands for the thickness of the respective adsorption layer.

4.2.1.2.4 Dependence of Adsorption Parameter K on Salt Concentration

The physical meaning of Equation 4.48 can be revealed by chemical-reaction considerations. For simplicity, let us consider *Langmuir*-type adsorption, that is, we treat the interface as a 2D lattice. We will use the notation θ_0 for the fraction of the free sites in the lattice, θ_1 for the fraction of sites containing adsorbed surfactant ion S^- , and θ_2 for the fraction of sites containing the complex of an adsorbed surfactant ion + a bound counterion. Obviously, we can write $\theta_0 + \theta_1 + \theta_2 = 1$. The adsorptions of surfactant ions and counterions can be expressed in the form:

$$\frac{\Gamma_1}{\Gamma_\infty} = \theta_1 + \theta_2; \quad \frac{\Gamma_2}{\Gamma_\infty} = \theta_2 \quad (4.50)$$

Following Kalinin and Radke [28], we consider the "reaction" of adsorption of S^- ions:



where A_0 symbolizes an empty adsorption site. In accordance with the rules of the chemical kinetics, we can express the rates of adsorption and desorption in the form:

$$r_{1,ads} = K_{1,ads}\theta_0c_{1s}, \quad r_{1,des} = K_{1,des}\theta_1 \quad (4.52)$$

where

c_{1s} is the subsurface concentration of surfactant

$K_{1,ads}$ and $K_{1,des}$ are constants

In view of Equation 4.50, we can write $\theta_0 = (\Gamma_\infty - \Gamma_1)/\Gamma_\infty$ and $\theta_1 = (\Gamma_1 - \Gamma_2)/\Gamma_\infty$. Thus, with the help of Equation 4.52 we obtain the net adsorption flux of surfactant:

$$Q_1 \equiv r_{1,ads} - r_{1,des} = K_{1,ads}c_{1s} \frac{(\Gamma_\infty - \Gamma_1)}{\Gamma_\infty} - K_{1,des} \frac{(\Gamma_1 - \Gamma_2)}{\Gamma_\infty} \quad (4.53)$$

Next, let us consider the reaction of counterion binding:



The rates of the direct and reverse reactions are, respectively,

$$r_{2,ads} = K_{2,ads}\theta_1c_{2s}, \quad r_{2,des} = K_{2,des}\theta_2 \quad (4.55)$$

where

$K_{2,ads}$ and $K_{2,des}$ are the respective rate constants
 c_{2s} is the subsurface concentration of counterions

Having in mind that $\theta_1 = (\Gamma_1 - \Gamma_2)/\Gamma_\infty$ and $\theta_2 = \Gamma_2/\Gamma_\infty$, with the help of Equation 4.55 we deduce an expression for the adsorption flux of counterions:

$$Q_2 \equiv r_{2,ads} - r_{2,des} = K_{2,ads}c_{2s} \frac{(\Gamma_1 - \Gamma_2)}{\Gamma_\infty} - K_{2,des} \frac{\Gamma_2}{\Gamma_\infty} \quad (4.56)$$

If we can assume that the reaction of counterion binding is much faster than the surfactant adsorption, then we can set $Q_2 \equiv 0$, and Equation 4.56 reduces to the Stern isotherm, Equation 4.47, with $K_2 \equiv K_{2,ads}/K_{2,des}$. Next, a substitution of Γ_2 from Equation 4.47 into Equation 4.53 yields [37]

$$Q_1 \equiv r_{1,ads} - r_{1,des} = K_{1,ads}c_{1s} \frac{(\Gamma_\infty - \Gamma_1)}{\Gamma_\infty} - K_{1,des}(1 + K_2c_{2s})^{-1} \frac{\Gamma_1}{\Gamma_\infty} \quad (4.57)$$

Equation 4.57 shows that the adsorption flux of surfactant is influenced by the subsurface concentration of counterions, c_{2s} . At last, if there is equilibrium between surface and subsurface, we have to set $Q_1 \equiv 0$ in Equation 4.57, and thus we obtain the Langmuir isotherm for an ionic surfactant:

$$Kc_{1s} = \frac{\Gamma_1}{\Gamma_\infty - \Gamma_1}, \quad \text{with } K \equiv \frac{K_{1,ads}}{K_{1,des}}(1 + K_2c_{2s}) \quad (4.58)$$

Note that $K_1 \equiv K_{1,ads}/K_{1,des}$. This result demonstrates that the linear dependence of K on c_{2s} (Equation 4.48) can be deduced from the reactions of surfactant adsorption and counterion binding, Equations 4.51 and 4.54. (For $I < 0.1$ M we have $\gamma_\pm \approx 1$ and then activities and concentrations of the ionic species coincide.)

4.2.1.2.5 Comparison of Theory and Experiment

As illustration, we consider the interpretation of experimental isotherms by Tajima et al. [40,42,43] for the surface tension σ versus SDS concentrations at 11 fixed concentrations of NaCl, see Figure 4.2. Processing the set of data for the interfacial tension $\sigma = \sigma(c_{1\infty}, c_{2\infty})$ as a function of the bulk concentrations of surfactant (DS^-) ions and Na^+ counterions, $c_{1\infty}$ and $c_{2\infty}$, we can determine the surfactant adsorption, $\Gamma_1(c_{1\infty}, c_{2\infty})$, the counterion adsorption, $\Gamma_2(c_{1\infty}, c_{2\infty})$, the surface potential, $\psi_s(c_{1\infty}, c_{2\infty})$, and the Gibbs elasticity $E_G(c_{1\infty}, c_{2\infty})$ for every desirable surfactant and salt concentrations.

The theoretical dependence $\sigma = \sigma(c_{1\infty}, c_{2\infty})$ is determined by the following *full set of equations*: Equation 4.44 for $i = 1, 2$; the Gouy Equation 4.36, Equation 4.39 (with σ_d expressed by Equation 4.41 and J from Table 4.2), the Stern isotherm 4.47, and one surfactant adsorption isotherm from Table 4.2, say the van der Waals one. Thus, we get a set of six equations for determining six unknown

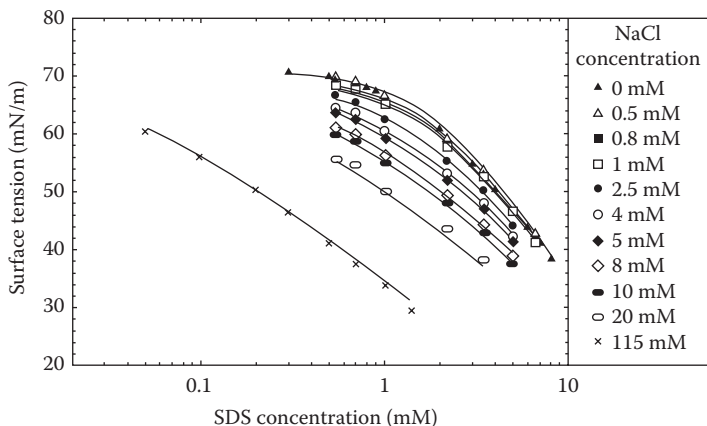


FIGURE 4.2 Plot of the surface tension σ vs. the concentration of SDS, $c_{1\infty}$, for 11 fixed NaCl concentrations. The symbols are experimental data by Tajima et al. [40,42,43]. The lines represent the best fit [42] with the full set of equations specified in the text, involving the van der Waals isotherms of adsorption and surface tension (Table 4.2).

variables: σ , Φ_s , a_{1s} , a_{2s} , Γ_1 and Γ_2 . (For $I < 0.1$ M the activities of the ions can be replaced by the respective concentrations.) The principles of the numerical procedure are described in Ref. [26].

The theoretical model contains four parameters, β , Γ_∞ , K_1 , and K_2 , whose values are to be obtained from the best fit of the experimental data. Note that all 11 curves in Figure 4.2 are fitted simultaneously [44]. In other words, the parameters β , Γ_∞ , K_1 , and K_2 are the same for all curves. The value of Γ_∞ , obtained from the best fit of the data in Figure 4.2, corresponds to $1/\Gamma_\infty = 29.8 \text{ \AA}^2$. The respective value of K_1 is $99.2 \text{ m}^3/\text{mol}$, which in view of Equation 4.49 gives a standard free energy of surfactant adsorption $\Delta\mu_1^{(0)} = 12.53kT$ per DS^- ion, that is 30.6 kJ/mol . The determined value of K_2 is $6.5 \times 10^{-4} \text{ m}^3/\text{mol}$, which after substitution in Equation 4.49 yields a standard free energy of counterion binding $\Delta\mu_2^{(0)} = 1.64kT$ per Na^+ ion, that is, 4.1 kJ/mol . The value of the parameter β is positive, $2\beta\Gamma_\infty/kT = +2.73$, which indicates attraction between the hydrocarbon tails of the

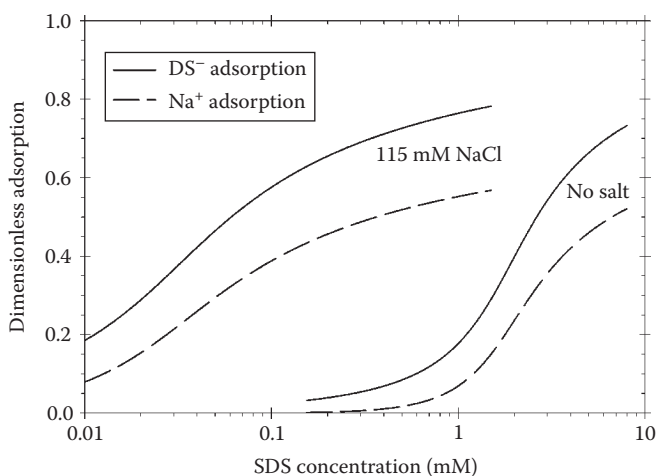


FIGURE 4.3 Plots of the dimensionless adsorptions of surfactant ions Γ^1/Γ_∞ (DS^- , the full lines), and counterions Γ^2/Γ_∞ (Na^+ , the dotted lines), vs. the surfactant (SDS) concentration, $c_{1\infty}$. The lines are calculated [44] for NaCl concentrations 0 and 115 mM using parameter values determined from the best fit of experimental data (Figure 4.2).

adsorbed surfactant molecules. However, this attraction is too weak to cause 2D phase transition. The van der Waals isotherm predicts such transition for $2\beta\Gamma_{\infty}/kT > 6.74$.

Figure 4.3 shows calculated curves for the adsorptions of surfactant, Γ_1 (the full lines), and counterions, Γ_2 (the dotted lines), versus the SDS concentration, $c_{1\infty}$. These lines represent the variations of Γ_1 and Γ_2 along the experimental curves, which correspond to the lowest and highest NaCl concentrations in Figure 4.2, viz. $c_{3\infty} = 0$ and 115 mM. We see that both Γ_1 and Γ_2 are markedly greater when NaCl is present in the solution. The highest values of Γ_1 for the curves in Figure 4.3 are 4.2×10^{-6} and 4.0×10^{-6} mol/m² for the solutions with and without NaCl, respectively. The latter two values compare well with the saturation adsorptions measured by Tajima et al. [42,43] for the same system by means of the radiotracer method, viz. $\Gamma_1 = 4.3 \times 10^{-6}$ and 3.2×10^{-6} mol/m² for the solutions with and without NaCl, respectively.

For the solution *without* NaCl the occupancy of the Stern layer, Γ_2/Γ_1 , rises from 0.15 to 0.73 and then exhibits a tendency to level off. The latter value is consonant with data of other authors [45–47], who have obtained values of Γ_2/Γ_1 up to 0.70–0.90 for various ionic surfactants; pronounced evidences for counterion binding have also been obtained also in experiments with solutions containing surfactant micelles [48–52]. As it could be expected, both Γ_1 and Γ_2 are higher for the solution *with* NaCl. These results imply that the counterion adsorption (binding) should be always be taken into account.

The fit of the data in Figure 4.2 also gives the values of the surface electric potential, ψ_s . For the solutions with 115 mM NaCl the model predicts surface potentials varying in the range $|\psi_s| = 55$ –95 mV within the experimental interval of surfactant concentrations, whereas for the solution without salt the calculated surface potential is higher: $|\psi_s| = 150$ –180 mV (for SDS ψ_s has a negative sign). Thus it turns out that measurements of surface tension, interpreted by means of an appropriate theoretical model, provide a method for determining the surface potential ψ_s in a broad range of surfactant and salt concentrations. The described approach could be also applied to solve the inverse problem, viz. to process data for the surface potential. In this way, the adsorption of surfactant on solid particles can be determined from the measured zeta-potential [53].

It is remarkable that the minimal (excluded) area per adsorbed surfactant molecule, $\alpha \equiv 1/\Gamma_{\infty}$, obtained from the best fit of surface tension data by the *van der Waals isotherm* practically coincides with the value of α estimated by molecular size considerations (i.e., from the maximal cross-sectional area of an amphiphilic molecule in a dense adsorption layer); see for example Figure 7.1 in Ref. [36]. This is illustrated in Table 4.5, which contains data for alkanols, alkanolic acids, (SDS), (DDBS), cocamidopropyl betaine (CAPB), and C_n -trimethyl ammonium bromides ($n = 12, 14,$ and 16). The second column of Table 4.5 gives the group whose cross-sectional area is used to calculate α . For molecules of circular cross section, we can calculate the cross-sectional area from the expression $\alpha = \pi r^2$, where r is the respective radius. For example [54], the radius of the SO_4^{2-} ion is $r =$

TABLE 4.5
Excluded Area per Molecule, α , Determined in Two Different Ways

Amphiphile	Group	α from Molecular Size (\AA^2)	α from Surface Tension Fits ^a (\AA^2)	References
Alkanols	Paraffin chain	21.0	20.9	[54]
Alkanolic acids	COO^-	22–24	22.6	[55,56]
SDS	SO_4^{2-}	30.0	30	[44,57]
DDBS	Benzene ring	35.3	35.6	[58]
CAPB	$\text{CH}_3\text{-N}^+\text{-CH}_3$	27.8	27.8	[59]
C_n TAB ($n = 12, 14, 16$)	$\text{N}(\text{CH}_3)_4^+$	37.8	36.5–39.5	[57,60]

^a Fit by means of the van der Waals isotherm.

3.09 Å, which yields $\alpha = \pi r^2 = 30.0 \text{ \AA}^2$. In the fits of surface tension data by the van der Waals isotherm, α was treated as an adjustable parameter, and the value $\alpha = 30 \text{ \AA}^2$ was obtained from the best fit. As seen in Table 4.5, excellent agreement between the values of α obtained from molecular size and from surface tension fits is obtained also for many other amphiphilic molecules [54–61].

It should be noted the result mentioned earlier holds only for the van der Waals (or Volmer) isotherm. Instead, if the Frumkin (or Langmuir) isotherm is used, the value of α obtained from the surface tension fits is about 33% greater than that obtained from molecular size [44]. A possible explanation of this difference could be the fact that the Frumkin (and Langmuir) isotherm is statistically derived for localized adsorption and is more appropriate to describe adsorption at solid interfaces. In contrast, the van der Waals (and Volmer) isotherm is derived for nonlocalized adsorption, and they provide a more adequate theoretical description of the surfactant adsorption at liquid–fluid interfaces. This conclusion refers also to the calculation of the surface (Gibbs) elasticity by means of the two types of isotherms [44].

The fact that α determined from molecular size coincides with that obtained from surface tension fits (Table 4.5) is very useful for applications. Thus, when fitting experimental data, we can use the value of α from molecular size, and thus to decrease the number of adjustable parameters. This fact is especially helpful when interpreting theoretically data for the surface tension of surfactant mixtures, such as SDS + dodecanol [54]; SDS + CAPB [59], and fluorinated + nonionic surfactant [61]. An additional way to decrease the number of adjustable parameters is to employ the Traube rule, which states that $\Delta\mu_i^{(0)}$ increases with $1.025kT$ when a CH_2 group is added to the paraffin chain; for details see Refs. [54,55,60].

4.2.2 DYNAMIC SURFACE TENSION

If the surface of an equilibrium surfactant solution is disturbed (expanded, compressed, renewed, etc.), the system will try to restore the equilibrium by exchange of surfactant between the surface and the subsurface layer (adsorption–desorption). The change of the surfactant concentration in the subsurface layer triggers a diffusion flux in the solution. In other words, the process of equilibration (relaxation) of an expanded adsorption monolayer involves two consecutive stages:

1. Diffusion of surfactant molecules from the bulk solution to the subsurface layer;
2. Transfer of surfactant molecules from the subsurface to the adsorption layer; the rate of transfer is determined by the height of the kinetic barrier to adsorption.

(In the case of desorption the processes have the opposite direction.) Such interfacial expansions are typical for foam generation and emulsification. The rate of adsorption relaxation determines whether the formed bubbles/drops will coalesce upon collision, and in final reckoning—how large will be the foam volume and the emulsion drop size [62,63]. In the following section, we focus our attention on the relaxation time of surface tension, $\tau\sigma$, which characterizes the interfacial dynamics.

The overall rate of surfactant adsorption is controlled by the slowest stage. If it is stage (1), we deal with *diffusion control*, while if stage (2) is slower, the adsorption occurs under *barrier (kinetic) control*. The next four sections are dedicated to processes under diffusion control (which are the most frequently observed), whereas in Section 4.2.2.5 we consider adsorption under barrier control. Finally, Section 4.2.2.6 is devoted to the dynamics of adsorption from micellar surfactant solutions.

Various experimental methods for dynamic surface tension measurements are available. Their operational time scales cover different time intervals [64,65]. Methods with a *shorter* characteristic operational time are the oscillating jet method [66–68], the oscillating bubble method [69–72], the fast-formed drop technique [73,74], the surface wave techniques [75–78], and the maximum bubble pressure method (MBPM) [57,79–84]. Methods of *longer* characteristic operational time are the inclined plate method [85], the drop-weight/volume techniques [86–90], the funnel [91] and

overflowing cylinder [60,92] methods, and the axisymmetric drop shape analysis (ADSA) [93,94]; see Refs. [64,65,95] for a more detailed review.

In this section, devoted to dynamic surface tension, we consider mostly *nonionic* surfactant solutions. In Section 4.2.2.4 we address the more complicated case of *ionic* surfactants. We will restrict our considerations to the simplest case of *relaxation of an initial uniform interfacial dilatation*. The more complex case of simultaneous adsorption and dilatation is considered elsewhere [57,64,80,84,92,95].

4.2.2.1 Adsorption under Diffusion Control

Here, we consider a solution of a *nonionic* surfactant, whose concentration, $c_1 = c_1(z, t)$, depends on the position and time because of the diffusion process. (As before, z denotes the distance to the interface, which is situated in the plane $z = 0$.) Correspondingly, the surface tension, surfactant adsorption, and the subsurface concentration of surfactant vary with time: $\sigma = \sigma(t)$, $\Gamma_1 = \Gamma_1(t)$, $c_{1s} = c_{1s}(t)$. The surfactant concentration obeys the equation of diffusion:

$$\frac{\partial c_1}{\partial t} = D_1 \frac{\partial^2 c_1}{\partial z^2} \quad (z > 0, t > 0) \quad (4.59)$$

where D_1 is the diffusion coefficient of the surfactant molecules. The exchange of surfactant between the solution and its interface is described by the boundary conditions

$$c_1(0, t) = c_{1s}(t), \quad \frac{d\Gamma_1}{dt} = D_1 \frac{\partial c_1}{\partial z} \quad (z = 0, t > 0) \quad (4.60)$$

The latter equation states that the rate of increase of the adsorption Γ_1 is equal to the diffusion influx of surfactant per unit area of the interface. Integrating Equation 4.59, along with 4.60, we can derive the equation of Ward and Tordai [96]:

$$\Gamma_1(t) = \Gamma_1(0) + \sqrt{\frac{D_1}{\pi}} \left[2c_{1\infty} \sqrt{t} - \int_0^t \frac{c_{1s}(\tau)}{\sqrt{t-\tau}} d\tau \right] \quad (4.61)$$

Solving Equation 4.61 together with some of the adsorption isotherms $\Gamma_1 = \Gamma_1(c_{1s})$ in Table 4.2, we can in principle determine the two unknown functions $\Gamma_1(t)$ and $c_{1s}(t)$. Because the relation $\Gamma_1(c_{1s})$ is nonlinear (except for the Henry isotherm), this problem, or its equivalent formulations, can be solved either numerically [97], or by employing appropriate approximations [80,98].

In many cases, it is convenient to use asymptotic expressions for the functions $\Gamma_1(t)$, $c_{1s}(t)$, and $\sigma(t)$ for *short times* ($t \rightarrow 0$) and *long times* ($t \rightarrow \infty$). A general asymptotic expression for the short times can be derived from Equation 4.61 substituting $c_{1s} \approx c_{1s}(0) = \text{constant}$:

$$\Gamma_1(t) = \Gamma_1(0) + 2\sqrt{\frac{D_1}{\pi}} [c_{1\infty} - c_{1s}(0)]\sqrt{t} \quad (t \rightarrow 0) \quad (4.62)$$

Analogous asymptotic expression can also be obtained for long times, although the derivation is not so simple. Hansen [99] derived a useful asymptotics for the subsurface concentration:

$$c_{1s}(t) = c_{1\infty} - \frac{\Gamma_{1e} - \Gamma(0)}{\sqrt{\pi D_1 t}} \quad (t \rightarrow \infty) \quad (4.63)$$

where $\Gamma_{1,e}$ is the equilibrium value of the surfactant adsorption. The validity of Hansen's Equation 4.63 was confirmed in subsequent studies by other authors [100,101].

In the following section, we continue our review of the asymptotic expressions considering separately the cases of *small* and *large* initial perturbations.

4.2.2.2 Small Initial Perturbation

When the deviation from equilibrium is small, then the adsorption isotherm can be linearized:

$$\Gamma_1(t) - \Gamma_{1,e} \approx \left(\frac{\partial \Gamma_1}{\partial c_1} \right)_e [c_{1s}(t) - c_e] \quad (4.64)$$

Here and hereafter, the subscript "e" means that the respective quantity refers to the equilibrium state. The set of linear Equations 4.59, 4.60, and 4.64 has been solved by Sutherland [102]. The result, which describes the relaxation of a *small* initial interfacial dilatation, reads:

$$\frac{\sigma(t) - \sigma_e}{\sigma(0) - \sigma_e} = \frac{\Gamma_1(t) - \Gamma_{1,e}}{\Gamma_1(0) - \Gamma_{1,e}} = \exp\left(\frac{t}{\tau_\sigma}\right) \operatorname{erfc}\left(\sqrt{\frac{t}{\tau_\sigma}}\right) \quad (4.65)$$

where

$$\tau_\sigma \equiv \frac{1}{D_1} \left(\frac{\partial \Gamma_1}{\partial c_1} \right)_e^2 \quad (4.66)$$

is the characteristic relaxation time of surface tension and adsorption, and

$$\operatorname{erfc}(x) \equiv \frac{2}{\sqrt{\pi}} \int_x^\infty \exp(-x^2) dx \quad (4.67)$$

is the so-called complementary error function [103,104]. The asymptotics of the latter function for small and large values of the argument are [103,104]:

$$\operatorname{erfc}(x) = 1 - \frac{2}{\sqrt{\pi}} x + O(x^3) \text{ for } x \ll 1; \quad \operatorname{erfc}(x) = \frac{e^{-x^2}}{\sqrt{\pi}x} \left[1 + O\left(\frac{1}{x^2}\right) \right] \text{ for } x \gg 1 \quad (4.68)$$

Combining Equations 4.65 and 4.68, we obtain the short-time and long-time asymptotics of the surface tension relaxation:

$$\frac{\sigma(t) - \sigma_e}{\sigma(0) - \sigma_e} = \frac{\Gamma_1(t) - \Gamma_{1,e}}{\Gamma_1(0) - \Gamma_{1,e}} = 1 - \frac{2}{\sqrt{\pi}} \sqrt{\frac{t}{\tau_\sigma}} + O\left[\left(\frac{t}{\tau_\sigma}\right)^{3/2}\right] \quad (t \ll \tau_\sigma) \quad (4.69)$$

$$\frac{\sigma(t) - \sigma_e}{\sigma(0) - \sigma_e} = \frac{\Gamma_1(t) - \Gamma_{1,e}}{\Gamma_1(0) - \Gamma_{1,e}} = \sqrt{\frac{\tau_\sigma}{\pi t}} + O\left[\left(\frac{\tau_\sigma}{t}\right)^{3/2}\right] \quad t \gg \tau_\sigma \quad (4.70)$$

Equation 4.70 is often used as a test to verify whether the adsorption process is under diffusion control: data for $\sigma(t)$ are plotted versus $1/\sqrt{t}$ and it is checked if the plot complies with a straight line; moreover, the intercept of the line gives σ_e . We recall that Equations 4.69 and 4.70 are valid in the case of a *small* initial perturbation; alternative asymptotic expressions for the case of *large* initial perturbation are considered in the next section.

With the help of the thermodynamic Equations 4.2 and 4.6, we derive

$$\frac{\partial \Gamma_1}{\partial c_1} = \frac{\partial \Gamma_1}{\partial \sigma} \frac{\partial \sigma}{\partial c_1} = \frac{\Gamma_1^2 kT}{c_1 E_G} \quad (4.71)$$

Thus Equation 4.66 can be expressed in an alternative form [37]:

$$\tau_\sigma = \frac{1}{D_1} \left(\frac{\Gamma_1^2 kT}{c_1 E_G} \right)^2 \quad (4.72)$$

Substituting E_G from Table 4.3 into Equation 4.72, we can obtain expressions for τ_σ corresponding to various adsorption isotherms. In the special case of Langmuir adsorption isotherm, we can present Equation 4.72 in the form [37]

$$\tau_\sigma = \frac{1}{D_1} \frac{(K\Gamma_\infty)^2}{(1 + Kc_1)^4} = \frac{1}{D_1} \frac{(K\Gamma_\infty)^2}{(1 + E_G / (\Gamma_\infty kT))^4} \quad (\text{for Langmuir isotherm}) \quad (4.73)$$

Equation 4.73 visualizes the very strong dependence of the relaxation time τ_σ on the surfactant concentration c_1 ; in general, τ_σ can vary with many orders of magnitude as a function of c_1 . Equation 4.73 shows also that high Gibbs elasticity corresponds to short relaxation time, and vice versa.

As a quantitative example let us take typical parameter values: $K_1 = 15 \text{ m}^3/\text{mol}$, $1/\Gamma_\infty = 40 \text{ \AA}^2$, $D_1 = 4.5 \times 10^{-6} \text{ cm}^2/\text{s}$, and $T = 298 \text{ K}$. Then with $c_1 = 6.5 \times 10^{-6} \text{ M}$, from Table 4.3 (Langmuir isotherm) and Equation 4.73, we calculate $E_G \approx 1.0 \text{ mN/m}$ and $\tau_\sigma \approx 5 \text{ s}$. In the same way, for $c_1 = 6.5 \times 10^{-4} \text{ M}$ we calculate $E_G \approx 100 \text{ mN/m}$ and $\tau_\sigma \approx 5 \times 10^{-4} \text{ s}$.

To directly measure the Gibbs elasticity E_G , or to precisely investigate the dynamics of surface tension, we need an experimental method, whose characteristic time is smaller compared to τ_σ . Equation 4.73 and the latter numerical example show that when the surfactant concentration is higher, the experimental method should be faster.

4.2.2.3 Large Initial Perturbation

By definition, we have *large initial perturbation* when at the initial moment the interface is clean of surfactant:

$$\Gamma_1(0) = 0, \quad c_{1s}(0) = 0 \quad (4.74)$$

In such case, the Hansen Equation 4.63 reduces to

$$c_{1s}(t) = c_{1\infty} - \frac{\Gamma_{1e}}{\sqrt{\pi D_1 t}} \quad (t \rightarrow \infty) \quad (4.75)$$

By substituting $c_{1s}(t)$ for c_1 in the Gibbs adsorption Equation 4.2, and integrating, we obtain the long-time asymptotics of the surface tension of a nonionic surfactant solution after a large initial perturbation:

$$\sigma(t) - \sigma_e = \left(\frac{\Gamma_1^2 kT}{c_1} \right)_e \left(\frac{1}{\pi D_1 t} \right)^{1/2} \quad (\text{large initial perturbation}) \quad (4.76)$$

with the help of Equation 4.72, we can bring Equation 4.76 into another form:

$$\sigma(t) - \sigma_e = E_G \left(\frac{\tau_\sigma}{\pi t} \right)^{1/2} \quad (\text{large initial perturbation}) \quad (4.77)$$

where E_G is given in Table 4.3. It is interesting to note that Equation 4.77 is applicable to both nonionic and ionic surfactants with the only difference that for nonionics τ_σ is given by Equation 4.66, whereas for ionic surfactants the expression for τ_σ is somewhat longer, see Refs. [37,105].

The equations mentioned earlier show that in the case of adsorption under diffusion control the long-time asymptotics can be expressed in the form

$$\sigma = \sigma_e + S t^{-1/2} \quad (4.78)$$

In view of Equations 4.70 and 4.77, the slope S of the dependence σ versus $t^{-1/2}$ is given by the expressions [105]

$$S_s = [\sigma(0) - \sigma_e] \left(\frac{\tau_\sigma}{\pi} \right)^{1/2} \quad (\text{small perturbation}) \quad (4.79)$$

$$S_l = E_G \left(\frac{\tau_\sigma}{\pi} \right)^{1/2} \quad (\text{large perturbation}) \quad (4.80)$$

As known, the surfactant adsorption Γ_1 monotonically increases with the rise of the surfactant concentration, c_1 . In contrast, the slope S_l is a nonmonotonic function of c_1 ; S_l exhibits a maximum at a certain concentration. To demonstrate that we will use the expression

$$S_l = \frac{\Gamma_{1,e}^2 kT}{c_1 \sqrt{\pi D_1}} \quad (4.81)$$

which follows from Equations 4.76 and 4.78. In Equation 4.81 we substitute the expressions for c_1 stemming from the Langmuir and Volmer adsorption isotherms (Table 4.2 with $c_1 = a_{1s}$); the result reads

$$\tilde{S}_l = \theta(1 - \theta) \quad (\text{for Langmuir isotherm}) \quad (4.82)$$

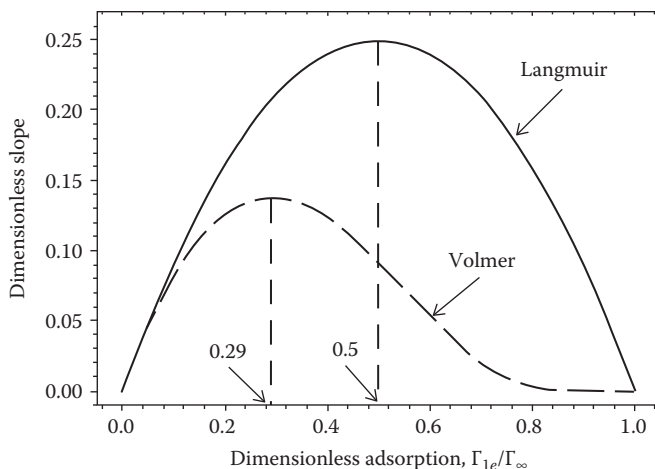


FIGURE 4.4 Plot of the dimensionless slope, \tilde{S}_l , vs. the dimensionless equilibrium surfactant adsorption, $\theta = \Gamma_{1,e}/\Gamma_\infty$, in accordance with Equations 4.82 and 4.83, corresponding to the cases of localized and nonlocalized adsorption.

$$\tilde{S}_l = \theta(1-\theta) \exp\left(-\frac{\theta}{1-\theta}\right) \quad (\text{for Volmer isotherm}) \quad (4.83)$$

where θ and \tilde{S}_l are the dimensionless adsorption and slope coefficient, respectively:

$$\theta = \frac{\Gamma_{1,e}}{\Gamma_\infty}, \quad \tilde{S}_l = \frac{S_l \sqrt{\pi D_1}}{kT K \Gamma_\infty^2} \quad (4.84)$$

Figure 4.4 compares the dependencies $\tilde{S}_l(\theta)$ given by Equations 4.82 and 4.83: we see that the former is symmetric and has a maximum at $\theta = 0.5$, whereas the latter is asymmetric with a maximum at $\theta \approx 0.29$. We recall that the Langmuir and Volmer isotherms correspond to *localized* and *nonlocalized* adsorption, respectively (see Section 4.2.1.1.2). Then Figure 4.4 shows that the symmetry/asymmetry of the plot \tilde{S}_l versus θ provides a *test* for verifying whether the adsorption is localized or nonlocalized. (The practice shows that the fits of *equilibrium* surface tension isotherms do not provide such a test: theoretical isotherms corresponding to localized and nonlocalized adsorption are found to fit surface tension data equally well!)

From another viewpoint, the nonmonotonic behavior of $S_l(\theta)$ can be interpreted as follows. Equation 4.80 shows that $S_l \propto E_G \sqrt{\tau_\sigma}$; then the nonmonotonic behavior stems from the fact that E_G is an increasing function of c_1 , whereas τ_σ is a decreasing function of c_1 . This qualitative conclusion is also valid for the case of ionic surfactant, as demonstrated in the next section.

4.2.2.4 Generalization for Ionic Surfactants

In the case of ionic surfactants, the dynamics of adsorption is more complicated because of the presence of a dynamic EDL. Indeed, the adsorption of surfactant at the interface creates surface charge, which increases in the course of the adsorption process. The charged interface repels the new-coming surfactant molecules, but attracts the conversely charged counterions (Figure 4.1); some of them bind to the surfactant headgroups thus decreasing the surface charge density and favoring the adsorption of new surfactant molecules. The theoretical description of the overall adsorption process involves the electro-diffusion equations for the surfactant ions, counterions and coions, and

the Poisson equation from electrostatics. Different analytical and numerical approaches to the solution of this problem have been proposed [13,60,105–114].

In Ref. [114], an approach to the dynamics of ionic surfactant adsorption was developed, which is simpler as both concept and application, but agrees very well with the experiment. Analytical asymptotic expressions for the dynamic surface tension of ionic surfactant solutions are derived in the general case of nonstationary interfacial expansion. Because the diffusion layer is much wider than the EDL, the equations contain a small parameter. The resulting perturbation problem is singular and it is solved by means of the method of matched asymptotic expansions [115]. The derived general expression for the dynamic surface tension is simplified for two important special cases, which are considered in the following section.

The first special case refers to adsorption at an *immobile interface* that has been initially perturbed, and to the *maximum bubble pressure method* (MBPM). The generalization of Equations 4.78 and 4.81 for this case reads [114]:

$$\sigma = \sigma_e + \frac{S_l}{(t_{\text{age}})^{1/2}}, \quad S_l \equiv \frac{kT\Gamma_{1,e}^2\lambda}{(\pi D_{\text{eff}})^{1/2}\gamma_{\pm}} \left(\frac{1}{c_{1\infty}} + \frac{1}{c_{2\infty}} \right) \quad (4.85a)$$

As usual, the subscript ‘e’ denotes equilibrium values; t_{age} is the age of the interface, which is defined as the period of time between the minimum pressure (bubble formation) and the maximum pressure (bubble detachment) in the case of MBPM; λ is a dimensionless parameter; $\lambda = 1$ for immobile interfaces; in the case of MBPM, λ is an apparatus constant that can be determined by calibration experiments [57]; as mentioned earlier, $c_{1\infty}$ and $c_{2\infty}$ are the bulk concentrations of surfactant ions and counterions, respectively; γ_{\pm} is the activity coefficient; D_{eff} is an effective diffusivity that depends on the diffusivities and bulk concentrations of surfactant ions, counterions, and inorganic coions: $D_{\text{eff}} = D_{\text{eff}}(D_1, D_2, D_3, c_{1\infty}, c_{2\infty}, c_{3\infty})$. The latter dependence is described by explicit formulas derived in Ref. [114]; see Equations 6.19 through 6.26 therein.

In the case of the cationic surfactant dodecyl trimethyl ammonium bromide ($C_{12}\text{TAB}$), the calculated dependence of D_{eff} on the surfactant and salt concentrations, $c_{1\infty}$ and $c_{3\infty}$, is illustrated in Figure 4.4. Because the range $c_{1\infty} \leq \text{CMC}$ is considered, the calculated curves end at the CMC.

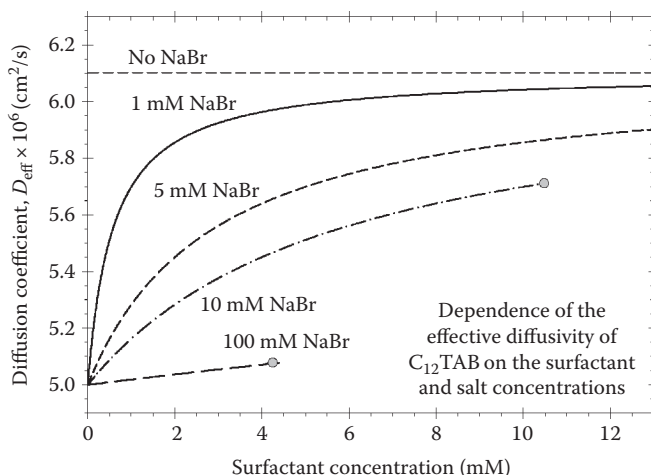


FIGURE 4.5 Dependence of the effective diffusivity, D_{eff} , on the surfactant concentration, $c_{1\infty}$, for various salt concentrations, $c_{3\infty}$, denoted in the figure. The curves are calculated by using the values of D_1 , D_2 , and D_3 given in Ref. [114] for the cationic surfactant $C_{12}\text{TAB}$. The end points of some curves correspond to the CMC.

At very low surfactant concentrations, $c_{1\infty} \rightarrow 0$, in the presence of salt ($c_{3\infty} > 0$), the effective diffusivity approaches its limiting value for diluted solutions, $D_{\text{eff}} \rightarrow D_1$. We see that D_{eff} increases with the rise of $c_{1\infty}$, except the case without added salt ($c_{3\infty} = 0$), for which D_{eff} is a constant: $1/D_{\text{eff}} = (1/D_1 + 1/D_2)/2$. The curves in Figure 4.5 show that D_{eff} decreases with the rise of salt concentration, $c_{3\infty}$, and becomes $\approx D_1$ for $c_{3\infty} = 100$ mM. Note that the salt concentration affects the dynamic surface tension, σ , also through $\Gamma_{1,e}$ and through the factor $(1/c_{1\infty} + 1/c_{2\infty})$ in Equation 4.85a; see Ref. [114] for details.

The accuracy of Equation 4.85a can be verified in the following way. Each of the dynamic surface tension isotherms for C_{12} TAB in Figure 4.6a are fitted by means of the equation $\sigma = \sigma_e + S_l/[a_\sigma + (t_{\text{age}})^{1/2}]$, and the parameters σ_e , a_σ , and S_l are determined from the best fit. Next, for each

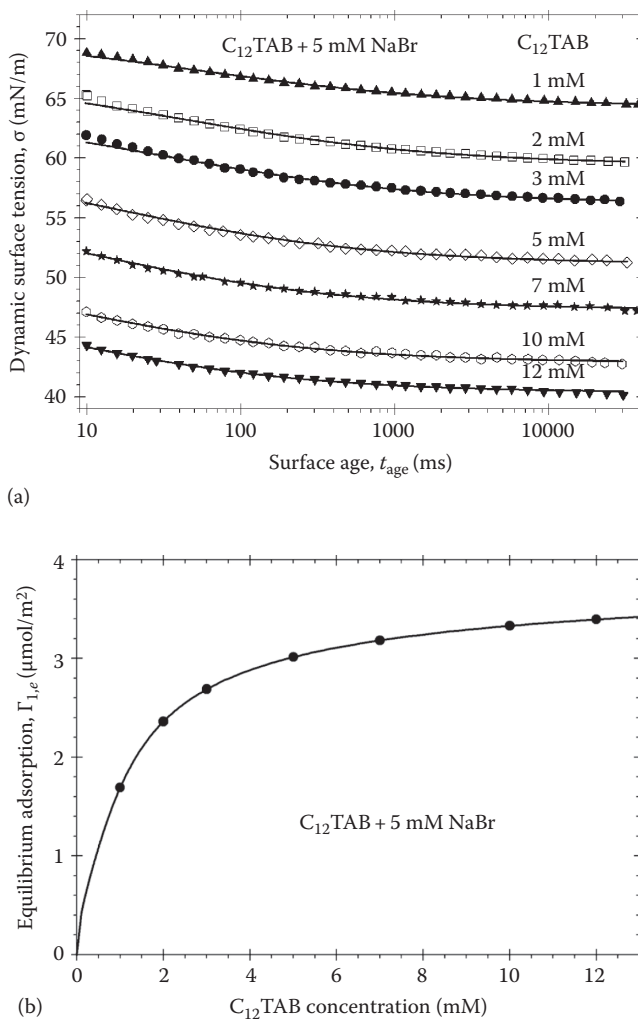


FIGURE 4.6 (a) Data for the dynamic surface tension, σ , vs. the surface age, t_{age} , measured by MBPM [57] at concentrations of C_{12} TAB denoted in the figure; the solid lines are fits (see the text). (b) Dependence of the equilibrium surfactant adsorption, $\Gamma_{1,e}$, on the C_{12} TAB concentration. The points are calculated by means of Equation 4.85a for S_l determined from the fits in Figure 4.6a. The solid lines are calculated independently from fits of surface tension data, σ_e vs. $c_{1\infty}$, by means of the van der Waals adsorption model. (From Danov, K.D. et al., *J. Colloid Interface Sci.*, 303, 56, 2006.)

value of S_i , we calculate the equilibrium surfactant adsorption, $\Gamma_{1,e}$, using Equation 4.85a and the theoretical value of D_{eff} from Figure 4.5; see the points in Figure 4.6b. For the used MBPM set up [57], the apparatus constant is $\lambda = 6.07$. The solid line in the latter figure represents the equilibrium surfactant adsorption independently calculated from the fit of equilibrium surface tension data by means of the van der Waals isotherm [114]. The excellent agreement between the points with the line in Figure 4.6b (no adjustable parameters) confirms the accuracy of Equation 4.85a.

The case of adsorption at an interface that is subjected to stationary expansion needs a special theoretical description. This case is experimentally realized with the strip method [95,116], and the overflowing cylinder method [60,92]. It could be realized also by a Langmuir trough. The interfacial expansion is characterized by the quantity $\dot{\alpha} = dA/(Adt)$, which represents the relative rate of increase of the interfacial area, A . For stationary processes, $\dot{\alpha} = \text{const.}$ is a parameter known from the experiment. In this case, the dynamic surface tension is given by the expression [114]:

$$\sigma = \sigma_e + kT\Gamma_{1,e}^2 \left(\frac{\pi\dot{\alpha}}{2D_{\text{eff}}} \right)^{1/2} \frac{1}{\gamma_{\pm}} \left(\frac{1}{c_{1\infty}} + \frac{1}{c_{2\infty}} \right) \quad (4.85b)$$

where D_{eff} is given by Equations 6.19 through 6.26 in Ref. [114]. Equation 4.85b does not contain the time, t , as it should be for a stationary process. For nonionic surfactants and for ionic surfactants at high salt concentrations the term $1/c_{2\infty}$ in Equation 4.85b disappears and $D_{\text{eff}} = D_1$.

4.2.2.5 Adsorption under Barrier Control

In general, the adsorption is under barrier (kinetic, transfer) control when the stage of surfactant transfer from the subsurface to the surface is much slower than the diffusion stage because of some kinetic barrier. The latter can be due to steric hindrance, spatial reorientation, or conformational changes accompanying the adsorption of molecules, including destruction of the shells of oriented water molecules wrapping the surfactant hydrocarbon tail in water [117]. We will restrict our considerations to the case of pure barrier control, without double layer effects. In such case the surfactant concentration is uniform throughout the solution, $c_1 = \text{constant}$, and the increase of the

TABLE 4.6
Rate of Surfactant Adsorption for Different Kinetic Models

Type of Isotherm	Rate of Reversible Adsorption
	$Q = r_{\text{ads}}(c_1, \Gamma_1) - r_{\text{des}}(\Gamma_1)$
Henry	$Q = K_{\text{ads}}c_1 - K_{\text{des}} \frac{\Gamma_1}{\Gamma_{\infty}}$
Freundlich	$Q = K_{\text{ads}}K^{m-1}c_1^m - K_{\text{des}} \frac{\Gamma_1}{\Gamma_{\infty}}$
Langmuir	$Q = K_{\text{ads}}c_1 \left(1 - \frac{\Gamma_1}{\Gamma_{\infty}} \right) - K_{\text{des}} \frac{\Gamma_1}{\Gamma_{\infty}}$
Frumkin	$Q = K_{\text{ads}}c_1 \left(1 - \frac{\Gamma_1}{\Gamma_{\infty}} \right) - K_{\text{des}} \frac{\Gamma_1}{\Gamma_{\infty}} \exp \left(-\frac{2\beta\Gamma_1}{kT} \right)$
Volmer	$Q = K_{\text{ads}}c_1 - K_{\text{des}} \frac{\Gamma_1}{\Gamma_{\infty} - \Gamma_1} \exp \left(\frac{\Gamma_1}{\Gamma_{\infty} - \Gamma_1} \right)$
van der Waals	$Q = K_{\text{ads}}c_1 - K_{\text{des}} \frac{\Gamma_1}{\Gamma_{\infty} - \Gamma_1} \exp \left(\frac{\Gamma_1}{\Gamma_{\infty} - \Gamma_1} - \frac{2\beta\Gamma_1}{kT} \right)$

adsorption $\Gamma_1(t)$ is solely determined by the transitions of surfactant molecules over the adsorption barrier, separating subsurface from surface:

$$\frac{d\Gamma_1}{dt} = Q \equiv r_{\text{ads}}(c_1, \Gamma_1) - r_{\text{des}}(\Gamma_1) \quad (4.86)$$

where r_{ads} and r_{des} are the rates of surfactant adsorption and desorption, respectively. The concept of barrier-limited adsorption originates from the works of Bond and Puls [118], and Doss [119], and has been further developed by other authors [120–127]. Table 4.6 summarizes some expressions for the total rate of adsorption under barrier control, Q . The quantities K_{ads} and K_{des} in Table 4.6 are the rate constants of adsorption and desorption, respectively. Their ratio is equal to the equilibrium constant of adsorption

$$\frac{K_{\text{ads}}}{K_{\text{des}}} = K \quad (4.87)$$

The parameters Γ_∞ and K are the same as in Tables 4.2 through 4.4. Setting $Q = 0$ (assuming equilibrium at surface–subsurface), from each expression in Table 4.6 we deduce the respective equilibrium adsorption isotherm in Table 4.2. In addition, for $\beta = 0$ the expressions for Q related to the Frumkin and van der Waals model reduce, respectively, to the expressions for Q in the Langmuir and Volmer models. For $\Gamma_1 \ll \Gamma_\infty$ both the Frumkin and Langmuir expressions in Table 4.6 reduce to the Henry expression.

Substituting Q from Table 4.6 into Equation 4.86, and integrating, we can derive explicit expressions for the relaxation of surfactant adsorption:

$$\frac{\sigma(t) - \sigma_e}{\sigma(0) - \sigma_e} \approx \frac{\Gamma_1(t) - \Gamma_{1,e}}{\Gamma_1(0) - \Gamma_{1,e}} = \exp\left(-\frac{t}{\tau_\sigma}\right) \quad (4.88)$$

Equation 4.88 holds for $\sigma(t)$ only in the case of small deviations from equilibrium, whereas there is not such a restriction concerning $\Gamma_1(t)$; the relaxation time in Equation 4.88 is given by the expressions

$$\tau_\sigma = \left(\frac{K_{\text{des}}}{\Gamma_\infty}\right)^{-1} \quad (\text{Henry and Freundlich}) \quad (4.89)$$

$$\tau_\sigma = \left(\frac{K_{\text{des}}}{\Gamma_\infty} + \frac{K_{\text{ads}}c_1}{\Gamma_\infty}\right)^{-1} \quad (\text{Langmuir}) \quad (4.90)$$

Equation 4.88 predicts that the perturbation of surface tension, $\Delta\sigma(t) = \sigma(t) - \sigma_e$, relaxes exponentially. This is an important difference with the cases of adsorption under diffusion and electro-diffusion control, for which $\Delta\sigma(t) \propto 1/\sqrt{t}$, cf. Equations 4.70, 4.76, and 4.78. Thus, a test to check whether or not the adsorption occurs under purely barrier control is to plot data for $\ln[\Delta\sigma(t)]$ versus t and to check if the plot complies with a straight line.

In the case of *ionic* surfactants, the adsorption of surfactant ions is accompanied by binding of counterions. In addition, the concentrations of the ionic species vary across the EDL (even at equilibrium). These effects are taken into account in Equation 4.57, which can be used as an expression for Q in the case of Langmuir barrier adsorption of an ionic surfactant.

In fact, a pure barrier regime of adsorption is not frequently observed. It is expected that the barrier becomes more important for substances of low surface activity and high concentration in the solution. Such adsorption regime was observed with propanol, pentanol, and 1,6 hexanoic acid [95], as well as with proteins [128].

It may happen that the characteristic times of diffusion and transfer across the barrier are comparable. In such case we deal with *mixed* kinetic regime of adsorption [129]. Insofar as the stages of diffusion and transfer are consecutive, the boundary conditions at the interface are

$$\frac{d\Gamma_1}{dt} = r_{\text{ads}}(c_1, \Gamma_1) - r_{\text{des}}(\Gamma_1) = D_1 \left(\frac{\partial c_1}{\partial z} \right)_{z=0} \quad (4.91)$$

The formal transition in Equation 4.91 from mixed to diffusion control of adsorption is not trivial and demands application of scaling and asymptotic expansions. The criterion for occurrence of adsorption under diffusion control (presence of equilibrium between subsurface and surface) is

$$\frac{aK_{\text{des}}}{D_1} \left(\frac{\partial \Gamma_1}{\partial c_1} \right)_e \gg 1 \quad (4.92)$$

where a is the characteristic thickness of the diffusion layer.

An important difference between the regimes of diffusion and barrier control is in the form of the respective initial conditions. In the case of large initial deformations, these are

$$\Gamma_1(0) = 0, \quad c_{1s}(0) = 0 \quad (\text{diffusion control}) \quad (4.93)$$

$$\Gamma_1(0) = 0, \quad c_{1s}(0) = c_{1\infty} \quad (\text{barrier control}) \quad (4.94)$$

Equation 4.93 reflects the fact that in diffusion regime the surface is always assumed to be equilibrated with the subsurface. In particular, if $\Gamma_1 = 0$, then we must have $c_{1s} = 0$. In contrast, Equation 4.94 stems from the presence of barrier: for time intervals shorter than the characteristic time of transfer, the removal of the surfactant from the interface ($\Gamma_1 = 0$) cannot affect the subsurface layer (because of the barrier) and then $c_{1s}(0) = c_{1\infty}$. This purely theoretical consideration implies that the effect of barrier could show up at the short times of adsorption, whereas at the long times the adsorption will occur under diffusion control [129,130]. The existence of barrier-affected adsorption regime at the short adsorption times could be confirmed or rejected by means of the fastest methods for measurement of dynamic surface tension.

4.2.2.6 Dynamics of Adsorption from Micellar Surfactant Solutions

4.2.2.6.1 Dynamic Equilibrium between Micelles and Monomers

At higher concentrations, spherical aggregates of surfactant molecules, called *micelles* [131,132], appear in the aqueous surfactant solutions (Figure 4.7). The number of monomers in a micelle (the aggregation number) is typically between 50 and 100, depending on the size of the surfactant head-group and the length of its hydrocarbon tail [36]. The micelles appear above a certain surfactant concentration termed the CMC. For concentrations above the CMC, the addition of surfactant to the solutions leads to the formation of more micelles, whereas the concentration of the monomers remains constant and equal to the CMC. In other words, the micelles, irrespective of their concentrations, exist in dynamic equilibrium with a background solution of monomers with concentration equal to the CMC. (Note that at high surfactant concentrations, the spherical micelles could undergo a transition to bigger aggregates, such as rodlike, disclike, and lamellar micelles [36,133–135].)

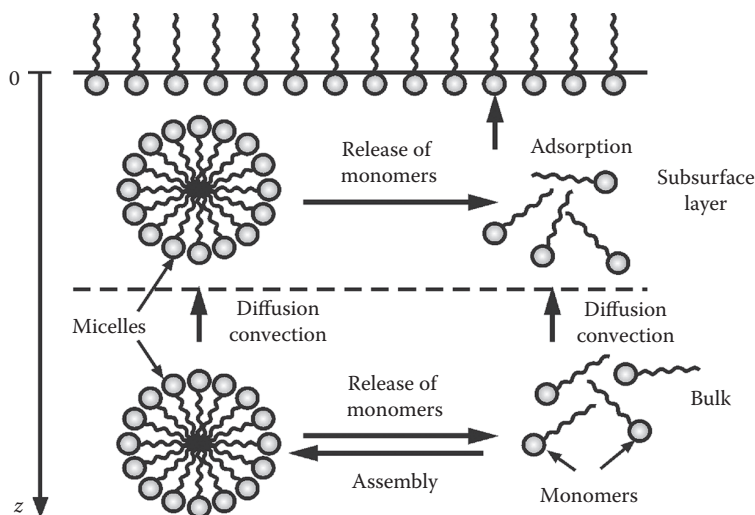


FIGURE 4.7 In the neighborhood of an expanded (nonequilibrium) adsorption monolayer, the micelles (the aggregates) release monomers to restore the equilibrium concentrations of surfactant monomers at the surface and in the bulk. The concentration gradients give rise to diffusion of both monomers and micelles. As a rule, the adsorbing component are the surfactant monomers, whereas the micelles are repelled by the interface and do not adsorb.

A detailed physicochemical model of the micelle–monomer equilibria was proposed [136], which is based on a full system of equations that express (1) chemical equilibria between micelles and monomers, (2) mass balances with respect to each component, and (3) the mechanical balance equation by Mitchell and Ninham [137], which states that the electrostatic repulsion between the headgroups of the ionic surfactant is counterbalanced by attractive forces between the surfactant molecules in the micelle. Because of this balance between repulsion and attraction, the equilibrium micelles are in tension free state (relative to the surface of charges), like the phospholipid bilayers [136,138]. The model is applicable to ionic and nonionic surfactants and to their mixtures and agrees very well with the experiment. It predicts various properties of single-component and mixed micellar solutions, such as the compositions of the monomers and the micelles, concentration of counterions, micelle aggregation number, surface electric charge and potential, effect of added salt on the CMC of ionic surfactant solutions, electrolytic conductivity of micellar solutions, etc. [136,139].

When surfactant molecules adsorb at an interface, the concentration of monomers in the subsurface layer decreases, which leads to release of monomers from the neighboring micelles, or to their complete decomposition. The decrease in the concentrations of monomers and micelles gives rise to corresponding diffusion fluxes from the bulk of solution toward the subsurface layer (Figure 4.7). In general, the role of the micelles as sources and carriers of monomers leads to a marked acceleration of surfactant adsorption.

The first models of micellar kinetics in spatially uniform solutions have been developed by Kresheck et al. [140] and Aniansson and Wall [141]. The existence of “fast” and “slow” processes of the micellar dynamics has been established. The *fast* process represents exchange of separate monomers between micelles and the surrounding solution. If the micelle releases monomers, its aggregation number could decrease to a critical value, after which a complete decomposition of the micelle to monomers takes place. This decomposition is known as the *slow* demicellization process [141].

The first theoretical model of surfactant adsorption from micellar solutions, proposed by Lucassen [142], uses the simplifying assumptions that the micelles are monodisperse and that the micellization happens as a single step, which is described as a reversible reaction of order n

(the micelle aggregation number). Later, more realistic models, which account for the multi-step character of the micellar process, were developed [143–145]. The assumption for a complete local dynamic equilibrium between monomers and micelles makes possible to use the equilibrium mass action law for the micellization reaction [142,146,147]. In such a case, the surfactant transfer corresponds to a conventional diffusion-limited adsorption characterized by an effective diffusion coefficient, D_{eff} , which depends on the micelle diffusivity, concentration, and aggregation number. D_{eff} is independent of the rate constants of the fast and slow demicellization processes: k_m and k_s . Joos et al. [146,147] confirmed experimentally that in some cases the adsorption from micellar solutions could be actually described as a diffusion-limited process characterized by an apparent diffusivity, D_{eff} . In other experiments, Joos et al. [95,148] established that sometimes the dynamics of adsorption from micellar solutions exhibits a completely different kinetic pattern: the interfacial relaxation is exponential, rather than inverse square root, as it should be for diffusion-limited kinetics. The theoretical developments [95,129,148] revealed that the exponential relaxation is influenced by the kinetics of micellization, and from the data analysis we could determine the rate constant of the fast process, k_m . The observation of different kinetic regimes for different surfactants and/or experimental methods makes the physical picture rather complicated.

A realistic model of the micellar kinetics was proposed [149] and applied to investigate the dynamics of adsorption at quiescent [150] and expanding [57,151] interfaces. The theoretical analysis reveals the existence of four different consecutive relaxation regimes (stages) for a given micellar solution: two exponential regimes and two inverse-square-root regimes, following one after another in alternating order. The results of these studies are briefly described in the following section, and the agreement between theory and experiment is illustrated.

4.2.2.6.2 The Four Kinetic Regimes of Adsorption from Micellar Solutions

In the theoretical model proposed in Refs. [149,150], the use of the quasi-equilibrium approximation (local chemical equilibrium between micelles and monomers) is avoided. The theoretical problem is reduced to a system of four nonlinear differential equations. The model has been applied to the case of surfactant adsorption at a quiescent interface [150], that is, to the relaxation of surface tension and adsorption after a small initial perturbation. The perturbations in the basic parameters of the micellar solution are defined in the following way:

$$\xi_1 \equiv \frac{h_a}{\Gamma_{p,0}} c_{1,p}; \quad \xi_c \equiv \frac{h_a}{\beta \Gamma_{p,0}} C_{m,p}; \quad \xi_m \equiv \frac{h_a c_{1,\text{eq}}}{s_{\text{eq}}^2 \Gamma_{p,0}} m_p \quad (4.95)$$

Here

$c_{1,p}$, $C_{m,p}$, and m_p are, respectively, the perturbations in the monomer concentration, c_1 , micelle concentration, C_m , the micelle mean aggregation number, m , the respective *dimensionless* perturbations are ξ_1 , ξ_c , and ξ_m ;

$\Gamma_{p,0}$ is the perturbation in the surfactant adsorption at the initial moment ($t = 0$);

s_{eq} is the halfwidth of the equilibrium micelle size distribution modeled by a Gaussian bell-like curve;

β and h_a are, respectively, the dimensionless bulk micelle concentration and the characteristic adsorption length, defined as follows:

$$\beta \equiv \frac{C_{\text{tot}} - \text{CMC}}{\text{CMC}}; \quad h_a = \left(\frac{d\Gamma}{dc_1} \right)_{\text{eq}} \quad (4.96)$$

where

C_{tot} is the total surfactant concentration

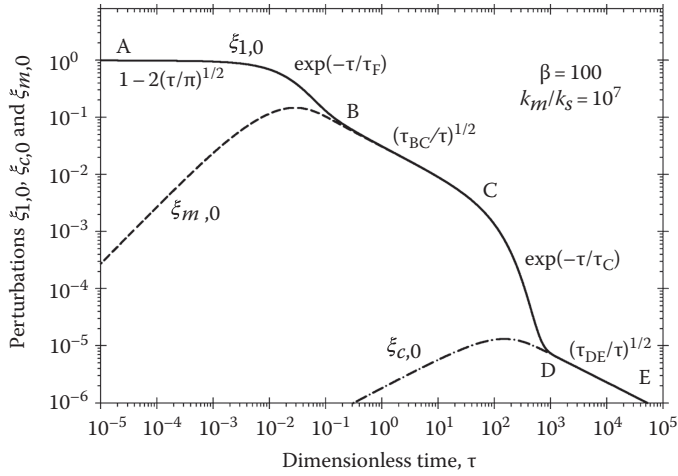


FIGURE 4.8 Time dependence of the perturbations in the subsurface monomer concentration, $\xi_{1,0}$, micelle concentration, $\xi_{c,0}$, and mean aggregation number, $\xi_{m,0}$, for $\beta = 100$. The curves are obtained by numerical solution of the general system of equations. (From Danov, K.D. et al., *Adv. Colloid Interface Sci.*, 119, 17, 2006.)

Γ is the surfactant adsorption

The dimensionless fluxes of the fast and slow demicellization processes, denoted by ϕ_m and ϕ_s , respectively, can be expressed as follows [150]:

$$\varphi_m = \xi_1 - \xi_m \tag{4.97}$$

$$\varphi_s = (m_{eq} - w s_{eq}) \xi_1 - m_{eq} \xi_c + s_{eq} w \xi_m \tag{4.98}$$

(Some small terms are neglected in Equations 4.97 and 4.98.) Here m_{eq} is the equilibrium micelle aggregation number $w = (m_{eq} - n_r)/s_{eq}$, where n_r is an aggregation number at the boundary between the regions of the rare aggregates and the abundant micelles [150]

Figure 4.8 shows results obtained by solving numerically the general system of equations in Ref. [150] for a relatively high micelle concentration, $\beta = 100$. The calculated curves $\xi_{1,0}(\tau)$, $\xi_{c,0}(\tau)$, and $\xi_{m,0}(\tau)$ represent the subsurface values (at $z = 0$, Figure 4.7) of the perturbations ξ_1 , ξ_c , and ξ_m , plotted versus the dimensionless time, $\tau = (D_1/h_a^2)t$, where D_1 is the diffusion coefficient of the surfactant monomers. Note that $\xi_{1,0}$ expresses not only the perturbation in the subsurface monomer concentration, but also the perturbations in the surface tension and adsorption [150]:

$$\frac{\sigma(t) - \sigma_e}{\sigma(0) - \sigma_e} = \frac{\Gamma(t) - \Gamma_e}{\Gamma(0) - \Gamma_e} = \xi_{1,0}(\tau) \tag{4.99}$$

where

- $\sigma(t)$ and $\Gamma(t)$ are the dynamic surface tension and adsorption, respectively
- $\sigma(0)$ and $\Gamma(0)$ are their initial values
- σ_e and Γ_e are their final equilibrium values

A typical value, $k_m/k_s = 10^7$, of the ratio of the rate constants of the fast and slow demicellization processes is used to calculate the curves in Figure 4.8.

The most important feature of the relaxation curves in Figure 4.8, which represents a kinetic diagram, is that $\xi_{m,0}$ merges with $\xi_{1,0}$ at a given point, denoted by B, while $\xi_{c,0}$ merges with $\xi_{1,0}$ (and $\xi_{m,0}$) at another point, denoted by D. The time moments, corresponding to the points B and D, are denoted by τ_B and τ_D , respectively. As seen in Figure 4.8, for $\tau > \tau_B$, we have $\xi_{1,0} = \xi_{m,0}$. In view of Equation 4.97, this means that for $\tau > \tau_B$ the flux of the fast micelle relaxation process, ϕ_m is equal to zero. In other words, for $\tau > \tau_B$ the monomers and micelles are equilibrated with respect to the *fast* micellar process. For a regular relaxation process, the theoretical analysis [150] yields the expression $\tau_B = s_{\text{eq}} h_a (2k_m/D_1)^{1/2}$. In addition, for $\tau > \tau_D$ we have $\xi_{c,0} = \xi_{1,0} = \xi_{m,0}$, and then Equation 4.98 indicates that $\phi_s = 0$, that is, the monomers and micelles are equilibrated with respect to the *slow* micellar process.

The computer modeling [150] shows that $\xi_{1,0}(\tau)$ exhibits two exponential (kinetic) regimes, AB and CD, and two inverse-square-root (diffusion) regimes, BC and DE, see Figure 4.8. In particular, the point C corresponds to the moment $\tau_C = (D_1/h_a^2)t_c \approx (\beta D_1 \sigma_{\text{eq}}^2)/(k_s h_a^2 m_{\text{eq}}^3)$, where t_c is the characteristic time of the slow micellar process; see Ref. [149]. τ_C also serves as a characteristic relaxation time of adsorption in the kinetic regime CD. The expressions for the other characteristic times, τ_F , τ_{BC} , and τ_{DE} (Figure 4.8) are [150] the following:

$$\tau_F = \frac{m_{\text{eq}} D_1}{\beta k_m h_a^2} \quad (\text{regime AB}) \quad (4.100)$$

$$\frac{1}{\tau_{BC}} = \frac{D_{BC}}{D_1} = (1 + u\beta)(1 + u\beta B_m) \quad (\text{regime BC}) \quad (4.101)$$

$$\frac{1}{\tau_{DE}} = \frac{D_{DE}}{D_1} = [1 + (u + m_{\text{eq}})\beta][1 + (u + m_{\text{eq}})\beta B_m] \quad (\text{regime DE}) \quad (4.102)$$

Here

D_{BC} and D_{DE} are the effective diffusivities of the micellar solutions in the regimes BC and DE, respectively; $u = s_{\text{eq}}^2/m_{\text{eq}}$

$B_m = D_m/D_1$; D_m is the mean diffusivity of the micelles

Typical parameter values are $u \approx 1$ and $B_m \approx 0.2$.

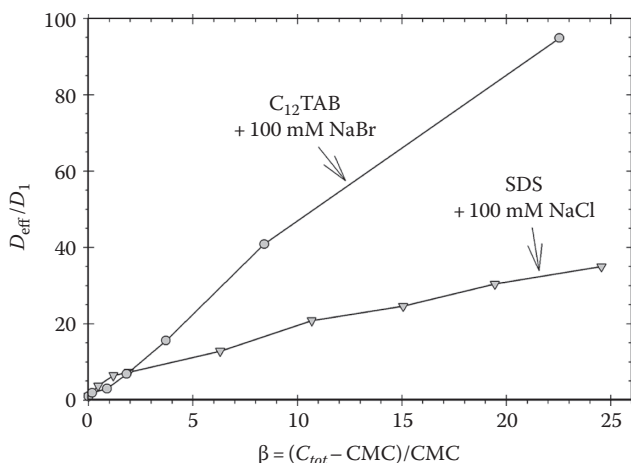


FIGURE 4.9 Plot of the dimensionless effective diffusivity of the micellar solution, D_{eff}/D_1 , vs. the dimensionless micelle concentration, β , obtained from dynamic surface tension values measured by the maximum bubble pressure method (MBPM) (From Christov, N.C. et al., *Langmuir*, 22, 7528, 2006); D_1 is the diffusivity of the surfactant monomers. The lines are guides to the eye.

It should be noted that in addition to the regular kinetic diagrams (Figure 4.8), for low micelle concentrations (β close to 1) we could observe “rudimentary” kinetic diagrams, characterized by merging or disappearance of the stages BC and CD [150,151].

The diffusion regimes BC and DE can be observed not only for adsorption at a quiescent interface, but also in the cases of stationary [151] and nonstationary [57] expansion of an interface. The expressions for the effective diffusivities, D_{BC} and D_{DE} , given by Equations 4.101 and 4.102, are valid in all these cases. In particular, the experimental data by Lucassen [142] correspond to the kinetic regime DE, while the experimental data by Joos et al. [147] correspond to the kinetic regime BC.

As an illustration, in Figure 4.9 we show experimental data for the ionic surfactants (SDS) and $C_{12}TAB + 100$ mM added inorganic electrolyte. The data are obtained by means of the MBPM described in Ref. [57]. To check whether the kinetic regime is DE, we substitute typical parameter values in Equation 4.102: $m_{eq} = 70$, $\beta = 20$, and $B_m = 0.2$, and as a result we obtain $D_{DE}/D_1 = 3.9 \times 10^5$, which is much greater than the experimental values of D_{eff}/D_1 in Figure 4.9. Consequently, the kinetic regime cannot be DE. On the other hand, a similar estimate of D_{BC}/D_1 from Equation 4.101 gives reasonable values. To demonstrate that, from the experimental values of D_{eff}/D_1 in Figure 4.9 we calculated u by means of Equation 4.101, substituting $B_m = 0.2$. For most of the concentrations we obtain values $0.4 < u < 2$, which seem reasonable. Values $u > 2$ are obtained at $\beta < 2$, which indicate that at the lowest micellar concentrations we are dealing with a rudimentary kinetic regime [150,151], rather than with the diffusion regime BC.

4.2.2.6.3 The Case of Stationary Interfacial Expansion

This special case of interfacial dynamics is realized with the strip method [95,147] and the overflowing cylinder method [60,92]. Because the adsorption process is stationary, the time, t , is not a parameter of state of the system. For this reason, in the kinetic diagrams (like Figure 4.10) we plot the perturbations versus the dimensionless rate of surface expansion, $\theta = (h_a^2/D_1)(dA/dt)/A$, where A is the interfacial area, and $dA/dt = \text{constant}$ is the interfacial expansion rate. In Figure 4.10, the total perturbations, $\xi_{1,T}$, $\xi_{c,T}$, and $\xi_{m,T}$, are plotted, which represent the local perturbations, $\xi_1(z)$, $\xi_c(z)$, and $\xi_m(z)$, integrated with respect to the normal coordinate z along the whole semiaxis $z > 0$ (Figure 4.7). As seen in Figure 4.10, we observe the same kinetic regimes, as in Figure 4.8, although the diagrams in the two figures look like mirror images: the “young” surface age (the regime AB) corresponds to

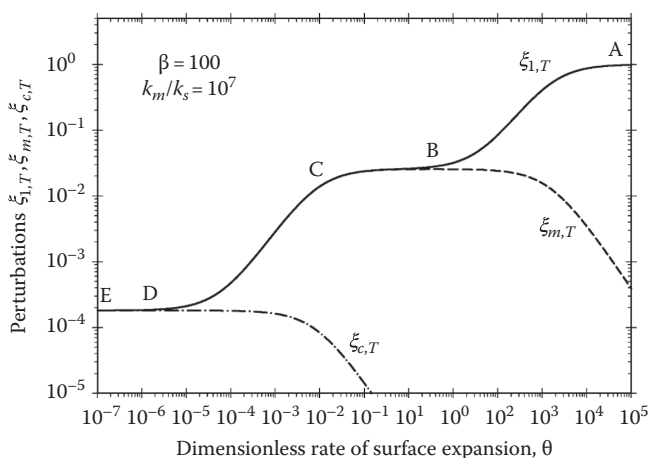


FIGURE 4.10 Total perturbations in monomer concentration, $\xi_{1,T}$, micelle concentration, $\xi_{c,T}$, and mean aggregation number, $\xi_{m,T}$, plotted vs. the dimensionless rate of surface expansion, θ , at micelle dimensionless concentration $\beta = 100$. The curves are obtained by numerical solution of the linear system of equations derived. (From Danov, K.D. et al., *Colloids Surf. A*, 282–283, 143, 2006.)

the left side of Figure 4.8, but to the right side of Figure 4.10. Analytical expressions for the adsorption and surface tension relaxation could be found in Ref. [151]. As mentioned earlier, the expressions for the effective diffusivities, D_{BC} and D_{DE} , given by Equations 4.101 and 4.102, are also valid in the case of stationary interfacial expansion. In particular, it has been found [151] that the kinetic regime of adsorption from the solutions of the nonionic surfactant polyoxyethylene-20 hexadecyl ether (Brij 58), measured by means of the strip method [147], corresponds to the regime BC.

We recall that in the regime BC the rate constants of the fast and slow micellar processes, k_m and k_s , do not affect the surfactant adsorption kinetics, and cannot be determined from the fit of the data. In principle, it is possible to observe the kinetic regime AB (and to determine k_m) with faster methods or with slower surfactants.

In summary, four distinct kinetic regimes of adsorption from micellar solutions exist, called AB, BC, CD, and DE; see Figures 4.8 and 4.10. In regime AB, the fast micellar process governs the adsorption kinetics. In regime BC, the adsorption occurs under diffusion control because the fast micellar process is equilibrated, while the slow process is negligible. In regime CD, the slow micellar process governs the adsorption kinetics. In regime DE, the adsorption occurs under diffusion control, because both the fast and slow micellar processes are equilibrated. Note that only the regimes BC and DE correspond to purely diffusion processes. For the regimes AB and CD, the rate constants of the fast and slow micellar processes, k_m and k_s , respectively, affect the surfactant adsorption kinetics, and could be in principle determined from the fit of experimental data. For the specific experimental examples considered here, the adsorption kinetics corresponds to the diffusion regime BC.

4.2.2.6.4 Kinetics of Oil Solubilization in Micellar Solutions

The term ‘solubilization’ was coined by McBain [152] to denote the increased solubility of a given compound, associated with the presence of surfactant micelles or inverted micelles in the solution. The most popular solubilization process is the transfer of oil molecules into the core of surfactant micelles. Thus, oil that has no solubility (or limited solubility) in the aqueous phase becomes water soluble in the form of solubilizate inside the micelles. This process has a central importance for washing of oily deposits from solid surfaces and porous media, and for removal of oily contaminants dispersed in water. The great practical importance of solubilization is related to its application in the everyday life: in the personal care and household detergency, as well as in various industrial processes [153].

The main actors in the solubilization process are the micelles of surfactant and/or copolymer. Their ability to uptake oil is of crucial importance [153,154]. The addition of copolymers, which form mixed micelles with the surfactants [155], is a way to control and improve the micelle solubilization performance. Two main kinetic mechanisms of solubilization have been established whose effectuation depends on the specific system:

1. *Solubilization as a bulk reaction*: Molecular dissolution and diffusion of oil into the aqueous phase takes place, with a subsequent uptake of oil molecules by surfactant micelles [156–161]. This mechanism is operative for oils (like benzene, hexane, etc.), which exhibit a sufficiently high solubility in pure water. Theoretical models have been developed and verified against the experiment [157,159–161]. The bulk solubilization includes the following processes. First, oil molecules are dissolved from the surface of an oil drop into water. Kinetically, this process can be characterized by a mass transfer coefficient. Next, by molecular diffusion, the oil molecules penetrate in the water phase, where they react

with the micelles. Thus, the concentration of free oil molecules diminishes with the distance from the oil–water interface. In other words, solubilization takes place in a certain zone around the droplet [159,160].

2. *Solubilization as a surface reaction*: This is the major solubilization mechanism for oils that are practically insoluble in water [156,158,160,162–170]. The uptake of such oils cannot happen in the bulk of the aqueous phase. The solubilization can be realized only at the oil–water interface. The mechanism may include (1) micelle adsorption, (2) uptake of oil, and (3) desorption of the swollen micelles [168–170]. Correspondingly, the theoretical description of the process involves the rate constants of the three consecutive steps. If the empty micelles are long rodlike aggregates, upon solubilization they usually break to smaller spherical aggregates [168,171]. For some systems (mostly solid solubilizates), the intermediate stages in the solubilization process may involve penetration of surfactant solution into the oily phase and formation of a *liquid crystalline phase* at the interface [172–176].

In the case of solubilization as surface reaction, the detailed kinetic mechanism could be multiform. Some authors [156,163] expect that the surfactant arrives at the interface in a monomeric form. Then, at the phase boundary mixed (or swollen) micellar aggregates are formed, which eventually desorb. This version of the model seems appropriate for solid solubilizates because hemimicelles can be formed at their surfaces, even at surfactant concentrations below the bulk CMC [177]. Another concept, presented by Plucinski and Nitsch [165], includes a step of partial fusion of the micelles with the oil–water interface, followed by a step of separation. Such mechanism could take place in the case when microemulsion drops, rather than micelles, are responsible for the occurrence of solubilization.

Experiments with various surfactant systems [166,170,178] showed that the solubilization rates for solutions of *ionic* surfactants are generally much lower than those for nonionic surfactants. This can be attributed to the electrostatic repulsion between the micelles and the similarly charged surfactant adsorption monolayer at the oil–water interface. On the other hand, copolymers have been found to form micelles, which solubilize various hydrophobic compounds well, even in the absence of low-molecular-weight surfactants [179–187]. Moreover, appropriately chosen copolymers can act as very efficient promoters of solubilization [160,168–170].

4.3 CAPILLARY HYDROSTATICS AND THERMODYNAMICS

4.3.1 SHAPES OF FLUID INTERFACES

4.3.1.1 Laplace and Young Equations

A necessary condition for mechanical equilibrium of a fluid interface is the Laplace equation of capillarity [188–191]:

$$2H\sigma = \Delta P \quad (4.103)$$

Here

H is the local mean curvature of the interface

ΔP is the local jump of the pressure across the interface

If $z = z(x, y)$ is the equation of the interface in Cartesian coordinates, then H can be expressed in the form [191]

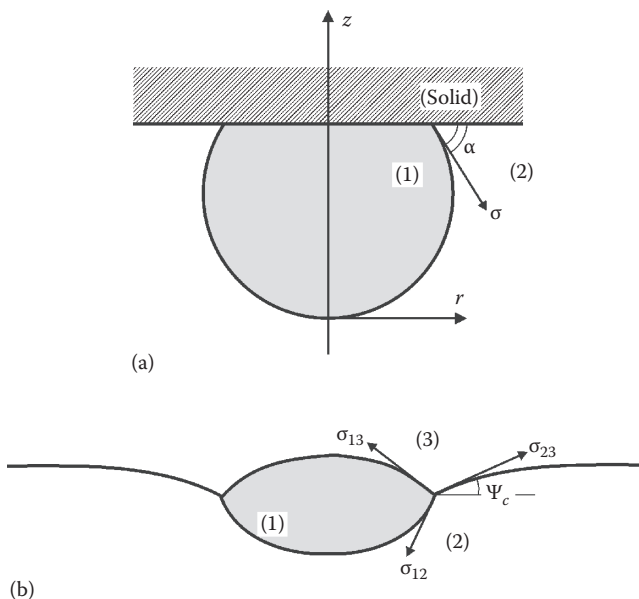


FIGURE 4.11 Sketch of fluid particle (1) attached to the interface between phases (2) and (3). (a) Fluid particle attached to solid interface; α is the contact angle; σ is the interfacial tension of the boundary between the two fluid phases. (b) Fluid particle attached to a fluid interface; σ_{12} , σ_{13} , and σ_{23} are the interfacial tensions between the respective phases; ψ_c is the slope angle of the outer meniscus at the contact line.

$$2H = \nabla_s \cdot \left[\frac{\nabla_s z}{\left(1 + |\nabla_s z|^2\right)^{1/2}} \right] \quad (4.104)$$

where ∇_s is the gradient operator in the plane xy . More general expressions for H can be found in the literature on differential geometry [191–193]. Equation 4.103, along with Equation 4.104, represents a second-order partial differential equation which determines the shape of the fluid interface. The interface is bounded by a *three-phase contact line* at which the boundary conditions for the differential equation are formulated. The latter are the respective necessary conditions for mechanical equilibrium at the contact lines. When one of the three phases is solid (Figure 4.11a), the boundary condition takes the form of Young [194] equation:

$$\sigma_{12} \cos \alpha = \sigma_{1s} - \sigma_{2s} \quad (4.105)$$

where

α is the three-phase contact angle

σ_{12} is the tension of the interface between the fluid phases 1 and 2

σ_{1s} and σ_{2s} are the tensions of the two fluid–solid interfaces

Insofar as the values of the three σ 's are determined by the intermolecular forces, contact angle α is the material characteristics of a given three-phase system. However, when the solid is not smooth and chemically homogeneous, then the contact angle exhibits hysteresis, that is, α has no defined equilibrium value [6,195]. Contact angle hysteresis can be observed even with molecularly smooth and homogeneous interfaces under dynamic conditions [196].

When all the three neighboring phases are fluids, then the boundary condition takes the form of the Neumann [197] vectorial triangle:

$$\sigma_{12}\nu_{12} + \sigma_{13}\nu_{13} + \sigma_{23}\nu_{23} = 0 \tag{4.106}$$

(see Figure 4.11b); here ν_{ik} is a unit vector, which is simultaneously normal to the contact line and tangential to the boundary between phases i and k . The Laplace, Young, and Neumann equations can be derived as conditions for minimum of the free energy of the system [37,191,198]; the effect of the line tension can also be taken into account in Equations 4.105 and 4.106 [198].

In the special case of spherical interface $H = 1/R$, with R being the sphere radius, and Equation 4.103 takes its most popular form, $2\sigma/R = \Delta P$. In the case of axisymmetric meniscus (z -is the axis of symmetry, Figure 4.11), the Laplace equation reduces to either of the following two equivalent forms [190,199]:

$$\frac{1}{r} \frac{d}{dr} \left[\frac{rz'}{(1+z'^2)^{1/2}} \right] = \frac{\Delta P}{\sigma}, \quad z = z(r) \tag{4.107}$$

$$-\frac{r''}{(1+r'^2)^{3/2}} + \frac{1}{r(1+r'^2)^{1/2}} = \frac{\Delta P}{\sigma}, \quad r = r(z) \tag{4.108}$$

Two equivalent parametric forms of Laplace equation are often used for calculations [190,199]:

$$\frac{d \sin \varphi}{dr} + \frac{\sin \varphi}{r} = \frac{\Delta P}{\sigma}, \quad \tan \varphi = \frac{dz}{dr} \tag{4.109}$$

or

$$\frac{d\varphi}{ds} = \frac{\Delta P}{\sigma} - \frac{\sin \varphi}{r}, \quad \frac{dr}{ds} = \cos \varphi, \quad \frac{dz}{ds} = \sin \varphi \tag{4.110}$$

Here

- φ is the meniscus running slope angle (Figure 4.11a)
- s is the arc length along the generatrix of the meniscus

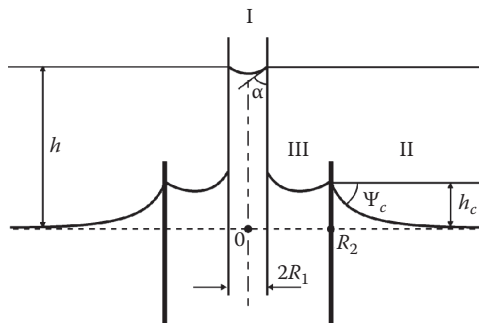


FIGURE 4.12 Capillary menisci formed around two coaxial cylinders of radii R_1 and R_2 . (I) Meniscus meeting the axis of revolution; (II) meniscus decaying at infinity; (III) meniscus confined between the two cylinders. h denotes the capillary raise of the liquid in the inner cylinder; h_c is the elevation of meniscus II at the contact line $r = R_2$.

Equation 4.110 is especially convenient for numerical integration, whereas Equation 4.109 may create numerical problems at the points with $\tan \varphi = \pm\infty$, like the particle equator in Figure 4.11a. A generalized form of Equation 4.109, with account for the interfacial (membrane) bending elastic modulus, k_c ,

$$\sigma \left(\frac{d \sin \varphi}{dr} + \frac{\sin \varphi}{r} \right) = \Delta P + \frac{k_c}{r} \cos \varphi \frac{d}{dr} \left\{ r \cos \varphi \frac{d}{dr} \left[\frac{1}{r} \frac{d}{dr} (r \sin \varphi) \right] \right\} \quad (4.111)$$

serves for description of the axisymmetric configurations of real and model cell membranes [37,200,201]. The Laplace equation can be generalized to also account for the interfacial bending moment (spontaneous curvature), shear elasticity, etc.; for review, see Refs. [37,200]. The latter effects are physically important for systems or phenomena like capillary waves [202], phospholipid and protein membranes [203–206], emulsions [207], and microemulsions [208].

4.3.1.2 Solutions of Laplace Equations for Menisci of Different Geometry

Very often, the capillary menisci have rotational symmetry. In general, there are three types of axially symmetric menisci corresponding to the three regions denoted in Figure 4.12: (1) meniscus meeting the axis of revolution, (2) meniscus decaying at infinity, and (3) meniscus confined between two cylinders, $0 < R_1 < r < R_2 < \infty$. These three cases are separately considered in the following section.

4.3.1.2.1 Meniscus Meeting the Axis of Revolution

This includes the cases of a bubble/droplet under a plate (Figure 4.11a), the two surfaces of a floating lens (Figure 4.11b), and any kind of sessile or pendant droplets/bubbles. Such a meniscus is a part of a sphere when the effect of gravity is negligible, that is when

$$\frac{\Delta \rho g b^2}{\sigma} \ll 1 \quad (4.112)$$

Here

g is the gravity acceleration

$\Delta \rho$ is the difference in the mass densities of the lower and the upper fluid

b is a characteristic radius of the meniscus curvature

For example, if Equation 4.112 is satisfied with $b = R_1$ (see Figure 4.12), the raise, h , of the liquid in the capillary is determined by means of the equation [6]

$$h = \frac{2\sigma \cos \alpha}{\Delta \rho g R_1} \quad (4.113)$$

When the gravity effect is not negligible, the capillary pressure, ΔP , becomes dependent on the z -coordinate:

$$\Delta P = \frac{2\sigma}{b} + \Delta \rho g z \quad (4.114)$$

Here b is the radius of curvature at the particle apex, where the two principal curvatures are equal (e.g., the bottom of the bubble in Figure 4.11a). Unfortunately, Equation 4.107, along with Equation

4.114, has no closed analytical solution. The meniscus shape can be exactly determined by numerical integration of Equation 4.110. Alternatively, various approximate expressions are available [199,209,210]. For example, if the meniscus slope is small, $z'^2 \ll 1$, Equation 4.107 reduces to a linear differential equation of Bessel type, whose solution reads

$$z(r) = \frac{2[I_0(qr) - 1]}{bq^2} \quad q \equiv \left(\frac{\Delta\rho g}{\sigma} \right)^{1/2} \tag{4.115}$$

where $I_0(x)$ is the modified Bessel function of the first kind and zeroth order [211,212]. Equation 4.115 describes the shape of the lower surface of the lens in Figure 4.11b; similar expression can also be derived for the upper lens surface.

4.3.1.2.2 *Meniscus Decaying at Infinity*

Examples are the outer menisci in Figures 4.11b and 4.12. In this case the action of gravity cannot be neglected insofar as the gravity keeps the interface flat far from the contact line. The capillary pressure is

$$\Delta P = \Delta\rho g z \tag{4.116}$$

As mentioned earlier, Equation 4.107, along with Equation 4.116, has no closed analytical solution. On the other hand, the region far from the contact line has always a small slope, $z'^2 \ll 1$. In this region Equation 4.107 can be linearized, and then in analogy with Equation 4.115 we derive

$$z(r) = AK_0(qr) \quad (z'^2 \ll 1) \tag{4.117}$$

where

A is a constant of integration

$K_0(x)$ is the modified Bessel function of the second kind and zeroth order [211,212]

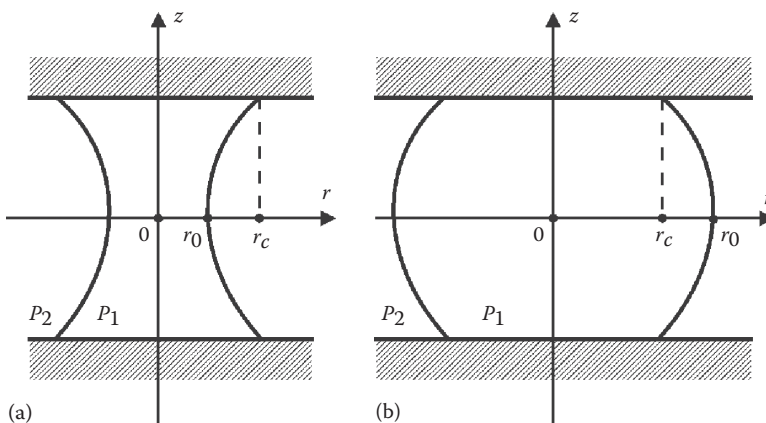


FIGURE 4.13 Concave (a) and convex (b) capillary bridges between two parallel plates. P_1 and P_2 denote the pressures inside and outside the capillary bridge, r_0 is the radius of its section with the midplane; r_c is the radius of the three-phase contact lines.

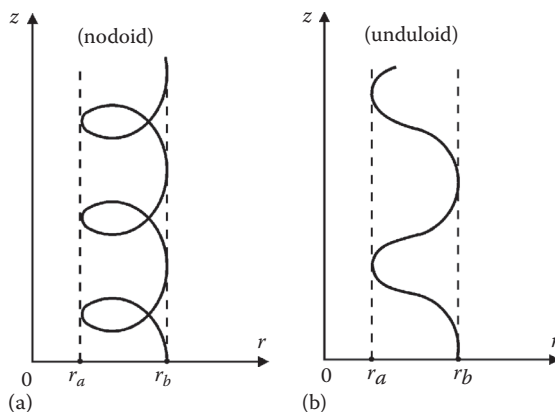


FIGURE 4.14 Typical shape of nodoid (a) and unduloid (b) plateau curves. Note that the curves are confined between two cylinders of radii r_a and r_b .

The numerical integration of Equation 4.110 can be carried out by using the boundary condition [199] $z'/z = -qK_1(qr)/K_0(qr)$ for some appropriately fixed $r \ll q^{-1}$ (see Equation 4.117). Alternatively, approximate analytical solutions of the problem are available [199,210,213]. In particular, Derjaguin [214] derived an asymptotic formula for the elevation of the contact line at the outer surface of a thin cylinder,

$$h_c = -R_1 \sin \psi_c \ln \left[\frac{qR_1 \gamma_e (1 + \cos \psi_c)}{4} \right], \quad (qR_1)^2 \ll 1 \quad (4.118)$$

where

R_1 is the radius of the contact line

ψ_c is the meniscus angle at the contact line (Figure 4.12)

q is defined by Equation 4.115

$\gamma_e = 1.781072418\dots$ is the constant of Euler–Masceroni [212]

4.3.1.2.3 Meniscus Confined between Two Cylinders ($0 < R_1 < r < R_2 < \infty$)

This is the case with the Plateau borders in real foams and emulsions, and with the model films in the Scheludko–Exerowa cell [215,216]; such is the configuration of the capillary bridges (Figure 4.13a) and of the fluid particles pressed between two surfaces (Figure 4.13b). When the gravitational deformation of the meniscus cannot be neglected, the interfacial shape can be determined by numerical integration of Equation 4.110, or by iteration procedure [217]. When the meniscus deformation caused by gravity is negligible, analytical solution can be found as described in the following section.

To determine the shape of the menisci depicted in Figure 4.13a and b, we integrate Equation 4.109 from r_0 to r to derive

$$\frac{dz}{dr} = \frac{k_1(r^2 - r_0^2) + r_0}{\pm [(r^2 - r_0^2)(r_1^2 - r^2)]^{1/2} |k_1|}, \quad k_1 \equiv \frac{P_1 - P_2}{2\sigma}, \quad r_1 \equiv \left| \frac{1 - k_1 r_0}{k_1} \right| \quad (4.119)$$

The pressures in phases 1 and 2, P_1 and P_2 , and r_0 are shown in Figure 4.13. Equation 4.119 describes curves, which after Plateau [189,190,218–220] are called “nodoid” and “unduloid” (see Figure 4.14). The nodoid (unlike the unduloid) has points with horizontal tangent, where $dz/dr = 0$.

Then with the help of Equation 4.119, we can deduce that the meniscus generatrix is a part of *nodoid* if $k_1 r_0 \in (-\infty, 0) \cup (1, +\infty)$, while the meniscus generatrix is a part of *unduloid* if $k_1 r_0 \in (0, 1)$.

In the special case, when $k_1 r_0 = 1$, the meniscus is spherical. In the other special case, $k_1 r_0 = 0$, the meniscus has the shape of *catenoid*, that is,

$$z = \pm r_0 \ln \left[\frac{r}{r_0} + \sqrt{\left(\frac{r}{r_0}\right)^2 - 1} \right], \quad (k_1 = 0) \tag{4.120}$$

The meniscus is concave and has a “neck” (Figure 4.13a) when $k_1 r_0 \in (-\infty, 1/2)$; in particular, the generatrix is nodoid for $k_1 r_0 \in (-\infty, 0)$, catenoid for $k_1 r_0 = 0$, and unduloid for $k_1 r_0 \in (0, 1/2)$. For the configuration depicted in Figure 4.13a, we have $r_1 > r_0$ (in Figure 4.14 $r_a = r_0, r_b = r_1$) and Equation 4.119 can be integrated to yield (see tables of integrals):

$$z(r) = \pm \left\{ r_0 F(\phi_1, q_1) + r_1 \operatorname{sgn} k_1 \left[E(\phi_1, q_1) - \frac{1}{r r_1} \sqrt{(r^2 - r_0^2)(r_1^2 - r^2)} \right] \right\} \quad (r_0 \leq r \leq r_1) \tag{4.121}$$

where

$\operatorname{sgn} x$ denotes the sign of x

$$q_1 = (1 - r_0^2/r_1^2)^{1/2}$$

$$\sin \phi_1 = q_1^{-1} (1 - r_0^2/r^2)^{1/2}$$

$F(\phi, q)$ and $E(\phi, q)$ are the standard symbols for elliptic integrals of the first and the second kind [211,212]

A convenient method for computation of $F(\phi, q)$ and $E(\phi, q)$ is the method of the arithmetic–geometric mean (see Ref. [211], Chapter 17.6).

The meniscus is convex (Figure 4.13b) when $k_1 r_0 \in (1/2, +\infty)$; in particular, the generatrix is unduloid for $k_1 r_0 \in (1/2, 1)$, circumference for $k_1 r_0 = 1$, and nodoid for $k_1 r_0 \in (1, +\infty)$. For the configuration depicted in Figure 4.13b, we have $r_0 > r_1$ (in Figure 4.14 $r_a = r_1, r_b = r_0$) and Equation 4.119 can be integrated to yield (see tables of integrals):

$$z(r) = \mp \left[\left(r_0 - \frac{1}{k_1} \right) F(\phi_2, q_2) - r_0 E(\phi_2, q_2) \right], \quad (r_1 \leq r \leq r_0) \tag{4.122}$$

where

$$q_2 = (1 - r_1^2/r_0^2)^{1/2}$$

$$\sin \phi_2 = q_2^{-1} (1 - r^2/r_0^2)^{1/2}$$

Additional information about the shapes, stability, and nucleation of capillary bridges, and for the capillary-bridge forces between particles, can be found in Chapter 11 of Ref. [37].

Small capillary bridges, called “pendular rings” [221], give rise to cohesion between the particles in the wet sand and to adhesion of particles to a flat plate [222]. In their study on the enhancement of rheology of three-phase (solid–oil–water) dispersions, Koos and Willenbacher [223] identified two states with different structures: (1) the *pendular state*, where the solid particles are interconnected with *concave* capillary bridges, and (2) the *capillary state*, where the particles are interconnected by *convex* capillary bridges; see Figure 4.13. In the former case, the bridging fluid wets the particles well (contact angle $\theta < 90^\circ$), whereas in the latter case the bridging fluid does not wet the particles well (contact angle $\theta > 90^\circ$). However in both cases the capillary bridging phenomenon leads to a

considerable enhancement of the rheological response of the dispersion at a minor volume fraction of the second fluid [223].

4.3.1.3 Gibbs–Thomson Equation

The dependence of the capillary pressure on the interfacial curvature leads to a difference between the chemical potentials of the components in small droplets (or bubbles) and in the large bulk phase. This effect is the driving force for phenomena like nucleation [224,225] and Ostwald ripening (see Section 4.3.1.4). Let us consider the general case of a multicomponent two-phase system; we denote the two phases by α and β . Let phase α be a liquid droplet of radius R . The two phases are supposed to coexist at equilibrium. Then we can derive [4,5,226,227]

$$\left(\mu_i^\beta\right)_R - \left(\mu_i^\beta\right)_{R=\infty} = \left(\mu_i^\alpha\right)_R - \left(\mu_i^\alpha\right)_{R=\infty} = V_i^\alpha \frac{2\sigma}{R} \quad (4.123)$$

where

- μ is chemical potential
- V_i is partial volume
- the superscripts denote phase
- the subscripts denote component

Equation 4.123 is derived under the following assumptions. When β is a gaseous phase, it is assumed that the partial volume of each component in the gas is much larger than its partial volume in the liquid α ; this is fulfilled far enough from the critical point [227]. When phase β is liquid, it is assumed that $P^\beta(R) = P^\beta(R = \infty)$, where P denotes pressure.

When phase β is an ideal gas, Equation 4.123 yields [4,5,226,227]

$$\frac{P_i^\beta(R)}{P_i^\beta(\infty)} = \exp\left(\frac{2\sigma V_i^\alpha}{RkT}\right) \quad (4.124)$$

where $P_i^\beta(R)$ and $P_i^\beta(\infty)$ denote, respectively, the equilibrium vapor pressure of component i in the droplet of radius R and in a large liquid phase of the same composition. Equation 4.124 shows that the equilibrium vapor pressure of a droplet increases with the decrease of the droplet size. (For a bubble, instead of a droplet, R must be changed to $-R$ in the right-hand side of Equation 4.124 and the tendency becomes the opposite.) Equation 4.124 implies that in an aerosol of polydisperse droplets the larger droplets will grow and the smaller droplets will diminish down to complete disappearance.

The small droplets are “protected” against disappearance when phase α contains a nonvolatile component. Then instead of Equation 4.124 we have

$$\frac{P_i^\beta(R)}{P_i^\beta(\infty)} = \frac{1 - X(R)}{1 - X(\infty)} \exp\left(\frac{2\sigma V_i^\alpha}{RkT}\right) \quad (4.125)$$

where X denotes the molar fraction of the nonvolatile component in phase α ; for $X(R) = X(\infty)$ Equation 4.125 reduces to Equation 4.124. Setting the left-hand side of Equation 4.125 equal to 1, we can determine the value $X(R)$ needed for a liquid droplet of radius R , surrounded by the gas phase β , to coexist at equilibrium with a large ($R = \infty$) liquid phase α of composition $X(\infty)$.

When both phases α and β are liquid, Equation 4.123 yields

$$\frac{X_i^\beta(R)}{X_i^\beta(\infty)} = \exp\left(\frac{2\sigma V_i^\alpha}{RkT}\right) \quad (4.126)$$

where

$X_i^\beta(R)$ denotes the equilibrium molar fraction of component i in phase β coexisting with a droplet of radius R

$X_i^\beta(\infty)$ denotes the value of $X_i^\beta(R)$ for $R \rightarrow \infty$, that is, for phase β coexisting with a large phase α of the same composition as the droplet

In the case of oil-in-water emulsion, X_i^β can be the concentration of the oil dissolved in the water. In particular, Equation 4.126 predicts that the large emulsion droplets will grow and the small droplets will diminish. This phenomenon is called Ostwald ripening (see Section 4.3.1.4). If the droplets (phase α) contain a component, which is insoluble in phase β , the small droplets will be protected against complete disappearance; a counterpart of Equation 4.125 can be derived:

$$\frac{X_i^\beta(R)}{X_i^\beta(\infty)} = \frac{1 - X(R)}{1 - X(\infty)} \exp\left(\frac{2\sigma V_i^\alpha}{RkT}\right) \quad (4.127)$$

where X denotes the equilibrium concentration in phase α of the component which is insoluble in phase β . Setting the left-hand side of Equation 4.127 equal to 1, we can determine the value $X(R)$ needed for an emulsion droplet of radius R , surrounded by the continuous phase β , to coexist at equilibrium with a large ($R = \infty$) liquid phase α of composition $X(\infty)$.

4.3.1.4 Kinetics of Ostwald Ripening in Emulsions

The Ostwald ripening is observed when the substance of the emulsion droplets (we will call it component 1) exhibits at least minimal solubility in the continuous phase, β . As discussed above earlier, the chemical potential of this substance in the larger droplets is lower than in the smaller droplets, see Equation 4.123. Then a diffusion transport of component 1 from the smaller toward the larger droplets will take place. Consequently, the size distribution of the droplets in the emulsion will change with time. The kinetic theory of Ostwald ripening was developed by Lifshitz and Slyozov [228] and Wagner [229] and further extended and applied by other authors [230–233]. The basic equations of this theory are the following.

The volume of an emulsion droplet grows (or diminishes) due to the molecules of component 1 supplied (or carried away) by the diffusion flux across the continuous medium. The balance of component 1 can be presented in the form [233]

$$\frac{4\pi}{3} \frac{d}{dt} R^3(t) = 4\pi DRV_1 [c_m(t) - c_{eq}(R)] \quad (4.128)$$

where

t is time

D is the diffusivity of component 1 in the continuous phase

V_1 is the volume per molecule of component 1

c_m is the number-volume concentration of component 1 in the continuous medium far away from the droplets surfaces

$c_{eq}(R)$ is the respective equilibrium concentration of the same component for a droplet of radius R as predicted by the Gibbs–Thomson equation

Note that Equation 4.128 is rigorous only for a diluted emulsion, in which the concentration of dissolved component 1 levels off at a constant value, $c = c_m$, around the middle of the space between each two droplets. Some authors [231] also add in the right-hand side of Equation 4.128 terms accounting for the convective mass transfer (in the case of moving droplets) and thermal contribution to the growth rate.

Because the theory is usually applied to droplets of diameter not smaller than micrometer (which are observable by optical microscope), the Gibbs–Thomson equation, Equation 4.126, can be linearized to yield [233]

$$c_{\text{eq}}(R) \approx c_{\infty} \left(1 + \frac{b}{R} \right), \quad b \equiv \frac{2\sigma V_1}{kT} \quad (4.129)$$

with c_{∞} being the value of c_{eq} for flat interface. With $\sigma = 50$ mN/m, $V_1 = 100 \text{ \AA}^3$, and $T = 25^\circ\text{C}$ we estimate $b = 2.5$ nm. The latter value justifies the linearization of Gibbs–Thomson equation for droplets of micrometer size.

Let $f(R, t)$ be the size distribution function of the emulsion droplets such that $f(R, t)dR$ is the number of particles per unit volume in the size range from R to $(R + dR)$. The balance of the number of particles in the system reads

$$df dR = (jdt)|_R - (jdt)|_{R+dR}, \quad \left(j \equiv f \frac{dR}{dt} \right) \quad (4.130)$$

The term in the left-hand side of Equation 4.130 expresses the change of the number of droplets whose radius belongs to the interval $[R, R + dR]$ during a time period dt ; the two terms in the right-hand side represent the number of the incoming and outgoing droplets in the size interval $[R, R + dR]$ during time period dt . Dividing both sides of Equation 4.130 by $(dR dt)$, we obtain the so-called continuity equation in the space of sizes [229–233]:

$$\frac{\partial f}{\partial t} + \frac{\partial j}{\partial R} = 0 \quad (4.131)$$

One more equation is needed to determine c_m . In a closed system this can be the total mass balance of component 1:

$$\frac{d}{dt} \left[c_m(t) + \frac{4\pi}{3} \int_0^{\infty} dR R^3 f(R, t) \right] = 0 \quad (4.132)$$

The first and the second terms in the brackets express the amount of component 1 contained in the continuous phase and in the droplets, respectively. This expression is appropriate for diluted emulsions when c_m is not negligible compared to the integral in the brackets.

Alternatively, in opened systems and in concentrated emulsions we can use a mean field approximation based on Equation 4.129 to obtain the following equation for c_m :

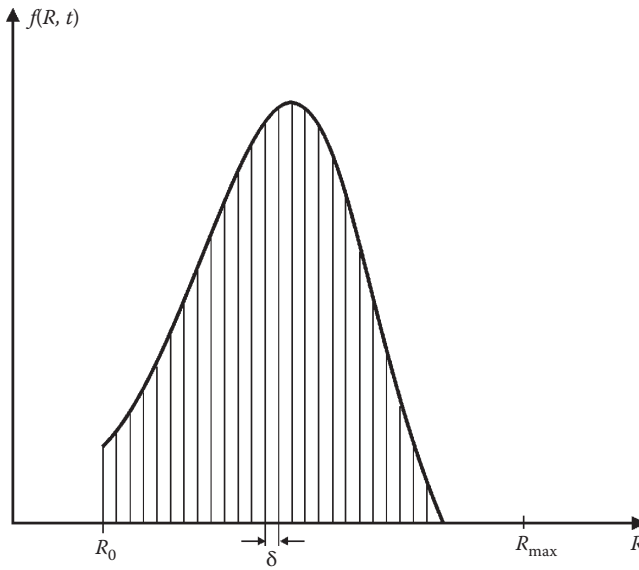


FIGURE 4.15 Sketch of the droplet size distribution function, $f(R, t)$ vs. the droplet radius R at a given moment t . δ is the length of the mesh used when solving the problem by discretization.

$$c_m(t) = c_\infty \left[1 + \frac{b}{R_m(t)} \right], \quad R_m(t) \equiv \frac{\int_{R_0}^{\infty} dR R f(R, t)}{\int_{R_0}^{\infty} dR f(R, t)} \tag{4.133}$$

where R_0 is a lower limit of the experimental distribution, typically $R_0 \approx 1 \mu\text{m}$ as smaller droplets cannot be observed optically. The estimates show that neglecting of integrals over the interval $0 < R < R_0$ in Equation 4.133 does not affect the value of R_m significantly. We see that Equation 4.133 treats each emulsion droplet as being surrounded by droplets of average radius R_m , which provide a medium concentration c_m in accordance with the Gibbs–Thomson equation, Equation 4.129. From Equations 4.128 through 4.131 and 4.133 we can derive a simple expression for the flux j :

$$j(R, t) = Q \left(\frac{1}{RR_m} - \frac{1}{R^2} \right) f(R, t), \quad Q \equiv Dbc_\infty V_l \tag{4.134}$$

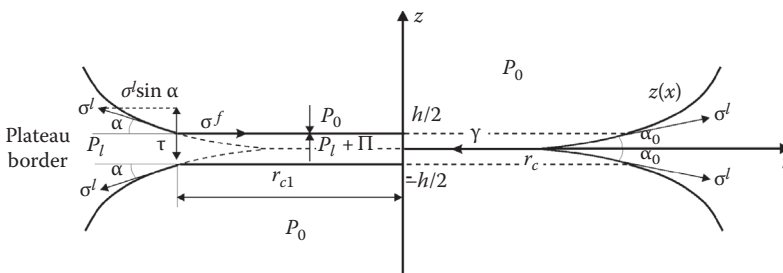


FIGURE 4.16 The detailed and membrane models of a thin liquid film (on the left- and right-hand side, respectively).

In calculations, we use the set of Equations 4.128, 4.131, and 4.132 or 4.133 to determine the distribution $f(R, t)$ at known distribution $f(R, 0)$ at the initial moment $t = 0$. In other words, the theory predicts the evolution of the system at a given initial state. From a computational viewpoint it is convenient to calculate $f(R, t)$ in a finite interval $R_0 \leq R < R_{\max}$ (see Figure 4.15). The problem can be solved numerically by discretization: the interval $R_0 \leq R < R_{\max}$ is subdivided into small portions of length δ , the integrals are transformed into sums, and the problem is reduced to solving a linear set of equations for the unknown functions $f_k(t) \equiv f(R_k, t)$, where $R_k = R_0 + k\delta$, $k = 1, 2, \dots$

In practice, the emulsions are formed in the presence of surfactants. At concentrations above the CMC the swollen micelles can serve as carriers of oil between the emulsion droplets of different size. In other words, surfactant micelles can play the role of mediators of the Ostwald ripening. Micelle-mediated Ostwald ripening has been observed in solutions of nonionic surfactants [234–236]. In contrast, it was found that the micelles do not mediate the Ostwald ripening in undecane-in-water emulsions at the presence of an *ionic* surfactant (SDS) [237]. It seems that the surface charge due to the adsorption of ionic surfactant (and the resulting double layer repulsion) prevents the contact of micelles with the oil drops, which is a necessary condition for micelle-mediated Ostwald ripening.

4.3.2 THIN LIQUID FILMS AND PLATEAU BORDERS

4.3.2.1 Membrane and Detailed Models of a Thin Liquid Film

Thin liquid films can be formed between two colliding emulsion droplets or between the bubbles in foam. Formation of thin films accompanies the particle–particle and particle–wall interactions in colloids. From a *mathematical* viewpoint, a film is thin when its thickness is much smaller than its lateral dimension. From a *physical* viewpoint, a liquid film formed between two macroscopic phases is *thin* when the energy of interaction between the two phases across the film is not negligible. The specific forces causing the interactions in a thin liquid film are called *surface forces*. Repulsive surface forces stabilize thin films and dispersions, whereas attractive surface forces cause film rupture and coagulation. This section is devoted to the *macroscopic* (hydrostatic and thermodynamic) theory of thin films, while the *molecular* theory of surface forces is reviewed in Section 4.4.

In Figure 4.16, a sketch of plane-parallel liquid film of thickness h is presented. The liquid in the film contacts with the bulk liquid in the *Plateau border*. The film is symmetrical, that is, it is formed between two *identical* fluid particles (drops, bubbles) of internal pressure P_0 . The more complex case of nonsymmetrical and curved films is reviewed elsewhere [238–240].

Two different, but supplementary, approaches (models) are used in the macroscopic description of a thin liquid film. The first of them, the “membrane approach,” treats the film as a membrane of zero thickness and one tension, γ , acting tangentially to the membrane (see the right-hand side of Figure 4.16). In the “detailed approach”, the film is modeled as a homogeneous liquid layer of thickness h and surface tension σ . The pressure P_0 in the fluid particles is larger than the pressure, P_l , of the liquid in the Plateau border. The difference

$$P_c = P_0 - P_l \quad (4.135)$$

represents the capillary pressure of the liquid meniscus. By making the balance of the forces acting on a plate of unit width along the y -axis and height h placed normally to the film at $-h/2 < z < h/2$ (Figure 4.16), we derive the Rusanov [241] equation:

$$\gamma = 2\sigma^f + P_c h \quad (4.136)$$

Equation 4.136 expresses a condition for equivalence between the membrane and detailed models with respect to the lateral force. To derive the normal force balance we consider a parcel of unit area from the film surface in the detailed approach. Because the pressure in the outer phase P_0 is larger

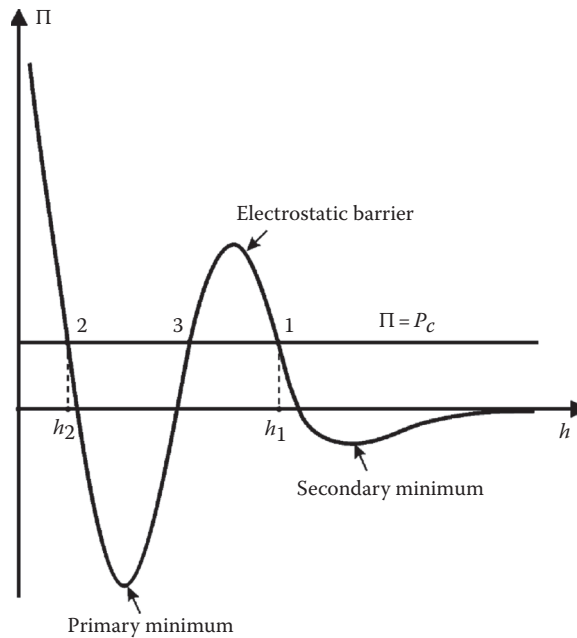


FIGURE 4.17 Sketch of a disjoining pressure isotherm of the DLVO type, Π vs. h . The intersection points of the $\Pi(h)$ -isotherm with the line $\Pi = P_c$ correspond to equilibrium films: $h = h_1$ (primary film), $h = h_2$ (secondary film). Point 3 corresponds to unstable equilibrium.

than the pressure inside the liquid, P_l , the mechanical equilibrium at the film surface is ensured by the action of an additional *disjoining* pressure, $\Pi(h)$, representing the surface force per unit area of the film surfaces [242]

$$\Pi(h) = P_0 - P_l = P_c \quad (4.137)$$

(see Figure 4.16). Note that Equation 4.137 is satisfied only at equilibrium; at nonequilibrium conditions the viscous force can also contribute to the force balance per unit film area. In general, the disjoining pressure, Π , depends on the film thickness, h . A typical $\Pi(h)$ -isotherm is depicted in Figure 4.17 (for details see Section 4.4). We see that the equilibrium condition, $\Pi = P_c$, can be satisfied at three points shown in Figure 4.17. Point 1 corresponds to a film, which is stabilized by the double layer repulsion; sometimes such a film is called the “primary film” or “common black film.” Point 3 corresponds to unstable equilibrium and cannot be observed experimentally. Point 2 corresponds to a very thin film, which is stabilized by the short range repulsion; such a film is called the “secondary film” or “Newton black film.” Transitions from common to Newton black films are often observed with foam films [243–246]. Note that $\Pi > 0$ means repulsion between the film surfaces, whereas $\Pi < 0$ corresponds to attraction.

4.3.2.2 Thermodynamics of Thin Liquid Films

In the framework of the membrane approach the film can be treated as a single surface phase, whose Gibbs–Duhem equation reads [238,247]:

$$d\gamma = -s^f dT - \sum_{i=1}^k \Gamma_i d\mu_i \quad (4.138)$$

where

γ is the film tension

T is temperature

s^f is excess entropy per unit area of the film

Γ_i and μ_i are the adsorption and the chemical potential of the i th component, respectively

The Gibbs–Duhem equations of the liquid phase (l) and the outer phase (o) read

$$dP_\chi = s_\chi^\chi dT + \sum_{i=1}^k n_i^\chi d\mu_i, \quad \chi = l, o \quad (4.139)$$

where

s_χ^χ and n_i^χ are entropy and number of molecules per unit volume

P_χ is pressure ($\chi = l, o$)

The combination of Equations 4.127 and 4.131 provides an expression for dP_c . Let us multiply this expression by h and subtract the result from the Gibbs–Duhem equation of the film, Equation 4.138. The result reads:

$$d\gamma = -\tilde{s} dT + h dP_c - \sum_{i=1}^k \tilde{\Gamma}_i d\mu_i \quad (4.140)$$

where

$$\tilde{s} = s^f + (s_v^o - s_v^l)h, \quad \tilde{\Gamma}_i = \Gamma_i + (n_i^o - n_i^l)h, \quad i = 1, \dots, k \quad (4.141)$$

An alternative derivation of the same equations is possible [248,249]. Imagine two equidistant planes separated at a distance h . The volume confined between the two planes is thought to be filled with the bulk liquid phase (l). Taking surface excesses with respect to the bulk phases we can derive Equations 4.140 and 4.141 with \tilde{s} and $\tilde{\Gamma}_i$ being the excess surface entropy and adsorption ascribed to the surfaces of this liquid layer [248,249]. A comparison between Equations 4.138 and 4.140 shows that there is one additional differential in Equation 4.140. It corresponds to one supplementary degree of freedom connected with the choice of the parameter h . To specify the model, we need an additional equation to determine h . For example, let this equation be

$$\tilde{\Gamma}_1 = 0 \quad (4.142)$$

Equation 4.142 requires h to be the thickness of a liquid layer from phase (l), containing the same amount of component 1 as the real film. This thickness is called the thermodynamic thickness of the film [249]. It can be on the order of the real film thickness if component 1 is chosen in an appropriate way, say the solvent in the film phase.

From Equations 4.137, 4.140, and 4.142, we obtain [248]

$$d\gamma = -\tilde{s} dT + h d\Pi - \sum_{i=2}^k \tilde{\Gamma}_i d\mu_i \quad (4.143)$$

A corollary of Equation 4.143 is the Frumkin [250] equation

$$\left(\frac{\partial \gamma}{\partial \Pi} \right)_{T, \mu_2, \dots, \mu_k} = h \quad (4.144)$$

Equation 4.144 predicts a rather weak dependence of the film tension γ on the disjoining pressure, Π , for equilibrium thin films (small h). By means of Equations 4.136 and 4.137, Equation 4.143 can be transformed to read [249]

$$2 d\sigma^f = -\tilde{s} dT - \Pi dh - \sum_{i=2}^k \tilde{\Gamma}_i d\mu_i \quad (4.145)$$

From Equation 4.145, we can derive the following useful relations [248]

$$2 \left(\frac{\partial \sigma^f}{\partial h} \right)_{T, \mu_2, \dots, \mu_k} = -\Pi \quad (4.146)$$

$$\sigma^f(h) = \sigma^l + \frac{1}{2} \int_h^\infty \Pi(h) dh \quad (4.147)$$

with σ^l being the surface tension of the bulk liquid. Equation 4.147 allows calculation of the film surface tension when the disjoining pressure isotherm is known.

Note that the thermodynamic equations mentioned earlier are, in fact, corollaries from the Gibbs–Duhem equation of the membrane approach Equation 4.138. There is an equivalent and complementary approach, which treats the two film surfaces as separate surface phases with their own fundamental equations [241,251,252]; thus for a flat symmetric film we postulate

$$dU^f = T dS^f + 2\sigma^f dA + \sum_{i=1}^k \mu_i dN_i^f - \Pi A dh \quad (4.148)$$

where

A is area

U^f , S^f , and N_i^f are, respectively, excess internal energy, entropy, and number of molecules ascribed to the film surfaces

Compared with the fundamental equation of a simple surface phase [5], Equation 4.148 contains an additional term, $\Pi A dh$, which takes into account the dependence of the film surface energy on the film thickness. Equation 4.148 provides an alternative thermodynamic definition of disjoining pressure:

$$\Pi = -\frac{1}{A} \left(\frac{\partial U^f}{\partial h} \right) \quad (4.149)$$

4.3.2.3 The Transition Zone between Thin Film and Plateau Border

4.3.2.3.1 Macroscopic Description

The thin liquid films formed in foams or emulsions exist in permanent contact with the bulk liquid in the Plateau border, encircling the film. From a macroscopic viewpoint, the boundary between film and Plateau border is treated as a three-phase contact line, the line at which the two surfaces of the Plateau border (the two concave menisci sketched in Figure 4.16) intersect at the plane of the film (see the right-hand side of Figure 4.16). The angle, α_0 , subtended between the two meniscus surfaces represents the thin film contact angle. The force balance at each point of the contact line is given by Equation 4.106 with $\sigma_{12} = \gamma$ and $\sigma_{13} = \sigma_{23} = \sigma^l$. The effect of the line tension, κ , can also be

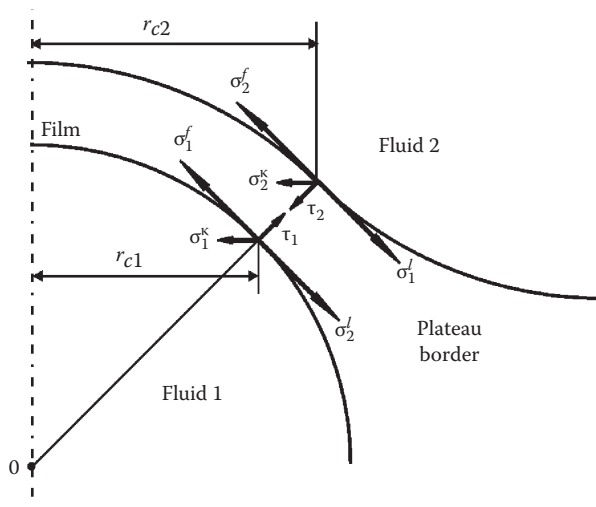


FIGURE 4.18 The force balance in each point of the two contact lines representing the boundary between a spherical film and the Plateau border (see Equation 4.153).

taken into account. For example, in the case of symmetrical flat film with circular contact line, like those depicted in Figure 4.16, we can write [252]

$$\gamma + \frac{\kappa}{r_c} = 2\sigma^j \cos \alpha_0 \quad (4.150)$$

where r_c is the radius of the contact line.

There are two film surfaces and two contact lines in the detailed approach (see the left-hand side of Figure 4.16). They can be treated thermodynamically as linear phases and a 1D counterpart of Equation 4.148 can be postulated [252]:

$$dU^L = T dS^L + 2\tilde{\kappa} dL + \sum_i \mu_i dN_i^L + \tau dh \quad (4.151)$$

Here

U^L , S^L , and N_i^L are linear excesses

$\tilde{\kappa}$ is the line tension in the detailed approach

$$\tau = \frac{1}{L} \left(\frac{\partial U^L}{\partial h} \right) \quad (4.152)$$

is a 1D counterpart of the disjoining pressure (see Equation 4.149). The quantity τ , called the *transversal tension*, takes into account the interaction between the two contact lines. The general force balance at each point of the contact line can be presented in the form of the following vectorial sum [238]

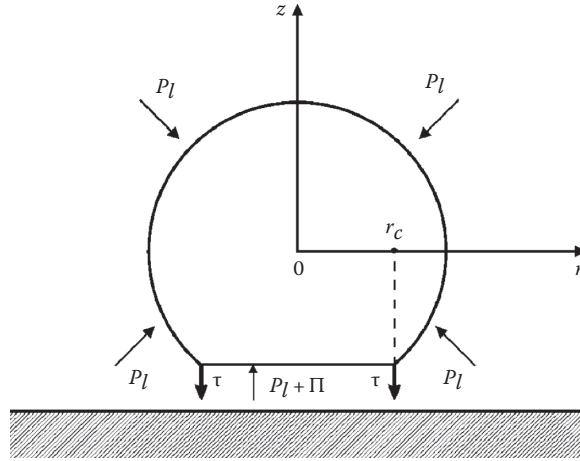


FIGURE 4.19 Sketch of the forces exerted on a fluid particle (bubble, drop, vesicle) attached to a solid surface: Π is disjoining pressure, τ is transversal tension, P_l is the pressure in the outer liquid phase.

$$\sigma_i^f + \sigma_i^l + \sigma_i^k + \tau_i = 0, \quad i = 1, 2 \quad (4.153)$$

The vectors taking part in Equation 4.153 are depicted in [Figure 4.18](#), where $|\sigma_i^k| = \tilde{\kappa}_i / r_{ci}$. For the case of a flat symmetric film ([Figure 4.16](#)) the tangential and normal projections of Equation 4.153, with respect to the plane of the film, read:

$$\sigma^f + \frac{\tilde{\kappa}}{r_{c1}} = \sigma^l \cos \alpha \quad (4.154)$$

$$\tau = \sigma^l \sin \alpha \quad (4.155)$$

Note that, in general $\alpha \neq \alpha_0$ (see [Figure 4.16](#)). Besides, both α_0 and α can depend on the radius of the contact line due to line tension effects. In the case of straight contact line from Equations 4.147 and 4.154, we derive [252]

$$\cos \alpha \Big|_{r_{c1}=\infty} = \frac{\sigma^f}{\sigma^l} = 1 + \frac{1}{2\sigma^l} \int_h^\infty \Pi(h) dh \quad (4.156)$$

Because $\cos \alpha \leq 1$, the surface tension of the film must be less than the bulk solution surface tension, $\sigma^f < \sigma^l$, and the integral term in Equation 4.156 must be negative in order for a nonzero contact angle to be formed. Hence, the contact angle, α , and the transversal tension, τ (see Equation 4.155), are integral effects of the long-range *attractive* surface forces acting in the transition zone between the film and Plateau border, where $h > h_1$ (see [Figure 4.17](#)).

In the case of a fluid particle attached to a surface ([Figure 4.19](#)) the integral of the pressure $P_l = P_0 - \Delta\rho gz$ over the particle surface equals the buoyancy force, F_b , which at equilibrium is counterbalanced by the disjoining pressure and transversal tension forces [238,253]:

$$2\pi r_{c1} \tau = F_b + \pi r_{c1}^2 \Pi \quad (4.157)$$

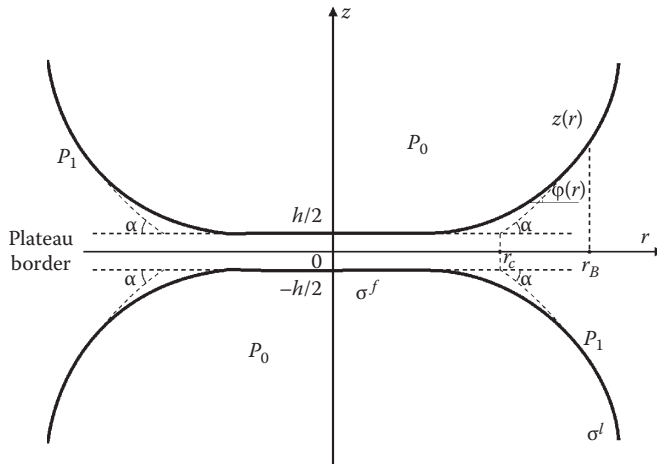


FIGURE 4.20 Liquid film between two attached fluid particles (bubbles, drops, vesicles). The solid lines represent the actual interfaces, whereas the dashed lines show the extrapolated interfaces in the transition zone between the film and the Plateau border.

F_b is negligible for bubbles of diameter smaller than ca 300 μm . Then the forces due to τ and Π counterbalance each other. Hence, at equilibrium the role of the repulsive disjoining pressure is to keep the film thickness uniform, whereas the role of the attractive transversal tension is to keep the bubble (droplet) attached to the surface. In other words, the particle sticks to the surface at its contact line where the long-range attraction prevails (see Figure 4.17), whereas the repulsion predominates inside the film, where $\Pi = P_c > 0$. Note that this conclusion is valid not only for particle–wall attachment, but also for particle–particle interaction. For zero contact angle τ is also zero (Equation 4.155) and the particle will rebound from the surface (the other particle), unless some additional external force keeps it attached.

4.3.2.3.2 Micromechanical Description

From a microscopic viewpoint, the transition between the film surface and the meniscus is smooth, as depicted in Figure 4.20. As the film thickness increases across the transition zone, the disjoining pressure decreases and tends to zero at the Plateau border (see Figures 4.17 and 4.20). The surface tension varies from σ^f for the film to σ^l for the Plateau border [254,255]. By using local force balance considerations, we can derive the equations governing the shape of the meniscus in the transition zone; in the case of axial symmetry (depicted in Figure 4.20), these equations read [255]:

$$\frac{d}{dr}(\sigma \sin \varphi) + \frac{1}{r} \sigma(r) \sin \varphi(r) = P_c - \Pi(h(r)) \quad (4.158)$$

$$-\frac{d}{dz}(\sigma \cos \varphi) + \frac{1}{r} \sigma(r) \sin \varphi(r) = P_c, \quad \tan \varphi(r) = \frac{dz}{dr} \quad (4.159)$$

where $\varphi(r)$ and $h(r) = 2z(r)$ are the running meniscus slope angle and thickness of the gap, respectively. Equations 4.158 and 4.159 allow calculation of the three unknown functions, $z(r)$, $\varphi(r)$, and $\sigma(r)$, provided that the disjoining pressure, $\Pi(h)$, is known from the microscopic theory. By eliminating P_c between Equations 4.158 and 4.159 we can derive [255]

$$\frac{d\sigma}{dz} = -\Pi(h(r))\cos\varphi(r) \quad (4.160)$$

This result shows that the hydrostatic equilibrium in the transition region is ensured by simultaneous variation of σ and Π . Equation 4.160 represents a generalization of Equation 4.146 for a film of uneven thickness and axial symmetry. Generalization of Equations 4.158 through 4.160 for the case of more complicated geometry is also available [238,239].

For the Plateau border we have $z \gg h$, $\Pi \rightarrow 0$, $\sigma \rightarrow \sigma' = \text{constant}$, and both Equations 4.158 and 4.159 reduce to Equation 4.109 with $\Delta P = P_c$. The macroscopic contact angle, α , is defined as the angle at which the *extrapolated* meniscus, obeying Equation 4.109, meets the *extrapolated* film surface (see the dashed line in Figure 4.20). The real surface, shown by solid line in Figure 4.20, differs from this *extrapolated* (idealized) profile, because of the interactions between the two film surfaces, which is taken into account in Equation 4.158, but not in Equation 4.109. To compensate for the difference between the real and idealized system, the line and transversal tensions are ascribed to the contact line in the macroscopic approach. In particular, the line tension makes up for the differences in surface tension and running slope angle [255]:

$$\frac{\tilde{\kappa}}{r_c} = \int_0^{r_B} \left[\left(\frac{\sigma \sin^2 \varphi}{r \cos \varphi} \right)^{\text{real}} - \left(\frac{\sigma \sin^2 \varphi}{r \cos \varphi} \right)^{\text{idealized}} \right] dr \quad (4.161)$$

whereas τ compensates for the differences in surface forces (disjoining pressure):

$$\tau = \frac{1}{r_c} \int_0^{r_B} [(\Pi)^{\text{id}} - \Pi(r)] r dr \quad (4.162)$$

where

$$\begin{aligned} (\Pi)^{\text{id}} &= P_c \quad \text{for } 0 < r < r_c \\ (\Pi)^{\text{id}} &= 0 \quad \text{for } r > r_c \end{aligned}$$

The superscripts “real” and “idealized” in Equation 4.161 mean that the quantities in the respective parentheses must be calculated for the real and idealized meniscus profiles; the latter coincide for $r > r_B$ (Figure 4.20). Results for $\tilde{\kappa}$ and τ calculated by means of Equations 4.161 and 4.162 can be found in Ref. [256].

In conclusion, it should be noted that the width of the transition region between a thin liquid film and Plateau border is usually very small [257]—below 1 μm . That is why the optical measurements of the meniscus profile give information about the thickness of the Plateau border in the region $r > r_B$ (Figure 4.20). Then if the data are processed by means of the Laplace equation (Equation 4.109), we determine the contact angle, α , as discussed earlier. In spite of being a purely macroscopic quantity, α characterizes the magnitude of the surface forces inside the thin liquid film, as implied by Equation 4.156. This has been pointed out by Derjaguin [257] and Princen and Mason [258].

4.3.2.4 Methods for Measuring Thin Film Contact Angles

Prins [259] and Clint et al. [260] developed a method of contact angle measurement for macroscopic flat foam films formed in a glass frame in contact with a bulk liquid. They measured the jump in

the force exerted on the film at the moment, when the contact angle is formed. Similar experimental setup was used by Yamanaka [261] for measurement of the velocity of motion of the three-phase contact line.

An alternative method, which can be used in both equilibrium and dynamic measurements with vertical macroscopic films, was developed by Princen and Frankel [262,263]. They determined the contact angle from the data for diffraction of a laser beam refracted by the Plateau border.

In the case of microscopic films, especially appropriate are the interferometric methods: light beams reflected or refracted from the liquid meniscus interfere and create fringes, which in turn give information about the shape of the liquid surfaces. The fringes are usually formed in the vicinity of the contact line, which provides a high precision of the extrapolation procedure used to determine the contact angle (see Figure 4.20). We can distinguish several interference techniques depending on how the interference pattern is created. In the usual interferometry the fringes are due to interference of beams reflected from the upper and lower meniscus. This technique can be used for contact angle measurements with foam films [217,264–266], emulsion films [267,268], and adherent biological cells [201]. The method is applicable for not-too-large contact angles ($\alpha < 8^\circ\text{--}10^\circ$); for larger meniscus slopes the region of fringes shrinks and the measurements are not possible.

The basic principle of the differential interferometry consists of an artificial splitting of the original image into two equivalent and overlapping images (see Françon [269] or Beyer [270]). Thus interferometric measurements are possible with meniscus surfaces of larger slope. The differential interferometry in transmitted light was used by Zorin et al. [271,272] to determine the contact angles of wetting and free liquid films. This method is applicable when the whole system under investigation is transparent to light.

Differential interferometry in reflected light allows for the measurement of the shape of the upper reflecting surface. This method was used by Nikolov et al. [253,273–275] to determine the contact angle, film, and line tension of foam films formed at the top of small bubbles floating at the surface of ionic and nonionic surfactant solutions. An alternative method is the holographic interferometry

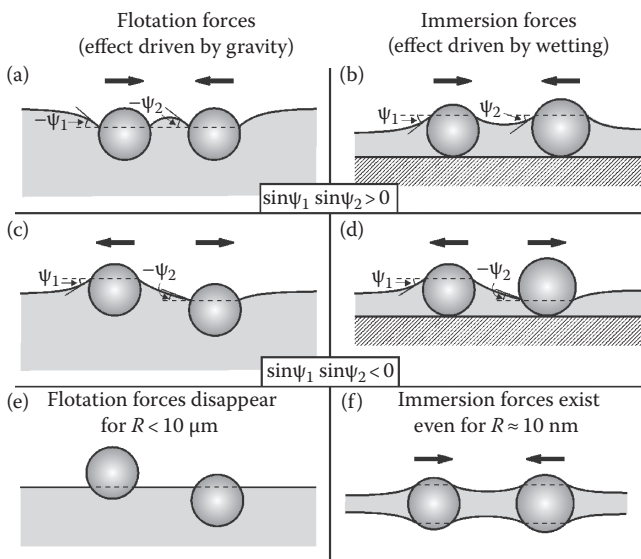


FIGURE 4.21 Flotation (a, c, e) and immersion (b, d, f) lateral capillary forces between two particles attached to fluid interface: (a) and (b) two similar particles; (c) a light and a heavy particle; (d) a hydrophilic and a hydrophobic particle; (e) small floating particles that do not deform the interface; (f) small particles captured in a thin liquid film deforming the interfaces due to the wetting effects.

applied by Picard et al. [276,277] to study the properties of bilayer lipid membranes in solution. Film contact angles can also be determined from the Newton rings of liquid lenses, which spontaneously form in films from micellar surfactant solutions [217].

Contact angles can also be determined by measuring several geometrical parameters characterizing the profile of the liquid meniscus and processing them by using the Laplace equation (Equation 4.109) [278,279]. The computer technique allows processing of many experimental points from meniscus profile and automatic digital image analysis.

Contact angles of microscopic particles against another phase boundary can be determined interferometrically, by means of a *film trapping technique* [280,281]. It consists in capturing of micrometer-sized particles, emulsion drops, and biological cells in thinning free foam films or wetting films. The interference pattern around the entrapped particles allows us to reconstruct the meniscus shape, to determine the contact angles, and to calculate the particle-to-interface adhesion energy [280,281].

A conceptually different method, called *gel trapping technique*, was developed by Paunov [282] for determining the three-phase contact angle of solid colloid particles at an air–water or oil–water interface. The method is applicable for particle diameters ranging from several hundred nanometers to several hundred micrometers. This technique is based on spreading of the particles on a liquid interface with a subsequent gelling of the water phase with a nonadsorbing polysaccharide. The particle monolayer trapped on the surface of the gel is then replicated and lifted up with poly(dimethylsiloxane) (PDMS) elastomer, which allows the particles embedded within the PDMS surface to be imaged with high resolution by using a scanning electron microscope (SEM), which gives information on the particle contact angle at the air–water or the oil–water interface [282]. This method has found applications for determining the contact angles of various inorganic [283,284] and organic [285,286] particles at liquid interfaces.

4.3.3 LATERAL CAPILLARY FORCES BETWEEN PARTICLES ATTACHED TO INTERFACES

4.3.3.1 Particle–Particle Interactions

The origin of the lateral capillary forces between particles captive at a fluid interface leads to deformation of the interface, which is supposed to be flat in the absence of particles. The larger the interfacial deformation, the stronger is the capillary interaction. It is known that two similar particles floating on a liquid interface attract each other [287–289] (see Figure 4.21a). This attraction appears because the liquid meniscus deforms in such a way that the gravitational potential energy of the two particles decreases when they approach each other. Hence the origin of this force is the particle weight (including the Archimedes force).

A force of capillary attraction also appears when the particles (instead of being freely floating) are partially immersed in a liquid layer on a substrate [290–292] (see Figure 4.21b). The deformation of the liquid surface in this case is related to the wetting properties of the particle surface, that is, to the position of the contact line and the magnitude of the contact angle, rather than to gravity.

To distinguish between the capillary forces in the case of floating particles and in the case of partially immersed particles on a substrate, the former are called lateral *flotation* forces and the latter, lateral *immersion* forces [289,292]. These two kinds of forces exhibit similar dependence on the interparticle separation but very different dependencies on the particle radius and surface tension of the liquid (see Refs. [37,293] for comprehensive reviews). The flotation and immersion forces can be both attractive (Figure 4.21a and b) and repulsive (Figure 4.21c and d). This is determined by the signs of the meniscus slope angles ψ_1 and ψ_2 at the two contact lines: the capillary force is attractive when $\sin \psi_1 \sin \psi_2 > 0$ and repulsive when $\sin \psi_1 \sin \psi_2 < 0$. In the case of flotation forces $\psi > 0$ for *light* particles (including bubbles) and $\psi < 0$ for *heavy* particles. In the case of immersion forces between particles protruding from an aqueous layer, $\psi > 0$ for *hydrophilic* particles and $\psi < 0$ for

hydrophobic particles. When $\psi = 0$ there is no meniscus deformation and, hence, there is no capillary interaction between the particles. This can happen when the weight of the particles is too small to create significant surface deformation (Figure 4.21e).

The immersion force appears not only between particles in wetting films (Figure 4.21b and d), but also in symmetric fluid films (Figure 4.21f). The theory provides the following asymptotic expression for calculating the lateral capillary force between two particles of radii R_1 and R_2 separated by a center-to-center distance L [37,288–293]:

$$F = 2\pi\sigma Q_1 Q_2 q K_1(qL) \left[1 + O\left(q^2 R_k^2\right) \right] \quad r_k \ll L \quad (4.163)$$

where

σ is the liquid–fluid interfacial tension

r_1 and r_2 are the radii of the two contact lines

$Q_k = r_k \sin \psi_k$ ($k = 1, 2$) is the “capillary charge” of the particle [289,292]; in addition

$$q^2 = \frac{\Delta\rho g}{\sigma} \quad (\text{in thick film})$$

$$q^2 = \frac{\Delta\rho q - \Pi'}{\sigma} \quad (\text{in thick films}) \quad (4.164)$$

Here

$\Delta\rho$ is the difference between the mass densities of the two fluids

Π' is the derivative of the disjoining pressure with respect to the film thickness

$K_1(x)$ is the modified Bessel function of the first order

The asymptotic form of Equation 4.163 for $qL \ll 1$ ($q^{-1} = 2.7$ mm for water),

$$F = \frac{2\pi\sigma Q_1 Q_2}{L} \quad r_k \ll L \ll q^{-1} \quad (4.165)$$

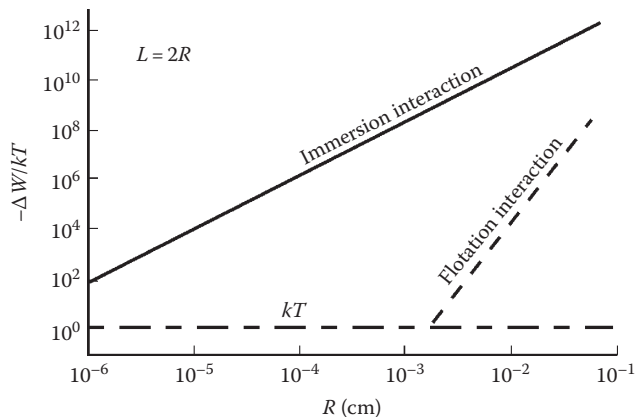


FIGURE 4.22 Plot of the capillary interaction energy in kT units, $\Delta W/kT$, vs. the radius, R , of two similar particles separated at a center-to-center distance $L = 2R$.

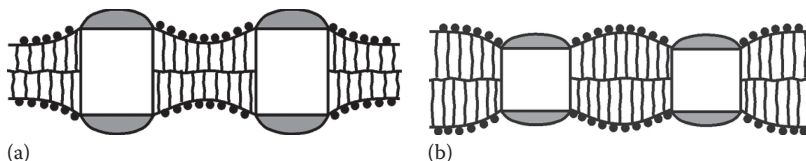


FIGURE 4.23 Inclusions (say, membrane proteins) in a lipid bilayer: the thickness of the inclusion can be greater (a) or smaller (b) than the thickness of the (nondisturbed) lipid bilayer. In both cases, the overlap of the deformations around the inclusions leads to an attraction between them (see Refs. [37,204].)

looks like a 2D analogue of Coulomb's law, which explains the name "capillary charge" of Q_1 and Q_2 . Note that the immersion and flotation forces exhibit the same functional dependence on the interparticle distance, see Equations 4.163 and 4.164. On the other hand, their different physical origin results in different magnitudes of the "capillary charges" of these two kinds of capillary force. In this aspect they resemble the electrostatic and gravitational forces, which obey the same power law, but differ in the physical meaning and magnitude of the force constants (charges, masses). In the special case when $R_1 = R_2 = R$ and $r_k \ll L \ll q^{-1}$, we can derive [292,293]

$$F \propto \left(\frac{R^6}{\sigma} \right) K_1(qL) \quad \text{for flotation force}$$

$$F \propto \sigma R^2 K_1(qL) \quad \text{for immersion force} \quad (4.166)$$

Hence, the flotation force decreases, while the immersion force increases, when the interfacial tension σ increases. Besides, the flotation force decreases much more strongly with the decrease of R than the immersion force. Thus $F_{\text{flotation}}$ is negligible for $R < 10 \mu\text{m}$, whereas $F_{\text{immersion}}$ can be significant even when $R = 10 \text{ nm}$. This is demonstrated in Figure 4.22 where the two types of capillary interactions are compared for a wide range of particle sizes. The values of the parameters used are: particle mass density $\rho_p = 1.05 \text{ g/cm}^3$, surface tension $\sigma = 72 \text{ mN/m}$, contact angle $\alpha = 30^\circ$, interparticle distance $L = 2R$, and thickness of the nondisturbed planar film $l_0 = R$. The drastic difference in the magnitudes of the two types of capillary forces is due to the different deformation of the water–air interface. The small floating particles are too light to create substantial deformation of the liquid surface, and the lateral capillary forces are negligible (Figure 4.21e). In the case of immersion forces the particles are restricted in the vertical direction by the solid substrate. Therefore, as the film becomes thinner, the liquid surface deformation increases, thus giving rise to a strong interparticle attraction.

As seen in Figure 4.22, the immersion force can be significant between particles whose radii are larger than few nanometers. It has been found to promote the growth of 2D crystals from colloid particles [294–297], viruses, and globular proteins [298–304]. Such 2D crystals have found various applications: in nanolithography [305], microcontact printing [306], as nanostructured materials in photo-electrochemical cells [307], in photocatalytic films [308], photo- and electro-luminescent semiconductor materials [309], as samples for electron microscopy of proteins and viruses [310], as immunosensors [311], etc. (for reviews see Refs. [37,312]).

In the case of interactions between inclusions in lipid bilayers (Figure 4.23), the elasticity of the bilayer interior must also be taken into account. The calculated energy of capillary interaction between integral membrane proteins turns out to be of the order of several kT [204]. Hence, this interaction can be a possible explanation for the observed aggregation of membrane proteins

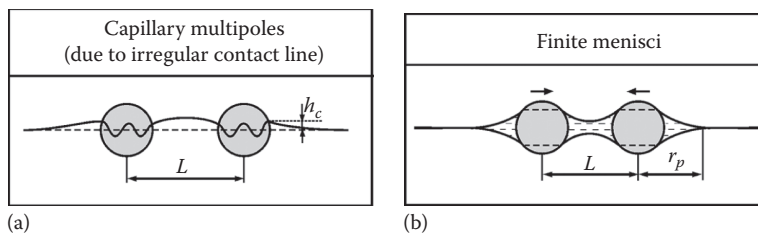


FIGURE 4.24 Special types of immersion capillary forces: (a) the contact line attachment to an irregular edge on the particle surface produces undulations in the surrounding fluid interface, which give rise to lateral capillary force between the particles. (b) When the size of particles, entrapped in a liquid film, is much greater than the nonperturbed film thickness, the meniscus surfaces meet at a finite distance, r_p ; in this case, the capillary interaction begins at $L \leq 2r_p$.

[204,313–316]. The lateral capillary forces have also been calculated for the case of particles captured in a *spherical* (rather than planar) thin liquid film or vesicle [316].

Lateral capillary forces between vertical cylinders or between spherical particles have been measured by means of sensitive electromechanical balance [317], piezo-transducer balance [318], and torsion microbalance [319]. Good agreement between theory and experiment has been established [318,319].

As already mentioned, the weight of micrometer-sized and sub micrometer-sized floating particles is not sufficient to deform the fluid interface and to bring about capillary force between the particles (Figure 4.21e). However, the situation changes if the contact line at the particle surface has *undulated* or *irregular* shape (Figure 4.24a). This may happen when the particle surface is rough, angular, or heterogeneous. In such cases, the contact line sticks to an edge or to the boundary between two domains of the heterogeneous surface. The undulated contact line induces undulations in the surrounding fluid interface [312,320–324]. Let $z = \zeta(x, y)$ be the equation describing the interfacial shape around such isolated particle. Using polar coordinates (r, φ) in the xy -plane, we can express the interfacial shape as a Fourier expansion:

$$\zeta(r, \varphi) = \sum_{m=1}^{\infty} r^{-m} [A_m \cos(m\varphi) + B_m \sin(m\varphi)] \quad (4.167)$$

where

r is the distance from the particle centre

A_m and B_m are coefficients

In analogy with electrical theory, Equation 4.167 can be interpreted as a multipole expansion: the terms with $m = 1, 2, 3, \dots$, play the role of capillary “dipoles,” “quadrupoles,” “hexapoles,” and *multipoles* [312,320–324]. The term with $m = 0$ (capillary “charge”) is missing because there is no axisymmetric contribution to the deformation (negligible particle weight). Moreover, the dipolar term with $m = 2$ is also absent because it is annihilated by a spontaneous rotation of the floating particle around a horizontal axis [321]. Therefore, the leading term becomes the quadrupolar one, with $m = 2$. The interaction between capillary quadrupoles has been investigated theoretically [321–324]. This interaction is nonmonotonic: attractive at long distances, but repulsive at short distances. Expressions for the rheological properties (surface dilatational and shear elasticity and yield stress) of Langmuir monolayers from angular particles have been derived [37,322,323].

Note that Equation 4.167 is approximate and holds for interparticle distances, which are much smaller than the characteristic capillary length, that is, $qr \ll 1$. The general form of the multipolar expansion, Equation 4.167, for arbitrary interparticle distances reads [321–324]:

$$\zeta(r, \varphi) = A_0 K_0(qr) + \sum_{m=1}^{\infty} A_m K_m(qr) \cos[m(\varphi - \varphi_{0,m})] \quad (4.167a)$$

where

A_m and $\varphi_{0,m}$ are constants of integration

K_m is the modified Bessel function of the second kind and m th order

The first term with $m = 0$ in the right-hand side of Equation 4.167a accounts for the contribution of the “capillary charges” (or “capillary monopoles”). Analytical expressions for the force and energy of interaction between two capillary multipoles of arbitrary order have been derived [324].

“Mesoscale” capillary multipoles have been experimentally realized by Bowden et al. [325,326], by appropriate hydrophobization or hydrophilization of the sides of floating plates. Interactions between capillary quadrupoles have been observed between floating particles, which have the shape of curved disks [327]. Loudet et al. [328–330] investigated experimentally and theoretically the capillary forces between adsorbed ellipsoidal particles and found that they behave as capillary quadrupoles. These authors noted that from a purely geometrical viewpoint, the condition of a constant contact angle cannot be met for anisotropic particles if the interface remains flat, which explains the reason for the quadrupolar interfacial deformation. Lateral capillary forces between ellipsoidal, cylindrical (rodlike), and other anisotropic particles have also been investigated by van Nierop et al. [331], Lehle et al. [332], Stebe et al. [333–337], and Yunker et al. [338] Gravitation-like instabilities due to the long-range attractive capillary forces between floating particles have also been studied [339].

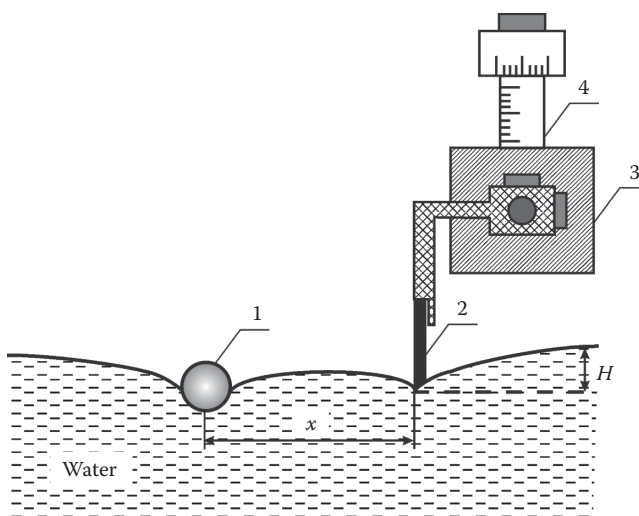


FIGURE 4.25 Experimental setup for studying the capillary interaction between a floating particle (1) and a vertical hydrophobic plate (2) separated at a distance, x . The edge of the plate is at a distance, H , lower than the level of the horizontal liquid surface far from the plate; (3) and (4) are micrometric table and screw; see Refs. [345,346].

At last, let us consider another type of capillary interactions—between particles surrounded by *finite* menisci. Such interactions appear when micrometer-sized or submicrometer-sized particles are captured in a liquid film of much smaller thickness (Figure 4.24b) [340–343]. If such particles are approaching each other, the interaction begins when the menisci around the two particles overlap, $L < 2r_p$ in Figure 4.24b. The capillary force in this case is nonmonotonic: initially the attractive force increases with the increase of interparticle distance, then it reaches a maximum and further decays [343]. In addition, there are hysteresis effects: the force is different on approach and separation at distances around $L = 2r_p$ [343].

4.3.3.2 Particle–Wall Interactions

The overlap of the meniscus around a floating particle with the meniscus on a vertical wall gives rise to a particle–wall interaction, which can be both repulsive and attractive. An example for a controlled meniscus on the wall is shown in Figure 4.25, where the “wall” is a hydrophobic teflon barrier whose position along the vertical wall can be precisely varied and adjusted.

Two types of boundary conditions at the wall are analyzed theoretically [37,344]: fixed contact line (Figure 4.25) or, alternatively, fixed contact angle. In particular, the lateral capillary force exerted on the particle depicted in Figure 4.25 is given by the following asymptotic expression [37,344]:

$$F = -\pi\sigma q \left[2Q_2 H e^{-qx} + r_2 H e^{-qx} - 2Q_2^2 K_1(qx) \right] \quad (4.168)$$

Here

Q_2 and r_2 are the particle capillary charge and contact line radius, respectively

H characterizes the position of the contact line on the wall with respect to the nondisturbed horizontal liquid surface (Figure 4.21)

x is the particle–wall distance

q is defined by Equation 4.164 (thick films)

The first term in the right-hand side of Equation 4.168 expresses the gravity force pushing the particle to slide down over the inclined meniscus on the wall; the second term originates from the pressure difference across the meniscus on the wall; the third term expresses the so-called capillary image force, that is, the particle is repelled by its mirror image with respect to the wall surface [37,344].

Static [345] and dynamic [346] measurements with particles near walls have been carried out. In the static measurements the equilibrium distance of the particle from the wall (the distance at which $F = 0$) has been measured and a good agreement with the theory has been established [345].

In the dynamic experiments [346] knowing the capillary force F (from Equation 4.168) and measuring the particle velocity, \dot{x} , we can determine the drag force, F_d :

$$F_d = m\ddot{x} - F, \quad F_d \equiv 6\pi\eta R_2 f_d \dot{x} \quad (4.169)$$

where

R_2 , m , and \ddot{x} are the particle radius, mass, and acceleration, respectively

η is the viscosity of the liquid

f_d is the drag coefficient

If the particle were in the bulk liquid, f_d would be equal to 1 and F_d would be given by the Stokes formula. In general, f_d differs from unity because the particle is attached to the interface. The experiment [346] results in f_d varying between 0.68 and 0.54 for particle contact angle varying from 49°

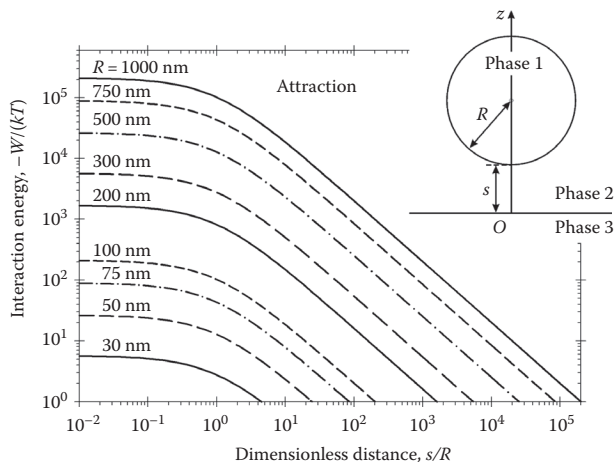


FIGURE 4.26 Plot of the interaction energy W (scaled with kT) vs. the dimensionless distance, s/R , between a charged glass particle (phase 1) and a planar interface; phase 2 is tetradecane; phase 3 is water. The curves correspond to different particle radii, R , denoted in the figure.

to 82° ; the data are in good quantitative agreement with the hydrodynamic theory of the drag coefficient [347]. In other words, the less the depth of particle immersion, the less the drag coefficient, as could be expected. However, if the floating particle is heavy enough, it deforms the surrounding liquid surface; the deformation travels together with the particle, thus increasing f_d several times [346]. The addition of surfactant strongly increases f_d . The latter effect can be used to measure the surface viscosity of adsorption monolayers from low molecular weight surfactants [348], which is not accessible to the standard methods for measurement of surface viscosity.

In the case of *protein* adsorption layers, the surface elasticity is so strong that the particle (Figure 4.25) is arrested in the adsorption film. Nevertheless, with heavier particles and at larger meniscus slopes, it is possible to break the protein adsorption layer. Based on such experiments, a method for determining surface elasticity and yield stress has been developed [349].

4.3.3.3 Electrically Charged Particles at Liquid Interfaces

4.3.3.3.1 Particle–Interface Interaction

Let us consider a spherical dielectric particle (phase 1), which is immersed in a nonpolar medium (phase 2), near its boundary with a third dielectric medium (phase 3); see the inset in Figure 4.26. The interaction is due to electric charges at the particle surface. The theoretical problem has been solved exactly, in terms of Legendre polynomials, for arbitrary values of the dielectric constants of

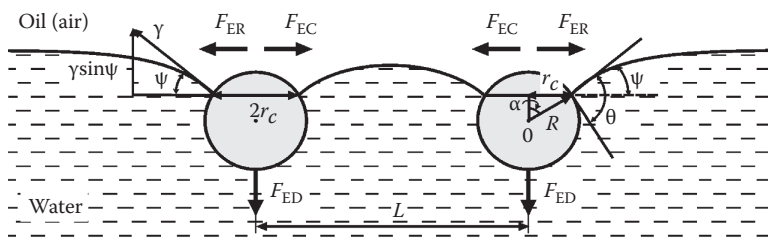


FIGURE 4.27 Sketch of two electrically charged particles attached to an oil–water interface. F_{ED} is the electro-dipping force, due to the image-charge effect, that pushes the particles into water and deforms the fluid interface around the particles. F_{ER} is the direct electric repulsion between the two like-charged particles. F_{EC} is the electrocapillary attraction, related to deformations in the fluid interface created by the electric field.

the three phases, and expressions for calculating the interaction force, F_z , and energy, W , have been derived [350]:

$$F_z = \frac{\beta_{23}Q^2}{4\epsilon_2(R+s)^2} f_z, \quad W = \int_s^\infty F_z ds = \frac{\beta_{23}Q^2}{4\epsilon_2(R+s)} w \quad (4.170)$$

Here

R is the particle radius

s is the distance between the particle surface and the fluid interface (inset in Figure 4.26)

$Q = 4\pi R^2 \sigma_{pn}$ is the total charge at the boundary particle–nonpolar fluid

f_z and w are dimensionless force and energy coefficients, respectively, which, in general, depend on the parameters s/R , β_{12} , and β_{23} , where $\beta_{ij} = (\epsilon_i - \epsilon_j)/(\epsilon_i + \epsilon_j)$; $i, j = 1, 2, 3$; ϵ_1 , ϵ_2 , and ϵ_3 are the dielectric constants of the respective phases

At long distances, $s/R > 1$, we have $f_z \approx w \approx 1$, and then Equation 4.170 reduces to the expressions for the force and energy of interaction between a point charge Q with the interface between phases 2 and 3. This is the known image charge effect. Expressions that allow us to calculate f_z and w for shorter distances ($s/R < 1$) are derived in Ref. [350].

In Figure 4.26, numerical results for the particle–interface interaction energy, W , scaled by the thermal energy kT , are plotted versus the relative distance, s/R , for various values of the particle radius, R . The other parameter values correspond to the following choice of the phases: phase 1 (the particle) is glass, phase 2 is tetradecane, and phase 3 is water. The curves in Figure 4.26 describe a strong and long-range attraction between the particle and the interface. The interaction energy, W , becomes comparable, or smaller than the thermal energy kT for particle radius $R < 30$ nm. On the other hand, for $R > 30$ nm W strongly increases with the particle size (in Equation 4.170 $Q^2 \sim R^4$ at fixed surface charge density, σ_{pn}) and reaches $W \approx 10^5 kT$ for $R = 1 \mu\text{m}$ at close contact. In addition, the range of interaction also increases, reaching $s/R \approx 10^5$ for $R = 1 \mu\text{m}$. In general, this is a strong and long-range interaction [350]. For example, water drops could attract charged hydrophobic particles dispersed in the oily phase, which would favor the formation of reverse particle-stabilized emulsions.

4.3.3.3.2 Forces of Electric Origin between Particles at a Liquid Interface

Figure 4.27 shows two particles attached to the interface between water and a nonpolar fluid (oil, air). In general, the particles experience three forces of electric origin: F_{ED} —electrodipping force [351]; F_{ER} —direct electric repulsion between the two particles across the oil [352], and F_{EC} —electric

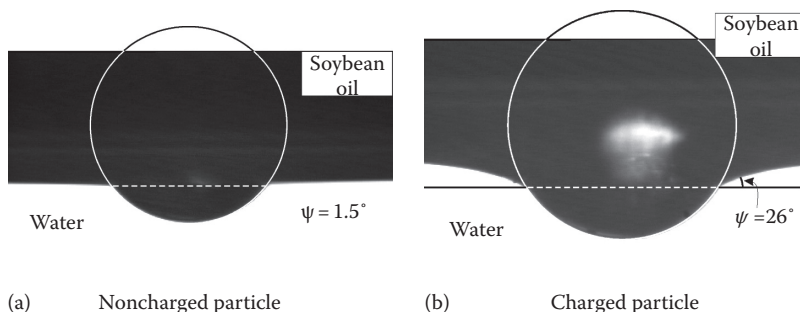


FIGURE 4.28 Side-view photographs of hydrophobized spherical glass particles at the boundary water–soybean oil (no added surfactants). (a) Noncharged particle of radius $R = 235 \mu\text{m}$: the meniscus slope angle due to gravity is relatively small, $\psi = 1.5^\circ$. (b) Charged particle of radius $R = 274 \mu\text{m}$: the experimental meniscus slope angle is $\psi = 26^\circ$ owing to the electro-dipping force; if this electric force were missing, the gravitational slope angle would be only $\psi = 1.9^\circ$.

field-induced capillary attraction [353], which is termed “electrocapillary force” for brevity. F_{ED} is normal to the oil–water interface and is directed toward the water phase. Physically, F_{ED} is a result of the electrostatic image-charge effect; see the previous section. F_{ED} is acting on each individual particle, while F_{ER} and F_{EC} are interaction forces between two (or more) particles. The presence of electric field leads to deformations in the fluid interface around the particles, which lead to the appearance of F_{EC} . The three forces, F_{ED} , F_{ER} , and F_{EC} , are separately considered in the following section.

4.3.3.3.3 Electrodipping Force, F_{ED}

At equilibrium, the electro-dipping force is counterbalanced by the interfacial tension force: $F_{ED} = 2\pi r_c \gamma \sin \psi$, where γ is the interfacial tension; r_c is the radius of the contact line on the particle surface; and ψ is the meniscus slope angle at the contact line (Figure 4.27) [351,353]. Consequently, F_{ED} can be determined from the experimental values of r_c , γ , and ψ . This approach was used to obtain the values of F_{ED} for silanized glass particles of radii 200–300 μm from photographs of these particles at an oil–water or air–water interface [351]. F_{ED} was found to be much greater than the vertical gravitational force acting on these particles.

As an illustration, Figure 4.28 compares the profiles of the liquid menisci around a noncharged particle and a charged particle. The particles represent hydrophobized glass spheres of density $\rho_p = 2.5 \text{ g/cm}^3$. The oil phase is purified soybean oil of density $\rho_{oil} = 0.92 \text{ g/cm}^3$. The oil–water interfacial tension is $\gamma = 30.5 \text{ mN/m}$. Under these conditions, the calculated surface tension force, $2\pi r_c \gamma \sin \psi$, which counterbalances the gravitational force (particle weight minus the Archimedes force), corresponds to meniscus slope angle $\psi = 1.5^\circ$, and the deformation of the liquid interface caused by the particle is hardly visible (Figure 4.28a). In contrast, for the charged particle (Figure 4.28b), the meniscus slope angle is much greater, $\psi = 26^\circ$. This is due to the fact that the interfacial tension force, $2\pi r_c \gamma \sin \psi$, has to counterbalance the electro-dipping force, which pushes the particle toward the water phase. Experimentally, it has been found that the angle ψ is insensitive to the concentration of NaCl in the aqueous phase, which means that (in the investigated case) the electro-dipping force is due to charges situated at the particle–oil interface [351,354]. With similar particles, the magnitude of F_{ED} at the air–water interface was found to be about six times smaller than at the oil–water interface [351]. Theoretically, the electro-dipping force, F_{ED} , can be calculated from the expression [354,355]:

$$F_{ED} = \left(\frac{4\pi}{\epsilon_n} \right) (\sigma_{pn} R)^2 (1 - \cos \alpha) f(\theta, \epsilon_{pn}) \quad (4.171)$$

Here

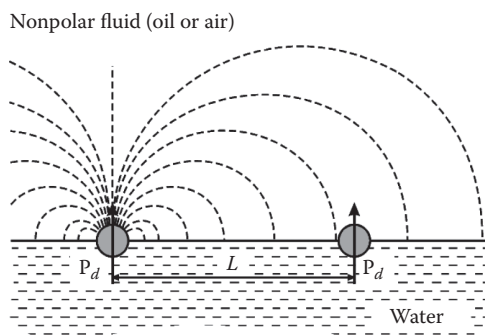


FIGURE 4.29 Two particles attached to the boundary water–nonpolar fluid and separated at a center-to-center distance L . In the nonpolar fluid (oil, air), the electric field of each particle in isolation is asymptotically identical to the field of a dipole of moment p_d . This field is created by charges at the particle–nonpolar fluid interface.

- ϵ_n is the dielectric constant of the nonpolar fluid (oil, air)
- σ_{pn} is the surface charge density at the boundary particle–nonpolar fluid
- $\epsilon_{pn} = \epsilon_p/\epsilon_n$ is the ratio of the respective two dielectric constants
- α is a central angle, while $\theta = \alpha + \psi$ is the contact angle (see Figure 4.27)

We could accurately calculate the dimensionless function $f(\theta, \epsilon_{pn})$ by means of the relation $f(\theta, \epsilon_{pn}) = f_R(\theta, \epsilon_{pn})/(1 - \cos \theta)$, where the function $f_R(\theta, \epsilon_{pn})$ is tabulated in Table 4.3 of Ref. [355] on the basis of the solution of the electrostatic boundary problem. The tabulated values can be used for a convenient computer calculation of $f_R(\theta, \epsilon_{pn})$ with the help of a four-point interpolation formula, Equation D.1 in Ref. [355]. From the experimental F_{ED} and Equation 4.171, we could determine the surface charge density, σ_{pn} , at the particle–oil and particle–air interface. Values of σ_{pn} in the range from 20 to 70 $\mu\text{C}/\text{m}^2$ have been obtained [351,354].

4.3.3.3.4 Direct Electric Repulsion, F_{ER}

Interactions of electrostatic origin were found to essentially influence the type of particle structures at oil–water [352,353,356–358] and air–water [359,360] interfaces. Two-dimensional hexagonal arrays of particles were observed in which the distance between the closest neighbors was markedly greater than the particle diameter [352,353,356–363]. The existence of such structures was explained by the action of direct electrostatic repulsion between like-charged particles. In many cases, the particle arrays are insensitive to the concentration of electrolyte in the aqueous phase [352,356,357]. This fact, and the direct interparticle force measurements by laser tweezers [356], leads to the conclusion that the electrostatic repulsion is due to charges at the particle–oil (or particle–air) interface, which give rise to electric repulsion across the nonpolar phase [352,356–359]. This repulsion is relatively long ranged because of the absence of a strong Debye screening of the electrostatic forces that is typical for the aqueous phase [364]. Evidences about the presence of electric charges on the surface of solid particles dispersed in liquid hydrocarbons could also be found in earlier studies [365,366].

For a particle in isolation, the charges at the particle–nonpolar fluid interface create an electric field in the oil that asymptotically resembles the electric field of a dipole (Figure 4.29). This field practically does not penetrate into the water phase, because it is reflected by the oil–water boundary owing to the relatively large dielectric constant of water. For a single particle, the respective electrostatic problem is solved in Ref. [355]. The asymptotic behavior of the force of electrostatic repulsion between two such particles–dipoles (Figure 4.29) is [355]:

$$F_{ER} = \frac{3p_d^2}{2\epsilon_n L^4} \left(\frac{R}{L} \ll 1 \right) \quad (4.172)$$

L is the center-to-center distance between the two particles; $p_d = 4\pi\sigma_{pn}DR^3 \sin^3\alpha$ is the effective particle dipole moment; as before, R is the particle radius and σ_{pn} is the electric charge density at the particle–nonpolar fluid interface; $D = D(\alpha, \epsilon_{pn})$ is a known dimensionless function, which can be calculated by means of Table 4.1 and Equation D.1 in Ref. [355]; $\epsilon_{pn} \equiv \epsilon_p/\epsilon_n$ is the ratio of the dielectric constants of the two phases. Equation 4.172 shows that F_{ER} asymptotically decays as $1/L^4$ like the force between two point dipoles. However, at shorter distances, the finite size of the particle is expected to lead to a Coulombic repulsion, $F_{ER} \sim 1/L^2$; see Refs. [356–358].

Monolayers from electrically charged micron-sized silica particles, spread on the air–water interface, were investigated and *surface pressure versus area* isotherms were measured by Langmuir trough and the monolayers' morphology was monitored by microscope [363]. The experiments showed that $\Pi \sim L^{-3}$ at large L , where Π is the surface pressure and L is the mean interparticle distance. A theoretical cell model was developed, which predicts not only the aforementioned asymptotic law but also the whole $\Pi(L)$ dependence. The model presumes a periodic distribution of

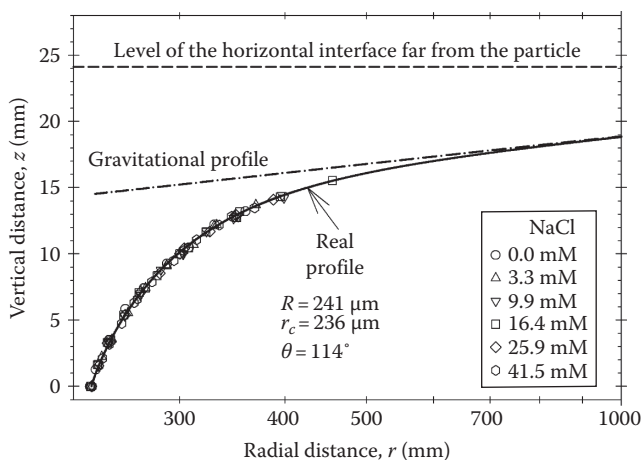


FIGURE 4.30 Profile of the oil (tetradecane)–water interface near the contact line of a charged glass particle, like that in Figure 4.28b: plot of experimental data from Ref. [354]; see Figure 4.27 for the notations. The dash-dot line shows the gravitational; profile calculated under the assumption that the particle is not charged. The difference between the real and the gravitational profiles represents the effect of electric field on the meniscus shape. The fact that the real (experimental) profile is insensitive to the concentration of NaCl in the water phase indicates that the electric charges are located at the particle–oil interface, so that the interfacial deformation is due to electric field in the oily phase.

the surface charge density, which induces a corresponding electric field in the air phase. Then, the Maxwell pressure tensor of the electric field in the air phase was calculated and integrated according to the Bakker’s formula [189] to determine the surface pressure. Thus, all *collective effects* from the electrostatic interparticle interactions were taken into account, as well as the effects from the particle finite size.

The effects of applied *vertical external electric field* on the electrostatic forces acting on a colloid particle at a horizontal liquid interface have also been investigated. By varying the strength of the electric field, it is possible to control the distances between the particles in nondensely packed 2D colloid crystals formed at liquid interfaces [367–370]. Theoretical expressions for the forces between floating uncharged [371] and charged [372] dielectric particles in the presence of external electric field were derived. The particles are located on the boundary water–nonpolar fluid (air, oil). The effects of the dielectric constants and contact angle (particle wettability) on the vertical electro-dipping force, F_{ED} , acting on each particle, and on the horizontal force between two particles, F_{ER} , were investigated. The external field polarizes the uncharged particles at the fluid interface. The vertical electric force on the particle can be directed upward or downward. The horizontal interparticle repulsion is dipolar and contact angle dependent. At given contact angle (for uncharged particles) and external electric field E_0 (for charged particles), the dipole moment is zero and the repulsion becomes short-range octupolar [371,372]. This minimal electrostatic repulsion could be weaker than the electrocapillary capillary attraction; see the next section.

4.3.3.3.5 Electrocapillary Force, F_{EC}

The electrocapillary forces between particles are due to the overlap of the deformations in the liquid interface created by the particles [353]. The deformations are due not only to the electro-dipping force that pushes the particle toward the water (and that determines the value of the angle ψ in Figure 4.28b), but also to the additional electric pressure (Maxwell stress) that is acting per unit area

of the oil–water (or air–water) interface owing to the presence of electric field in the nonpolar fluid (see Figure 4.29) [351,353,354,373–375]. The direction of this electric pressure is from the water toward the nonpolar fluid.

The electric field–induced deformation of a liquid interface around charged particles at the interface tetradecane–water has been quantitatively examined in Ref. [354]. An example is given in Figure 4.30. Far from the particle, the interface is flat and horizontal. For particles of radii $R = 200\text{--}300\ \mu\text{m}$, both gravitational and electric field induced deformations are present. The gravitational deformation is predominant at longer distances, whereas the electric field deformation is significant near the particle. The latter deformation is insensitive to the variation of the concentration of NaCl in the aqueous phase (Figure 4.30), which indicates that this deformation is due to electric charges at the particle–oil interface. Good agreement between experiment (the symbols) and theory (the solid line) has been obtained.

In Ref. [376], the two-particle electrocapillary problem was solved in bipolar coordinates without using any superposition approximations. The following expression (power expansion) was obtained for two identical floating particles with contact radius r_c , which are separated at a center-to-center distance L (see Figure 4.27):

$$F_x = \frac{3p_d^2}{2\epsilon_n L^4} \left[1 - \frac{2\delta}{5} + \frac{5\delta}{2} \left(\frac{r_c}{L} \right)^2 - \frac{15\delta}{2} \left(\frac{r_c}{L} \right)^3 + \frac{175\delta}{32} \left(\frac{r_c}{L} \right)^4 + \dots \right] \quad (4.172a)$$

$\delta = \tan \psi$, where ψ is the meniscus slope angle for each particle in isolation (Figure 4.27). In Equation 4.172a, the first term in the brackets is F_{ER} in Equation 4.172, whereas the next terms, which are proportional to the meniscus deformation angle δ , give F_{EC} . Because for micrometer and submicrometer particles δ is a small quantity, it turns out that for uniform distribution of the surface charges, the electrocapillary attraction is weaker than the electrostatic repulsion at interparticle distances, at which the dipolar approximation is applicable, so that the net force, F_x , is repulsive [376]. The final conclusion from the theoretical analysis is that the direct electrostatic repulsion dominates over the capillary attraction when the surface charge is *uniformly* distributed; no matter whether the surface charge is on the polar–liquid or nonpolar–fluid side of the particle.

Electric field–induced attraction that *prevails* over the electrostatic repulsion was established (both experimentally and theoretically) in the case of not-too-small floating particles, for which the interfacial deformation due to gravity is not negligible [377,378]. If the surface charge is *anisotropically* distributed (this may happen at low surface charge density), the electric field

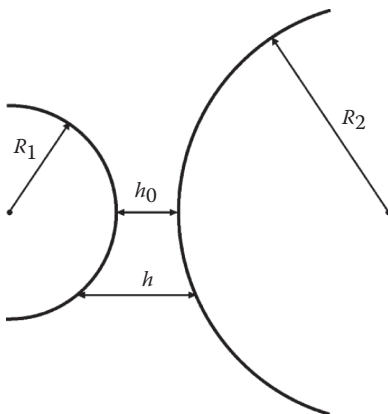


FIGURE 4.31 Two spherical particles of radii R_1 and R_2 ; the shortest and the running surface-to-surface distances are denoted by h_0 and h , respectively.

produces a saddle-shaped deformation in the liquid interface near the particle, which is equivalent to a “capillary quadrupole.” The interaction of the latter with the axisymmetric gravitational deformation around the other particle (which is equivalent to a “capillary charge”) gives rise to a capillary force that decays $\propto 1/L^3$, that is, slower than $F_{ER} \propto 1/L^4$. In such a case, we are dealing with a *hybrid attraction* between a gravity-induced “capillary charge” and an electric field–induced “capillary quadrupole” [378,379].

4.4 SURFACE FORCES

4.4.1 DERJAGUIN APPROXIMATION

The excess surface free energy per unit area of a plane-parallel film of thickness h is [14,380]

$$f(h) = \int_h^\infty \Pi(h) dh \quad (4.173)$$

where, as before, Π denotes disjoining pressure. Derjaguin [381] derived an approximate formula, which expresses the energy of interaction between two spherical particles of radii R_1 and R_2 through integral of $f(h)$:

$$U(h_0) = \frac{2\pi R_1 R_2}{R_1 + R_2} \int_{h_0}^\infty f(h) dh \quad (4.174)$$

Here, h_0 is the shortest distance between the surfaces of the two particles (see [Figure 4.31](#)). In the derivation of Equation 4.174 it is assumed that the interaction between two parcels from the particle surfaces, separated at the distance h , is approximately the same as that between two similar parcels in a plane-parallel film. This assumption is correct when the range of action of the surface forces and the distance h_0 are small compared to the curvature radii R_1 and R_2 . It has been established, both experimentally [36] and theoretically [382], that Equation 4.174 provides a good approximation in the range of its validity.

Equation 4.174 can be generalized for smooth surfaces of arbitrary shape (not necessarily spheres). For that purpose, the surfaces of the two particles are approximated with paraboloids in the vicinity of the point of closest approach ($h = h_0$). Let the principle curvatures at this point be c_1 and c_1' for the first particle, and c_2 and c_2' for the second particle. Then the generalization of Equation 4.174 reads [380]:

$$U(h_0) = \frac{2\pi}{\sqrt{C}} \int_{h_0}^\infty f(h) dh \quad (4.175)$$

$$C \equiv c_1 c_1' + c_2 c_2' + (c_1 c_2 + c_1' c_2') \sin^2 \omega + (c_1 c_2' + c_1' c_2) \cos^2 \omega$$

where ω is the angle subtended between the directions of the principle curvatures of the two approaching surfaces. For two spheres, we have $c_1 = c_1' = 1/R_1, c_2 = c_2' = 1/R_2$, and Equation 4.175 reduces to Equation 4.174.

For two cylinders of radii r_1 and r_2 crossed at angle ω we have $c_1 = c_2 = 0; c_1' = 1/r_1, c_2' = 1/r_2$ and Equation 4.175 yields

$$U(h_0) = \frac{2\pi\sqrt{r_1 r_2}}{\sin \omega} \int_{h_0}^{\infty} f(h) dh \quad (4.176)$$

Equation 4.176 is often used in connection to the experiments with the surface force apparatus (SFA) [36,383], in which the interacting surfaces are two crossed cylindrical mica sheets. The divergence in Equation 4.176 for $\omega = 0$ reflects the fact that the axes of the two infinitely long cylinders are parallel for $\omega = 0$ and thus the area of the interaction zone becomes infinite.

The Derjaguin's formula is applicable to any type of force law (attractive, repulsive, oscillatory) if only (1) the range of the forces, and (2) the surface-to-surface distance are much smaller than the surface curvature radii. This formula is applicable to any kind of surface force, irrespective of its physical origin: van der Waals, electrostatic, steric, oscillatory-structural, depletion, etc. It reduces the two-particle interaction problem to the simpler problem for interactions in plane-parallel films.

4.4.2 VAN DER WAALS SURFACE FORCES

The van der Waals interaction between molecules i and j obeys the law:

$$u_{ij}(r) = -\frac{\alpha_{ij}}{r^6} \quad (4.177)$$

where

- u_{ij} is the potential energy of interaction
- r is the distance between the two molecules
- α_{ij} is a constant characterizing the interaction

In fact, the van der Waals forces represent an averaged dipole–dipole interaction, which is a superposition of three main terms: (1) orientation interaction: interaction between two permanent dipoles [384]; (2) induction interaction: interaction between one permanent dipole and one induced dipole [385]; (3) dispersion interaction: interaction between two induced dipoles [386]. The theory yields [36]:

$$\alpha_{ij} = \frac{1}{(4\pi\epsilon_0)^2} \left[\frac{p_i^2 p_j^2}{3kT} + (p_i^2 \alpha_{0j} + p_j^2 \alpha_{0i}) + \frac{3\alpha_{0i} \alpha_{0j} h_p \nu_i \nu_j}{2(\nu_i + \nu_j)} \right] \quad (4.178)$$

where

- p_i and α_{0i} are molecular dipole moment and electronic polarizability, respectively;
- h_p is the Planck constant
- ν_i is the orbiting frequency of the electron in the Bohr atom

For van der Waals interactions between molecules in a gas phase, the orientation interaction can yield from 0% (nonpolar molecules) up to 70% (molecules of large permanent dipole moment, like H₂O) of the value of α_{ij} ; the contribution of the induction interaction in α_{ij} is usually low, about 5%–10%; the contribution of the dispersion interaction might be between 24% (water) and 100% (nonpolar hydrocarbons); for numerical data, see Ref. [36].

According to the *microscopic* theory by Hamaker [387], the van der Waals interaction between two macroscopic bodies can be found by integration of Equation 4.177 over all couples of molecules, followed by subtraction of the interaction energy at infinite separation between the bodies. The result depends on the geometry of the system. For a plane-parallel film from component 3 located between two semi-infinite phases composed from components 1 and 2, the van der Waals interaction energy per unit area and the respective disjoining pressure, stemming from Equation 4.166, are [387]

$$f_{\text{vw}} = -\frac{A_H}{12\pi h^2}, \quad \Pi_{\text{vw}} = -\frac{\partial f_{\text{vw}}}{\partial h} = -\frac{A_H}{6\pi h^3} \quad (4.179)$$

where

h is the thickness of the film

A_H is the compound Hamaker constant [14]

$$A_H = A_{33} + A_{12} - A_{13} - A_{23} \quad (A_{ij} = \pi^2 \rho_i \rho_j \alpha_{ij}, i, j = 1, 2, 3) \quad (4.180)$$

A_{ij} is the Hamaker constant of components i and j

ρ_i and ρ_j are the molecular number densities of phases i and j built up from components i and j , respectively

If A_{ii} and A_{jj} are known, we can calculate A_{ij} by using the Hamaker approximation

$$A_{ij} = (A_{ii}A_{jj})^{1/2} \quad (4.181)$$

In fact, Equation 4.181 is applicable to the dispersion contribution in the van der Waals interaction [36].

When components 1 and 2 are identical, A_H is positive (see Equation 4.180); therefore, the van der Waals interaction between identical bodies, in any medium, is always attractive. Besides, two dense bodies (even if nonidentical) will attract each other when placed in medium 3 of low density (gas, vacuum). When the phase in the middle (component 3) has intermediate Hamaker constant between those of bodies 1 and 2, A_H can be negative and the van der Waals disjoining pressure can be repulsive (positive). Such is the case of an aqueous film between mercury and gas [388].

Lifshitz et al. [389,390] developed an alternative approach to the calculation of the Hamaker constant A_H in condensed phases, called the *macroscopic* theory. The latter is not limited by the assumption for pair-wise additivity of the van der Waals interaction (see also Refs. [36,380,391]). The Lifshitz theory treats each phase as a continuous medium characterized by a given uniform dielectric permittivity, which is dependent on the frequency, ν , of the propagating electromagnetic waves. For the symmetric configuration of two identical phases “ i ” interacting across a medium “ j ,” the macroscopic theory provides the expression [36]

$$A_H \equiv A_{iji} = A_{iji}^{(\nu=0)} + A_{iji}^{(\nu>0)} = \frac{3}{4} kT \left(\frac{\varepsilon_i - \varepsilon_j}{\varepsilon_i + \varepsilon_j} \right)^2 + \frac{3h_p \nu_e (n_i^2 - n_j^2)^2}{16\sqrt{2} (n_i^2 + n_j^2)^{3/2}} \quad (4.182)$$

where

ε_i and ε_j are the dielectric constants of phases i and j , respectively;

n_i and n_j are the respective refractive indices for visible light

h_p is the Planck constant

ν_e is the main electronic absorption frequency which is $\approx 3.0 \times 10^{15}$ Hz for water and the most organic liquids [36]

The first term in the right-hand side of Equation 4.182, $A_{iji}^{(\nu=0)}$, is the so-called zero-frequency term, expressing the contribution of the orientation and induction interactions. Indeed, these two contributions to the van der Waals force represent electrostatic effects. Equation 4.182 shows that the zero-frequency term can never exceed $(3/4)kT \approx 3 \times 10^{-21}$ J. The last term in Equation 4.182, $A_{iji}^{(\nu>0)}$,

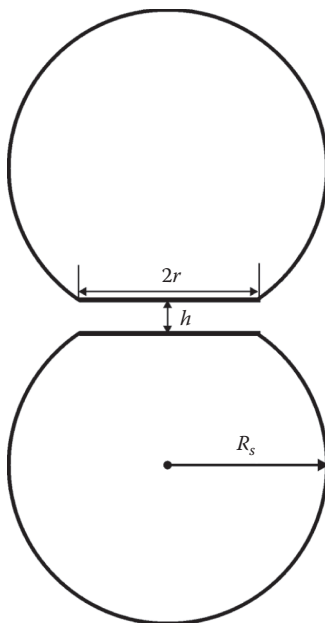


FIGURE 4.32 Thin film of radius r and thickness h formed between two attached fluid particles; the spherical part of the particle surface has radius R_s .

accounts for the dispersion interaction. If the two phases, i and j , have comparable densities (as for emulsion systems, say oil–water–oil), then $A_{ji}^{(v>0)}$ and $A_{ji}^{(v=0)}$ are comparable by magnitude. If one of the phases, i or j , has a low density (gas, vacuum), we obtain $A_{ji}^{(v>0)} \gg A_{ji}^{(v=0)}$. In the latter case, the Hamaker microscopic approach may give comparable $A_{ji}^{(v>0)}$ and $A_{ji}^{(v=0)}$ in contradiction to the Lifshitz macroscopic theory, which is more accurate for condensed phases.

A geometrical configuration, which is important for disperse systems, is the case of two spheres of radii R_1 and R_2 interacting across a medium (component 3). Hamaker [387] has derived the following expression for the van der Waals interaction energy between two spheres:

$$U(h_0) = -\frac{A_H}{12} \left(\frac{y}{x^2 + xy + x} + \frac{y}{x^2 + xy + x + y} + 2 \ln \frac{x^2 + xy + x}{x^2 + xy + x + y} \right) \quad (4.183)$$

where

$$\begin{aligned} x &= \frac{h_0}{2R_1} \\ y &= \frac{R_2}{R_1} \leq 1 \end{aligned} \quad (4.184)$$

h_0 is the same as in [Figure 4.31](#).

For $x \ll 1$ Equation 4.183 reduces to

$$U(h_0) \approx -\frac{A_H}{12} \frac{y}{(1+y)x} = -\frac{2\pi R_1 R_2}{R_1 + R_2} \frac{A_H}{12\pi h_0} \quad (4.185)$$

Equation 4.185 can be also derived by combining Equation 4.179 with the Derjaguin approximation (Equation 4.174). It is worthwhile noting that the logarithmic term in Equation 4.183 can be neglected only if $x \ll 1$. For example, even when $x = 5 \times 10^{-3}$, the contribution of the logarithmic term amounts to about 10% of the result (for $y = 1$); consequently, for larger values of x this term must be retained.

Another geometrical configuration, which corresponds to two colliding deformable emulsion droplets, is sketched in [Figure 4.32](#). In this case the interaction energy is given by the expression [392]

$$U(h,r) = -\frac{A_H}{12} \left[\frac{3}{4} + \frac{R_s}{h} + 2 \ln \left(\frac{h}{R_s} \right) + \frac{r^2}{h^2} - \frac{2r^2}{R_s h} \right] \quad (h, r \ll R_s) \quad (4.186)$$

where

h and r are the thickness and the radius of the flat film formed between the two deformed drops, respectively,

R_s is the radius of the spherical part of the drop surface (see [Figure 4.32](#)).

Equation 4.186 is a truncated series expansion; the exact formula, which is more voluminous, can be found in Ref. [392]. Expressions for U for other geometrical configurations are also available [37,391].

The asymptotic behavior of the dispersion interaction at large intermolecular separations does not obey Equation 4.177; instead $u_{ij} \propto 1/r^7$ due to the electromagnetic retardation effect established by Casimir and Polder [393]. Several different expressions have been proposed to account for this effect in the Hamaker constant [391].

The orientation and induction interactions are electrostatic effects, so they are not subjected to electromagnetic retardation. Instead, they are subject to Debye screening due to the presence of electrolyte ions in the liquid phases. Thus for the interaction across an electrolyte solution, the screened Hamaker constant is given by the expression [36,394]

$$A_H = 2\kappa h A_0 e^{-2\kappa h} + A_d \quad (4.187)$$

where

A_0 denotes the contribution of the (non-screened) orientation and induction interactions to the Hamaker constant

A_d is the contribution of the dispersion interaction

κ is the Debye screening parameter: $\kappa = \kappa_c I^{1/2}$ (see Equation 4.34)

Equation 4.187 is accurate to within 15% for $\kappa h > 2$; see Ref. [36].

4.4.3 ELECTROSTATIC SURFACE FORCES

4.4.3.1 Two Identically Charged Planes

First, we consider the electrostatic (double layer) interaction between two identical charged plane parallel surfaces across solution of symmetrical $Z:Z$ electrolyte. The charge of a counterion (i.e., ion with charge opposite to that of the surface) is $-Ze$, whereas the charge of a coion is $+Ze$ ($Z = \pm 1, \pm 2, \dots$) with e being the elementary charge. If the separation between the two planes is very large, the number concentration of both counterions and coions would be equal to its bulk value, n_0 , in the middle of the film. However, at finite separation, h , between the surfaces the two EDLs overlap and the counterion and coion concentrations in the middle of the film, n_{10}

and n_{20} , are no longer equal. Because the solution inside the film is supposed to be in electrochemical (Donnan) equilibrium with the bulk electrolyte solution of concentration n_0 , we can write [395] $n_{10}n_{20} = n_0^2$, or alternatively

$$n_{10} = \frac{n_0}{\sqrt{m}}, \quad n_{20} = n_0\sqrt{m}, \quad m \equiv \frac{n_{20}}{n_{10}} \quad (4.188)$$

As pointed out by Langmuir [396], the electrostatic disjoining pressure, Π_{el} , can be identified with the excess osmotic pressure in the middle of the film:

$$\Pi_{el} = kT(n_{10} + n_{20} - 2n_0) = n_0kT(m^{1/4} - m^{-1/4})^2 \quad (4.189)$$

Equation 4.189 demonstrates that for two identically charged surfaces, Π_{el} is always positive, that is, corresponds to repulsion between the surfaces. In general, we have $0 < m \leq 1$ because the coions are repelled from the film due to the interaction with the film surfaces. To find the exact dependence of Π_{el} on the film thickness, h , we have to solve the Poisson–Boltzmann equation for the distribution of the electrostatic potential inside the film. The solution provides the following connection between Π_{el} and h for symmetric electrolytes [380,397]:

$$\Pi_{el} = 4n_0kT \cot^2 \theta, \quad \kappa h = 2F(\varphi, \theta) \sin \theta \quad (4.190)$$

where

$F(\varphi, \theta)$ is the elliptic integral of the first kind
 φ is related with θ as follows

$$\cos \varphi = \frac{\cot \theta}{\sinh(Z\Phi_s/2)} \quad (\text{fixed surface potential } \Phi_s) \quad (4.191)$$

$$\tan \varphi = (\tan \theta) \sinh\left(\frac{Z\Phi_\infty}{2}\right) \quad (\text{fixed surface charge } \sigma_s) \quad (4.192)$$

$$\cosh(Z\Phi_\infty) = 1 + \frac{1}{2} \left(\frac{Ze\sigma_s}{\epsilon\epsilon_0kT\kappa} \right)^2, \quad \Phi_s \equiv \frac{e\psi_s}{kT} \quad (4.193)$$

Here

Φ_s is the dimensionless surface potential
 Φ_∞ is the value of Φ_s for $h \rightarrow \infty$

Equation 4.190 expresses the dependence $\Pi_{el}(h)$ in a parametric form: $\Pi_{el}(\theta)$, $h(\theta)$. Fixed surface potential or charge means that Φ_s or σ_s does not depend on the film thickness h . The latter is important to be specified when integrating $\Pi(h)$ or $f(h)$ (in accordance with Equations 4.173 or 4.176) to calculate the interaction energy.

In principle, it is possible neither the surface potential nor the surface charge to be constant [398]. In such case a condition for *charge regulation* is applied, which represents the condition for dynamic equilibrium with respect to the counterion exchange between the Stern and diffuse parts of the EDL (i.e., condition for constant electrochemical potentials of the ionic species). As discussed in Section 4.2.1.2.3, the Stern layer itself can be considered as a Langmuir adsorption layer of counterions. We can relate the maximum possible surface charge density (due to all the surface ionizable groups) to Γ_1 in Equation 4.47: $\sigma_{\max} = Ze\Gamma_1$. Likewise, the effective surface charge density, σ_s , which

is smaller by magnitude than σ_{\max} (because some ionizable groups are blocked by adsorbed counterions) can be expressed as $\sigma_s = Ze(\Gamma_1 - \Gamma_2)$. Then, with the help of Equation 4.44, the Stern isotherm (Equation 4.47) can be represented in the form

$$\frac{\sigma_{\max} - \sigma_s}{\sigma_{\max}} = \left[1 + (K_2 I)^{-1} \exp(Z\Phi_s) \right]^{-1} \tag{4.194}$$

The product $Z\Phi_s$ is always positive. At high surface potential, $Z\Phi_s \rightarrow \infty$, from Equation 4.194 we obtain $\sigma_s \rightarrow \sigma_{\max}$, that is, there is no blocking of surface ionizable by adsorbed counterions.

When the film thickness is large enough ($\kappa h \geq 1$) the difference between the regimes of constant potential, constant charge, and charge regulation becomes negligible, that is, the usage of each of them leads to the same results for $\Pi_{el}(h)$ [14].

When the dimensionless electrostatic potential in the middle of the film

$$\Phi_m = \frac{e}{kT} \psi_m = -\frac{1}{2Z} \ln m \tag{4.195}$$

is small enough (the film thickness, h , is large enough), we could use the superposition approximation, that is, we could assume that $\Phi_m \approx 2\Phi_1(h/2)$, where Φ_1 is the dimensionless electric potential at a distance $h/2$ from the surface (of the film) when the other surface is removed at infinity. Because

$$Z\Phi_1\left(\frac{h}{2}\right) = 4e^{-\kappa h/4} \tanh\left(\frac{Z\Phi_s}{4}\right) \tag{4.196}$$

from Equations 4.189, 4.195, and 4.196, we obtain a useful asymptotic formula [399]

$$\Pi_{el} \approx n_0 kT Z^2 \Phi_m^2 \approx 64 n_0 kT \left(\tanh \frac{Z\Phi_s}{4} \right)^2 e^{-\kappa h} \tag{4.197}$$

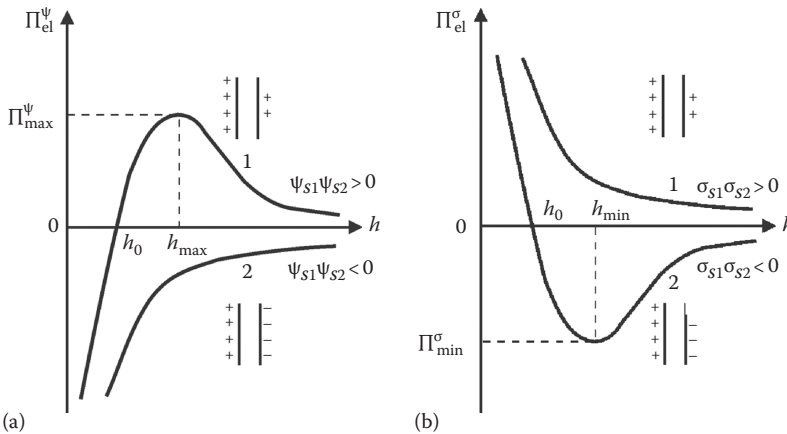


FIGURE 4.33 Electrostatic disjoining pressure at (a) fixed surface potential, Π_{el}^ψ , and (b) fixed surface charge density, Π_{el}^σ , both of them plotted vs. the film thickness h . ψ_{s1} and ψ_{s2} are the potentials of the two surfaces; σ_{s1} and σ_{s2} are the respective surface charge densities.

It should be noted that if Φ_s is large enough, the hyperbolic tangent in Equation 4.197 is identically 1, and Π_{el} (as well as f_{el}) becomes independent of the surface potential (or charge). Equation 4.197 can be generalized for the case of 2:1 electrolyte (bivalent counterion) and 1:2 electrolyte (bivalent coion) [400]:

$$\Pi_{el} = 432n_{(2)}kT \left(\tanh \frac{v_{i,j}}{4} \right)^2 e^{-\kappa h} \quad (4.198)$$

where $n_{(2)}$ is the concentration of the bivalent ions, the subscript “ $i;j$ ” takes value “2:1” or “1:2,” and

$$v_{2:1} = \ln \left[\frac{3}{1 + 2e^{-\Phi_s}} \right], \quad v_{1:2} = \ln \left[\frac{2e^{\Phi_s} + 1}{3} \right] \quad (4.199)$$

4.4.3.2 Two Nonidentically Charged Planes

Contrary to the case of two identically charged surfaces, which always repel each other (see Equation 4.189), the electrostatic interaction between two plane-parallel surfaces of different potentials, ψ_{s1} and ψ_{s2} , can be either repulsive or attractive [380,401]. Here, we will restrict our considerations to the case of low surface potentials, when the Poisson–Boltzmann equation can be linearized. Despite that it is not too general quantitatively, this case exhibits qualitatively all features of the electrostatic interaction between different surfaces.

If $\psi_{s1} = \text{constant}$, and $\psi_{s2} = \text{constant}$, then the disjoining pressure at constant surface potential reads [380]:

$$\Pi_{el}^{\psi} = \frac{\epsilon\epsilon_0\kappa^2}{2\pi} \frac{2\psi_{s1}\psi_{s2} \cosh \kappa h - (\psi_{s1}^2 + \psi_{s2}^2)}{\sinh^2 \kappa h} \quad (4.200)$$

When the two surface potentials have opposite signs, that is, when $\psi_{s1}\psi_{s2} < 0$, Π_{el}^{ψ} is negative for all h and corresponds to electrostatic attraction (see Figure 4.33a). This result could have been anticipated, because two charges of opposite sign attract each other. More interesting is the case, when $\psi_{s1}\psi_{s2} > 0$, but $\psi_{s1} \neq \psi_{s2}$. In the latter case, the two surfaces repel each other for $h > h_0$, whereas they attract each other for $h < h_0$ (Figure 4.33a); h_0 is determined by the equation $\kappa h_0 = \ln(\psi_{s2}/\psi_{s1})$; $\psi_{s2} > \psi_{s1}$. In addition, the electrostatic repulsion has a maximum value of

$$\Pi_{el}^{\psi}(\text{max}) = \frac{\epsilon\epsilon_0\kappa^2}{2\pi} \psi_{s1}^2 \quad \text{at } h_{\text{max}} = \frac{1}{\kappa} \operatorname{arccosh} \frac{\psi_{s2}}{\psi_{s1}}, \quad \psi_{s2} > \psi_{s1} \quad (4.201)$$

Similar electrostatic disjoining pressure isotherm has been used to interpret the experimental data for aqueous films on mercury [388]. It is worthwhile noting that $\Pi_{el}^{\psi}(\text{max})$ depends only on ψ_{s1} , that is, the maximum repulsion is determined by the potential of the surface of lower charge.

If $\sigma_{s1} = \text{constant}$, and $\sigma_{s2} = \text{constant}$, then instead of Equation 4.200 we have [380]

$$\Pi_{el}^{\sigma}(h) = \frac{1}{2\epsilon\epsilon_0} \frac{2\sigma_{s1}\sigma_{s2} \cosh \kappa h + \sigma_{s1}^2 + \sigma_{s2}^2}{\sinh^2 \kappa h} \quad (4.202)$$

When $\sigma_1\sigma_2 > 0$, Equation 4.202 yields $\Pi_{el}^\sigma > 0$ for every h (see Figure 4.33b). However, when $\sigma_1\sigma_2 < 0$, Π_{el}^σ is repulsive for small thickness, $h < h_0$ and attractive for larger separations, $h > h_0$; h_0 is determined by the equation $\kappa h_0 = \ln(-\sigma_{s2}/\sigma_{s1})$; $|\sigma_{s2}| > |\sigma_{s1}|$. The electrostatic disjoining pressure in this case has a minimum value

$$\Pi_{el}^\sigma(\min) = \frac{1}{\epsilon\epsilon_0} \sigma_{s1}\sigma_{s2}, \quad \text{at } h_{\min} = \frac{1}{\kappa} \operatorname{arccosh}\left(-\frac{\sigma_{s2}}{\sigma_{s1}}\right) \quad (4.203)$$

Finally, it should be noted that all curves depicted in Figure 4.24 decay exponentially at $h \rightarrow \infty$. An asymptotic expression for Z:Z electrolytes, which generalizes Equation 4.197, holds [380,399]:

$$\Pi_{el}(h) = 64n_0kT\gamma_1\gamma_2e^{-\kappa h}, \quad \gamma_k \equiv \tanh\left(\frac{Ze\psi_{sk}}{4kT}\right), k = 1,2 \quad (4.204)$$

Equation 4.204 is valid for both low and high surface potentials, only if $\exp(-\kappa h) \ll 1$.

4.4.3.3 Two Charged Spheres

When the EDLs are thin compared with the particle radii ($\kappa^{-1} \ll R_1, R_2$) and the gap between the particles is small ($h_0 \ll R_1, R_2$), we can use Equation 4.204 in conjunction with the Derjaguin approximation, Equations 4.173 and 4.174. The result for the energy of electrostatic interaction between two spheres reads:

$$U_{el}(h_0) = \frac{128\pi R_1 R_2}{\kappa^2(R_1 + R_2)} n_0kT\gamma_1\gamma_2e^{-\kappa h} \quad (4.205)$$

Equation 4.205 is valid for any values of the surface potentials ψ_{s1} and ψ_{s2} but only for $\exp(\kappa h) \gg 1$. Complementary expressions, which are valid for every $h \ll R_1, R_2$, but for small surface potentials, can be derived by integrating Equations 4.200 and 4.202, instead of Equation 4.204. In this way, for $\psi_{s1} = \text{constant}$ and $\psi_{s2} = \text{constant}$, we can derive [402]:

$$U_{el}^\psi(h_0) = \frac{\pi\epsilon\epsilon_0 R_1 R_2}{R_1 + R_2} \left[(\psi_{s1} + \psi_{s2})^2 \ln(1 + e^{-\kappa h_0}) + (\psi_{s1} - \psi_{s2})^2 \ln(1 - e^{-\kappa h_0}) \right] \quad (4.206)$$

or, alternatively, for $\sigma_{s1} = \text{constant}$ and $\sigma_{s2} = \text{constant}$ we obtain [403]:

$$U_{el}^\sigma(h_0) = \frac{-\pi R_1 R_2}{\epsilon\epsilon_0 \kappa^2 (R_1 + R_2)} \left[(\sigma_{s1} + \sigma_{s2})^2 \ln(1 - e^{-\kappa h_0}) + (\sigma_{s1} - \sigma_{s2})^2 \ln(1 + e^{-\kappa h_0}) \right] \quad (4.207)$$

The range of validity of the different approximations involved in the derivations of Equations 4.205 through 4.207 is discussed in the book by Russel et al. [404].

As mentioned earlier, Equations 4.205 through 4.207 hold for $h_0 \ll R$. In the opposite case, when h_0 is comparable to or larger than the particle radius R , we can use the equation [14]:

$$U_{el}(h_0) = \frac{4\pi\epsilon\epsilon_0\psi_s^2 R^2}{2R + h_0} e^{-\kappa h_0} \quad (4.208)$$

stemming from the theory of Debye and Hückel [405] for two identical particles. Equation 4.208 was derived by using the superposition approximation (valid for weak overlap of the two EDLs)

and the linearized Poisson–Boltzmann equation. A simple approximate formula, representing in fact interpolation between Equations 4.208 and 4.206 (the latter for $R_1 = R_2 = R$), has been derived by McCartney and Levine [406]:

$$U_{\text{el}}^{\psi}(h_0) = 4\pi\epsilon\epsilon_0 R\psi_s^2 \frac{R+h_0}{2R+h_0} \ln\left(1 + \frac{Re^{-\kappa h_0}}{R+h_0}\right) \quad (4.209)$$

Equation 4.209 has the advantage to give a good approximation for every h_0 provided that the Poisson–Boltzmann equation can be linearized. Similar expressions for the energy of electrostatic interaction between two deformed droplets or bubbles (Figure 4.32) can be derived [392].

4.4.4 DLVO THEORY

The first quantitative theory of interactions in thin liquid films and dispersions is the DLVO theory called after the names of the authors Derjaguin and Landau [407] and Verwey and Overbeek [399]. In this theory, the total interaction is supposed to be a superposition of van der Waals and double layer interactions. In other words, the total disjoining pressure and the total interaction energy are presented in the form:

$$\Pi = \Pi_{\text{vw}} + \Pi_{\text{el}}, \quad U = U_{\text{vw}} + U_{\text{el}} \quad (4.210)$$

A typical curve, Π versus h , exhibits a maximum representing a barrier against coagulation and two minima, called primary and secondary minimum (see Figure 4.17); the U versus h curve has a similar shape. The primary minimum appears if strong short-range repulsive forces (e.g., steric forces) are present. With small particles, the depth of the secondary minimum is usually small ($U_{\text{min}} < kT$). If the particles cannot overcome the barrier, coagulation (flocculation) does not take place, and the dispersion is stable due to the electrostatic repulsion, which gives rise to the barrier. With larger colloidal particles ($R > 0.1 \mu\text{m}$), the secondary minimum could be deep enough to cause coagulation and even formation of ordered structures of particles [408].

By addition of electrolyte or by decreasing the surface potential of the particles, we can suppress the electrostatic repulsion and thus decrease the height of the barrier. According to DLVO theory, the critical condition determining the onset of rapid coagulation is

$$U(h_{\text{max}}) = 0, \quad \left. \frac{dU}{dh} \right|_{h_{\text{max}}} = 0 \quad (4.211)$$

where $h = h_{\text{max}}$ denotes the position of the barrier.

By using Equation 4.175 for U_{vw} and Equation 4.205 for U_{el} we derive from Equations 4.210 and 4.211 the following criterion for the threshold of rapid coagulation of identical particles ($R_1 = R_2 = R$; $\gamma_1 = \gamma_2 = \gamma$):

$$\frac{\kappa^6}{n_0^2} = \left[\frac{768\pi}{A_H} kT e^{-1} \tanh^2\left(\frac{Ze\psi_s}{4kT}\right) \right]^2 \quad (4.212)$$

For a $Z:Z$ electrolyte, substituting $\kappa^2 = (2Z^2 e^2 n_0)/(\epsilon_0 \epsilon kT)$ into Equation 4.212, we obtain:

$$n_0(\text{critical}) \propto \frac{1}{Z^6} \tanh^4\left(\frac{Ze\psi_s}{4kT}\right) \quad (4.213)$$

When ψ_s is high enough, the hyperbolic tangent equals 1 and Equation 4.213 yields n_0 (critical) $\propto Z^{-6}$ which is, in fact, the empirical rule established earlier by Schulze [409] and Hardy [410].

4.4.5 NON-DLVO SURFACE FORCES

After 1980, a number of surface forces have been found out which are not taken into account by conventional DLVO theory. They are considered separately in the following section.

4.4.5.1 Ion Correlation Forces

As shown by Debye and Hückel [405], due to the strong electrostatic interaction between the ions in a solution, the positions of the ions are correlated in such a way that a counterion atmosphere appears around each ion, thus screening its Coulomb potential. The energy of formation of the counterion atmospheres gives a contribution to the free energy of the system called correlation energy [25]. The correlation energy also affects a contribution to the osmotic pressure of the electrolyte solution, which can be presented in the form [25]

$$\Pi_{\text{osm}} = kT \sum_{i=1}^k n_i - \frac{kT\kappa^2}{24\pi} \quad (4.214)$$

The first term in the right-hand side of the Equation 4.214 corresponds to an ideal solution, whereas the second term takes into account the effect of electrostatic interactions between the ions (the same effect is accounted for thermodynamically by the activity coefficient, see Equation 4.31).

The expression for Π_{el} in the DLVO theory (Equation 4.189) obviously corresponds to an ideal solution, the contribution of the ionic correlations being neglected. Hence, in a more general theory instead of Equation 4.210, we could write:

$$\Pi = \Pi_{\text{vw}} + \Pi_{\text{el}} + \Pi_{\text{cor}} \quad (4.215)$$

where Π_{cor} is the contribution of the ionic correlations to the disjoining pressure. The theory of Π_{cor} takes into account the following effects: (1) the different ionic concentration (and hence the different Debye screening) in the film compared to that in the bulk solution; (2) the energy of deformation of the counterion atmosphere due to the image forces; and (3) the energy of the long-range

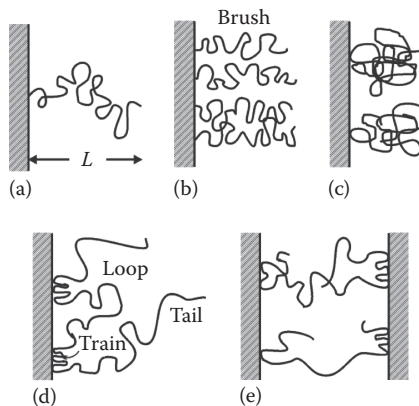


FIGURE 4.34 Polymeric chains adsorbed at an interface: (a) terminally anchored polymer chain of mean end-to-end distance L ; (b) a brush of anchored chains; (c) adsorbed (but not anchored) polymer coils; (d) configuration with a loop, trains and tails; (e) bridging of two surfaces by adsorbed polymer chains.

correlations between charge density fluctuations in the two opposite EDLs. For calculating Π_{cor} , both numerical solutions [411,412] and analytical expressions [413–415] have been obtained. For example, in the case when the electrolyte is symmetrical ($Z:Z$) and $\exp(-\kappa h) \ll 1$ we can use the asymptotic formula [413]

$$\Pi_{\text{cor}} = \Pi_{\text{el}} \frac{Z^2 e^2 \kappa}{16\pi\epsilon\epsilon_0 kT} (\ln 2 + 2I_C) + O(e^{-\kappa h}) \quad (4.216)$$

where Π_{el} is the conventional DLVO electrostatic disjoining pressure,

$$I_C = \frac{1}{2}(1+J)\ln 2 + \frac{2-2z^3+z}{2z(2z^2-1)^2} - \frac{1}{2}(1-J)\ln(z+z^2) - \frac{\sqrt{z^2-1}}{z} [1+J+4(2z^2-1)^{-3}] \arctan \sqrt{\frac{z-1}{z+1}}$$

$$J \equiv \frac{2z^2-3}{(2z^2-1)^3}, \quad z \equiv \left[1 + \left(\frac{e\sigma_s}{2\epsilon\epsilon_0 kT\kappa} \right)^2 \right]^{1/2}$$

The results for the case of symmetric electrolytes are the following. Π_{cor} is negative and corresponds to attraction, which can be comparable by magnitude with Π_{vw} . In the case of 1:1 electrolyte, Π_{cor} is usually a small correction to Π_{el} . In the case of 2:2 electrolyte, however, the situation can be quite different: the attractive forces, $\Pi_{\text{cor}} + \Pi_{\text{vw}}$, prevails over Π_{el} and the total disjoining pressure, Π , becomes negative. The effect of Π_{cor} is even larger in the presence of ions of higher valence. Short-range net attractive ion-correlation forces have been measured by Marra [416,417] and Kjellander et al. [418,419] between highly charged anionic bilayer surfaces in CaCl_2 solutions. These forces are believed to be responsible for the strong adhesion of some surfaces (clay and bilayer membranes) in the presence of divalent counterions [36,418,420]. In Ref. [421], the attraction mechanism and the structure of counterionic correlations are discussed in the limit of strong coupling based on numerical and analytical investigations and for various geometries (planar, spherical, and cylindrical) of charged objects.

The theory predicts ion-correlation attraction not only across water films with overlapping EDLs, but also across *oily* films intervening between two water phases. In the latter case, Π_{cor} is not zero because the ions belonging to the two outer double layers interact across the thin dielectric (oil) film. The theory for such a film [422] predicts that Π_{cor} is negative (attractive) and strongly dependent on the dielectric permittivity of the oil film; Π_{cor} can be comparable by magnitude with Π_{vw} ; $\Pi_{\text{el}} = 0$ in this case.

4.4.5.2 Steric Interaction

4.4.5.2.1 Physical Background

The steric interaction between two surfaces appears when chain molecules, attached at some point(s) to a surface, dangle out into the solution (see Figure 4.34). When two such surfaces approach each other, the following effects take place [36,423–425]: (1) The entropy decreases due to the confining of the dangling chains which results in a repulsive osmotic force known as *steric* or *overlap* repulsion. (2) In a poor solvent, the segments of the chain molecules attract each other; hence the overlap of the two approaching layers of polymer molecules will be accompanied with some *inter-segment attraction*; the latter can prevail for small overlap, however at the distance of larger overlap

it becomes negligible compared with the osmotic repulsion. (3) Another effect, known as the *bridging attraction*, occurs when two opposite ends of chain molecule can attach (adsorb) to the opposite approaching surfaces, thus forming a bridge between them (see Figure 4.34e).

Steric interaction can be observed in foam or emulsion films stabilized with nonionic surfactants or with various polymers, including proteins. The usual nonionic surfactants molecules are anchored (grafted) to the liquid interface by their hydrophobic moieties. When the surface concentration of adsorbed molecules is high enough, the hydrophilic chains are called to form a brush (Figure 4.34b). The coils of macromolecules, like proteins, can also adsorb at a liquid surface (Figure 4.34c). Sometimes, the configurations of the adsorbed polymers are very different from the statistical coil: loops, trains, and tails can be distinguished (Figure 4.34d).

The osmotic pressure of either dilute or concentrated polymer solutions can be expressed in the form [426]:

$$\frac{P_{\text{osm}}}{nkT} = \frac{1}{N} + \frac{1}{2}nv + \frac{1}{3}n^2w + \dots \quad (4.217)$$

Here

N is the number of segments in the polymer chain

n is the number segment density

v and w account for the pair and triplet interactions, respectively, between segments

In fact, v and w are counterparts of the second and third virial coefficients in the theory of imperfect gases [11]; v and w can be calculated if information about the polymer chain and the solvent is available [404]:

$$w^{1/2} = \frac{\bar{v}m}{N_A}, \quad v = w^{1/2}(1 - 2\chi) \quad (4.218)$$

where

\bar{v} (m³/kg) is the specific volume per segment

m (kg/mol) is the molecular weight per segment

N_A is the Avogadro number

χ is the Flory parameter

The latter depends on both the temperature and the energy of solvent–segment interaction. Then, v can be zero (see Equation 4.218) for some special temperature, called the *theta temperature*. The solvent at the theta temperature is known as the *theta solvent* or *ideal solvent*. The theta temperature for polymer solutions is a counterpart of the Boil temperature for imperfect gases: this is the temperature at which the intermolecular (intersegment) attraction and repulsion are exactly counterbalanced. In a good solvent, however, the repulsion due mainly to the excluded volume effect dominates the attraction and $v > 0$. In contrast, in a poor solvent the intersegment attraction prevails, so $v < 0$.

4.4.5.2.2 Thickness of the Polymer Adsorption Layer

The steric interaction between two approaching surfaces appears when the film thickness becomes of the order of, or smaller than, $2L$ where L is the mean-square end-to-end distance of the hydrophilic portion of the chain. If the chain was entirely extended, then L would be equal to Nl with l being the length of a segment; however, due to the Brownian motion $L < Nl$. For an anchored chain, like that depicted in Figure 4.34a, in a theta solvent, L can be estimated as [404]

$$L \approx L_0 \equiv l\sqrt{N} \quad (4.219)$$

In a good solvent $L > L_0$, whereas in a poor solvent $L < L_0$. In addition, L depends on the surface concentration, Γ , of the adsorbed chains, that is, L is different for an isolated molecule and for a brush (see Figure 4.34a and b). The mean field approach [404] applied to polymer solutions provides the following equation for calculating L

$$\tilde{L}^3 - \left(1 + \frac{1}{9}\tilde{\Gamma}^2\right)\tilde{L}^{-1} = \frac{1}{6}\tilde{\nu} \quad (4.220)$$

where \tilde{L} , $\tilde{\Gamma}$, and $\tilde{\nu}$ are the dimensionless values of L , Γ , and ν defined as follows:

$$\tilde{L} = \frac{L}{l\sqrt{N}}, \quad \tilde{\Gamma} = \frac{\Gamma N\sqrt{w}}{l}, \quad \tilde{\nu} = \frac{\nu\Gamma N^{3/2}}{l} \quad (4.221)$$

For an isolated adsorbed molecule ($\tilde{\Gamma} = 0$) in an ideal solvent ($\tilde{\nu} = 0$) Equation 4.220 predicts $\tilde{L} = 1$, that is, $L = L_0$.

4.4.5.2.3 Overlap of Adsorption Layers

We now consider the case of terminally anchored chains, like those depicted in Figure 4.34a and b. Dolan and Edwards [427,428] calculated the steric interaction free energy per unit area, f , as a function on the film thickness, h , in a theta solvent:

$$f(h) = \Gamma kT \left[\frac{\pi^2}{3} \frac{L_0^2}{h^2} - \ln \left(\frac{8\pi}{3} \frac{L_0^2}{h^2} \right) \right] \quad \text{for } h < L_0\sqrt{3} \quad (4.222)$$

$$f(h) = 4\Gamma kT \exp \left(-\frac{3h^2}{2L_0^2} \right) \quad \text{for } h > L_0\sqrt{3} \quad (4.223)$$

where L_0 is the end-to-end distance as defined by Equation 4.219. The boundary between the power-law regime ($f \propto 1/h^2$) and the exponential decay regime is at $h = L_0\sqrt{3} \approx 1.7L_0$, the latter being slightly less than $2L_0$, which is the intuitively expected onset of the steric overlap. The first term in the right-hand side of Equation 4.222 comes from the osmotic repulsion between the brushes, which opposes the approach of the two surfaces; the second term is negative and accounts effectively for the decrease of the elastic energy of the initially extended chains when the thickness of each of the two brushes, pressed against each other, decreases.

In the case of good solvent, the disjoining pressure $\Pi = -df/dh$ can be calculated by means of Alexander–de Gennes theory as [429,430]:

$$\Pi(h) = kT\Gamma^{3/2} \left[\left(\frac{2L_g}{h} \right)^{9/4} - \left(\frac{h}{2L_g} \right)^{3/4} \right] \quad \text{for } h < 2L_g, L_g = N(\Gamma l^5)^{1/3} \quad (4.224)$$

where L_g is the thickness of a brush in a good solvent [431]. The positive and the negative terms in the right-hand side of Equation 4.224 correspond to osmotic repulsion and elastic attraction. The

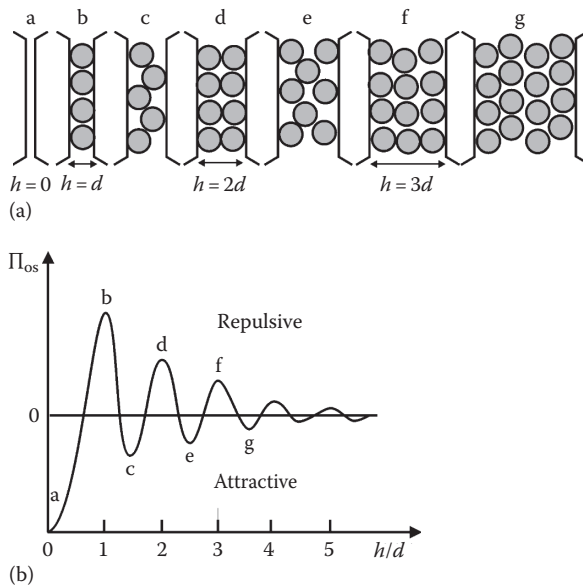


FIGURE 4.35 (a) Sketch of the consecutive stages of the thinning of a liquid film containing spherical particles; (b) plot of the related oscillatory structural component of disjoining pressure, Π_{0s} , vs. the film thickness h ; see Ref. [36] for details.

validity of Alexander–de Gennes theory was experimentally confirmed by Taunton et al. [432] who measured the forces between two brush layers grafted on the surfaces of two crossed mica cylinders.

In the case of adsorbed molecules, like those in Figure 4.34c, which are not anchored to the surface, the measured surface forces depend significantly on the rate of approaching of the two surfaces [433,434]. The latter effect can be attributed to the comparatively low rate of exchange of polymer between the adsorption layer and the bulk solution. This leads to a hysteresis of the surface force: different interaction on approach and separation of the two surfaces [36]. In addition, we can observe two regimes of steric repulsion: (1) weaker repulsion at larger separations due to the overlap of the tails (Figure 4.34d) and (2) stronger repulsion at smaller separations indicating overlap of the loops [435].

4.4.5.3 Oscillatory Structural Forces

4.4.5.3.1 Origin of the Structural Forces

Oscillatory structural forces appear in two cases: (1) in thin films of pure solvent between two smooth *solid* surfaces and (2) in thin liquid films containing colloidal particles (including macromolecules and surfactant micelles). In the first case, the oscillatory forces are called the *solvation forces* [36,436]. They are important for the short-range interactions between solid particles and dispersions. In the second case, the structural forces affect the stability of foam and emulsion films, as well as the flocculation processes in various colloids. At higher particle concentrations, the structural forces stabilize the liquid films and colloids [437–441]. At lower particle concentrations, the structural forces degenerate into the so-called *depletion attraction*, which is found to destabilize various dispersions [442,443].

In all cases, the oscillatory structural forces appear when monodisperse spherical (in some cases ellipsoidal or cylindrical) particles are confined between the two surfaces of a thin film. Even one “hard wall” can induce ordering among the neighboring molecules. The oscillatory structural force is a result of overlap of the structured zones at two approaching surfaces [444–447]. A simple

connection between density distribution and structural force is given by the contact value theorem [36,447,448]:

$$\Pi_{\text{os}}(h) = kT[n_s(h) - n_s(\infty)] \quad (4.225)$$

where

Π_{os} is the disjoining pressure component due to the oscillatory structural forces

$n_s(h)$ is the particle number density in the subsurface layer as a function of the distance between the walls, h

Figure 4.35 illustrates the variation of n_s with h and the resulting disjoining pressure, Π_{os} . We see that in the limit of very small separations, as the last layer of particles is eventually squeezed out, $n_s \rightarrow 0$ and

$$\Pi_{\text{os}}(h) \rightarrow -kTn_s(\infty) \quad \text{for } h \rightarrow 0 \quad (4.226)$$

In other words, at small separations Π_{os} is negative (attractive). Equation 4.226 holds for both solvation forces and colloid structural forces. In the latter case, Equation 4.226 represents the osmotic pressure of the colloid particles and the resulting attractive force is known as the *depletion force* (Section 4.4.5.3.3).

The wall induces structuring in the neighboring fluid only if the magnitude of the surface roughness is negligible in comparison with the particle diameter, d . Indeed, when surface irregularities are present, the oscillations are smeared out and oscillatory structural force does not appear. If the film surfaces are fluid, the role of the surface roughness is played by the interfacial fluctuation capillary waves, whose amplitude (between 1 and 5 Å) is comparable with the diameter of the solvent molecules. For this reason, oscillatory solvation forces (due to structuring of solvent molecules) are observed only with liquid films, which are confined between smooth solid surfaces [36]. In order for structural forces to be observed in foam or emulsion films, the diameter of the colloidal particles must be much larger than the amplitude of the surface corrugations. The period of the oscillations is always about the particle diameter [36,441].

The theories developed for calculating the oscillatory force are based on modeling by means of the integral equations of statistical mechanics [449–453] or numerical simulations [454–457]. As a rule, these approaches are related to complicated theoretical expressions or numerical procedures, in contrast with the Derjaguin–Landau–Verwey–Overbeek (DLVO) theory, one of its main advantages being its simplicity [36]. To overcome this difficulty, some relatively simple semiempirical expressions have been proposed [458,459] on the basis of fits of theoretical results for hard-sphere fluids.

The following semiempirical formula for the oscillatory structural component of disjoining pressure reads was proposed in Ref. [458]:

$$\begin{aligned} \Pi_{\text{os}}(h) &= P_0 \cos\left(\frac{2\pi h}{d_1}\right) \exp\left(\frac{d^3}{d_1^2 d_2} - \frac{h}{d_2}\right) \quad \text{for } h > d \\ &= -P_0 \quad \text{for } 0 < h < d \end{aligned} \quad (4.227)$$

where

d is the diameter of the hard spheres

d_1 and d_2 are the period and the decay length of the oscillations which are related to the particle volume fraction, ϕ , as follows [458]

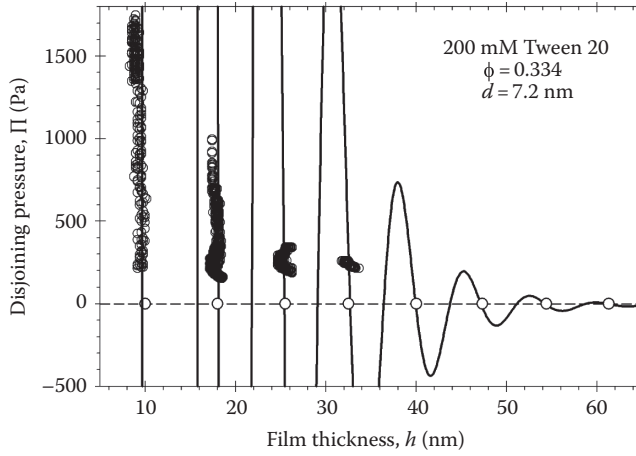


FIGURE 4.36 Plot of disjoining pressure, Π , vs. film thickness, h : comparison of experimental data for a foam film from Ref. [461] (thin-film pressure balance) with the theoretical curve (the solid line) calculated by means of Equation 4.230. The film is formed from 200 mM aqueous solution of the nonionic surfactant Tween 20. The volume fraction of the micelles ($\phi = 0.334$) is determined from the film contact angle; the micelle diameter ($d = 7.2$ nm) is determined by dynamic light scattering. The points on the horizontal axis denote the respective values of h for the stratification steps measured by a thin-film pressure balance.

$$\frac{d_1}{d} = \sqrt{\frac{2}{3}} + 0.237\Delta\phi + 0.633(\Delta\phi)^2; \quad \frac{d_2}{d} = \frac{0.4866}{\Delta\phi} - 0.420 \quad (4.228)$$

Here

$\Delta\phi = \phi_{\max} - \phi$ with $f_{\max} = \pi/(3\sqrt{2})$ being the value of ϕ at close packing

P_0 is the particle osmotic pressure determined by means of the Carnahan–Starling formula [460]

$$P_0 = nkT \frac{1 + \phi + \phi^2 - \phi^3}{(1 - \phi)^3}, \quad n = \frac{6\phi}{\pi d^3} \quad (4.229)$$

where n is the particle number density. For $h < d$, when the particles are expelled from the slit into the neighboring bulk suspension, Equation 4.227 describes the depletion attraction. On the other hand, for $h > d$ the structural disjoining pressure oscillates around P_0 as defined by Equation 4.229 in agreement with the results of Kjellander and Sarman [451]. The finite discontinuity of Π_{os} at $h = d$ is not surprising as, at this point, the interaction is switched over from oscillatory to depletion regime. It should be noted that in oscillatory regime, the concentration dependence of Π_{os} is dominated by the decay length d_2 in the exponent (see Equations 4.227 and 4.228). Roughly speaking, for a given distance h , the oscillatory disjoining pressure Π_{os} increases five times when ϕ is increased with 10% [458]. The comparison with available numerical data showed that Equation 4.227 is accurate everywhere except in the region of the first (the highest) oscillatory maximum.

A semiempirical expression for $\Pi_{\text{os}}(H)$, which is accurate in the whole region $0 \leq H < \infty$, including the region of the first maximum, was proposed by Trokhymchuk et al. [459]:

$$\begin{aligned} \Pi_{\text{os}} &= \Pi_0 \cos(\omega h + \varphi_2) e^{-\kappa h} + \Pi_1 e^{-(d-h)\delta} & \text{for } h \geq d \\ \Pi_{\text{os}} &= -P_0 & \text{for } 0 \leq h < d \end{aligned} \quad (4.230)$$

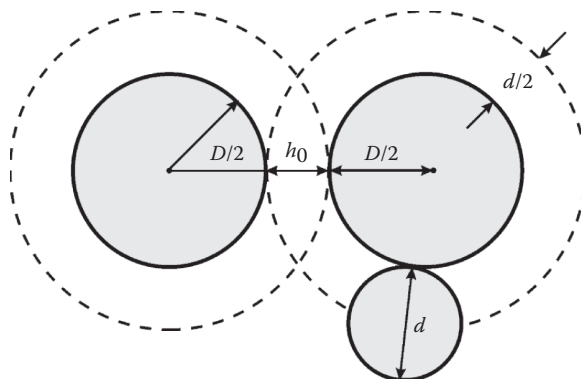


FIGURE 4.37 Overlap of the depletion zones around two particles of diameter D separated at a surface-to-surface distance h_0 ; the smaller particles have diameter d .

Here, Π_0 , Π_1 , ω , φ_2 , κ , and δ are universal functions of particle volume fraction, ϕ , tabulated in Ref. [459]. Equation 4.230 compares very well with existing computer simulation data [459].

The interactions between the micelles in a nonionic surfactant solution can be adequately described as interactions in a hard-sphere fluid. Experiments with foam films formed from aqueous solutions of two *nonionic* surfactants, Brij 35 and Tween 20, which contain spherical micelles of diameters in the range 7–9 nm, have been carried out [461]. From the measured contact angles, the micelle aggregation number and volume fraction have been determined. In addition, from the measured disjoining pressure isotherms the micelle diameter has been found. In other words, the liquid-film measurements could give information about the micelles, which is analogous to that obtainable by dynamic and static light scattering. As an illustration, Figure 4.36 shows the comparison of theory and experiment for the nonionic surfactant Tween 20. The experimental $\Pi_{os}(h)$ dependence is obtained by using the porous-plate cell by Mysels and Jones, known also as *thin-film pressure balance* [462]. The points on the horizontal axis correspond to the thickness of the metastable states of the film measured by the Scheludko–Exerowa capillary cell [215,216]. The solid line is calculated by means of Equation 4.230 for particle (micelle) diameter determined by light scattering and micelle volume fraction determined from the contact angle of the thin liquid film [461]. The short-range repulsion at $h \approx 10$ nm (Figure 4.36) corresponds to the steric repulsion between the hydrophilic headgroups of the surfactant molecules. Excellent agreement between Equation 4.230 and experimental data obtained by colloidal-probe *atomic force microscopy* (CP-AFM) for micellar solutions of Brij 35 has also been reported [463].

The predictions of different quantitative criteria for stability–instability transitions were investigated [461], having in mind that the oscillatory forces exhibit both maxima, which play the role of barriers to coagulation, and minima that could produce flocculation or coalescence in colloidal dispersions (emulsions, foams, suspensions). The interplay of the oscillatory force with the van der Waals surface force was taken into account. Two different kinetic criteria were considered, which give similar and physically reasonable results about the stability–instability transitions. Diagrams were constructed, which show the values of the micelle volume fraction, for which the oscillatory barriers can prevent the particles from coming into close contact, or for which a strong flocculation in the depletion minimum or a weak flocculation in the first oscillatory minimum could be observed [461].

4.4.5.3.2 Oscillatory Solvation Forces

When the role of hard spheres, like those depicted in Figure 4.35, is played by the molecules of solvent, the resulting volume exclusion force is called the *oscillatory solvation force*, or sometimes when the

solvent is water, *oscillatory hydration force* [36]. The latter should be distinguished from the *monotonic* hydration force, which has different physical origin and is considered separately in Section 4.4.5.4.

Measurement of the oscillatory solvation force became possible after the precise SFA had been constructed [36]. This apparatus allowed measuring measure the surface forces in thin liquid films confined between molecularly smooth mica surfaces and in this way to check the validity of the DLVO theory down to thickness of about 5 Å, and even smaller. The experimental results with nonaqueous liquids of both spherical (CCl₄) or cylindrical (linear alkanes) molecules showed that at larger separations the DLVO theory is satisfied, whereas at separations on the order of several molecular diameters an oscillatory force is superimposed over the DLVO force law. In aqueous solutions, oscillatory forces were observed at higher electrolyte concentrations with periodicity of 0.22–0.26 nm, about the diameter of the water molecule [36]. As mentioned earlier, the oscillatory solvation forces can be observed only between smooth solid surfaces.

4.4.5.3.3 Depletion Force

Bondy [464] observed coagulation of rubber latex in presence of polymer molecules in the disperse medium. Asakura and Oosawa [442] published a theory, which attributed the observed interparticle attraction to the overlap of the depletion layers at the surfaces of two approaching colloidal particles (see Figure 4.37). The centers of the smaller particles, of diameter, d , cannot approach the surface of a bigger particle (of diameter D) at a distance shorter than $d/2$, which is the thickness of the depletion layer. When the two depletion layers overlap (Figure 4.37), some volume between the large particles becomes inaccessible for the smaller particles. This gives rise to an osmotic pressure, which tends to suck out the solvent between the bigger particles, thus forcing them against each other. The total depletion force experienced by one of the bigger particles is [442]

$$F_{\text{dep}} = -kTnS(h_0) \quad (4.231)$$

where the effective depletion area is

$$\begin{aligned} S(h_0) &= \frac{\pi}{4}(2D + d + h_0)(d - h_0) & \text{for } 0 \leq h_0 \leq d \\ S(h_0) &= 0 & \text{for } d \leq h_0 \end{aligned} \quad (4.232)$$

Here

h_0 is the shortest distance between the surfaces of the larger particles
 n is the number density of the smaller particles

By integrating Equation 4.233, we can derive an expression for the depletion interaction energy between the two larger particles, $U_{\text{dep}}(h_0)$. For $D \gg d$, this expression reads:

$$\frac{U_{\text{dep}}(h_0)}{kT} \approx -\frac{3}{2}\phi \frac{D}{d^3} (d - h_0)^2 \quad 0 \leq h_0 \leq d \quad (4.233)$$

where $\phi = \pi nd^3/6$ is the volume fraction of the small particles. The maximum value of U_{dep} at $h_0 = 0$ is $U_{\text{dep}}(0)/kT \approx -3\phi D/(2d)$. For example, if $D/d = 50$ and $\phi = 0.1$, then $U_{\text{dep}}(0) = 7.5kT$. This depletion attraction turns out to be large enough to cause flocculation in dispersions. De Hek and Vrij [443] studied systematically the flocculation of sterically stabilized silica suspensions in cyclohexane by polystyrene molecules. Patel and Russel [465] investigated the phase separation and rheology of aqueous polystyrene latex suspensions in the presence of polymer (Dextran T-500).

The stability of dispersions is often determined by the competition between electrostatic repulsion and depletion attraction [466]. Interplay of steric repulsion and depletion attraction was studied theoretically by van Lent et al. [467] for the case of polymer solution between two surfaces coated with anchored polymer layers. Joanny et al. [468] and Russel et al. [404] re-examined the theory of depletion interaction by taking into account the internal degrees of freedom of the polymer molecules. Their analysis confirmed the earlier results of Asakura and Oosawa [442].

The depletion interaction is always present when a film is formed from micellar surfactant solution; the micelles play the role of the smaller particles. At higher micellar concentrations, the volume exclusion interaction becomes more complicated: it follows the oscillatory curve depicted in Figure 4.34. In this case only, the first minimum (that at $h \rightarrow 0$) corresponds to the conventional depletion force.

In the case of plane-parallel films the depletion component of disjoining pressure is

$$\begin{aligned} \Pi_{\text{dep}}(h) &= -nkT & h < d \\ \Pi_{\text{dep}}(h) &= 0 & h > d \end{aligned} \quad (4.234)$$

which is similar to Equation 4.226. This is not surprising because in both cases we are dealing with the excluded volume effect. Evans and Needham [469] succeeded to measure the depletion energy of two interacting bilayer surfaces in a concentrated Dextran solution; their results confirm the validity of Equation 4.236. The effect of polymer polydispersity on the depletion interaction between two plates immersed in a nonadsorbing polymer solution was studied by self-consistent field theory [470]. The results showed that as the two plates approach, the polymers with different chain lengths are excluded from the gap gradually for conformational entropy penalty, and the range of the depletion potential increases and the depth of the potential decreases with increasing polydispersity. Depletion force in a bidisperse granular layer was investigated in experiments and simulations of vertically vibrated mixtures of large and small steel spheres [471].

The interaction between a colloidal hard sphere and a wall or between two spheres in a dilute suspension of infinitely thin rods was calculated numerically [472]. The method allowed to studying the effect of polydispersity on the depletion interaction. It was observed that both the depth and the range of the depletion potential increase drastically if the relative standard deviation of the length distribution is larger than 0.25. In contrast, the potential is virtually indistinguishable from that caused by monodisperse rods, if the standard deviation is ≤ 0.1 [472]. Shear-affected depletion interaction with disc-shaped particles was experimentally investigated [473]. Synergistic effects of polymers and surfactants on depletion forces were also examined. It was established that the formation of relatively large complexes (aggregates) of polymer and surfactant creates a significant depletion force between the particle and plate [474]. A detailed review on depletion surface forces can be found in the book by Lekkerkerker and Tuinier [475].

4.4.5.3.4 Colloid Structural Forces

In the beginning of the twentieth century, Johannott [476] and Perrin [477] observed that *foam* films decrease their thickness by several stepwise transitions. The phenomenon was called *stratification*. Bruil and Lyklema [478] and Friberg et al. [479] studied systematically the effect of ionic surfactants and electrolytes on the occurrence of the stepwise transitions. Keuskamp and Lyklema [480] anticipated that some oscillatory interaction between the film surfaces must be responsible for the observed phenomenon. Kruglyakov et al. [481,482] reported the existence of stratification with *emulsion* films.

It should be noted that the explanation of the stepwise transitions in the film thickness as a layer-by-layer thinning of an ordered structure of spherical micelles within the film (see Figure 4.35) was first given by Nikolov et al. [437–441]. Before that it was believed that the stepwise transitions are due to the formation of a *lamella*-liquid-crystal structures of surfactant molecules in the films. One of the direct proofs was given by Denkov et al. [483,484], who succeeded in freezing foam films at

TABLE 4.7
Measured Period of the Structural Force,^a Δh , and Micelle Aggregation Number, N_{agg} , Calculated from Equation 4.235

c_s (mM)	Experimental Δh (nm) from Ref. [513]	Aggregation Number N_{agg} from Equation 4.235	N_{agg} from Literature
<i>Sodium dodecyl sulfate (SDS)</i>			
30	15.3	48	50 [515], 55 [516], 59 [517]
40	14.7	61	60 [518], 62 [519], 64 [517]
50	13.7	65	64 [515,517,520], 65 [521]
100	10.6	65	64 [515,517,520], 65 [521]
<i>Cetyl trimethylammonium bromide (CTAB)</i>			
10	25.8	95	92 [522], 95 [523,524], 98 [525]
20	21.8	119	—
30	19.9	137	100 [524]
40	18.0	136	—
50	16.6	135	139 [526], 140 [524]
<i>Cetyl pyridinium chloride (CPC)</i>			
10	21.2	52	45–90 [527], 56 [528]
20	18.7	75	78 [513]
30	16.6	80	82 [525]
40	15.8	93	—
50	14.6	93	87 [529]

^a Data from Refs. [513,514].

various stages of stratification. The electron microscope pictures of such vitrified stratifying films containing latex particles (144 nm in diameter) and bacteriorhodopsin vesicles (44 nm in diameter) showed ordered particle arrays of hexagonal packing [484]. The mechanism of stratification was studied experimentally and theoretically in Ref. [485], where the appearance and expansion of black spots in the stratifying films were described as being a process of condensation of vacancies in a colloid crystal of ordered micelles within the film.

The stable branches of the oscillatory curves have been detected by means of a thin-film pressure balance [461,486,487]. Oscillatory forces due to surfactant micelles and microemulsion droplets have also been measured by means of a SFA [488,489]; by atomic force microscopy [463,490]; by a light scattering method [491], in asymmetric films [492], in emulsion films [493], and in films containing solid colloidal spheres [437,438,494–502]. Such forces are also observed in more complex systems like protein solutions, surfactant–polymer mixtures, and ABA amphiphilic block copolymers, where A and B denote, respectively, hydrophilic and hydrophobic parts of the molecule [503–511].

In the case of liquid films that contain *charged* colloid particles (micelles), the *oscillatory period*, Δh , is considerably greater than the particle diameter [437,438]. In this case, the theoretical prediction of Δh demands the use of density functional theory calculations and/or Monte Carlo simulations [456,512]. However, the theory, simulations, and experiments showed that a simple inverse-cubic-root relation, $\Delta h = c_m^{-1/3}$, exists between Δh and the bulk number concentration of micelles (particles), c_m [437,438,498,512–514].

The validity of the semiempirical $\Delta h = c_m^{-1/3}$ law is limited at low and high particle concentrations, characterized by the effective particle volume fraction (particle + counterion atmosphere) [502]. The decrease of the effective particle volume fraction can be experimentally accomplished not only

by dilution, but also by addition of electrolyte that leads to shrinking of the counterion atmosphere [500]. The inverse-cubic-root law, $\Delta h = c_m^{-1/3}$, which can be interpreted as an osmotic pressure balance between the film and the bulk [513], is fulfilled in a wide range of particle/micelle concentrations that coincide with the range where stratification (step-wise thinning) of free liquid films formed from particle suspension and micellar solution is observed [139,437–439,493–496,513,514], and where the surface force measured by CP-AFM [463,490,498–502] or SFA [488,489] exhibits oscillations.

Because the validity of the $\Delta h = c_m^{-1/3}$ law has been proven in numerous studies, it can be used for determining the aggregation number, N_{agg} , of ionic surfactant micelles [513]. Indeed, $c_m = (c_s - \text{CMC})/N_{\text{agg}}$, where c_s and CMC are the total input surfactant concentration and the CMC expressed as number of molecules per unit volume. The combination of the latter expression with $\Delta h = c_m^{-1/3}$ law yields [513,514]:

$$N_{\text{agg}} = (c_s - \text{CMC})(\Delta h)^3 \quad (4.235)$$

Values of N_{agg} determined from the experimental Δh for foam films containing micelles [513,514] using Equation 4.235 are shown in Table 4.7 for three ionic surfactants, sodium dodecylsulfate (SDS, CMC = 8 mM), cetyl trimethyl ammonium bromide (CTAB, CMC = 0.9 mM), and cetyl pyridinium chloride (CPC, CMC = 0.9 mM) at 25°C. As seen in Table 4.7, the micelle aggregation numbers determined in this way compare very well with data for N_{agg} obtained by other methods.

As mentioned earlier, the experimental Δh is significantly greater than the diameter of the ionic micelle. Δh can be considered as an effective diameter of the charged particle, d_{eff} , which includes its counterion atmosphere. A semiempirical expression for calculating Δh was proposed in [513,514]:

$$d_{\text{eff}} = d_h \left\{ 1 + \frac{3}{d_h^3} \int_{d_h}^{\infty} \left[1 - \exp\left(-\frac{3u_{\text{el}}(r)}{kT}\right) \right] r^2 dr \right\}^{1/3} \quad (4.236)$$

where

$$\frac{u_{\text{el}}(r)}{kT} = \frac{r}{4L_B} \left[\frac{e}{kT} \Psi\left(\frac{r}{2}\right) \right]^2 \quad (4.237)$$

Here

d_h is the hydrodynamic diameter of the micelle

k is the Boltzmann constant

T is the absolute temperature

$u_{\text{el}}(r)$ is the energy of electrostatic interaction of two micelles in the solution

$\Psi(r)$ is the distribution of the electrostatic potential around a given ionic micelle in the solution

r is radial coordinate;

$L_B \equiv e^2/(4\pi\epsilon_0\epsilon kT)$ is the Bjerrum length ($L_B = 0.72$ nm for water at 25°C); ϵ_0 is the permittivity of vacuum; ϵ is the dielectric constant of the solvent (water); and e is the elementary charge

Equation 4.237 reduces the two-particle problem to the single-particle problem; see Refs. [513,514] for details.

It was found [513] that the relationship $d_{\text{eff}} = c_m^{-1/3} = \Delta h$ is satisfied in the whole concentration range where stratifying films are observed; d_{eff} is calculated from Equation 4.236, whereas Δh is experimentally determined from the stratification steps of foam films. In contrast, for $d_{\text{eff}} < c_m^{-1/3}$ the foam films do not stratify and the oscillations of disjoining pressure vanish. This may happen at low micelle concentrations, or at sufficiently high salt concentrations [513]. Thus, the relation between d_{eff} and c_m can be used as a criterion for the existence of oscillatory structural force with charged colloidal particles.

4.4.5.4 Repulsive Hydration and Attractive Hydrophobic Forces

These two surface forces are observed in thin aqueous films. Their appearance is somehow connected with the unique properties of the water as solvent: small molecular size, large dipole moment, high dielectric constant, formation of an extensive hydrogen-bonding network, and of EDLs near interfaces [36,530].

4.4.5.4.1 Repulsive Hydration Forces

The existence of a short-range (≤ 4 nm) repulsive pressure was first observed in experiments on the swelling of clays [531,532] and on the stabilization of foam films [533]. This short-range repulsion has been called the “hydration force” [534]. The school of Derjaguin terms this effect “structural component of disjoining pressure” [535]. Indications for its action were found in measurements of interactions between phospholipid bilayers by Parsegian et al. [536,537]. Israelachvili et al. [538–540] and Pashley [541–543] examined the validity of the DLVO theory [399,407] at small film thickness by an SFA in experiments with films from aqueous electrolyte solutions confined between two curved mica surfaces, bare or covered by adsorbed layers. At electrolyte concentrations below 10^{-4} M, they observed the typical DLVO maximum. However, at electrolyte concentrations higher than 10^{-3} M they did not observe the expected DLVO maximum and primary minimum [540]. Instead a strong short-range repulsion was detected, which can be empirically described by exponential law [36]:

$$f_{\text{hydr}}(h) = f_0 e^{-h/\lambda_0} \quad (4.238)$$

where the decay length $\lambda_0 \approx 0.6\text{--}1.1$ nm for 1:1 electrolytes and f_0 depends on the hydration of the surfaces but is usually about $3\text{--}30$ mJ/m². Similar repulsion was detected between silica sheets [544,545] and dihexadecyl phosphate monolayers deposited on a solid surface [546].

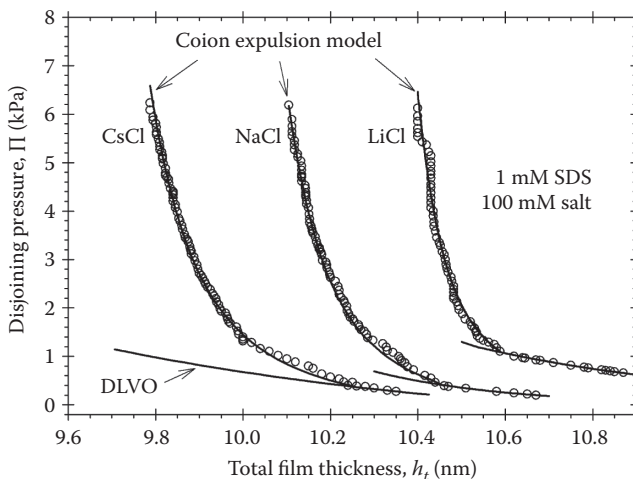


FIGURE 4.38 Plot of the disjoining pressure Π vs. the total thickness h_t of foam films formed from 1 mM aqueous solutions of SDS in the presence of 100 mM electrolyte: LiCl, NaCl and CsCl. At greater thicknesses, the $\Pi(h_t)$ dependence obeys the DLVO theory, whereas at the small thickness the steep parts of the curves are in agreement with the coion-expulsion model. The distances between the experimental curves measured with different electrolytes are due to the different sizes of the hydrated Cs^+ , Na^+ , and Li^+ counterions. (From Kralchevsky, P.A. et al., *Curr. Opin. Colloid Interface Sci.*, 16, 517, 2011.)

The conventional electrostatic (double layer) repulsion is suppressed if the solution's ionic strength is increased [399,407]. In contrast, the hydration repulsion is detected at higher ionic strengths [540], at which it is the main stabilizing factor in liquid films and colloidal dispersions. Such strong repulsion at high salt concentrations was observed between apoferritin molecules in solutions [547,548] and between the adsorption layers of this and other proteins on solid surfaces and colloidal particles [549,550]. In general, the hydration force plays an important role for the stability of proteins in physiological media. Hydration forces have also been observed between DNA molecules in aqueous solutions [551,552]. Effects of monovalent anions of the Hofmeister series and other solutes on the hydration repulsion between phospholipid bilayers have been experimentally investigated [553–556]. The hydration repulsion affects the stability of emulsions [557]; the rheology of concentrated suspensions [558]; the interactions of biological cells [559]; and the fusion rate of vesicles in the cellular inter-organelle traffic [560]. Additional information can be found in several review articles [561–566].

The physical importance of the hydration force is that it stabilizes dispersions at high electrolyte concentrations preventing coagulation in the primary minimum of the DLVO curve (Figure 4.17). For example, Healy et al. [567] found that even high electrolyte concentrations cannot cause coagulation of amphoteric latex particles due to binding of strongly hydrated Li^+ ions at the particle surfaces. If the Li^+ ions are replaced by weakly hydrated Cs^+ ions, the hydration repulsion becomes negligible, compared with the van der Waals attraction, and the particles coagulate as predicted by the DLVO theory. Hence, the hydration repulsion can be regulated by ion exchange.

The aforementioned studies indicate that hydration repulsion is observed in (at least) two types of systems. (1) *charged* interfaces at relatively high electrolyte concentrations, where electrostatic and osmotic effects related to the presence of bound and mobile counterions are expected to play an essential role and (2) *electroneutral* surfaces with zwitterionic surface groups, like phospholipid bilayers, where the water structuring near the polar surface and surface charge discreteness could be the main sources of the observed repulsion. Correspondingly, for the theoretical explanation of the hydration repulsion different models have been proposed, which could be adequate for different systems. The most important theoretical models are as follows:

1. *Water-structuring models*. In these models, the short-range repulsive interaction is attributed to alignment of water dipoles in the vicinity of a hydrophilic surface, where the range of the surface force is determined by the orientation correlation length of the solvent molecules [568–570]. Due to the strong orientation of water molecules near polar surfaces, we could expect that there are fewer configurations available to maintain the bulk water structure, which represents a loss of entropy that leads to a repulsive force [571]. The existence of such effects has been confirmed by molecular dynamics (MD) simulations [572,573].
2. *Image-charge models*. These models take into account the discreteness of surface charges, which induces orientation in the adjacent water dipoles [574–577]. Dipoles due to zwitterionic surface groups, for example, phospholipid headgroups [578], have been also taken into consideration in models of the electrostatic interaction between planar dipole lattices [579–583].
3. *Dielectric-saturation models* attribute the hydration repulsion to the presence of a layer with lower dielectric constant, ϵ , in the vicinity of the interfaces. Models with a stepwise [584,585] and continuous [586] variation of ϵ have been proposed.
4. *Excluded-volume models* take into account the fact that the finite size of the ions leads to a lower counterion concentration near a charged surface, and to a weaker Debye screening of the electrostatic field (in comparison with the point-ion model), which results in a stronger repulsion between two charged surfaces at short separations [587,588].

5. *Coion expulsion model*. This model [589] assumes that at sufficiently small thicknesses all coions are pressed out of the film so that it contains only counterions dissociated from the ionized surface groups. Under such conditions, the screening of the electric field of the film surface weakens, which considerably enhances the electrostatic repulsion in comparison with that predicted by the DLVO theory. Such reduced screening of the electric field could exist only in a narrow range of film thicknesses, which practically coincides with the range where the hydration repulsion is observed.

Let us consider in more details the *coion expulsion model*, also called “reduced screening model” [589]. This model was developed to explain the strong short-range repulsion detected in foam films; see Figure 4.38. It was found [589] that the excluded volume model [588] cannot explain the observed large deviations from the DLVO theory. Quantitative data interpretation was obtained by assuming that all *coions* have been pressed out of the thin film (see Figure 4.1). In such case, the Poisson–Boltzmann equation acquires the form

$$\frac{d^2\Phi}{dx^2} = \frac{1}{2} \kappa^2 e^\Phi \quad (4.239)$$

where

Φ is the dimensionless electric potential
 κ is the Debye screening length

$$\Phi \equiv \frac{e|\psi|}{kT} \quad \kappa^2 \equiv \frac{2e^2 a_{2\infty}}{\epsilon\epsilon_0 kT} \quad (4.240)$$

The notations are the same as in Equation 4.237; in particular, $\psi(x)$ is the dimensional electrostatic potential, x is a coordinate perpendicular to the surfaces of the plane-parallel film, and $a_{2\infty} = \gamma_{\pm} c_{2\infty}$ is the activity of counterions in the bulk solution, which is in contact with the film; see Equation 4.30. The first integral of Equation 4.239 reads:

$$\frac{d\Phi}{dx} = \kappa(e^\Phi - e^{\Phi_m})^{1/2} \quad (4.241)$$

Here, Φ_m is the value of Φ in the middle of the film. Integrating Equation 4.241 between the middle of the film and the film surface, one can derive [589]

$$\exp\Phi_s = \frac{\exp\Phi_m}{\cos^2[(\kappa h/4)\exp(\Phi_m/2)]} \quad (4.242)$$

where Φ_s is the value of Φ at the film surface, whereas h is the thickness of the aqueous core of the foam film. The right-hand side of Equation 4.242 has singularities for those h values, for which the cosine in the denominator is equal to zero. For this reason, the region of physical applicability of Equation 4.10 (and of the RS model) corresponds to h values, for which the argument of the cosine is between 0 and $\pi/2$:

$$0 < h < \frac{2\pi}{\kappa} \exp\left(-\frac{\Phi_m}{2}\right) \quad (4.243)$$

In the experiments in Ref. [589], 100 mM electrolyte is present, which leads to $\kappa^{-1} \approx 1$ nm, and the midplane potential is $\Phi_m \approx 0.7$, so that $\exp(-\Phi_m/2) \approx 0.705$. Then, Equation 4.243 reduces to $0 < h < 4.4$ nm. This range of h values includes the range of thicknesses, where the hydration force is operative. In the experiments in Ref. [589], the hydration repulsion appears in the interval $0 < h < 3.71$ nm irrespective of the kind of counterion (Li^+ , Na^+ , or Cs^+). Note that in Figure 4.38 the data are plotted versus the total film thickness, h_t , which includes not only the water core, but also the two surfactant adsorption layers at the film surfaces.

As already mentioned, the electrostatic component of disjoining pressure can be defined as the excess osmotic pressure in the film midplane with respect to the bulk solution, see Equation 4.189. Hence, if all coions are expelled from the film, the expression for the disjoining pressure acquires the form [589]:

$$\Pi_{\text{el}} = kT a_{2\infty} (e^{\Phi_m} - 2) \quad (4.244)$$

For a given surface electric potential, Φ_s , Equations 4.242 and 4.244 determine the $\Pi(h)$ dependence in a parametric form: $h = h(\Phi_m)$ and $\Pi = \Pi(\Phi_m)$. As seen in Figure 4.38, excellent agreement between theory and experiment has been achieved for reasonable parameter values [589].

4.4.5.4.2 Hydrophobic Attraction

The water does not spread spontaneously on hydrocarbons and the aqueous films on hydrophobic surfaces are rather unstable [590]. The cause for these effects is an attractive *hydrophobic* force, which is found to appear in aqueous films in contact with hydrophobic surfaces. The experiments showed that the nature of the hydrophobic surface force is different from the van der Waals and double layer interactions [591–595]. The measurements indicate that the hydrophobic interaction decays exponentially with the increase of the film thickness, h . The hydrophobic free energy per unit area of the film can be described by means of the empirical equation [36]

$$f_{\text{hydrophobic}} = -2\gamma e^{-h/\lambda_0} \quad (4.245)$$

where typically $\gamma = 10\text{--}50$ mJ/m², and $\lambda_0 = 1\text{--}2$ nm in the range $0 < h < 10$ nm. Larger decay length, $\lambda_0 = 12\text{--}16$ nm, was reported by Christenson et al. [595] for the range $20 < h < 90$ nm. This long-range attraction could entirely dominate the van der Waals forces. Ducker et al. [596] measured the force between hydrophobic and hydrophilic silica particles and air bubbles by means of an atomic force microscope.

It was found experimentally that 1:1 and 2:2 electrolytes reduce considerably the long-range part of the hydrophobic attraction [594,595]. The results suggest that this reduction could be due to ion adsorption or ion exchange at the surfaces rather than to the presence of electrolyte in the solution itself. Therefore, the physical implication (which might seem trivial) is that the hydrophobic attraction across aqueous films can be suppressed by making the surfaces more hydrophilic. Besides, some special polar solutes are found to suppress the hydrophobic interaction at molecular level in the bulk solution, for example, urea, $(\text{NH}_2)_2\text{CO}$, dissolved in water can cause proteins to unfold. The polar solutes are believed to destroy the hydrogen-bond structuring in water; therefore they are sometimes called chaotropic agents [36].

There is no generally accepted explanation of the hydrophobic surface force. One of the possible explanations is that the hydrogen bonding in water (and other associated liquids) could be the main underlying factor [36,597]. The related qualitative picture of the hydrophobic interaction is the following. If there were no thermal motion, the water molecules would form an ice-like tetrahedral network with four nearest neighbors per molecule (instead of 12 neighbors at close packing), because this configuration is favored by the formation of hydrogen bonds. However, due to the

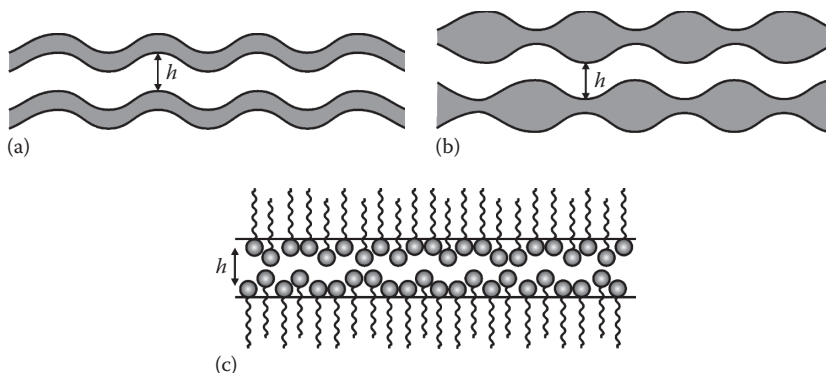


FIGURE 4.39 Surface forces due to configurational confinement of thermally excited modes into a narrow region of space between two approaching interfaces: (a) bending mode of membrane fluctuations giving rise to the undulation force; (b) squeezing mode of membrane fluctuations producing the peristaltic force; (c) fluctuating protrusion of adsorbed amphiphilic molecules engendering the protrusion surface force.

thermal motion a water molecule forms only about 3–3.5 transient hydrogen bonds with its neighbors in the liquid [598] with lifetime of a hydrogen bond being about 10^{-11} s. When a water molecule is brought in contact with a non-hydrogen-bonding molecule or surface, the number of its possible favorable configurations is decreased. This effect also reduces the number of advantageous configurations of the neighbors of the subsurface water molecules and some ordering propagates in the depth of the liquid. This ordering might be initiated by the orientation of the water dipoles at a water–air or water–hydrocarbon interface with the oxygen atom being oriented toward the hydrophobic phase [599–602]. Such ordering in the vicinity of the hydrophobic wall is entropically unfavorable. When two hydrophobic surfaces approach each other, the entropically unfavored water is ejected into the bulk, thereby reducing the total free energy of the system. The resulting attraction could in principle explain the hydrophobic forces. The existing phenomenological theory [597] has been generalized to the case of asymmetric films [603], and has been applied to interpret experimental data for breakage of emulsion and foam films at low surfactant and high electrolyte concentrations [604,605].

Another hypothesis for the physical origin of the hydrophobic force considers a possible role of formation of gaseous capillary bridges between the two hydrophobic surfaces (see Figure 4.13a) [36,606,607]. In this case, the hydrophobic force would be a kind of capillary-bridge force; see Chapter 11 in Ref. [37]. Such bridges could appear spontaneously, by nucleation (spontaneous dewetting), when the distance between the two surfaces becomes smaller than a certain threshold value, of the order of several hundred nanometers. Gaseous bridges could appear even if there is no dissolved gas in the water phase; the pressure inside a bridge can be as low as the equilibrium vapor pressure of water (e.g., $P_0 = 2337$ Pa at 20°C , which is only 2.3% of the atmospheric pressure) owing to the high interfacial curvature of the nodoid-shaped bridges; see Section 4.3.1.2.3 and Ref. [37].

For example, at air–water–solid contact angle $\theta = 90^\circ$ – 110° the maximal length of a nodoid-shaped capillary bridge, h_{\max} , can be estimated from the analytical asymptotic formula [37,312]:

$$h_{\max} = \frac{-2\sigma \cos \theta}{P - P_0} \quad (90^\circ < \theta < 110^\circ) \quad (4.246)$$

Substituting $P = 1$ atm for the outer pressure, $P_0 = 2337$ Pa for the inner pressure (the equilibrium vapor pressure of water at 20°C), $\sigma = 72.75$ mN/m for the surface tension of water, and $\theta = 94^\circ$, from Equation 4.246 we calculate $h_{\max} = 103$ nm for a vapor-filled bridge between two parallel

hydrophobic plates in water. This value of h_{\max} is close to the distances at which the experimentally observed long-range hydrophobic attraction begins to operate. A number of studies [608–616] provide evidence in support of the capillary-bridge origin of the long-range hydrophobic surface force. In particular, the observation of “steps” in the experimental data was interpreted as an indication for separate acts of bridge nucleation [612].

As discussed in Ref. [617], at present, the accumulated experimental data indicate for the existence of three different force-law regimes of the hydrophobic surface force. At film thickness $h \leq 1\text{--}1.5$ nm, a pure *short-range* hydrophobic force is operative, which is probably related to water structuring effects and hydrogen bonds at the water–hydrophobic interface. At intermediate distances, $1.5 < h < 15$ nm, a *long-range* hydrophobic force is acting, which is possibly due to an enhanced Hamaker constant associated with the “proton-hopping” polarizability of water. Finally, at $h > 15$ nm a *super-long-range* attraction is observed, which could be due to gaseous capillary bridges (bridging cavities) or to the electrostatic patch-charge attraction [618].

4.4.5.5 Fluctuation Wave Forces

All fluid interfaces, including liquid membranes and surfactant lamellas, are involved in a thermal fluctuation wave motion. The configurational confinement of such thermally excited modes within the narrow space between two approaching interfaces gives rise to short-range repulsive surface forces, which are considered in the following section.

4.4.5.5.1 Undulation Forces

The undulation force arises from the configurational confinement related to the *bending mode* of deformation of two fluid bilayers. This mode consists in undulation of the bilayer at constant bilayer area and thickness (Figure 4.39a). Helfrich et al. [619,620] established that two such bilayers, apart at a mean distance h , experience a repulsive disjoining pressure given by the expression:

$$\Pi_{\text{und}}(h) = \frac{3\pi^2(kT)^2}{64k_i h^3} \quad (4.247)$$

where k_i is the bending elastic modulus of the bilayer as a whole. The experiment [621] and the theory [37,204] show that k_i is of the order of 10^{-19} J for lipid bilayers. The undulation force has been measured, and the dependence $\Pi_{\text{und}} \propto h^{-3}$ was confirmed experimentally [622–624].

4.4.5.5.2 Peristaltic Force

The peristaltic force [625] originates from the configurational confinement related to the peristaltic (squeezing) mode of deformation of a fluid bilayer (Figure 4.39b). This mode of deformation consists in fluctuation of the bilayer thickness at fixed position of the bilayer midsurface. The peristaltic deformation is accompanied with extension of the bilayer surfaces. Israelachvili and Wennerström [625] demonstrated that the peristaltic disjoining pressure is related to the stretching modulus, k_s , of the bilayer:

$$\Pi_{\text{per}}(h) \approx \frac{2(kT)^2}{\pi^2 k_s h^5} \quad (4.248)$$

The experiment [626] gives values of k_s varying between 135 and 500 mN/m, which depend on temperature and composition of the lipid membrane.

4.4.5.5.3 Protrusion Force

Due to the thermal motion, the protrusion of an amphiphilic molecule in an adsorption monolayer (or micelle) may fluctuate about the equilibrium position of the molecule (Figure 4.39c). In other

words, the adsorbed molecules are involved in a discrete wave motion, which differs from the continuous modes of deformation considered earlier. Aniansson et al. [627,628] analyzed the energy of protrusion in relation to the micelle kinetics. They assumed the energy of molecular protrusion to be of the form $u(z) = \alpha z$, where z is the distance out of the surface ($z > 0$) and determined $\alpha \approx 3 \times 10^{-11}$ J/m for single-chained surfactants. The average length of the Brownian protrusion of the amphiphilic molecules is on the order of $\lambda \equiv kT/\alpha$ [625].

By using a mean-field approach, Israelachvili and Wennerström [625] derived the following expression for the protrusion disjoining pressure which appears when two protrusion zones overlap (Figure 4.39c):

$$\Pi_{\text{protr}}(h) = \frac{\Gamma kT}{\lambda} \frac{(h/\lambda) \exp(-h/\lambda)}{1 - (1 + h/\lambda) \exp(-h/\lambda)} \quad (4.249)$$

where

λ is the characteristic protrusion length; $\lambda = 0.14$ nm at 25°C for surfactants with paraffin chain

Γ denotes the number of protrusion sites per unit area

Note that Π_{protr} decays exponentially for $h \gg \lambda$, but $\Pi_{\text{protr}} \propto h^{-1}$ for $h < \lambda$, that is, Π_{protr} is divergent at $h \rightarrow 0$. The respective interaction free energy (per unit film area) is

$$f_{\text{protr}} = \int_h^{\infty} \Pi_{\text{protr}}(\hat{h}) d\hat{h} = -\Gamma kT \ln \left[1 - \left(1 + \frac{h}{\lambda} \right) \exp\left(\frac{-h}{\lambda}\right) \right] \quad (4.250)$$

Equation 4.249 was found to fit well experimental data for the disjoining pressure of liquid films stabilized by adsorbed protein molecules: bovine serum albumin (BSA) [629]. In that case, Γ was identified with the surface density of the loose secondary protein adsorption layer, while λ turned out to be about the size of the BSA molecule. A more detailed statistical approach to the theoretical modeling of protrusion force was proposed [630].

4.5 HYDRODYNAMIC INTERACTIONS IN DISPERSIONS

4.5.1 BASIC EQUATIONS AND LUBRICATION APPROXIMATION

In addition to the surface forces (see Section 4.4), two colliding particles in a liquid medium also experience hydrodynamic interactions due to the viscous friction, which can be rather long range (operative even at distances above 100 nm). The hydrodynamic interaction among particles depends on both the type of fluid motion and the type of interfaces. The quantitative description of this interaction is based on the classical laws of mass conservation and momentum balance for the bulk phases [630–636]:

$$\frac{\partial \rho}{\partial t} + \text{div}(\rho \mathbf{v}) = 0 \quad (4.251)$$

$$\frac{\partial}{\partial t}(\rho \mathbf{v}) + \text{div}(\rho \mathbf{v} \mathbf{v} - \mathbf{P} - \mathbf{P}_b) = 0 \quad (4.252)$$

where

ρ is the mass density

\mathbf{v} is the local mass average velocity

\mathbf{P} is the hydrodynamic stress tensor

\mathbf{P}_b is the body-force tensor which accounts for the action of body forces such as gravity, electrostatic forces (the Maxwell tensor), etc.

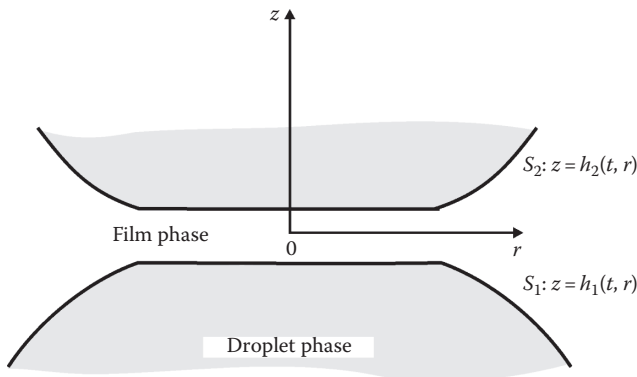


FIGURE 4.40 Sketch of a plane-parallel film formed between two identical fluid particles.

In a fluid at rest, and in the absence of body forces, the only contact force given by the hydrodynamic stress tensor is the scalar thermodynamic pressure, p , and \mathbf{P} can be written as $\mathbf{P} = -p\mathbf{I}$, where \mathbf{I} is the unit tensor in space. For a fluid in motion, the viscous forces become operative and

$$\mathbf{P} = -p\mathbf{I} + \mathbf{T} \quad (4.253)$$

where \mathbf{T} is the viscous stress tensor. From the definition of the stress tensor (Equation 4.253), it follows that the resultant hydrodynamic force, \mathbf{F} , exerted by the surrounding fluid on the particle surface, S , and the torque, \mathbf{M} , applied to it are given by the expressions [631,633]

$$\mathbf{F} = \int_S \mathbf{P} \cdot \mathbf{n} dS, \quad \mathbf{M} = \int_S \mathbf{r}_0 \times \mathbf{P} \cdot \mathbf{n} dS \quad (4.254)$$

where

\mathbf{r}_0 is the position vector of a point of S with respect to an arbitrarily chosen coordinate origin

\mathbf{n} is the vector of the running unit normal to the surface S

In the presence of body forces, the total force, \mathbf{F}_{tot} , and torque, \mathbf{M}_{tot} , acting on the particle surface are

$$\mathbf{F}_{\text{tot}} = \mathbf{F} + \int_S \mathbf{P}_b \cdot \mathbf{n} dS, \quad \mathbf{M}_{\text{tot}} = \mathbf{M} + \int_S \mathbf{r}_0 \times \mathbf{P}_b \cdot \mathbf{n} dS \quad (4.255)$$

The dependence of the viscous stress on the velocity gradient in the fluid is a constitutive law, which is usually called the bulk rheological equation. The general linear relation between the viscous stress tensor, \mathbf{T} , and the rate of strain tensor,

$$\mathbf{D} = \frac{1}{2} [\nabla \mathbf{v} + (\nabla \mathbf{v})^T] \quad (4.256)$$

(the superscript T denotes conjugation) reads

$$\mathbf{T} = \zeta(\text{div } \mathbf{v})\mathbf{I} + 2\eta \left[\mathbf{D} - \frac{1}{3}(\text{div } \mathbf{v})\mathbf{I} \right] \quad (4.257)$$

The latter equation is usually referred to as the Newtonian model or Newton's law of viscosity. In Equation 4.257, ζ is the dilatational bulk viscosity and η is the shear bulk viscosity. The usual liquids comply well with the Newtonian model. On the other hand, some concentrated macromolecular solutions, colloidal dispersions, gels, etc., may exhibit non-Newtonian behavior; their properties are considered in detail in some recent review articles and books [636–641]. From Equations 4.252 and 4.257, one obtains the Navier–Stokes equation [642,643]:

$$\rho \frac{d\mathbf{v}}{dt} = -\nabla p + \left(\zeta + \frac{1}{3} \eta \right) \nabla(\nabla \cdot \mathbf{v}) + \eta \nabla^2 \mathbf{v} + \mathbf{f}, \quad (\mathbf{f} \equiv \nabla \cdot \mathbf{P}_b) \quad (4.258)$$

for homogeneous Newtonian fluids, for which the dilatational and shear viscosities, ζ and η , do not depend on the spatial coordinates. In Equation 4.258, the material derivative d/dt can be presented as a sum of a local time derivative and a convective term:

$$\frac{d}{dt} = \frac{\partial}{\partial t} + (\mathbf{v} \cdot \nabla) \quad (4.259)$$

If the density, ρ , is constant, the equation of mass conservation (Equation 4.251) and the Navier–Stokes equation 4.258 reduce to

$$\text{div } \mathbf{v} = 0, \quad \rho \frac{d\mathbf{v}}{dt} = -\nabla p + \eta \nabla^2 \mathbf{v} + \mathbf{f} \quad (4.260)$$

For low shear stresses in the dispersions, the characteristic velocity, V_z , of the relative particle motion is small enough in order for the Reynolds number, $\text{Re} = \rho V_z L / \eta$, to be a small parameter, where L is a characteristic length scale. In this case, the inertia terms in Equations 4.258 and 4.260 can be neglected. Then, the system of equations becomes linear and the different types of hydrodynamic motion become additive [404,644,645]; for example, the motion in the liquid flow can be presented as a superposition of elementary translation and rotational motions.

The basic equations can be further simplified in the framework of the lubrication approximation, which can be applied to the case when the Reynolds number is small and when the distances between the particle surfaces are much smaller than their radii of curvature (Figure 4.40) [646,647]. There are two ways to take into account the molecular interactions between the two particles across the liquid film intervening between them: (1) the body force approach and (2) the disjoining pressure approach. The former approach treats the molecular forces as components of the body force, \mathbf{f} (Equation 4.258); consequently, they give contributions to the normal and tangential stress boundary conditions [648,649]. In the case (2), the molecular interactions are incorporated only in the normal stress boundary conditions at the particle surfaces. When the body force can be expressed as a gradient of potential, $\mathbf{f} = \nabla U$ (that is $\mathbf{P}_b = \mathbf{U}\mathbf{I}$), the two approaches are equivalent [650].

If two particles are interacting across an electrolyte solution, the equations of continuity and the momentum balance, Equation 4.260, in lubrication approximation read [651,652]

$$\begin{aligned} \nabla_{\parallel} \cdot \mathbf{v}_{\parallel} + \frac{\partial v_z}{\partial z} = 0, \quad \eta \frac{\partial^2 v_{\parallel}}{\partial z^2} = \nabla_{\parallel} \cdot p + kT \sum_{i=1}^N z_i c_i \nabla_{\parallel} \Phi \\ \frac{\partial p}{\partial z} + kT \sum_{i=1}^N z_i c_i \frac{\partial \Phi}{\partial z} = 0 \end{aligned} \quad (4.261)$$

where

\mathbf{v}_{II} and ∇_{II} are the projection of the velocity and the gradient operator on the plane xy ; the z -axis is (approximately) perpendicular to the film surfaces S_1 and S_2 (see Figure 4.40)

$c_i = c_i(r, z, t)$ is the ion concentration ($i = 1, 2, \dots, N$)

Φ is the dimensionless electric potential (see Sections 4.2.1.2 and 4.2.2)

It turns out that in lubrication approximation, the dependence of the ionic concentrations on the z coordinate comes through the electric potential $\Phi(r, z, t)$: we obtain a counterpart of the Boltzmann equation $c_i = c_{i,n}(r, z, t)\exp(-z_i\Phi)$, where $c_{i,n}$ refers to an imaginary situation of “switched off” electric charges ($\Phi \equiv 0$). The kinematic boundary condition for the film surfaces has the form:

$$\frac{\partial h_j}{\partial t} + \mathbf{u}_j \cdot \nabla_{\text{II}} h_j = (v_z)_j \quad \text{at } S_j (j = 1, 2) \quad (4.262)$$

where

\mathbf{u}_i is the velocity projection in the plane xy at the corresponding film surface S_i , which is close to the interfacial velocity

$(v_z)_i$ is the z component of the velocity at the surface S_i

The general solution of Equations 4.261 and 4.262 could be written as:

$$p = p_n + kT \sum_{i=1}^N (c_i - c_{i,n}) \quad (4.263)$$

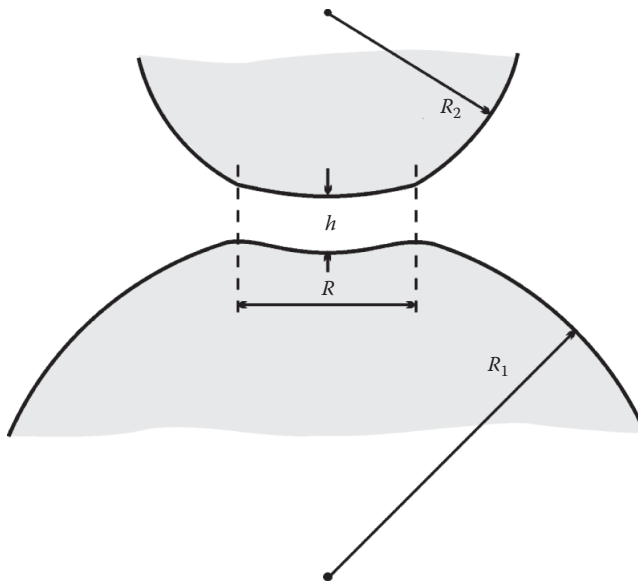


FIGURE 4.41 Sketch of a film between two nonidentical fluid particles of radii R_1 and R_2 . The film thickness and radius are denoted by h and R .

$$\begin{aligned} \mathbf{v}_{\parallel} = & \frac{(z-h_1)(z-h_2)}{2\eta} \nabla_{\parallel} p_n + \frac{h_2-z}{h} \mathbf{u}_1 + \frac{z-h_1}{h} \mathbf{u}_2 \\ & + \frac{kTh^2}{4\eta} \sum_{i=1}^N \left[m_{2,i}(z) - \frac{h_2-z}{h} m_{2,i}(h_1) - \frac{z-h_1}{h} m_{2,i}(h_2) \right] \nabla_{\parallel} c_{i,n} \end{aligned} \quad (4.264)$$

Here $h = h_2 - h_1$ is the local film thickness; the meaning of $p_n(x, y, t)$ is analogous to that of $c_{i,n}(x, y, t)$; the functions, $m_{k,i}(z)$, account for the distribution of the i th ionic species in the EDL:

$$\begin{aligned} m_{0,i} & \equiv \exp(-z_i\Phi) - 1 \\ m_{k,i}(z) & \equiv \frac{2}{h} \int_0^z m_{k-1,i}(\hat{z}) d\hat{z} \quad (k = 1, 2, 3, i = 1, 2, \dots, N) \end{aligned} \quad (4.265)$$

The equation determining the local thickness, h , of a film with fluid surfaces (or, alternatively, determining the pressure distribution at the surfaces of the gap between two solid particles of known shape) is

$$\begin{aligned} \frac{\partial h}{\partial t} + \nabla_{\parallel} \cdot \left[\frac{h}{2} (\mathbf{u}_1 + \mathbf{u}_2) \right] & = \frac{1}{12\eta} \nabla_{\parallel} \cdot (h^3 \nabla_{\parallel} p) \\ & + \frac{kT}{8\eta} \nabla_{\parallel} \cdot \left\{ h^3 \sum_{i=1}^N [m_{2,i}(h_1) + m_{2,i}(h_2) - m_{3,i}(h_2) + m_{3,i}(h_1)] \nabla_{\parallel} c_{i,n} \right\} \end{aligned} \quad (4.266)$$

The problem for the interactions upon central collisions of two axisymmetric particles (bubbles, droplets, or solid spheres) at small surface-to-surface distances was first solved by Reynolds [646] and Taylor [653,654] for solid surfaces and by Ivanov et al. [655,656] for films of uneven thickness. Equation 4.266 is referred to as the general equation for films with deformable surfaces [655,656] (see also the more recent reviews [240,657,658]). The asymptotic analysis [659–661] of the dependence of the drag and torque coefficient of a sphere, which is translating and rotating in the neighborhood of a solid plate, is also based on Equation 4.266 applied to the special case of stationary conditions.

Using Equation 4.255, one can obtain expressions for the components of the total force exerted on the particle surface, S , in the lubrication approximation:

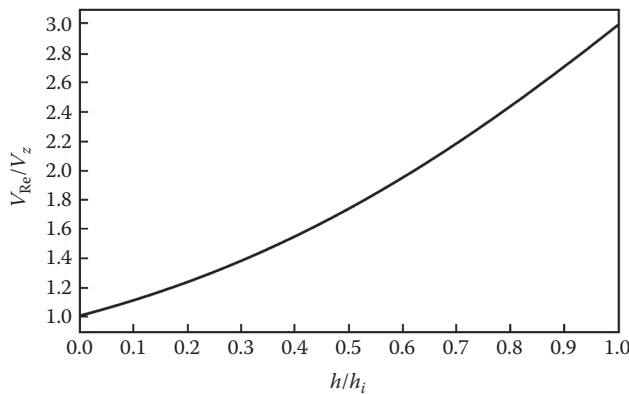


FIGURE 4.42 Plot of V_{Re}/V_z vs. h/h_i for two fluid particles (Equation 4.270) which are deformed because of the viscous friction in the transition zone between the film and the bulk phase (see Figure 4.41).

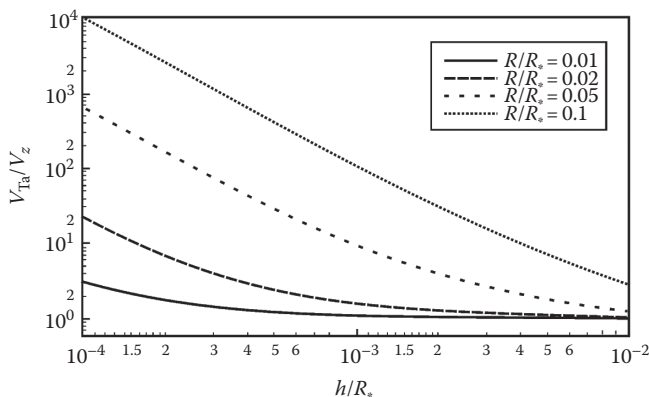


FIGURE 4.43 Plot of V_{Ta}/V_z vs. h/R_* for various values of the dimensionless film radius, R/R_* . V_{Ta} corresponds to two nondeformed (spherical) particles (Equation 4.271), whereas V_z is the velocity of approach of two deformed particles (Equation 4.270).

$$F_{\text{tot},z} = \int_S \left[p_n + kT \sum_{i=1}^N (c_{is} - c_{i,n}) + \Pi_{\text{nel}} - p_\infty \right] dS \quad (4.267)$$

$$\mathbf{F}_{\text{tot},\Pi} = - \int_S \left(\eta \frac{\partial \mathbf{v}_\Pi}{\partial z} + \frac{2kT}{\kappa_c^2} \frac{\partial \Phi}{\partial z} \nabla_\Pi \Phi \right) dS \quad (4.268)$$

where

p_∞ is the pressure at infinity in the meniscus region (Figure 4.40)

$\Pi_{\text{nel}} \equiv \Pi - \Pi_{\text{el}}$ accounts for the contribution of nonelectrostatic (non-double-layer) forces to the disjoining pressure (see Section 4.4)

The normal and the lateral force resultants, F_z and \mathbf{F}_Π , are the hydrodynamic resistance and shear force, respectively.

4.5.2 INTERACTION BETWEEN PARTICLES OF TANGENTIALLY IMMOBILE SURFACES

The surfaces of fluid particles can be treated as tangentially immobile when they are covered by dense surfactant adsorption monolayers that can resist tangential stresses [240,657,658,662,663]. In such a case, the bubbles or droplets behave as flexible balls with immobile surfaces. When the fluid particles are rather small (say, microemulsion droplets), they can behave like hard spheres; therefore, some relations considered in the following section, which were originally derived for solid particles, can also be applied to fluid particles.

4.5.2.1 Taylor and Reynolds Equations, and Influence of the Particle Shape

In the case of two axisymmetric particles moving along the z -axis toward each other with velocity $V_z = -dh/dt$, Equation 4.266 can be integrated; and from Equation 4.267, the resistance force can be calculated. The latter turns out to be proportional to the velocity and bulk viscosity and depends on the shape in a complex way. For particles with tangentially immobile surfaces and without surface electric charge ($\mathbf{u}_1 = \mathbf{u}_2 = 0$, $\Phi = 0$) Charles and Mason [664] have derived

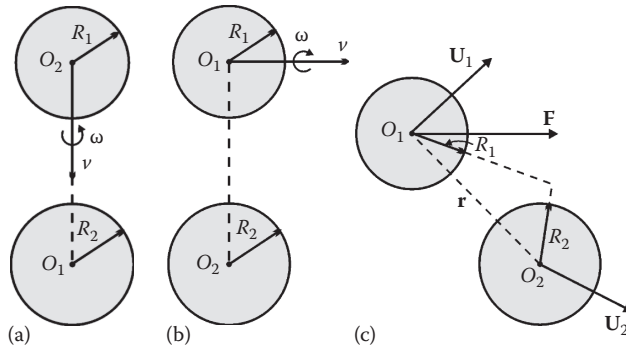


FIGURE 4.44 Types of hydrodynamic interactions between two spherical particles: (a) motion along and rotation around the line of centers; (b) motion along and rotation around an axis perpendicular to the line of centers; (c) the first particle moves under the action of an applied external force, F , whereas the second particle is subjected to the hydrodynamic disturbance created by the motion of the first particle.

$$F_z = 6\pi\eta V_z \int_0^\infty \frac{r^3}{h^3} dr \tag{4.269}$$

where r is the radial coordinate in a cylindrical coordinate system. In the case of two particles of different radii, R_1 and R_2 , film radius R , and uniform film thickness h (see Figure 4.41), from Equation 4.269 the following expression can be derived [665,666]:

$$F_z = \frac{3}{2} \pi\eta V_z \frac{R_*^2}{h} \left(1 + \frac{R^2}{hR_*} + \frac{R^4}{h^2 R_*^2} \right), \quad R_* \equiv \frac{2R_1 R_2}{R_1 + R_2} \tag{4.270}$$

This geometrical configuration has proved to be very close to the real one in the presence of electrostatic disjoining pressure [256]. The Charles–Mason formula (Equation 4.269) and Equation 4.267 have been used to calculate the velocity of film thinning for a large number of cases, summarized by Hartland [667] in tables for more than 50 cases (2D and 3D small drops, fully deformed large drops subjected to large forces, 2D hexagonal drops, etc.).

Setting $R = 0$ in Equation 4.270, we can derive a generalized version of the Taylor formula [653,654] for the velocity of approach of two nondeformable spheres under the action of an external (nonviscous) force, F_z [666]:

$$V_{Ta} = \frac{2hF_z}{3\pi\eta R_*^2} \tag{4.271}$$

When a solid sphere of radius R_c approaches a flat solid surface, we may use the Taylor formula with $R_* = 2R_c$ when the gap between the two surfaces is small compared to R_c . In fact Equation 4.271 does not appear in any of the G.I. Taylor’s publications but it was published in the article by Hardy and Bircumshaw [653] (see Ref. [654]).

In the case when two plane-parallel ellipsoidal discs of tangentially immobile surfaces are moving against each other under the action of an external force, $F_{tot,z}$, from Equations 4.266 and 4.267, we can derive the Reynolds equation [646] for the velocity of film thinning:

$$V_{\text{Re}} = \frac{F_z h^3 (a^2 + b^2)}{3\pi\eta a^3 b^3} \quad (4.272)$$

where a and b are the principal radii of curvature. If there is a contribution of the disjoining pressure, Π , the Reynolds equation for a flat axisymmetrical film ($a = b = R$) between two fluid particles of capillary pressure P_c can be written in the form [216]:

$$V_{\text{Re}} = \frac{2F_z h^3}{3\pi\eta R^4} = \frac{2(P_c - \Pi)h^3}{3\eta R^2} \quad (4.273)$$

From Equations 4.270 and 4.273, the ratio between the Reynolds velocity and the velocity of film thinning for a given force is obtained. In Figure 4.42, this ratio is plotted as a function of the film thickness, h , divided by inversion thickness, $h_i = R^2/R_*$ [657]. We see that the influence of the viscous friction in the zone encircling the film (this influence is not accounted for in Equation 4.273) decreases the velocity of thinning about three times for the larger distances, whereas for the small distances this influence vanishes. From Equations 4.270 and 4.271, the ratio between the Taylor velocity (corresponding to nondeformable spheres) and the approaching velocity of two deformable particles can be calculated. The dependence of this ratio on the distance between the particles for different film radii is illustrated in Figure 4.43. We see that an increase of the film radius, R , and a decrease of the distance, h , lead to a decrease in the velocity. The existence of a film between the particles can decrease the velocity of particle approach, V_{z^*} , by several orders of magnitude.

4.5.2.2 Interactions among Nondeformable Particles at Large Distances

The hydrodynamic interaction between members of a group of small particles suspended in a viscous fluid has fundamental importance for the development of adequate models for calculating the particle collective diffusion coefficient and the effective viscosity of suspension [404,644,664,668,669]. The Stokesian resistance is determined for a number of specific particle shapes under the condition that the particles are located so far apart that the hydrodynamic interactions can be ignored [644].

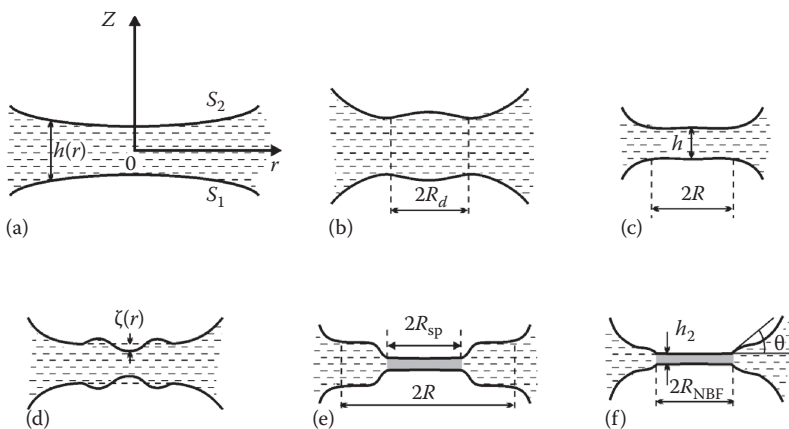


FIGURE 4.45 Main stages of formation and evolution of a thin liquid film between two bubbles or drops: (a) mutual approach of slightly deformed surfaces; (b) at a given separation, the curvature at the center inverts its sign and a dimple arises; (c) the dimple disappears, and eventually an almost plane-parallel film forms; (d) due to thermal fluctuations or other disturbances the film either ruptures or transforms into a thinner Newton black film (e), which expands until reaching the final equilibrium state (f).

A general theory applicable to a single particle of arbitrary shape has been developed by Brenner [670,671]. This method gives the first-order correction (with respect to the particle volume fraction) of the viscosity and diffusivity. Matrix relations between resistance and velocity for the pure translational and rotational motions of the members of a general multiparticle system involved in a linear shear flow are given by Brenner and O'Neill [672]. In principle, from these relations we can further obtain the higher-order terms in the series expansion of viscosity and diffusivity with respect to the powers of the particle volume fraction.

At present, the only multiparticle system for which exact values of the resistance tensors can be determined is that of two spheres. It turns out that all types of hydrodynamic flows related to the motion of two spherical particles (of radii R_1 and R_2) can be expressed as superpositions of the elementary processes depicted in Figure 4.44 [404,633,644,645,673–682].

The first particle moves toward the second immobile particle and rotates around the line of centers (see Figure 4.44a). This is an axisymmetric rotation problem (a 2D hydrodynamic problem) which was solved by Jeffery [674] and Stimson and Jeffery [675] for two identical spheres moving with equal velocities along their line of centers. Cooley and O'Neill [676,677] calculated the forces for two nonidentical spheres moving with the same speed in the same direction, or alternatively, moving toward each other. A combination of these results permits evaluation of the total forces and torques acting on the particles.

The first particle then moves along an axis perpendicular to the center line and rotates around this axis, whereas the second particle is immobile; see Figure 4.44b (this is a typical 3D hydrodynamic problem). The contribution of this asymmetric motion of the spheres to the resistance tensors was determined by Davis [678] and O'Neill and Majumdar [679].

The first particle moves with linear velocity, \mathbf{U}_1 , under the action of an applied external force, \mathbf{F} , whereas the second particle is subjected to the hydrodynamic disturbances (created by the motion of the first particle) and moves with a linear velocity, \mathbf{U}_2 (see Figure 4.44c). As a rule, this is a 3D hydrodynamic problem. For this case, Batchelor [683] and Batchelor and Wen [684] have derived the following expressions for the instantaneous translational velocities of the two particles in an otherwise quiescent and unbounded fluid:

$$\mathbf{U}_1 = \frac{\mathbf{F}}{6\pi\eta R_1} \cdot \left[A_{11}(r) \frac{\mathbf{r}\mathbf{r}}{r^2} + B_{11}(r) \left(\mathbf{I} - \frac{\mathbf{r}\mathbf{r}}{r^2} \right) \right] \quad (4.274)$$

$$\mathbf{U}_2 = \frac{\mathbf{F}}{6\pi\eta(R_1 + R_2)} \cdot \left[A_{12}(r) \frac{\mathbf{r}\mathbf{r}}{r^2} + B_{12}(r) \left(\mathbf{I} - \frac{\mathbf{r}\mathbf{r}}{r^2} \right) \right] \quad (4.275)$$

where \mathbf{r} is the vector connecting the particle centers and $r = |\mathbf{r}|$. Expressions for the mobility functions A_{ij} and B_{ij} ($i, j = 1, 2$) at large values of the dimensionless distance $s = 2r/(R_1 + R_2)$ and comparable particle radii $\lambda = R_2/R_1 = O(1)$ have been derived by Jeffrey and Onishi [685] and Davis and Hill [682]. The derived far-field expansions are

$$1 - B_{11} = \frac{68\lambda^5}{(1+\lambda)^6 s^6} + \frac{32\lambda^3(10-9\lambda^2+9\lambda^4)}{(1+\lambda)^8 s^8} + \frac{192\lambda^5(35-18\lambda^2+6\lambda^4)}{(1+\lambda)^{10} s^{10}} + O(s^{-12})$$

$$B_{11} - A_{11} = \frac{60\lambda^3}{(1+\lambda)^4 s^4} - \frac{60\lambda^3(8-\lambda^2)}{(1+\lambda)^6 s^6} + \frac{32\lambda^3(20-123\lambda^2+9\lambda^4)}{(1+\lambda)^8 s^8}$$

$$+ \frac{64\lambda^2(175+1500\lambda-426\lambda^2+18\lambda^4)}{(1+\lambda)^{10} s^{10}} + O(s^{-12})$$

$$\begin{aligned}
A_{11} - \frac{2A_{12}}{1+\lambda} = & 1 - \frac{3}{(1+\lambda)s} + \frac{4(1+\lambda^2)}{(1+\lambda)^3 s^3} - \frac{60\lambda^3}{(1+\lambda)^4 s^4} + \frac{32\lambda^3(15-4\lambda^2)}{(1+\lambda)^6 s^6} - \frac{2400\lambda^3}{(1+\lambda)^7 s^7} \\
& - \frac{192\lambda^3(5-22\lambda^2+3\lambda^4)}{(1+\lambda)^8 s^8} + \frac{1920\lambda^3(1+\lambda^2)}{(1+\lambda)^9 s^9} - \frac{256\lambda^5(70-375\lambda-120\lambda^2+9\lambda^3)}{(1+\lambda)^{10} s^{10}} \\
& - \frac{1536\lambda^3(10-151\lambda^2+10\lambda^4)}{(1+\lambda)^{11} s^{11}} + O(s^{-12})
\end{aligned} \tag{4.276}$$

$$\begin{aligned}
B_{11} - \frac{2B_{12}}{1+\lambda} = & 1 - \frac{3}{2(1+\lambda)s} - \frac{2(1+\lambda^2)}{(1+\lambda)^3 s^3} - \frac{68\lambda^5}{(1+\lambda)^6 s^6} - \frac{32\lambda^3(10-9\lambda^2+9\lambda^4)}{(1+\lambda)^8 s^8} \\
& - \frac{192\lambda^5(35-18\lambda^2+6\lambda^4)}{(1+\lambda)^{10} s^{10}} - \frac{16\lambda^3(560-553\lambda^2+560\lambda^4)}{(1+\lambda)^{11} s^{11}} + O(s^{-12})
\end{aligned}$$

In the case of a small heavy sphere falling through a suspension of large particles (fixed in space), we have $\lambda \gg 1$; the respective expansions, corresponding to Equation 4.276, were obtained by Fuentes et al. [686]. In the opposite case, when $\lambda \ll 1$, the suspension of small background spheres will reduce the mean velocity of a large heavy particle (as compared with its Stokes velocity [687]) because the suspension behaves as an effective fluid of larger viscosity as predicted by the Einstein viscosity formula [683,686].

4.5.2.3 Stages of Thinning of a Liquid Film

Experimental and theoretical investigations [238,246,657,658,663,688,689] show that during the approach of two fluid colloidal particles, a flat liquid film can appear between their closest regions (see Figure 4.32). The hydrodynamic interactions as well as the buoyancy, the Brownian, electrostatic, van der Waals, and steric forces and other interactions can be involved in film formation [207,256,665,690,691]. The formation and the evolution of a foam or emulsion film usually follow the stages shown in Figure 4.45.

Under the action of an outer driving force, the fluid particles approach each other. The hydrodynamic interaction is stronger at the front zones and leads to a weak deformation of the interfaces in this front region. In this case, the usual hydrodynamic capillary number, $Ca = \eta V_z / \sigma$, which is a small parameter for nondeformable surfaces, should be modified to read $Ca = \eta V_z R_* / \sigma h$, where the distance, h , between the interfaces is taken into account. The shape of the gap between two drops for different characteristic times was calculated numerically by many authors [691–711]. Experimental investigation of these effects for symmetric and asymmetric drainage of foam films were carried out by Joye et al. [700,701]. In some special cases, the deformation of the fluid particle can be very fast: for example, the bursting of a small air bubble at an air–water interface is accompanied by a complex motion resulting in the production of a high-speed liquid jet (see Boulton-Stone and Blake [711]).

When a certain small separation, h_i , the inversion thickness, is reached, the sign of the curvature in the contact of the fluid particles (drops, bubbles) changes. A concave lens-shaped formation called a *dimple* is formed (see Frankel and Mysels [712]). This stage is also observed for asymmetric films [701]. A number of theoretical studies have described the development of a dimple at the initial stage of film thinning [691–711,713]. The inversion thickness can be calculated from a simple equation in which the van der Waals interaction is explicitly taken into account (see Section 4.4.2) [240,656,691]

$$h_i = \frac{F_z(\sigma_1 + \sigma_2)}{4\pi\sigma_1\sigma_2} \left(1 - \frac{A_H R_*}{12F_z h_i} \right) \quad (4.277)$$

where

σ_1 and σ_2 are the interfacial tensions of the phase boundaries S_1 and S_2
 in this case F_z is the external force (of nonviscous and non-van der Waals origin) experienced by
 the approaching particles
 A_H is the Hamaker constant

In the case, when the van der Waals force is negligible, Equation 4.277 reduces to $h_i = F_z(\sigma_1 + \sigma_2)/(4\pi\sigma_1\sigma_2)$ [240,656]. Danov et al. [665] have shown that in the case of Brownian flocculation of identical small droplets, h_i obeys the following transcendental equation:

$$h_i = \frac{kT}{2\pi\sigma z_i} \left\{ \int_0^{z_i} \left(\frac{z_i}{z} \right)^2 \frac{\gamma(z)}{\gamma(z_i)} \exp \left[\frac{U(z) - U(z_i)}{kT} \right] \frac{dz}{z_i} \right\}^{-1} \quad (4.278)$$

where

kT is the thermal energy
 $\gamma(z) = F_z/V_z$ is the hydrodynamic resistance given by Equation 4.270
 U is the potential energy due to the surface forces (see Equation 4.175)
 z is the distance between the droplet mass centers

These authors pointed out that with an increase of droplet size the role of the Brownian force in the film formation decreases, but for micrometer-sized liquid droplets the Brownian force is still by several orders of magnitude greater than the buoyancy force due to gravity. If the driving force is large enough, so that it is able to overcome the energy barrier created by the electrostatic repulsion and/or the increase of the surface area during the droplet deformation, then film with a dimple will be formed. On the contrary, at low electrolyte concentration (i.e., strong electrostatic repulsion) such

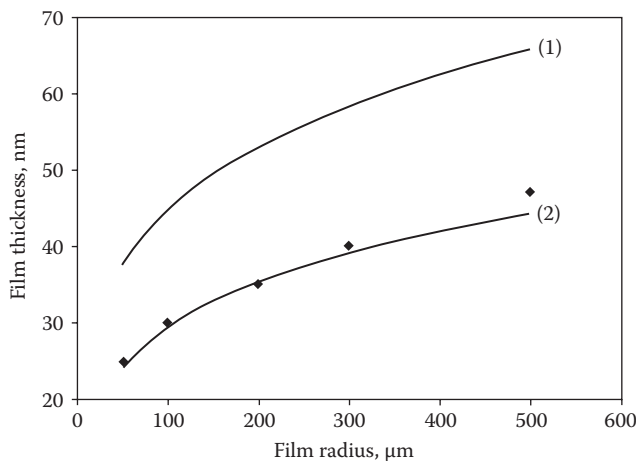


FIGURE 4.46 Dependence of the critical thickness, h_{cr} , on the radius, R , of foam films. (The experimental points are data from Manev, E.D. et al., *J. Colloid Interface Sci.*, 97, 591, 1984.) The films are formed from a solution of 4.3×10^{-4} M SDS + 0.25 M NaCl. Curve 1 is the prediction of the simplified theory [720], whereas Curve 2 is calculated using Equations 4.281 through 4.283; no adjustable parameters.

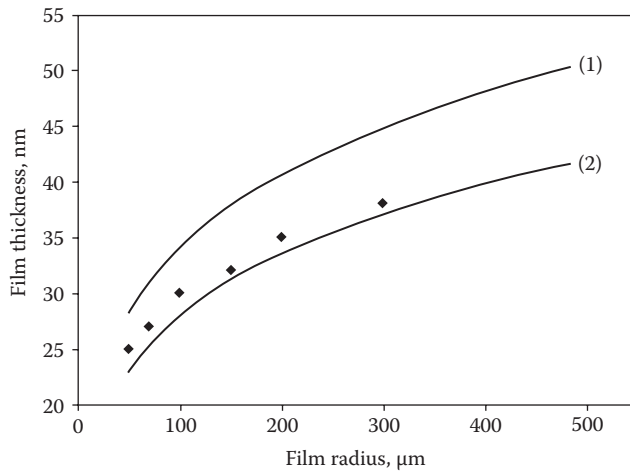


FIGURE 4.47 Critical thickness, h_{cr} , vs. radius, R , of emulsion films, toluene–water–toluene. The experimental points are data from Ref. [722]; the films are formed from a solution of 4.3×10^{-4} M SDS + 0.1 M NaCl. Curve 1 is the prediction of the simplified theory [720], whereas Curve 2 is calculated using Equations 5.281 through 5.283; no adjustable parameters.

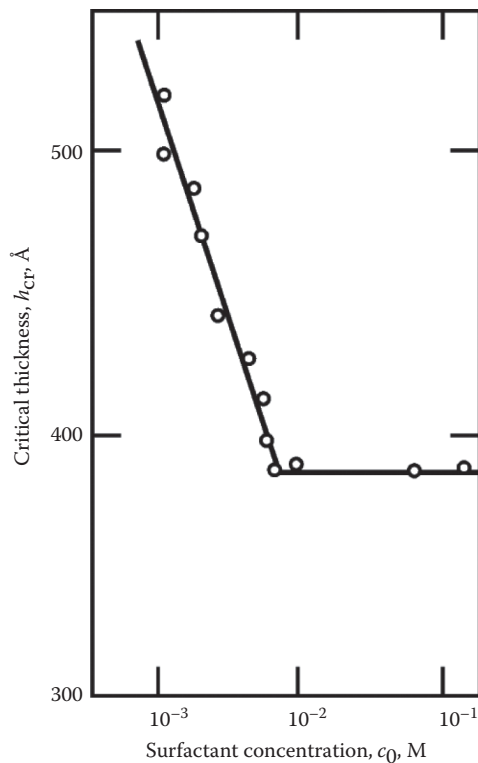


FIGURE 4.48 Dependence of the critical thickness, h_{cr} , of aniline films on the concentration of dodecanol, c_0 [723]. (Modified from Ivanov, I.B., *Pure Appl. Chem.*, 52, 1241, 1980.)

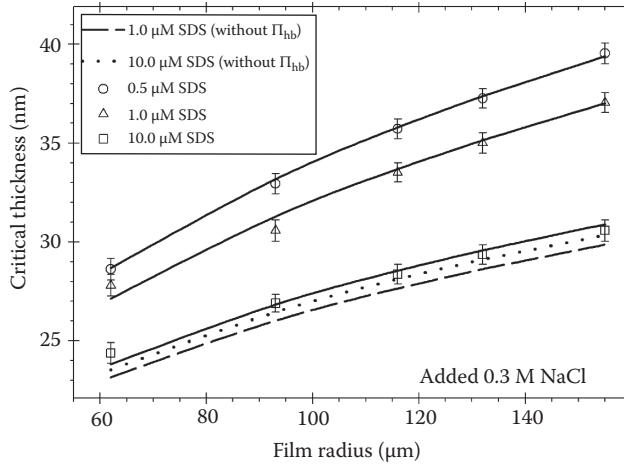


FIGURE 4.49 Critical thickness, h_{cr} , vs the film radius at a 0.3 M fixed concentration of NaCl for three SDS concentrations: 0.5; 1; 10 μM . The dashed and dash-dotted lines, for 1 and 10 μM SDS, respectively, are computed using an absence of the hydrophobic attraction. The solid lines are fits of the experimental points with $\lambda_0 = 15.8 \text{ nm}$.

a dimple might not appear. Parallel experiments [714] on the formation and thinning of emulsion films of macroscopic and microscopic areas, prepared in the Scheludko–Exerowa cell [215,216] and in a miniaturized cell, show that the patterns and the time scales of the film evolution in these two cases are significantly different. There is no dimple formation in the case of thin liquid films of small diameters [714].

In the case of predominant van der Waals attraction, instead of a dimple, a reverse bell-shape deformation, called a *pimple*, appears and the film quickly ruptures [691,698,707,710,713]. The thickness, h_p , at which the pimple appears, can be calculated from the relationship [691]:

$$h_p = \left(\frac{A_H R_*}{12F_z} \right)^{1/2} \tag{4.279}$$

The pimple formation thickness depends significantly on the radius, R_* . If a drop of tangentially immobile surfaces and radius R_d is driven by the buoyancy force, then we have:

$$F_z = \frac{4}{3} \pi R_d^3 \Delta \rho g \tag{4.280}$$

where

- $\Delta \rho$ is the density difference
- g is the gravity acceleration

For the collision of this drop with another immobile one, we have $h_p^2 = A_H / (16\pi \Delta \rho g R_d^2)$. We see that h_p is inversely proportional to the drop radius. For typical values of the Hamaker constant $A_H = 4 \times 10^{-20} \text{ J}$, density difference $\Delta \rho = 0.12 \text{ g/cm}^3$, and $R_d = 10 \mu\text{m}$, the thickness of pimple formation is $h_p = 82.3 \text{ nm}$. Note that this thickness is quite large. The pimple formation can be interpreted as the onset of instability without fluctuations (stability analysis of the film intervening between the drops has been carried out elsewhere [62]).

As already mentioned, if the van der Waals force (or other attractive force) is not predominant, first a dimple forms in the thinning liquid films. Usually the dimple exists for a short period of time; initially it grows, but as a result of the swift outflow of liquid it decreases and eventually disappears. The resulting plane-parallel film thins at almost constant radius R . When the electrostatic repulsion is strong, a thicker primary film forms (see point 1 in Figure 4.17). From the viewpoint of conventional DLVO theory, this film must be metastable. Indeed, the experiments with microscopic foam films, stabilized with sodium octyl sulfate or SDS in the presence of different amount of electrolyte [715], show that a black spot may suddenly form and a transition to secondary (Newton black) film may occur (see point 2 in Figure 4.17). The rate of thinning depends not only on the capillary pressure (the driving force) but also very strongly on the surfactant concentration (for details, see Section 4.5.3.2).

The appearance of a secondary film (or film rupture, if the secondary film is not stable) is preceded by corrugation of the film surfaces due to thermally excited fluctuations or outer disturbances. When the derivative of the disjoining pressure, $\partial\Pi/\partial h$, is positive, the amplitude of the fluctuations (ζ in Figure 4.45d) spontaneously grows. As already mentioned, the instability leads to rupture of the film or to formation of black spots. The theory of film stability was developed by de Vries [716], Vrij [717], Felderhof [648], Sche and Fijnaut [649], Ivanov et al. [718], Gumerman and Homsy [719], Malhotra and Wasan [720], Maldarelli and Jain [650], and Valkovska et al. [721]. On the basis of the lubrication approximation for tangentially immobile surfaces, Ivanov et al. [718] and Valkovska et al. [721] derived a general expression for the critical film thickness, h_{cr} , by using long-waves stability analysis:

$$h_{cr} = h_{tr} \left(\frac{\sigma h_{tr}^2}{kT} \right)^{1/4} \exp \left(- \frac{k_{cr}^2 R^2}{32 h_{cr}^3} \int_{h_{cr}}^{h_{tr}} \frac{h^3 \Pi'}{P_c - \Pi} dh \right) \quad (4.281)$$

where k_{cr} is the wave number of the critical wave defined as

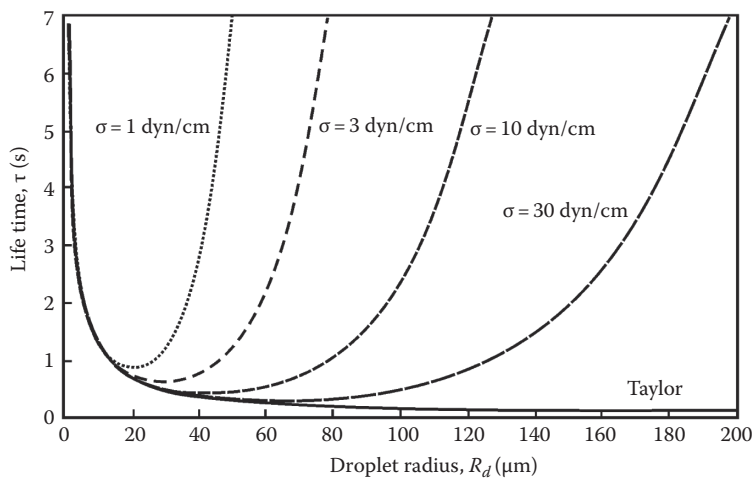


FIGURE 4.50 Calculated lifetime, τ , of drops approaching a fluid interface in Taylor regime (the solid line) and in Reynolds regime (the other lines) as a function of the droplet radius, R_d .

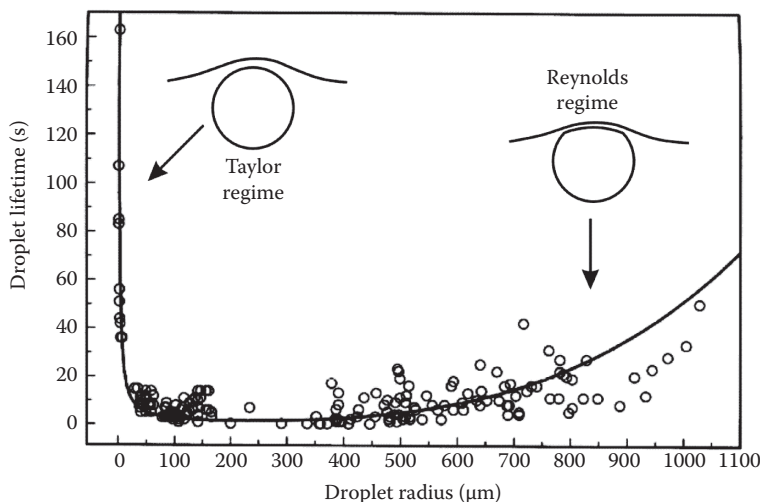


FIGURE 4.51 Stability of oil drops pressed by buoyancy against a large oil–water interface. Measured lifetime, (the points), is plotted vs droplet radius in a system consisting of soybean oil and aqueous solution of $4 \cdot 10^{-4}$ wt% BSA + 0.15 M NaCl (pH = 6.4). The solid line is drawn in accordance to Equation 4.284.

$$k_{cr}^2 = \frac{(1/\sigma) \int_{h_{cr}}^{h_{tr}} (h^3 \Pi' / (P_c - \Pi)) dh}{\int_{h_{cr}}^{h_{tr}} h^6 / (P_c - \Pi) dh} \quad (4.282)$$

In Equation 4.282, h_{tr} is the so-called transitional thickness [717,718,721] at which the increase of free energy due to the increased film area and the decrease of free energy due to the van der Waals interaction in the thinner part (Figure 4.45d) compensate each other. At h_{tr} the most rapidly growing fluctuation (the critical wave) becomes unstable. The transitional thickness obeys the following equation [718,721]:

$$\frac{24h_{cr}^3 [P_c - \Pi(h_{tr})]}{R^2 k_{cr}^2 h_{tr}^4} + \frac{\sigma k_{cr}^2 h_{cr}^3}{2h_{cr}^3} = \Pi'(h_{tr}) \quad (4.283)$$

Figures 4.46 and 4.47 show the critical thicknesses of rupture, h_{cr} , for foam and emulsion films, respectively, plotted versus the film radius [722]. In both cases the film phase is the aqueous phase, which contains 4.3×10^{-4} M SDS + added NaCl. The emulsion film is formed between two toluene drops. Curve 1 is the prediction of a simpler theory, which identifies the critical thickness with the transitional one [720]. Curve 2 is the theoretical prediction of Equations 4.281 through 4.283 (no adjustable parameters); in Equation 4.182 for the Hamaker constant the electromagnetic retardation effect has also been taken into account [404]. In addition, Figure 4.48 shows the experimental dependence of the critical thickness versus the concentration of surfactant (dodecanol) for aniline films. Figures 4.46 through 4.48 demonstrate that when the film area increases and/or the electrolyte concentration decreases the critical film thickness becomes larger. Figure 4.49 shows the critical thickness of foam film rupture for three concentrations of SDS in the presence of 0.3 M NaCl [605]. The dashed and dash-dotted lines, for 1 and 10 μ M SDS, respectively, are computed assuming only the van der Waals attraction (no adjustable parameter). The deviation of the predicted values of h_{cr} from the measured is because of the hydrophobic interaction (Section 4.4.5.4.2). The solid lines

represent fits with the decay length of the hydrophobic interactions $\lambda_0 = 15.8$ nm using Equations 4.281 through 4.283.

The surface corrugations do not necessarily lead to film rupture. Instead, black spots (secondary films of very low thickness; h_2 in Figure 4.17) can be formed. The typical thickness of plane-parallel films at stage c (Figure 4.45c) is about 200 nm, while the characteristic thickness h_2 of the Newton black film (Figure 4.45e and f) is about 5–10 nm. The black spots either coalesce or grow in diameter, forming an equilibrium secondary (Newton black) film with a thickness h_2 and radius R_{sp} . These spots grow until they cover the whole film area.

After the entire film area is occupied by the Newton black film, the film radius increases until it reaches its equilibrium value, $R = R_{NBF}$ (Figure 4.45f). Finally, the equilibrium contact angle is established. For more details about this last stage of film thinning, see part IV.C of Ref. [240].

4.5.2.4 Dependence of Emulsion Stability on the Droplet Size

Experimental data [724,725] show that the emulsion stability correlates well with the lifetime of separate thin emulsion films or of drops coalescing with their homophase. To simplify the treatment we will consider here the lifetime of a single drop pressed against its homophase under the action of gravity. To define the *lifetime* (or drainage time) τ , we assume that in the initial and final moments the film has some known thicknesses h_{in} and h_f :

$$\tau = \int_{h_f}^{h_{in}} \frac{dh}{V_z} = \frac{3\pi\eta R_*^2}{2F_z} \left[\ln\left(\frac{h_{in}}{h_f}\right) + \frac{R^2}{h_f R_*} \left(1 - \frac{h_f}{h_{in}}\right) + \frac{R^4}{2h_f^2 R_*^2} \left(1 - \frac{h_f^2}{h_{in}^2}\right) \right] \quad (4.284)$$

The final thickness, h_f , may coincide with the critical thickness of film rupture. Equation 4.284 is derived for tangentially immobile interfaces from Equation 4.270 at a fixed driving force (no disjoining pressure).

In the case of gravity-driven coalescence of a droplet with its homophase, the driving force is given by Equation 4.280 and the mean drop radius is $R_* = 2R_d$. Then from Equations 4.280 and 4.284 we can deduce the droplet lifetime in the so-called Taylor regime, corresponding to nondeformed droplets ($R = 0$):

$$\tau_{Ta} = \frac{6\pi\eta R_d^2}{F_z} \ln\left(\frac{h_{in}}{h_f}\right) = \frac{9\eta}{2gR_d\Delta\rho} \ln\left(\frac{h_{in}}{h_f}\right) \quad (4.285)$$

We see that τ_{Ta} depends logarithmically on the ratio of the initial and final thickness. Moreover, in the Taylor regime the lifetime, τ , decreases with the increase of the driving force, F_z , and the drop radius, R_d . The latter fact is confirmed by the experimental data of Dickinson et al. [726].

In the case of deformed drops ($R \neq 0$), the drainage time, τ , is determined by Equation 4.284, and in such a case the fluid particles approach each other in the Reynolds regime [657,723]. The dependence of τ on R_d in Equation 4.284 is very complex, because the driving force, F_z , and the film radius, R , depend on R_d . The film radius can be estimated from the balance of the driving and capillary force [657,723]:

$$R^2 = \frac{F_z R_d}{2\pi\sigma} \quad (4.286)$$

In this regime, the lifetime, τ , increases with an increase of the driving force, F_z . This is exactly the opposite trend compared to the results for the Taylor regime (see Equation 4.285). The result can be rationalized in view of Reynolds equation (Equation 4.273). In the numerator of this equation,

$F_z \propto R_d^3$, whereas in the denominator $R^4 \propto R_d^8$ (see Equation 4.286); as a result, the drainage rate becomes proportional to R_d^{-5} , that is, V_z decreases as the droplet radius increases.

The numerical results from Equations 4.284 through 4.286 for the lifetime or drainage time, τ , versus the droplet radius, R_d , are plotted in Figure 4.50 for parameter values typical for emulsion systems: $\Delta\rho = 0.2 \text{ g/cm}^3$, $\eta = 1 \text{ cP}$, $h_f = 5 \text{ nm}$, and $h_{in} = R_d/10$. The various curves in Figure 4.50 correspond to different values of the surface tension, σ , shown in the Figure 4.50. The left branches of the curves correspond to the Taylor regime (nondeformed droplets), whereas the right branches correspond to the Reynolds regime (formation of film between the droplets). The presence of a deep minimum on the τ versus R_d curve was first pointed out by Ivanov [727,728]. The theoretical dependencies in Figure 4.50 agree well with experimental data [652,729–731] for the lifetime of oil droplets pressed by the buoyancy force against a large oil–water interface in a system containing protein BSA (Figure 4.51).

4.5.3 EFFECT OF SURFACE MOBILITY

The hydrodynamic interactions between fluid particles (drops, bubbles) suspended in a liquid medium depend on the interfacial mobility. In the presence of surfactants, the bulk fluid motion near an interface disturbs the homogeneity of the surfactant adsorption monolayer. The ensuing surface tension gradients act to restore the homogeneous equilibrium state of the monolayer. The resulting transfer of adsorbed surfactant molecules from the regions of lower surface tension toward the regions of higher surface tension constitutes the Marangoni effect. The analogous effect, for which the surface tension gradient is caused by a temperature gradient, is known as the Marangoni effect of thermocapillarity. In addition, the interfaces possess specific surface rheological properties (surface elasticity and dilatational and shear surface viscosities), which give rise to the so-called Boussinesq effect (see the following section) [732].

4.5.3.1 Diffusive and Convective Fluxes at an Interface—Marangoni Effect

To take into account the influence of surfactant adsorption, Equations 4.251 and 4.252 are to be complemented with transport equations for each of the species ($k = 1, 2, \dots, N$) in the bulk phases [631,634,641,662,663]

$$\frac{\partial c_k}{\partial t} + \text{div}(c_k \mathbf{v} + \mathbf{j}_k) = r_k \quad (k = 1, 2, \dots, N) \quad (4.287)$$

where

c_k and \mathbf{j}_k are bulk concentration and flux, respectively, of the k th species—note that \mathbf{j}_k includes the molecular diffusive flux, the flux driven by external forces (e.g., electrodiffusion [651,662,663]) and the thermodiffusion flux [662]

r_k is the rate of production due to chemical reactions, including surfactant micellization or micelle decay

The surface mass balance equation for the adsorption, Γ_k , has the form [651,662,663]:

$$\frac{\partial \Gamma_k}{\partial t} + \nabla_s \cdot (\Gamma_k \mathbf{v}_s + \mathbf{j}_k^s) = r_k^s + \mathbf{n} \cdot \langle \mathbf{j}_k \rangle \quad (4.288)$$

where

\mathbf{n} is the unit normal to the interface directed from phase 1 to phase 2

$\langle \rangle$ denotes the difference between the values of a given physical quantity at the two sides of the interface

∇_s is the surface gradient operator [733]

\mathbf{v}_s is the local material surface velocity

\mathbf{j}_k^s is the 2D flux of the k th component along the interface

r_k^s accounts for the rate of production of the k th component due to interfacial chemical reactions and could include conformational changes of adsorbed proteins

Equation 4.288 provides a boundary condition for the normally resolved flux, \mathbf{j}_k . From another viewpoint, Equation 4.288 represents a 2D analogue of Equation 4.287. The interfacial flux, \mathbf{j}_k^s , can also contain contributions from the interfacial molecular diffusion, electrodiffusion, and thermodiffusion. A simple derivation of the time-dependent convective-diffusion equation for surfactant transport along a deforming interface is given by Brenner and Leal [734–737], Davis et al. [669], and Stone [738]. If the molecules are charged, the bulk and surfaces electrodiffusion fluxes can be expressed in the form [651,739,740]:

$$\mathbf{j}_k = -D_k(\nabla C_k + z_k c_k \nabla \Phi), \quad \mathbf{j}_k^s = -D_k^s(\nabla_s \Gamma_k + z_k \Gamma_k \nabla_s \Phi) \quad (4.289)$$

for the bulk and interfacial phase. Here, D_k and D_k^s are the bulk and surface collective diffusion coefficients, respectively, which are connected with the diffusion coefficients of individual molecules, $D_{k,0}$ and $D_{k,0}^s$, through the relationship [740]

$$D_k = \frac{D_{k,0}}{kT} \frac{K_b(\phi_k)}{(1-\phi_k)} \frac{\partial \mu_k}{\partial \ln \phi_k}, \quad D_k^s = \frac{D_{k,0}^s}{kT} K_s(\Gamma_k) \frac{\partial \mu_k^s}{\partial \ln \Gamma_k} \quad (4.290)$$

where μ_k and μ_k^s are the bulk and surface chemical potentials, respectively. The dimensionless bulk friction coefficient, K_b , accounts for the change in the hydrodynamic friction between the fluid and the particles (created by the hydrodynamic interactions between the particles). The dimensionless surface mobility coefficient, K_s , accounts for the variation of the friction of a molecule in the adsorption layer. Feng [741] has determined the surface diffusion coefficient, the dilatational elasticity, and the viscosity of a surfactant adsorption layer by theoretical analysis of experimental data. Stebe and Maldarelli [742,743] studied theoretically the surface diffusion driven by large adsorption gradients. The determination of bulk and surface diffusion coefficients from experimental data for the drainage of nitrobenzene films stabilized by different concentrations of dodecanol was reported [739].

Note that the adsorption isotherms, relating the surface concentration, Γ_k , with the subsurface value of the bulk concentration, c_k (see Section 4.2.2.1), or the respective kinetic Equation 4.86 for adsorption under barrier control (see Section 4.2.2.5), should also be employed in the computations based on Equations 4.287 through 4.290 in order for a complete set of equations to be obtained.

Another boundary condition is the equation of the interfacial momentum balance [634,635,641,663]:

$$\nabla_s \cdot \boldsymbol{\sigma} = \mathbf{n} \cdot \langle \mathbf{P} + \mathbf{P}_b \rangle \quad (4.291)$$

where $\boldsymbol{\sigma}$ is the interfacial stress tensor, which is a 2D counterpart of the bulk stress tensor, \mathbf{P} . Moreover, a 2D analogue of Equations 4.253, 4.256, and 4.257, called the Boussinesq–Scriven constitutive law, can be postulated for a fluid interface [240,641,663,732,744–748]:

$$\boldsymbol{\sigma} = \sigma_a \mathbf{I}_s + (\eta_{dl} - \eta_{sh})(\nabla_s \cdot \mathbf{v}_s) \mathbf{I}_s + \eta_{sh} \left[(\nabla_s \mathbf{v}_s) \cdot \mathbf{I}_s + \mathbf{I}_s \cdot (\nabla_s \mathbf{v}_s)^T \right] \quad (4.292)$$

where

η_{dl} and η_{sh} are the interfacial dilatational and shear viscosities, respectively

\mathbf{I}_s is the unit surface idemfactor [733]

σ_a is the scalar adsorption part of the surface tension (see Section 4.2.1.2.2)

In view of the term $\sigma_a \mathbf{I}_s$ in Equation 4.292, the Marangoni effects are hidden in the left-hand side of the boundary condition (Equation 4.291) through the surface gradient of σ_a :

$$\nabla_s \sigma_a = - \sum_{k=1}^N \frac{E_k}{\Gamma_k} \nabla_s \Gamma_k - \frac{E_T}{T} \nabla_s T, \quad E_k = - \left(\frac{\partial \sigma_a}{\partial \ln \Gamma_k} \right)_{T, \Gamma_{j \neq k}}, \quad E_T = - \left(\frac{\partial \sigma_a}{\partial \ln T} \right)_{\Gamma_k} \quad (4.293)$$

where

E_k is the Gibbs elasticity for the k th surfactant species (see Equation 4.6)

E_T represents the thermal analogue of the Gibbs elasticity

The thermocapillary migration of liquid drops or bubbles and the influence of E_T on their motion are investigated in a number of works [749–751].

In fact, Equation 4.292 describes an interface as a 2D Newtonian fluid. On the other hand, a number of non-Newtonian interfacial rheological models have been described in the literature [752–773]. Tambe and Sharma [756] modeled the hydrodynamics of thin liquid films bounded by viscoelastic interfaces, which obey a generalized Maxwell model for the interfacial stress tensor. These authors [757,758] also presented a constitutive equation to describe the rheological properties of fluid interfaces containing colloidal particles. A new constitutive equation for the total stress was proposed by Horozov et al. [759], Danov et al. [760], and Ivanov et al. [761] who applied a local approach to the interfacial dilatation of adsorption layers.

The interfacial rheology of protein adsorption layers has been intensively studied in relation to the properties of foams and emulsions stabilized by proteins and their mixtures with lipids or surfactants. Detailed information on the investigated systems, experimental techniques, and theoretical models can be found in Refs. [762–769]. The shear rheology of the adsorption layers of many proteins follows the viscoelastic thixotropic model [770–772], in which the surface shear elasticity and viscosity depend on the surface shear rate. The surface rheology of saponin adsorption layers has been investigated in Ref. [773].

If the temperature is not constant, the bulk heat transfer equation complements the system and involves Equations 4.251, 4.252, and 4.287. The heat transfer equation is a special case of the energy balance equation. It should be noted that more than 20 various forms of the overall differential energy balance for multicomponent systems are available in the literature [631,634]. The corresponding boundary condition can be obtained as an interfacial energy balance [663,748]. Based on the derivation of the bulk [774,775] and interfacial [760,775,776] entropy inequalities (using the

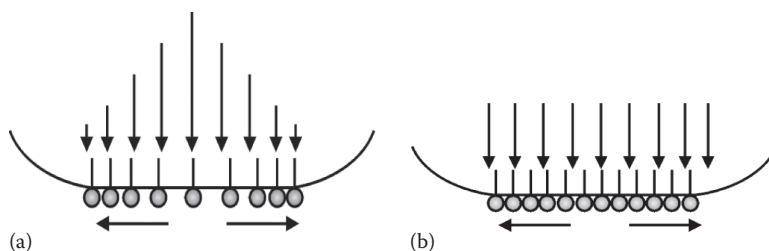


FIGURE 4.52 Damping of convection-driven surface tension gradients by influx of surfactant from the drop interior. (a) Since the mass transport is proportional to the perturbation, the larger the perturbation, the stronger the flux tending to eliminate it. (b) Uniform surfactant distribution is finally reached.

Onsager theory), various constitutive equations for the thermodynamic mass, heat, and stress fluxes have been obtained.

4.5.3.2 Fluid Particles and Films of Tangentially Mobile Surfaces

When the surface of an emulsion droplet is mobile, it can transmit the motion of the outer fluid to the fluid within the droplet. This leads to a special pattern of the fluid flow and affects the dissipation of energy in the system. The problem concerning the approach of two nondeformed (spherical) drops or bubbles of pure phases has been investigated by many authors [657,685,686,692,693,777–782]. A number of solutions, generalizing the Taylor equation (Equation 4.271), have been obtained. For example, the velocity of central approach, V_z , of two spherical drops in pure liquid is related to the hydrodynamic resistance force, F_z , by means of a Padé-type expression derived by Davis et al. [692]:

$$V_z = \frac{2hF_z}{3\pi\eta R_*^2} \frac{1 + 1.711\xi + 0.461\xi^2}{1 + 0.402\xi}, \quad \xi = \frac{\eta}{\eta_d} \sqrt{\frac{R_*}{2h}} \quad (4.294)$$

where

h is the closest surface-to-surface distance between the two drops
 η_d is the viscosity of the disperse phase (the liquid in the droplets)

In the limiting case of solid particles, we have $\eta_d \rightarrow \infty$, and Equation 4.294 reduces to the Taylor equation (Equation 4.271). Note that in the case of close approach of two drops ($\xi \gg 1$), the velocity V_z is proportional to \sqrt{h} . This implies that the two drops can come into contact ($h = 0$) in a finite period of time ($\tau < \infty$) under the action of a given force, F_z , because the integral in Equation 4.284 is convergent for $h_f = 0$. This is in contrast to the case of immobile interfaces ($\xi \ll 1$), when $V_z \propto h$ and $\tau \rightarrow \infty$ for $h_f \rightarrow 0$.

In the other limiting case, that of two nondeformed gas bubbles ($\eta_d \rightarrow 0$) in pure liquid, Equation 4.294 cannot be used; instead, V_z can be calculated from the expression [782,783]

$$V_z = \frac{F_z}{\pi\eta R_d [\ln(R_d/h + 1) + 2.5407]} \quad (4.295)$$

Note that in this case $V_z \propto (\ln h)^{-1}$, and the integral in Equation 4.284 is convergent for $h_f \rightarrow 0$. In other words, the theory predicts that the lifetime, τ , of a doublet of two colliding spherical bubbles in pure liquid is finite. Of course, the real lifetime of a doublet of bubbles or drops is affected by the surface forces for $h < 100$ nm, which should be accounted for in F_z and which may lead to the formation of thin film in the zone of contact [207,392].

In the case of droplets with equal radii, R_d , in a pure liquid (without surfactant), two asymptotic expressions are derived for small interdroplet distances [783]:

1. At not very large droplet viscosity:

$$\frac{F_z}{\pi\eta R_d V_z} = \frac{3\pi^2\eta_d}{16\eta} \sqrt{\frac{R_d}{h}} + \left(1 - \frac{\eta_d^2}{3\eta^2}\right) \ln\left(\frac{R_d}{h} + 1\right) + 2.5407 \quad \text{at } \frac{\eta_d}{\eta} \sqrt{\frac{R_d}{h}} < 1 \quad (4.296)$$

2. At very large viscosity of the drop phase:

$$\frac{F_z}{\pi\eta R_d V_z} = \frac{3R_d}{2h} - \frac{9\pi^2\eta}{64\eta_d} \left(\frac{R_d}{h}\right)^{3/2} \quad \text{at } \frac{\eta_d}{\eta} \sqrt{\frac{h}{R_d}} \gg 1 \quad (4.297)$$

Note that for $\eta_d = 0$ Equation 4.296 reduces to Equation 4.295. The second term in the right-hand side of Equation 4.297 represents a correction to the Taylor equation (Equation 4.271).

Next, let us consider the case of deformed fluid particles (Figure 4.32). A number of theoretical studies [784–787] have been devoted to the thinning of plane-parallel liquid films of pure liquid phases (no surfactant additives). Ivanov and Traykov [786] derived the following exact expressions for the velocity of thinning of an emulsion film:

$$V_z = \left(\frac{32\Delta P^2}{\rho_d \eta_d R^4} \right)^{1/3} h^{5/3}, \quad \frac{V_z}{V_{Re}} = \frac{1}{\varepsilon_e}, \quad \varepsilon_e \equiv \left(\frac{\rho_d \eta_d h^4 F_z}{108\pi \eta^3 R^4} \right)^{1/3} \quad (4.298)$$

where

ρ_d is the density of the disperse phase

V_{Re} is the Reynolds velocity defined by Equation 4.273

ε_e is the so-called emulsion parameter

Substituting typical parameter values in Equations 4.294 and 4.298 we can check that at a given constant force the velocity of thinning of an emulsion film is smaller than the velocity of approach of two nondeformed droplets and much larger than V_{Re} . It is interesting to note that the velocity of thinning as predicted by Equation 4.298 does not depend on the viscosity of the continuous phase, η , and its dependence on the drop viscosity, η_d , is rather weak. There are experimental observations confirming this prediction (see Ref. [34], p. 381).

The presence of surfactant adsorption monolayers decreases the mobility of the droplet (bubble) surfaces. This is due to the Marangoni effect (see Equation 4.293). From a general viewpoint, we may expect that the interfacial mobility will decrease with the increase of surfactant concentration until eventually the interfaces become immobile at high surfactant concentrations (see Section 4.5.2); therefore, a pronounced effect of surfactant concentration on the velocity of film drainage should be expected. This effect really exists (see Equation 4.299), but in the case of emulsions it is present only when the surfactant is predominantly soluble in the continuous phase.

Traykov and Ivanov [787] established (both theoretically and experimentally) the interesting effect that when the surfactant is dissolved in the disperse phase (i.e., in the emulsion droplets), the droplets approach each other just as in the case of pure liquid phases, that is, Equation 4.298 holds. Qualitatively, this effect can be attributed to the fact that the convection-driven surface tension gradients are rapidly damped by the influx of surfactant from the drop interior; in this way, the Marangoni effect is suppressed. Indeed, during the film drainage the surfactant is carried away toward the film border, and a nonequilibrium distribution depicted in Figure 4.52a appears. Because, however, the mass transport is proportional to the perturbation, the larger the deviation from equilibrium, the stronger the flux tending to eliminate the perturbation (the surfactant flux is denoted by thick arrows in Figure 4.52b). In this way, any surface concentration gradient (and the related Marangoni effect) disappears. The emulsion films in this case behave as if surfactant is absent.

In the opposite case, when the surfactant is soluble in the continuous phase, the Marangoni effect becomes operative and the rate of film thinning becomes dependent on the surface (Gibbs) elasticity (see Equation 4.293). Moreover, the convection-driven local depletion of the surfactant monolayers in the central area of the film surfaces gives rise to fluxes of bulk and surface diffusion of surfactant molecules. The exact solution of the problem [651,655,689,739,740,787] gives the following expression for the rate of thinning of symmetrical planar films (of both foam and emulsion type):

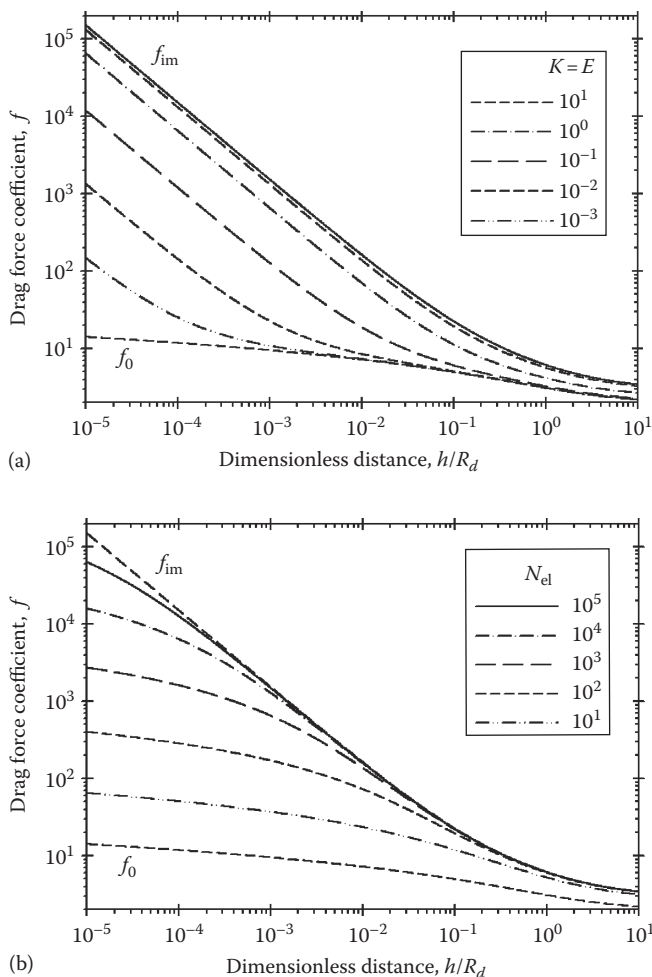


FIGURE 4.53 Dependence of the drag force coefficient, f , on the dimensionless distance, h/R_d . (a) For surfactant concentrations above the CMC at different surface viscosities. (b) For different values of the surface elasticity, the effects of surface viscosities and the viscosity of drop phase are neglected.

$$\frac{V_z}{V_{Re}} = 1 + \frac{1}{\varepsilon_e + \varepsilon_f}, \quad \frac{1}{\varepsilon_f} = \frac{6\eta D_s}{hE_G} + \frac{3\eta D}{\Gamma(\partial\sigma/\partial c)} \quad (4.299)$$

where

as usual, D and D_s are the bulk and interfacial collective diffusion coefficients (see Equation 4.290)

E_G is the Gibbs elasticity

ε_f is the so-called foam parameter [723]

In the special case of foam film, one substitutes $\varepsilon_e = 0$ in Equation 4.299. Note that the diffusive surfactant transport, which tends to restore the uniform adsorption monolayers, damps the surface tension gradients (which oppose the film drainage) and thus accelerates the film thinning. However, at large surfactant concentrations, the surface elasticity, E_G , prevails, ε_f increases, and, consequently, the thinning rate decreases down to the Reynolds velocity, $V_z \rightarrow V_{Re}$ (see Equation 4.299). Similar expressions for the rate of film thinning, which are appropriate for various ranges

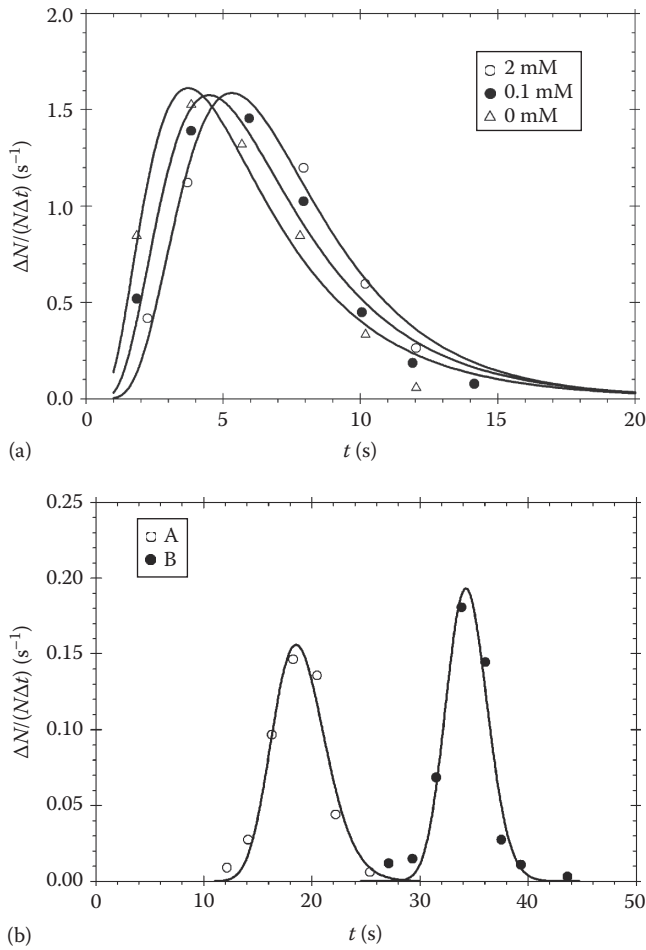


FIGURE 4.54 Histograms for the lifetimes of emulsion films: $\Delta N/N$ is the relative number of films that have ruptured during a time interval Δt . (a) Surfactant in the drops: benzene films between water drops containing surfactant sodium octylsulfonate of concentration: 0 M, 0.1 mM, and 2 mM; (b) Surfactant in the film: (A) benzene film with 0.1 M of lauryl alcohol dissolved in the film, (B) water film with 2 mM of sodium octylsulfonate inside. (From Traykov, T.T. et al., *Int. J. Multiphase Flow*, 3, 485, 1977.)

of values of the interfacial parameters, can be found in the literature [240,655,656,703,788,789]. A table describing the typical ranges of variation of the interfacial properties (Γ , E_G , D , D_s , $\partial\sigma/\partial c$, etc.) for emulsion and foam systems can be found in Ref. [240], Table 4.2 therein. For $h < 100$ nm, the influence of the disjoining pressure should be taken into account (see Equation 4.273). In some studies [240,666,756,790–793], the effect of the interfacial viscosity on the rate of thinning and the lifetime of plane-parallel films is investigated; this effect is found to decrease when the film thickness, h , becomes smaller and/or the film radius, R , becomes larger.

Note that Equation 4.299 does not hold in the limiting case of foam films ($\epsilon_e = 0$) at low surfactant concentration, $\epsilon_f \rightarrow 0$. The following expression is available for this special case [723]:

$$\frac{V_z}{V_{Re}} = \frac{(1 + 1/\epsilon_f)}{[1 + 4h^2/(3R^2\epsilon_f)]} \tag{4.300}$$

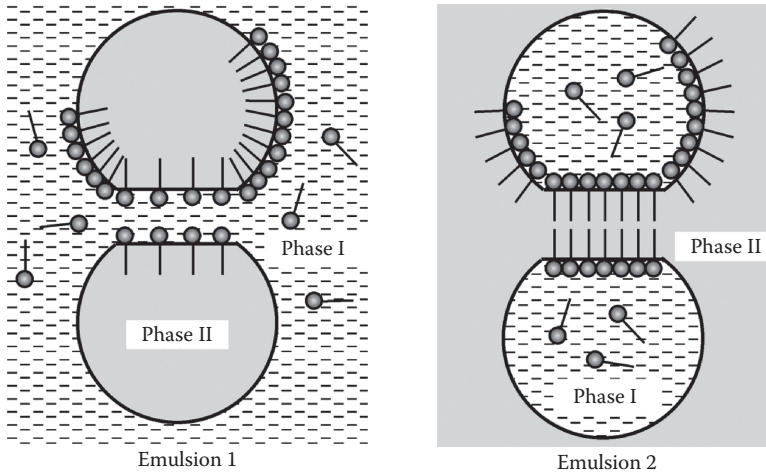


FIGURE 4.55 The two possible types of emulsions obtained just after the homogenization; the surfactant is soluble into Phase I.

The merit of this equation is that it gives as limiting cases both V_z/V_{Re} for foam films without surfactant, $\varepsilon_f \rightarrow 0$, and Equation 4.299 with $\varepsilon_e = 0$ (note that in the framework of the lubrication approximation, used to derive Equation 4.299, the terms $\propto h^2/R^2$ are being neglected). Equation 4.300 has also some shortcomings, which are discussed in Ref. [723].

Another case, which is not described by the above equations mentioned earlier, is the approach of two nondeformed (spherical) bubbles in the presence of surfactant. The velocity of approach in this case can be described by means of the expression [656,666,728,740]:

$$\frac{V_z}{V_{Ta}} = \frac{h_s}{2h} \left\{ \left[\frac{h(1+b)}{h_s} + 1 \right] \ln \left[\frac{h_s}{h(1+b)} + 1 \right] - 1 \right\}^{-1} \quad (4.301)$$

where the parameters b and h_s account for the influence of bulk and surface diffusivity of surfactants, respectively. From Equation 4.290 these parameters are calculated to be [740]

$$b \equiv \frac{3\eta c D_0 K_b(\phi)}{kT\Gamma^2(1-\phi)}, \quad h_s \equiv \frac{6\eta D_0^s K_s(\Gamma)}{kT\Gamma} \quad (4.302)$$

A generalization of Equation 4.301 to the more complicated case of two nondeformed (spherical) emulsion droplets with account for the influence of surface viscosity and the solubility of surfactants in both phases has been published in Ref. [783]. The terms related to the surface viscosities K and E , and the surface elasticity N_{el} are scaled with the drop radius, R_d , as follows [783]:

$$K \equiv \frac{\eta_{dl}}{\eta R_d}, \quad E \equiv \frac{\eta_{sh}}{\eta R_d}, \quad N_{el} \equiv \frac{E_G R_d}{\eta D_s} \quad (4.303)$$

Thus, with the increase of the drop radius the surface viscosity becomes less important and the suppression of surface mobility by the Marangoni effect increases. [Figure 4.53](#) shows the dependence

of the drag force coefficient, $f = F_z/(\pi\eta V_z R_d)$, on the dimensionless distance between the droplets, h/R_d . For surfactant concentrations above the CMC, the surfactant relaxation time is so small that the interfacial tension changes insignificantly during the motion of the drops. In this case, the drag force coefficient depends on the bulk and surface viscosities (Figure 4.53a). One sees that with the increase of K and E the drag force changes from the values for two bubbles, f_0 (see Equation 4.295), to those for tangentially immobile drop surfaces, f_{im} (see Equation 4.297). If the effect of bulk and surface viscosities is negligible, then f depends on the surface elasticity, N_{el} (Figure 4.53b). Note that the effect of surface elasticity is inversely proportional to the surface diffusion coefficient (Equation 4.303). A faster surface diffusion suppresses the gradients of the surface tension and decreases N_{el} .

Returning to the parameter values, we note that usually $\epsilon_e \ll \epsilon_f$ and $\epsilon_e \ll 1$. Then, comparing the expressions for V_z/V_{Re} as given by Equations 4.298 and 4.299, we conclude that the rate of thinning is much greater when the surfactant is dissolved in the droplets (the disperse phase) in comparison with the case when the surfactant is dissolved in the continuous phase. This prediction of the theory was verified experimentally by measuring the number of films that rupture during a given period of time [794], as well as the rate of thinning. When the surfactant was dissolved in the drop phase, the average lifetime was the same for all surfactant concentrations (Figure 4.54a), in agreement with Equation 4.298. For the emulsion film with the same, but inverted, liquid phases (the former continuous phase becomes disperse phase, and vice versa), that is, the surfactant is in the film phase, the average lifetime is about 70 times longer—compare curves in Figure 4.54a with curve B in Figure 4.54b. The theoretical conclusions have been also checked and proved in experimental measurements with nitroethane droplets dispersed in an aqueous solution of the cationic surfactant hexadecyl trimethyl ammonium chloride (HTAC) [725].

4.5.3.3 Bancroft Rule for Emulsions

There have been numerous attempts to formulate simple rules connecting the emulsion stability with the surfactant properties. Historically, the first one was the Bancroft rule [795], which states that “to have a *stable* emulsion the surfactant must be soluble in the continuous phase.” A more sophisticated criterion was proposed by Griffin [796] who introduced the concept of hydrophilic–lipophilic balance (HLB). As far as emulsification is concerned, surfactants with an HLB number in the range of 3–6 must form water-in-oil (W/O) emulsions, whereas those with HLB numbers from 8 to 18 are expected to form oil-in-water (O/W) emulsions. Different formulae for calculating the HLB numbers are available; for example, the Davies expression [797] reads

$$\text{HLB} = 7 + (\text{hydrophilic group number}) - 0.475n_c \quad (4.304)$$

where n_c is the number of $-\text{CH}_2-$ groups in the lipophilic part of the molecule. Shinoda and Friberg [798] proved that the HLB number is not a property of the surfactant molecules only, but also depends strongly on the temperature (for nonionic surfactants), on the type and concentration of added electrolytes, on the type of oil phase, etc. They proposed using the phase inversion temperature (PIT) instead of HLB for characterization of the emulsion stability.

Davis [799] summarized the concepts about HLB, PIT, and Winsor’s ternary phase diagrams for the case of microemulsions and reported topological ordered models connected with the Helfrich membrane bending energy. Because the curvature of surfactant lamellas plays a major role in determining the patterns of phase behavior in microemulsions, it is important to reveal how the optimal microemulsion state is affected by the surface forces determining the curvature energy [239,800,801]. It is hoped that lattice models [802,803] and membrane curvature models [804,805] will lead to predictive formulae for the microemulsion design.

Ivanov et al. [723,727,728,806] have proposed a semiquantitative theoretical approach that provides a straightforward explanation of the Bancroft rule for emulsions. This approach is

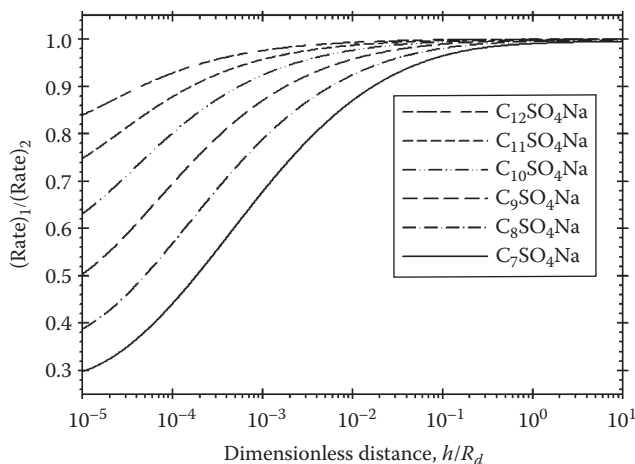


FIGURE 4.56 Ratio of the coalescence rates of emulsion 1 and emulsion 2 vs. the dimensionless distance, h/R_d , for water drops stabilized by sodium alkyl sulfates ($C_n\text{SO}_4\text{Na}$) in hexadecane at concentrations close to the CMC.

based on the idea of Davies and Rideal [34] that both types of emulsions are formed during the homogenization process, but only the one with lower coalescence rate survives. If the initial drop concentration for both emulsions is the same, the coalescence rates for the two emulsions— $(\text{Rate})_1$ for emulsion 1 and $(\text{Rate})_2$ for emulsion 2 (Figure 4.55)—will be proportional to the respective coalescence rate constants, $k_{c,1}$ and $k_{c,2}$ (see Section 4.6), and inversely proportional to the film lifetimes, τ_1 and τ_2 :

$$\frac{(\text{Rate})_1}{(\text{Rate})_2} \approx \frac{k_{c,1}}{k_{c,2}} \approx \frac{\tau_2}{\tau_1} \approx \frac{V_1}{V_2} \quad (4.305)$$

Here V_1 and V_2 denote the respective velocities of film thinning. After some estimates based on Equations 4.273, 4.284, 4.298, and 4.299, we can express the ratio in Equation 4.305 in the form:

$$\frac{(\text{Rate})_1}{(\text{Rate})_2} \approx (486\rho_d D_s^3)^{1/3} \left(\frac{h_{cr,1}^3}{h_{cr,2}^2} \right)^{1/3} \left(\frac{\eta_d}{R^2} \right)^{1/3} \frac{P_c - \Pi_1}{E_G(P_c - \Pi_2)^{2/3}} \quad (4.306)$$

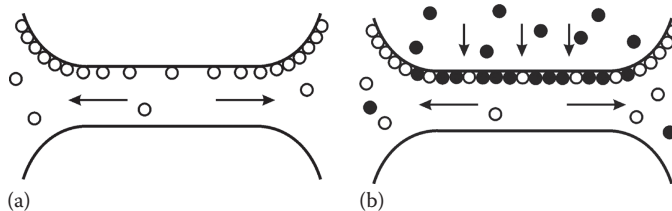


FIGURE 4.57 (a) Nonuniform surface distribution of an emulsifier due to drag from the draining film. (b) Suppression of the surface tension gradients by a demulsifier added in the drop phase.

where $h_{cr,1}$ and $h_{cr,2}$ denote the critical thickness of film rupture for the two emulsions in Figure 4.55. Many conclusions can be drawn, regarding the type of emulsion to be formed:

1. If the disjoining pressures, Π_1 and Π_2 , are zero, the ratio in Equation 4.306 will be very small. Hence, emulsion 1 (surfactant soluble in the continuous phase) will coalesce much more slowly and it will survive. This underlines the crucial importance of the surfactant location (which is connected with its solubility), thus providing a theoretical foundation for Bancroft's rule. The emulsion behavior in this case will be controlled almost entirely by the hydrodynamic factors (kinetic stability).
2. The disjoining pressure, Π , plays an important role. It can substantially change and even reverse the behavior of the system if it is comparable by magnitude with the capillary pressure, P_c . For example, if $(P_c - \Pi_2) \rightarrow 0$ at a finite value of $P_c - \Pi_1$ (which may happen, e.g., for an O/W emulsion with oil-soluble surfactant), the ratio in Equation 4.306 may become much larger than unity, which means that emulsion 2 will become thermodynamically stable. In some cases, the stabilizing disjoining pressure is large enough for emulsions with a very high volume fraction of the disperse phase (above 95% in some cases) to be formed [807].
3. The Gibbs elasticity, E_G , favors the formation of emulsion 1, because it slows down the film thinning. On the other hand, increased surface diffusivity, D_s , decreases this effect, because it helps the interfacial tension gradients to relax, thus facilitating the formation of emulsion 2.
4. The film radius, R , increases and the capillary pressure, P_c , decreases with the drop radius, R_d . Therefore, larger drops will tend to form emulsion 1, although the effect is not very pronounced.
5. The difference in critical thicknesses of the two emulsions only slightly affects the rate ratio in Equation 4.306, although the value of h_{cr} itself is important.
6. The viscosity of the continuous phase, η , has no effect on the rate ratio, which depends only slightly on the viscosity of the drop phase, η_d . This is in agreement with the experimental observations (see Ref. [34]).
7. The interfacial tension, σ , affects the rate ratio directly only through the capillary pressure, $P_c = 2\sigma/R_d$. The electrolyte primarily affects the electrostatic disjoining pressure, Π , which decreases as the salt content increases, thus destabilizing the O/W emulsion. It can also influence the stability by changing the surfactant adsorption (including the case of nonionic surfactants).
8. The temperature strongly affects the solubility and surface activity of nonionic surfactants [3]. It is well known that at higher temperature nonionic surfactants become more oil soluble, which favors the W/O emulsion. Thus, solubility may change the type of emulsion formed at the PIT. The surface activity has numerous implications and the most important is the change of the Gibbs elasticity, E_G , and the interfacial tension, σ .
9. Surface-active additives (cosurfactants, demulsifiers, etc.), such as fatty alcohols in the case of ionic surfactants, may affect the emulsifier partitioning between the phases and its adsorption, thereby changing the Gibbs elasticity and the interfacial tension. The surface-active additives may also change the surface charge (mainly by increasing the spacing among the emulsifier ionic headgroups), thus decreasing the repulsive electrostatic disjoining pressure and favoring the W/O emulsion. Polymeric surfactants and adsorbed proteins increase the steric repulsion between the film surfaces. They may favor either O/W or W/O emulsions, depending on their conformation at the interface and their surface activity.
10. The interfacial bending moment, B_0 , can also affect the type of the emulsion, although this is not directly visible from Equation 4.306. (Note that $B_0 = -4k_c H_0$, where H_0 is the so-called spontaneous curvature and k_c is the interfacial curvature elastic modulus [200]. Typically, B_0 is of the order of 5×10^{-11} N.) Usually, for O/W emulsions, B_0 opposes the

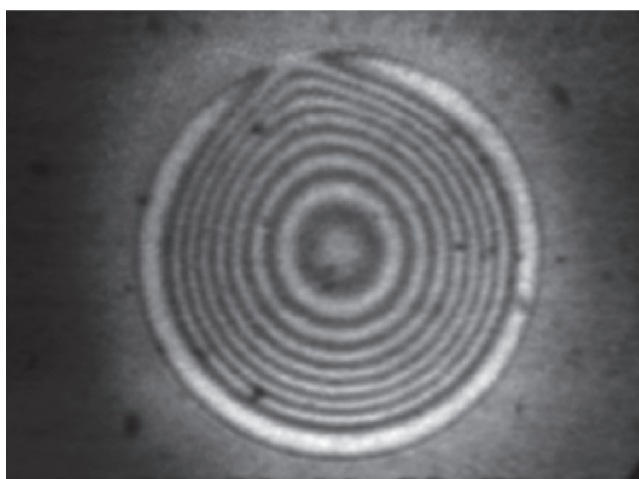
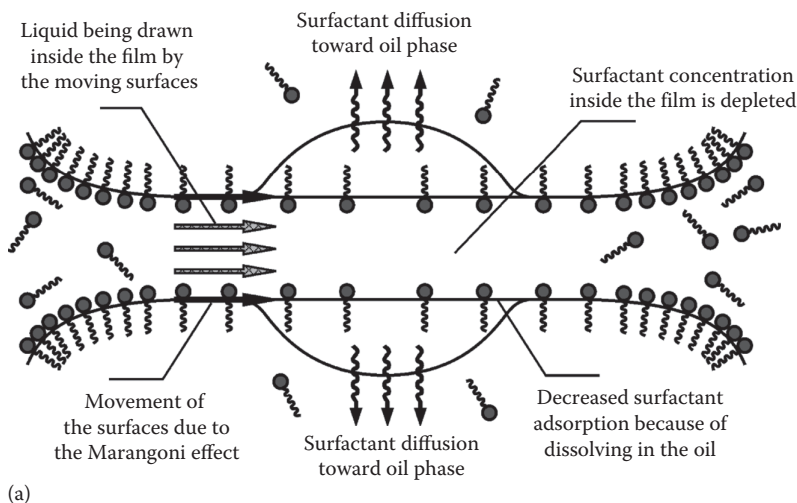


FIGURE 4.58 Spontaneous cyclic dimpling caused by surfactant diffusion from the aqueous film toward the two adjacent oil phases. (a) Schematic presentation of the process. (b) Photograph of a large dimple just before flowing out; the interference fringes in reflected light allow determination of the dimple shape.

flattening of the droplet surfaces in the zone of collision (Figure 4.32), but for W/O emulsions favors the flattening [207]. This effect might be quantified by the expression for the curvature contribution in the energy of droplet–droplet interaction [207]:

$$W_c = \frac{-2\pi R^2 B_0}{R_d}, \quad \left(\frac{R}{R_d}\right)^2 \ll 1 \quad (4.307)$$

It turns out that $W_c > 0$ for the droplet collisions in an O/W emulsion, while $W_c < 0$ for a W/O emulsion [207]. Consequently, the interfacial bending moment stabilizes the O/W emulsions but destabilizes the W/O ones. There is supporting experimental evidence [808] for microemulsions, that is, for droplets of rather small size. Moreover, the effect of the bending moment can be important even for micrometer-sized droplets [207]. This is because the bent area increases faster ($R^2 \propto R_d^2$)

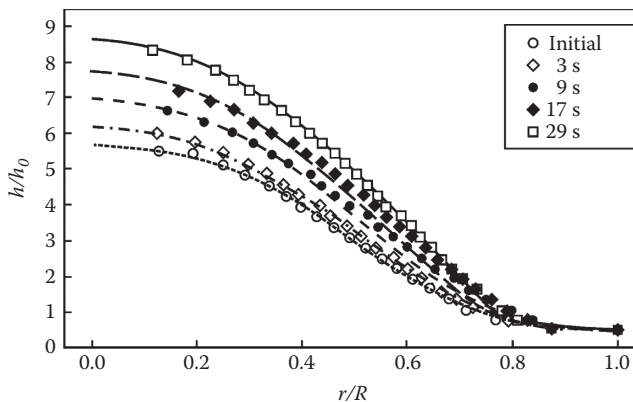


FIGURE 4.59 Comparison between the theory of cyclic dimpling (the lines) and the experimental data (the points) for the dimple shape, $h(r)$, determined from the interference fringes (see Figure 4.58b); emulsifier is anionic surfactant sodium nonylphenol polyoxyethylene-25 sulfate and the oil phase is styrene.

than the bending energy per unit area which decreases ($W_c/R^2 \propto 1/R_d$) when the droplet radius, R_d , increases (see Equation 4.307).

For micron-sized emulsion droplets the capillary pressure can be so high that a film may not appear between the drops. In such case, instead of Equation 4.306, we can use analogous expression for nondeformed (spherical) drops [783,809]. Figure 4.56 shows the calculated ratio of the coalescence rates of emulsion 1 and emulsion 2 for two water drops (with dissolved sodium alkyl sulfates, $C_n\text{SO}_4\text{Na}$) in hexadecane at concentrations close to the CMC. The degree of surface coverage was 0.7 and all parameters are obtained from the fits of surface tension isotherms [783]. The increase of the surfactant chainlength makes the difference between two systems insignificant. In the calculations, the effect of disjoining pressure has not been taken into account. Thus, at concentrations close to the CMC, the two systems have a similar hydrodynamic behavior. The emulsion stability is controlled by the considerable difference between the values of the disjoining pressure in the cases where the surfactants are in the continuous and in the disperse phases.

4.5.3.4 Demulsification

It has been known for a long time [34] that one way to destroy an emulsion is to add a surfactant, which is soluble in the drop phase—this method is termed *chemical demulsification*. To understand the underlying process, let us consider two colliding emulsion droplets with film formed in the zone of collision (see Figures 4.32 and 4.57). As discussed earlier, when the liquid is flowing out of the film, the viscous drag exerted on the film surfaces (from the side of the film interior) carries away the adsorbed emulsifier toward the film periphery. Thus, a nonuniform surface distribution of the emulsifier (shown in Figure 4.57a by empty circles) is established. If demulsifier (the closed circles in Figure 4.57b) is present in the drop phase, it will occupy the interfacial area freed by the emulsifier. The result will be a saturation of the adsorption layer, as shown in Figure 4.57b. If the demulsifier is sufficiently surface active, its molecules will be able to decrease substantially, and even to eliminate completely the interfacial tension gradients, thus changing the emulsion to type 2 (see Figure 4.55 and Section 4.5.3.2). This leads to a strong increase in the rate of film thinning, rapid drop coalescence, and emulsion destruction [727,728]. The mechanism mentioned earlier suggests that the demulsifier has to possess the following properties:

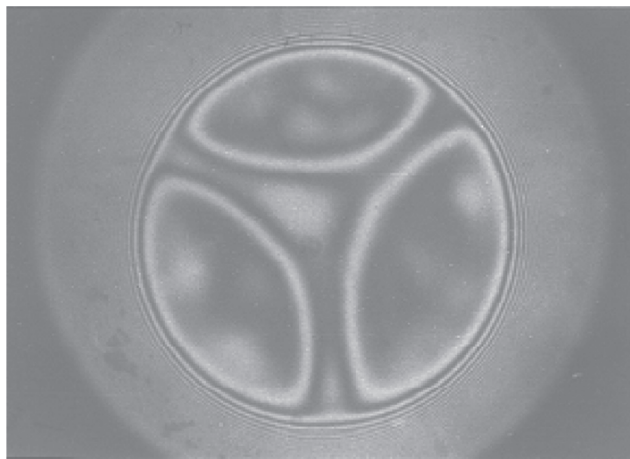
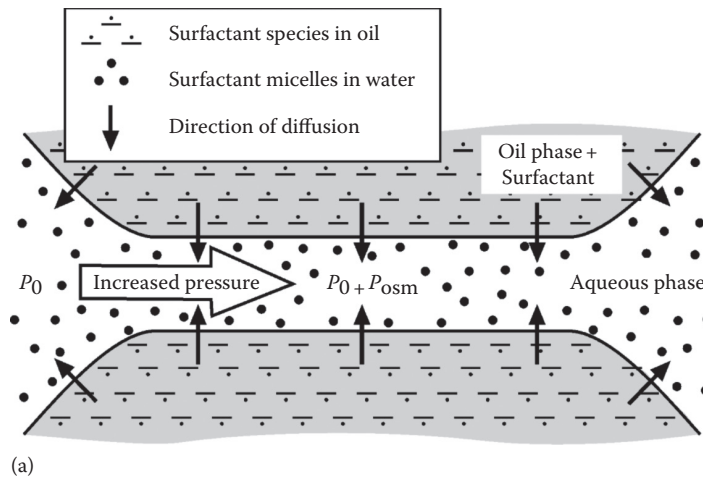


FIGURE 4.60 Osmotic swelling of an aqueous film formed between two oil droplets. (a) The surfactant dissolved in the oil is transferred by diffusion toward the film, where it forms micelles, the osmotic effects of which increase the local pressure. (b) Photograph of a typical pattern from a circular film with channels.

1. It must be soluble in the drop phase or in both phases, but in the latter case its solubility in the drop phase must be much higher.
2. Its diffusivity and concentration must be large enough to provide a sufficiently large demulsifier flux toward the surfaces and thus eliminate the gradients of the interfacial tension.
3. Its surface activity must be comparable and even higher than that of the emulsifier; otherwise, even though it may adsorb, it will not be able to suppress the interfacial tension gradients.

4.5.4 INTERACTIONS IN NONPREEQUILIBRATED EMULSIONS

The common nonionic surfactants are often soluble in both water and oil phases. In the practice of emulsion preparation, the surfactant (the emulsifier) is initially dissolved in one of the liquid phases and then the emulsion is prepared by homogenization. In such a case, the initial distribution

of the surfactant between the two phases of the emulsion is not in equilibrium; therefore, surfactant diffusion fluxes appear across the surfaces of the emulsion droplets. The process of surfactant redistribution usually lasts from many hours to several days, until finally equilibrium distribution is established. The diffusion fluxes across the interfaces, directed either from the continuous phase toward the droplets or the reverse, are found to stabilize both thin films and emulsions. In particular, even films, which are thermodynamically unstable, may exist several days because of the diffusion surfactant transfer; however, they rupture immediately after the diffusive equilibrium has been established. Experimentally, this effect manifests itself in phenomena called *cyclic dimpling* [810] and *osmotic swelling* [811]. These two phenomena, as well as the equilibration of two phases across a film [812,813], are described and interpreted in the following section.

4.5.4.1 Surfactant Transfer from Continuous to Disperse Phase (Cyclic Dimpling)

The phenomenon of cyclic dimpling was first observed [728,810] with xylene films intervening between two water droplets in the presence of the nonionic emulsifier Tween 20 or Tween 80 (initially dissolved in water but also soluble in oil). The same phenomenon also has been observed with other emulsion systems.

After the formation of such an emulsion film, it lowers down to an equilibrium thickness (approximately 100 nm), determined by the electrostatic repulsion between the interfaces. As soon as the film reaches this thickness, a dimple spontaneously forms in the film center and starts growing (Figure 4.58a). When the dimple becomes bigger and approaches the film periphery, a channel forms connecting the dimple with the aqueous phase outside the film (Figure 4.58b). Then, the water contained in the dimple flows out leaving an almost plane-parallel film behind. Just afterward, a new dimple starts to grow and the process repeats again. The period of this cyclic dimpling remains approximately constant for many cycles and could be from a couple of minutes up to more than 10 min. It was established that this process is driven by the depletion of the surfactant concentration on the film surfaces due to the dissolving of surfactant in the adjacent drop phases. The depletion triggers a surface convection flux along the two film surfaces and a bulk diffusion flux in the film interior. Both fluxes are directed toward the center of the film. The surface convection causes a tangential movement of the film surfaces; the latter drag along a convective influx of solution in the film, which feeds the dimple. Thus, the cyclic dimpling appears to be a process leading to stabilization of the emulsion films and emulsions due to the influx of additional liquid in the region between the droplets, which prevents them from a closer approach, and eventually, from coalescence.

Combining the general equation of films with deformable interfaces (Equation 4.266), the mass balance (Equations 4.287 and 4.288), and the boundary condition for the interfacial stresses (Equation 4.292), we can derive [814–817]:

$$\frac{\partial h}{\partial t} + \frac{1}{3\eta r} \frac{\partial}{\partial r} \left\{ rh^3 \frac{\partial}{\partial r} \left[\frac{\sigma}{r} \frac{\partial}{\partial r} \left(r \frac{\partial h}{\partial r} \right) + \Pi(h) \right] \right\} = \frac{1}{2r} \frac{\partial}{\partial r} \left(\frac{jhr^2}{\Gamma} \right) \quad (4.308)$$

where

- j is the diffusion flux in the drop phase
- r is radial coordinate
- $h(r, t)$ is the film thickness
- σ is surface tension
- Γ is adsorption
- Π is disjoining pressure

The comparison between the numerical calculations based on Equation 4.308 and the experimental data for the cyclic dimpling with the anionic surfactant sodium nonylphenol polyoxyethylene-25

sulfate shows a very good agreement (Figure 4.59). The experimental points are obtained from the interference fringes (see Figure 4.58). The shape in the initial moment, $t = 0$, serves as an initial condition for determining $h(r, t)$ by solving Equation 4.308. The curves for $t = 3, 9, 17,$ and 29 s represent theoretical predictions. The scaling parameters along the h - and r -axes in Figure 4.59 are $h_0 = 350$ nm and $R = 320$ μ m, with the latter the film radius; the only adjustable parameter is the diffusion flux, j .

4.5.4.2 Surfactant Transfer from Disperse to Continuous Phase (Osmotic Swelling)

Velev et al. [725] reported that emulsion films, formed from preequilibrated phases containing the nonionic surfactant Tween and 0.1 M NaCl, spontaneously thin to Newton black films (thickness ≈ 10 nm) and then rupture. However, when the nonionic surfactant Tween 20 or Tween 60 is initially dissolved in the xylene drops and the film is formed from the nonpreequilibrated phases, no black film formation and rupture are observed [728,811]. Instead, the films have a thickness above 100 nm, and we observe formation of channels of larger thickness connecting the film periphery with the film center (Figure 4.60). We may observe that the liquid is circulating along the channels for a period from several hours to several days. The phenomenon continues until the redistribution of the surfactant between the phases is accomplished. This phenomenon occurs only when the background surfactant concentration in the continuous (the aqueous) phase is not lower than the CMC. These observations can be interpreted in the following way.

Because the surfactant concentration in the oil phase (the disperse phase) is higher than the equilibrium concentration, surfactant molecules cross the oil–water interface toward the aqueous phase. Thus, surfactant accumulates within the film, because the bulk diffusion throughout the film is not fast enough to transport promptly the excess surfactant into the Plateau border. As the background surfactant concentration in the aqueous phase is not less than CMC, the excess surfactant present in the film is packed in the form of micelles (denoted by black dots in Figure 4.60a). This decreases the chemical potential of the surfactant inside the film. Nevertheless, the film is subjected to osmotic swelling because of the increased concentration of micelles within. The excess osmotic pressure

$$P_{\text{osm}} = kTC_{\text{mic}} \geq P_c \quad (4.309)$$

counterbalances the outer capillary pressure and arrests further thinning of the film. Moreover, the excess osmotic pressure in the film gives rise to a convective outflow of solution: this is the physical origin of the observed channels (Figure 4.60b).

Experimental data [728,811] show that the occurrence of the above phenomenon is the same for initial surfactant concentration in the water varying from 1 up to 500 times the CMC, if only some amount of surfactant is also initially dissolved in the oil. This fact implies that the value of the surfactant chemical potential inside the oil phase is much greater than that in the aqueous phase, with the latter closer to its value at the CMC in the investigated range of concentrations.

4.5.4.3 Equilibration of Two Droplets across a Thin Film

In the last two sections, we considered mass transfer from the film toward the droplets and the reverse, from droplets toward the film. In both cases, the diffusion fluxes lead to stabilization of the film. Here we consider the third possible case corresponding to mass transfer from the first droplet toward the second one across the film between them. In contrast with the former two cases, in the last case the mass transfer is found to destabilize the films. Experimentally, the diffusion transfer of alcohols, acetic acid, and acetone was studied [818,819]. The observed destabilization of the films can be attributed to the appearance of Marangoni instability [812], which

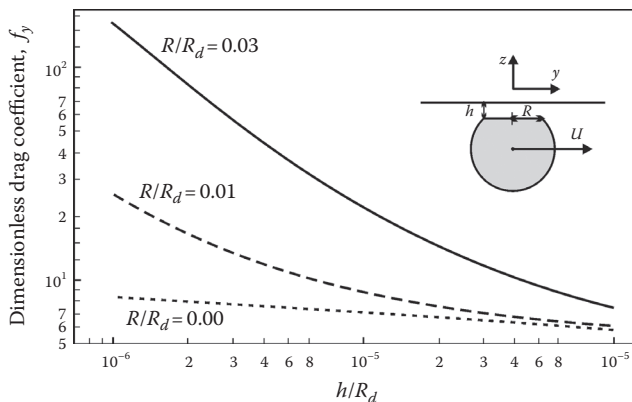


FIGURE 4.61 Deformed fluid particle (the inset) moving tangentially to an immobile solid surface: plot of the dimensionless drag coefficient, f_y , vs. the dimensionless film thickness, h/R_d , for three values of the dimensionless film radius, R/R_d (see Equation 5.317).

manifests itself through the growth of capillary waves at the interfaces, which eventually can lead to film rupture.

The Marangoni instabilities can appear not only in thin films, but also in the simpler case of a single interface. In this case, the Marangoni instability may bring about spontaneous emulsification. This effect has been theoretically investigated by Sterling and Scriven [820], whose work stimulated numerous theoretical and experimental studies on spontaneous emulsification. Lin and Brenner [821] examined the role of the heat and mass transfer in an attempt to check the hypothesis of Holly [822] that the Marangoni instability can cause the rupture of tear films. Their analysis was extended by Castillo and Velarde [823], who accounted for the tight coupling of the heat and mass transfer and showed that it drastically reduces the threshold for Marangoni convection. Instability driven by diffusion flux of dissolved oil molecules across an asymmetric liquid film (oil–water–air film) has been theoretically investigated [813]. It was found that even small decrements of the water–air surface tension, caused by the adsorbed oil, are sufficient to trigger the instability.

4.5.5 HYDRODYNAMIC INTERACTION OF A PARTICLE WITH AN INTERFACE

There are various cases of particle–interface interactions, which require separate theoretical treatment. The simpler case is the hydrodynamic interaction of a solid particle with a solid interface. Other cases are the interactions of fluid particles (of tangentially mobile or immobile interfaces) with a solid surface; in these cases, the hydrodynamic interaction is accompanied by deformation of the particle. On the other hand, the colloidal particles (both solid and fluid) may hydrodynamically interact with a fluid interface, which thereby undergoes a deformation. In the case of fluid interfaces, the effects of surfactant adsorption, surface diffusivity, and viscosity affect the hydrodynamic interactions. A special class of problems concerns particles attached to an interface, which are moving throughout the interface. Another class of problems is related to the case when colloidal particles are confined in a restricted space within a narrow cylindrical channel or between two parallel interfaces (solid and/or fluid); in the latter case, the particles interact simultaneously with both film surfaces.

The theoretical contributions are limited to the case of low Reynolds number [644,645,723,824–826,830–832] (mostly for creeping flows, see Section 4.5.1), avoiding the difficulties arising from the nonlinearity of the equations governing the fluid motion at higher velocities. Indeed, for low Reynolds numbers, the term $\mathbf{v} \cdot \nabla \mathbf{v}$ in the Navier–Stokes equation (see Equations 4.258 through 4.260) is negligible, and we may apply the method of superposition to solve the resulting linear set

of equations. This means that we may first solve the simpler problems about the particle elementary motions: (1) particle translation (without rotation) in an otherwise immobile liquid, (2) particle rotation (without translation) in an otherwise immobile liquid, and (3) streamlining of an immobile particle by a Couette or Poiseuille flow. Once the problems about the elementary motions have been solved, we may obtain the linear and angular velocity of the real particle motion combining the elementary flows. The principle of combination is based on the fact that for low Reynolds numbers the particle acceleration is negligible, and the net force and torque exerted on the particle must be zero. In other words, the hydrodynamic drag forces and torques originating from the particle translation and rotation are counterbalanced by those originating from the streamlining:

$$\mathbf{F}_{\text{translation}} + \mathbf{F}_{\text{rotation}} + \mathbf{F}_{\text{streamlining}} = \mathbf{0}, \quad \mathbf{M}_{\text{translation}} + \mathbf{M}_{\text{rotation}} + \mathbf{M}_{\text{streamlining}} = \mathbf{0} \quad (4.310)$$

That is the reason why we will now consider expressions for \mathbf{F} and \mathbf{M} for various types of elementary motions.

4.5.5.1 Particle of Immobile Surface Interacting with a Solid Wall

The force and torque exerted on a solid particle were obtained in the form of a power series with respect to R_d/l , where R_d is the particle radius and l is the distance from the center of the particle to the wall. Lorentz [827] derived an asymptotic expression for the motion of a sphere along the normal to a planar wall with an accuracy of up to R_d/l . Faxen [828] developed the method of reflection for a sphere moving between two parallel planes in a viscous fluid. Using this method, Wakiya [829] considered the cases of motion in flow of Couette and Poiseuille; however, the method employed by him cannot be applied to small distances to the wall [668]. The next important step was taken by Dean and O'Neil [830] and O'Neil [831], who found an exact solution for the force and the torque acting on a spherical particle moving tangentially to a planar wall at an arbitrary distance from the wall. The limiting case of small distances between the particle and the wall was examined by several authors [550–552,705]. Instead of an exact solution of the problem the authors derived asymptotic formulae for the force and torque. Keh and Tseng [833] presented a combined analytical–numerical study for the slow motion of an arbitrary axisymmetric body along its axis of revolution, with the latter normal to a planar surface. The inertial migration of a small solid sphere in a Poiseuille flow was calculated by Schonberg and Hinch [834] for the case when the Reynolds number for the channel is of the order of unity.

In the following section, we present expressions for the forces and torques for some of the elementary motions. In all cases we assume that the Reynolds number is small, the coordinate plane xy is parallel to the planar wall, and h is the shortest surface-to-surface distance from the particle to the wall.

First, we consider the case of a pure translational motion: a solid spherical particle of radius R_d that translates along the y -axis with a linear velocity U and angular velocity $\omega \equiv 0$ in an otherwise quiescent fluid. In spite of the fact that the particle does not rotate, it experiences a torque, \mathbf{M} , directed along the x -axis, due to friction with the viscous fluid. The respective asymptotic expressions [659–661] for the components of the drag force, \mathbf{F} , and torque, \mathbf{M} , read

$$F_x = 0, \quad F_y = -6\pi\eta UR_d f_y, \quad M_x = -8\pi\eta UR_d^2 m_x, \quad M_y = 0 \quad (4.311)$$

$$f_y = \left(\frac{8}{15} + \frac{16}{375} \frac{h}{R_d} \right) \ln \left(\frac{2R_d}{h} \right) + 0.58461 + O \left(\frac{h}{R_d} \right) \quad (4.312)$$

$$m_x = \left(\frac{1}{10} + \frac{43}{250} \frac{h}{R_d} \right) \ln \left(\frac{2R_d}{h} \right) - 0.26227 + O \left(\frac{h}{R_d} \right) \quad (4.313)$$

where f_y and m_x are dimensionless drag force and torque coefficients, respectively.

Second, we consider the case of pure rotation: a solid spherical particle of radius R_d is situated at a surface-to-surface distance, h , from a planar wall and rotates with angular velocity, ω , around the x -axis in an otherwise quiescent fluid. The corresponding force and torque resultants are [659–661]

$$F_x = 0, \quad F_y = -6\pi\eta\omega R_d^2 f_y, \quad M_x = -8\pi\eta\omega R_d^3 m_x, \quad M_y = 0 \tag{4.314}$$

$$f_y = \frac{2}{15} \ln\left(\frac{R_d}{h}\right) - 0.2526 + O\left(\frac{h}{R_d}\right), \quad m_x = \frac{2}{5} \ln\left(\frac{R_d}{h}\right) + 0.3817 + O\left(\frac{h}{R_d}\right) \tag{4.315}$$

From Equations 4.311 through 4.315, it follows that the force and the torque depend weakly (logarithmically) on the distance, h , as compared to the Taylor or Reynolds laws (Equations 4.271 and 4.272).

As discussed in Sections 4.5.2.1 and 4.5.3.2, a fluid particle in the presence of high surfactant concentration can be treated as a deformable particle of tangentially immobile surfaces. Such a particle deforms when pressed against a solid wall (see the inset in Figure 4.61). To describe the drag

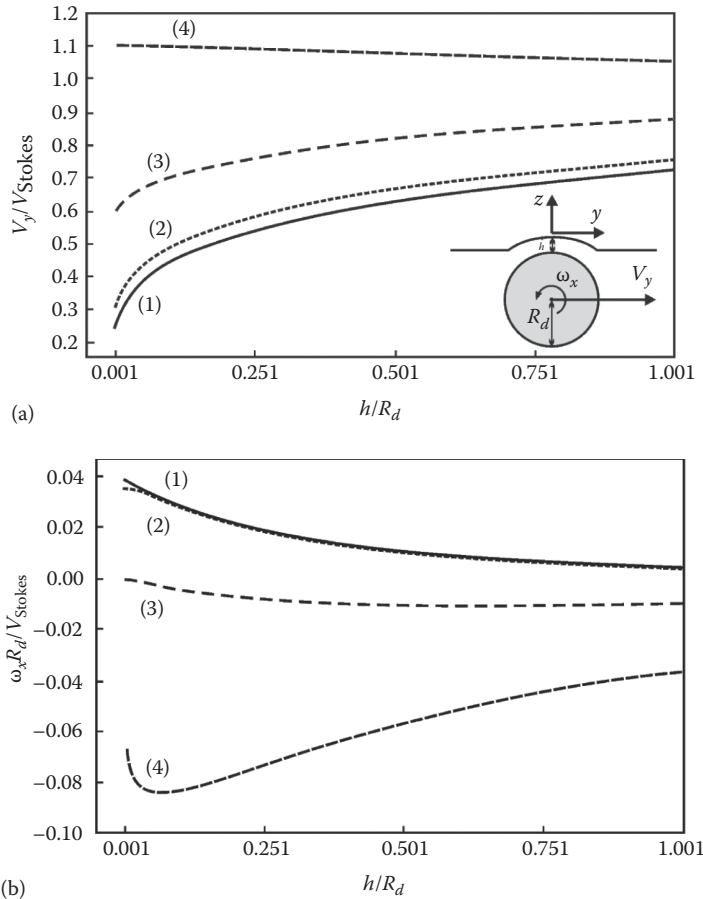


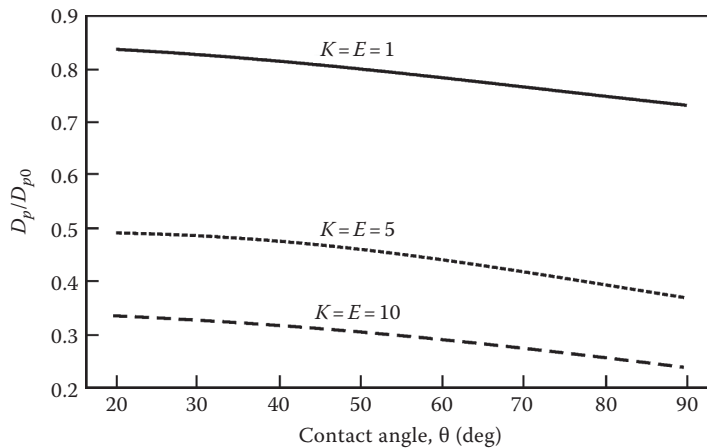
FIGURE 4.62 Spherical particle moving tangentially to a viscous interface: plots of the stationary dimensionless linear (V_y/V_{Stokes}) (a) and angular ($\omega_x R_d/V_{Stokes}$) (b) velocities vs. the dimensionless thickness, h/R_d . The curves correspond to various surface viscosities: (1) $K = E = \infty$ (solid surfaces); (2) $K = E = 100$; (3) $K = E = 10$, and (4) $K = E = 1$ (see Equation 4.303).

due to the film intervening between the deformed particle and the wall, we may use the expression derived by Reynolds [646] for the drag force exerted on a planar solid ellipsoidal disc, which is parallel to a solid wall and is moving along the y -axis at a distance h from the wall:

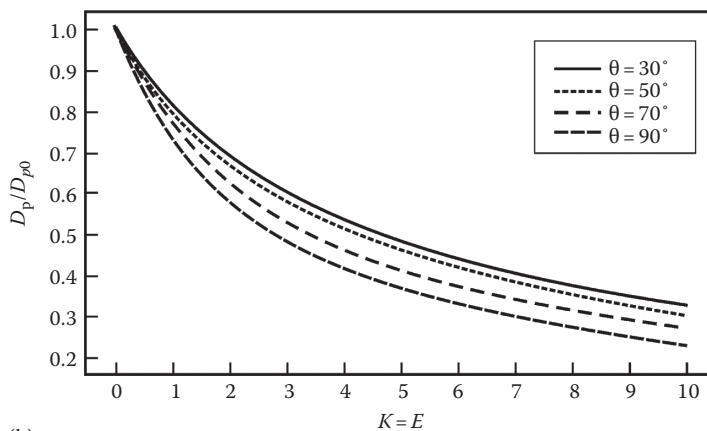
$$F_x = 0, \quad F_y = -\pi\eta U \frac{h}{ab} \quad (4.316)$$

Here, a and b are the semiaxes of the ellipse; for a circular disc (or film), we have $a = b = R$. By combining Equations 4.311 and 4.312 with Equation 4.316, we can derive an expression for the net drag force experienced by the deformed particle (the inset in Figure 4.61) when it moves along the y -axis with a linear velocity U :

$$F_y = -6\pi\eta UR_d f_y, \quad f_y = \frac{R^2}{6hR_d} + \left(\frac{8}{15} + \frac{16}{375} \frac{h}{R_d} \right) \ln \left(\frac{2R_d}{h} \right) + 0.58461 + O \left(\frac{h}{R_d} \right) \quad (4.317)$$



(a)



(b)

FIGURE 4.63 Effect of adsorbed surfactant on the surface diffusivity, D_p , of a Brownian particle attached to a fluid interface: (a) plot of D_p/D_{p0} vs. particle contact angle, θ , for various surface viscosities (see Equation 4.303); (b) plot of D_p/D_{p0} vs. the dimensionless surface viscosity, $K = E$, for various θ .

Here

h and R denote the film thickness and radius

R_d is the curvature radius of the spherical part of the particle surface

The dependence of the dimensionless drag coefficient, f_y , on the distance h for different values of the ratio R/R_d is illustrated in Figure 4.61. The increase of R/R_d and the decrease of h/R_d may lead to an increase of the drag force, f_y , by an order of magnitude. That is the reason the film between a deformed particle and a wall can be responsible for the major part of the energy dissipation. Moreover, the formation of doublets and flocks of droplets separated by liquid films seems to be of major importance for the rheological behavior of emulsions.

4.5.5.2 Fluid Particles of Mobile Surfaces

Let us start with the case of pure phases, when surfactant is missing and the fluid–liquid interfaces are mobile. Under these conditions, the interaction of an emulsion droplet with a planar solid wall was investigated by Ryskin and Leal [835], and numerical solutions were obtained. A new formulation of the same problem was proposed by Liron and Barta [836]. The case of a small droplet moving in the restricted space between two parallel solid surfaces was solved by Shapira and Haber [837,838]. These authors used the Lorentz reflection method to obtain analytical solutions for the drag force and the shape of a small droplet moving in Couette flow or with constant translational velocity.

The more complicated case, corresponding to a viscous fluid particle approaching the boundary between two pure fluid phases (all interfaces deformable), was investigated by Yang and Leal [839,840], who succeeded in obtaining analytical results.

Next, we proceed with the case when surfactant is present and the Marangoni effect becomes operative. Classical experiments carried out by Lebedev [841] and Silvey [842] show that the measured velocity of sedimentation, U , of small fluid droplets in a viscous liquid (pure liquid phases assumed) does not obey the Hadamar [843] and Rybczynski [844] equation:

$$F = 2\pi\eta UR_d \frac{3\eta_d + 2\eta}{\eta_d + \eta} \quad (4.318)$$

where F is the drag force. The limiting case $\eta_d \rightarrow 0$ corresponds to bubbles, whereas in the other limit, $\eta_d \rightarrow \infty$, Equation 4.318 describes solid particles. Note that Equation 4.318 is derived for the motion of a spherical fluid particle (drop or bubble) of viscosity η_d in a liquid of viscosity η in the absence of any surfactant. The explanation of the contradiction between theory and experiment [841,842] turned out to be very simple: even liquids that are pure from the viewpoint of the spectral analysis may contain some surface-active impurities, whose bulk concentration might be vanishingly low, but which can provide a dense adsorption layer at the restricted area of the fluid particle surface. Then, the effects of Gibbs elasticity and interfacial viscosity substantially affect the drag coefficient of the fluid particle. The role of the latter two effects was investigated by Levich [662], Edwards et al. [663], and He et al. [845] for the motion of an emulsion droplet covered with a monolayer of insoluble surfactant (adsorption and/or desorption not present). These authors used the Boussinesq–Scriven constitutive law of a viscous fluid interface (Equation 4.292), and established that only the dilatational interfacial viscosity, η_{dl} , but not the shear interfacial viscosity, η_{sh} , influences the drag force. If the surfactant is soluble in both phases and the process of adsorption is diffusion controlled (see Section 4.2.2.1), the generalization of Equation 4.318 is [783]

$$F = 2\pi\eta UR_d \left[3 - \left(1 + \frac{\eta_d}{\eta} + \frac{2\eta_{dl}}{\eta R_d} + \frac{R_d E_G}{3\eta D_s} \frac{2}{2 + 2(R_d D/h_a D_s) + (R_d D_d/h_{d,a} D_s)} \right)^{-1} \right] \quad (4.319)$$

where

D_d is the surfactant diffusion coefficient in the drop phase

c and c_d are the concentrations of surfactant in the continuous and drop phases, respectively

$h_a = \partial\Gamma/\partial c$ and $h_{d,a} = \partial\Gamma/\partial c_d$ are the slopes of adsorption isotherms with respect to the surfactant concentration

In the limiting case without surfactant, Equation 4.319 is reduced to the Hadamar [843] and Rycbczynski [844] equation (Equation 4.318).

A recently developed experimental technique [846–850] gives the possibility to measure precisely the instantaneous velocity of rising bubbles in a solution as a function of time and the distance to the starting point. The sensitivity of this technique allows one to determine trace amounts of impurities in water.

Danov et al. [347,851–854] investigated theoretically the hydrodynamic interaction of a fluid particle with a fluid interface in the presence of surfactant. The numerical results of these authors reveal that there is a strong influence of both shear and dilatational interfacial viscosities on the motion of the fluid particle when the particle–interface distance, h , is approximately equal to or smaller than the particle radius, R_d . For example, in the presence of an external force acting parallel to the interface (along the y -axis), the stationary motion of the spherical particle close to the viscous interface is a superposition of a translation along the y -axis with velocity V_y , and a rotation (around the x -axis) with an angular velocity, ω_x (see the inset in Figure 4.62a). The numerical results of Danov et al. [853,854] for V_y and ω_x normalized by the Stokes velocity, $V_{\text{Stokes}} = F/(6\pi\eta R_d)$, are plotted in Figure 4.62a and b versus h/R_d for four different types of interfaces: (1) solid particle and solid wall (see Equations 4.311 through 4.313); (2) fluid particle and fluid interface for $K = E = 100$ (for the definition of K and E see Equation 4.303); (3) the same system as (2) but for $K = E = 10$; (4) the same system as (2) but for $K = E = 1$. (For the definition of the interfacial viscosities, η_{dl} and η_{sh} , see Equation 4.292). As seen in Figure 4.62a, the velocity of the sphere, V_y , is less than V_{Stokes} for the solid (1) and the highly viscous (2) interfaces, and V_y noticeably decreases when the distance h decreases. However, in case (4), corresponding to low surface viscosities, the effect is quite different: V_y/V_{Stokes} is greater than unity (the sphere moves faster near the interface than in the bulk), and its dependence on h is rather weak. The result about the angular velocity, ω_x , is also intriguing (Figure 4.62b). The stationary rotation of a sphere close to a solid (1) or highly viscous (2) interface is in positive direction, that is, $\omega_x > 0$. For the intermediate interfacial viscosity (3), the sphere practically does not rotate, whereas, for the interfaces of low viscosity (4), the drop rotates in the opposite direction, that is, $\omega_x < 0$. The inversion of the sign of ω_x is due to the fact that the friction of the particle with the bulk fluid below it (see the inset in Figure 4.62a) becomes stronger than the friction with the interface above the particle.

Finally, we consider the case of a solid particle attached to a liquid–fluid interface. This configuration is depicted in Figure 4.21e; note that the position of the particle along the normal to the interface is determined by the value of the three-phase contact angle. Stoos and Leal [855] investigated the case when such an attached particle is subjected to a flow directed normally to the interface. These authors determined the critical capillary number, beyond which the captured particle is removed from the interface by the flow.

Danov et al. [347] examined the case of an attached particle moving along a liquid–gas interface under the action of an applied force directed tangentially to the interface. The effects of the contact angle (the depth of immersion), as well as the effect of adsorbed surfactant on the drag force, were investigated. These authors also calculated the surface diffusion coefficient of a Brownian particle

attached to the liquid surface. Let D_p and D_{p0} be the particle surface diffusion coefficient in the presence and absence of surfactant, respectively. In Figure 4.63a, we plot the results for D_p/D_{p0} versus the solid–liquid–gas contact angle, θ , for three different values of the parameters K and E characterizing the surface viscosities (see Equation 4.303): (1) $K = E = 1$; (2) $K = E = 5$, and (3) $K = E = 10$. The relatively small slope of the curves in Figure 4.63a indicates that D_p/D_{p0} depends less significantly on the contact angle, θ , than on the surface viscosity characterized by K and E . Note, however, that D_{p0} itself depends markedly on θ : the absolute value of D_{p0} is smaller for the smaller values of θ (for deeper immersion of the particle in the liquid phase). Figure 4.63b presents the calculated dependence of D_p/D_{p0} on the surface viscosity characterized by K and E ($K = E$ is used in the calculations) for various fixed values of the contact angle, θ . Apparently, the particle mobility decreases faster for the smaller values of K and then tends to zero insofar as the fluid surface “solidifies” for the higher values of the surface viscosities. The experimental data from measurements of the drag coefficient of spherical particles attached to fluid interfaces [346] showed very good agreement with the predictions of the theory [347].

The role of surface viscosity and elasticity on the motion of a solid particle trapped in a thin film, at an interface, or at a membrane of a spherical vesicle has been recently investigated in Refs. [856,857]. The theoretical results [856,857] have been applied to process the experimental data for the drag coefficient of polystyrene latex particles moving throughout the membrane of a giant lipid vesicle [858–864]. Thus, the interfacial viscosity of membranes has been determined. The motion of particles with different shapes trapped in thin liquid films and at Langmuir monolayers is studied intensively both theoretically and experimentally because of biological and medical applications [865–887].

4.5.6 BULK RHEOLOGY OF DISPERSIONS

The description of the general rheological behavior of colloidal dispersions requires information regarding the drag forces and torques experienced by the individual particles [404,888,889]. In

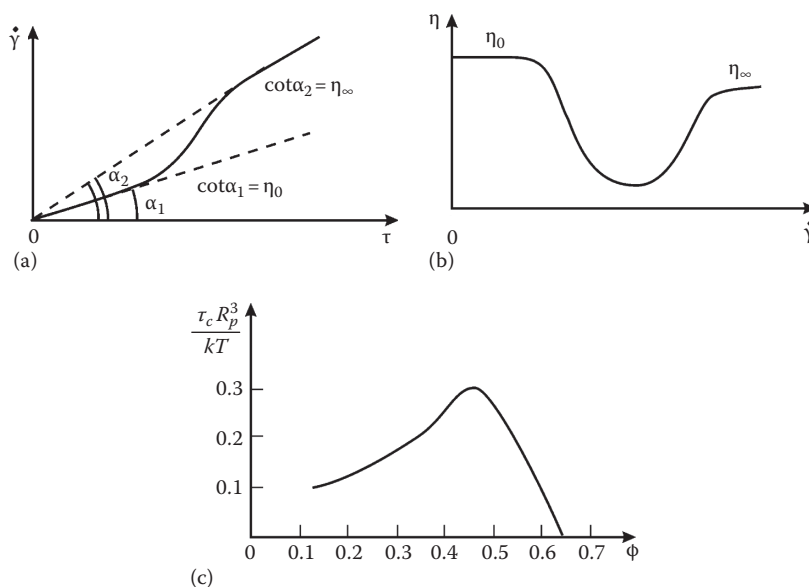


FIGURE 4.64 Qualitative presentation of basic relations in rheology of suspensions: (a) rate of strain, $\dot{\gamma}$, vs. applied stress, τ (see Equation 4.326); (b) average viscosity of a suspension, η , vs. rate of strain, $\dot{\gamma}$; (c) dimensionless parameter τ_c (Equation 4.330) vs. particle volume fraction ϕ .

dilute systems, the hydrodynamic interactions between the particles can be neglected and their motion can be treated independently. In contrast, when the particle concentration is higher, the effect of hydrodynamic interactions between a spherical particle and an interface on the drag force and torque acquires considerable importance. The viscosity and the collective diffusion coefficient of colloidal dispersions can also be strongly affected also by long-range surface forces, like the electrostatic double layer force.

Long ago Einstein [890] obtained a formula for the diffusion coefficient for solid spheres in the dilute limit:

$$D = \frac{kT}{6\pi\eta_m R_p} \quad (4.320)$$

where

R_p is the particle radius

η_m is the viscosity of the liquid medium

This relation was later generalized by Kubo [891] for the cases when the hydrodynamic resistance becomes important. The further development in this field is reviewed by Davis [824].

The particle–particle interactions lead to a dependence of the viscosity, η , of a colloidal dispersion on the particle volume fraction, ϕ . Einstein [892] showed that for a suspension of spherical particles in the dilute limit:

$$\eta = \eta_m[1 + 2.5\phi + O(\phi^2)] \quad (4.321)$$

Later Taylor [893] generalized Equation 4.321 for emulsion systems taking into account the viscous dissipation of energy due to the flow inside the droplets. Oldroyd [894] took into account the effect of surface viscosity and generalized the theory of Taylor [893] to diluted monodisperse emulsions whose droplets have viscous interfaces. Taylor [895], Fröhlich and Sack [896], and Oldroyd [897] applied asymptotic analysis to derive the next term in Equation 4.321 with respect to the capillary number. Thus, the effect of droplet interfacial tension was included. This generalization may be important at high shear rates. Another important generalization is the derivation of appropriate expressions for the viscosity of suspensions containing particles with different shapes [644,645]. A third direction of generalization of Equation 4.321 is to calculate the next term in the series with respect to the volume fraction, ϕ . Batchelor [898] took into account the long-range hydrodynamic interaction between the particles to derive:

$$\eta = \eta_m[1 + 2.5\phi + 6.2\phi^2 + O(\phi^3)] \quad (4.322)$$

From a mathematical viewpoint, Equation 4.322 is an exact result; however, from a physical viewpoint, Equation 4.322 is not entirely adequate to the real dispersions, as not only the long-range hydrodynamic interactions are operative in colloids. A number of empirical expressions have been proposed in which the coefficient multiplying ϕ^2 varies between 5 and 14 [899]. The development of new powerful numerical methods helped for a better understanding of the rheology of emulsions [900–908]. The simple shear and Brownian flow of dispersions of elastic capsules, rough spheres, and liquid droplets were studied in Refs. [901,905,907,908]. The effect of insoluble surfactants and the drop deformation on the hydrodynamic interactions and on the rheology of dilute emulsions are the subject of investigation in Refs. [902,904,906]. Loewenberg

TABLE 4.8
Maximum Packing Volume Fraction, ϕ_{\max} , for Various Arrangements of Monodisperse Spheres

Arrangement	ϕ_{\max}
Simple cubic	0.52
Minimum thermodynamically stable configuration	0.548
Hexagonally packed sheets just touching	0.605
Random close packing	0.637
Body-centered cubic packing	0.68
Face-centered cubic/hexagonal close packed	0.74

TABLE 4.9
Values of $[\eta]$ and ϕ_{\max} for a Number of Dispersions Obtained by Fitting Experimental Data by Means of Equation 4.331

System	$[\eta]$	ϕ_{\max}	$[\eta]\phi_{\max}$	References
Spheres (submicron)	2.7	0.71	1.92	De Kruijff et al. [899]
Spheres (40 μm)	3.28	0.61	2.00	Giesekus [926]
Ground gypsum	3.25	0.69	2.24	Turian and Yuan [927]
Titanium dioxide	4.0	0.55	2.75	Turian and Yuan [927]
Glass rods (30 \times 700 μm)	9.25	0.268	2.48	Clarke [928]
Quartz grains (53–76 μm)	4.8	0.371	2.15	Clarke [928]
<i>Glass fibers</i>				
Axial ratio-7	3.8	0.374	1.42	Giesekus [926]
Axial ratio-14	4.03	0.26	1.31	Giesekus [926]
Axial ratio-21	6.0	0.233	1.40	Giesekus [926]

and Hinch [900,903] discussed the basic ideas of the numerical simulations of concentrated emulsion flows. These works are aimed at giving a theoretical interpretation of various experimental results for dilute and concentrated dispersions. When the Peclet number is not small, the convective term in the diffusion equation (Equations 4.287 and 4.288) cannot be neglected and the respective problem has no analytical solution. Thus, a complex numerical investigation has to be applied [909,910].

The formulae of Einstein [890,892], Taylor [893], and Oldroyd [894] have been generalized for dilute emulsions of mobile surfaces with account for the Gibbs elasticity and the bulk and surface diffusion and viscosity [911]:

$$\frac{\eta}{\eta_m} = 1 + \left(1 + \frac{3}{2} \langle \varepsilon_m \rangle\right) \phi + O(\phi^2), \quad \langle \varepsilon_m \rangle \equiv \frac{\sum R_d^3 \varepsilon_m}{\sum R_d^3} \quad (4.323)$$

where $\langle \varepsilon_m \rangle$ is the average value of the interfacial mobility parameter, ε_m , for all droplets in the control volume. The mobility parameter of individual drops, ε_m , and the effective surfactant diffusion coefficient, D_{eff} , are [911]

$$\varepsilon_m \equiv \frac{(\eta_d/\eta_m) + (2/5)((R_d E_G/2\eta_m D_{\text{eff}}) + (3\eta_{\text{dl}} + 2\eta_{\text{sh}})/R_d \eta_m)}{1 + (\eta_d/\eta_m) + (2/5)((R_d E_G/2\eta_m D_{\text{eff}}) + (3\eta_{\text{dl}} + 2\eta_{\text{sh}})/R_d \eta_m)} \quad (4.324)$$

$$D_{\text{eff}} \equiv D_s + \frac{R_d D}{2h_a} + \frac{R_d D_d}{3h_{d,a}} \quad (4.325)$$

(see Equation 4.319 and the following section). If the droplet size distribution in the emulsion and the interfacial rheological parameters are known, then the average value $\langle \varepsilon_m \rangle$ can be estimated. For monodisperse emulsions, the average value, $\langle \varepsilon_m \rangle$, and the interfacial mobility parameter, ε_m , are equal. In the special case of completely mobile interfaces, that is, $R_d E_G/(\eta_m D_{\text{eff}}) \rightarrow 0$ and $(3\eta_{\text{dl}} + 2\eta_{\text{sh}})/(R_d \eta_m) \rightarrow 0$, the mobility parameter, ε_m , does not depend on the droplet size, and from Equation 4.324 and 4.325, the Taylor [891] formula is obtained. It is important to note that the Taylor formula takes into account only the bulk properties of the phases (characterized by η_d/η_m); in such a case ε_m is independent of R_d and the Taylor equation is also applicable to polydisperse emulsions. If only the Marangoni effect is neglected ($E_G \rightarrow 0$), then Equations 4.324 and 4.325 become equivalent to the Oldroyd [894] formula, which is originally derived only for monodisperse emulsions.

For higher values of the particle volume fraction, the rheological behavior of the colloidal dispersions becomes rather complex. We will consider qualitatively the observed phenomena, and next we will review available semiempirical expressions.

For a simple shear (Couette) flow, the relation between the applied stress, τ , and the resulting shear rate, $\dot{\gamma}$, can be expressed in the form:

$$\tau = \eta \dot{\gamma} \quad (4.326)$$

(e.g., when a liquid is sheared between two plates parallel to the xy plane, we have $\dot{\gamma} = \partial v_x / \partial z$.) A typical plot of $\dot{\gamma}$ versus τ is shown in Figure 4.64a. For low and high shear rates, we observe Newtonian behavior ($\eta = \text{constant}$), whereas in the intermediate region a transition from the lower shear rate viscosity, η_0 , to the higher shear rate viscosity, η_∞ , takes place. This is also visualized in Figure 4.64b, where the viscosity of the colloidal dispersion, η , is plotted versus the shear rate, $\dot{\gamma}$; note that in the intermediate zone η has a minimum value [636,640].

Note also that both η_0 and η_∞ depend on the particle volume fraction, ϕ . De Kruif et al. [899] proposed the semiempirical expansions:

$$\frac{\eta_0}{\eta_m} = 1 + 2.5\phi + (4 \pm 2)\phi^2 + (42 \pm 10)\phi^3 + \dots \quad (4.327)$$

$$\frac{\eta_\infty}{\eta_m} = 1 + 2.5\phi + (4 \pm 2)\phi^2 + (25 \pm 7)\phi^3 + \dots \quad (4.328)$$

as well as two empirical expressions which can be used in the whole range of values of ϕ :

$$\frac{\eta_0}{\eta_m} = \left(1 - \frac{\phi}{0.63}\right)^{-2}, \quad \frac{\eta_\infty}{\eta_m} = \left(1 - \frac{\phi}{0.71}\right)^{-2} \quad (4.329)$$

In regard to the dependence of η on the shear stress, τ , Russel et al. [404] reported that for the intermediate values of τ , corresponding to non-Newtonian behavior (Figure 4.64a and b), the experimental data correlate reasonably well with the expression:

$$\frac{\eta - \eta_\infty}{\eta - \eta_0} = \frac{1}{1 + (\tau/\tau_c)^n} \quad (4.330)$$

with $1 \leq n \leq 2$, where τ_c is the value of τ for which $\eta = (\eta_0 + \eta_\infty)/2$. In its own turn, τ_c depends on the particle volume fraction ϕ (see Figure 4.64c). We see that τ_c increases with the volume fraction, ϕ , in dilute dispersions then passes through a maximum and finally decreases down to zero; note that $\tau_c \rightarrow 0$ corresponds to $\eta \rightarrow \eta_\infty$. The peak at $\phi \approx 0.5$ is the only indication that the hard-sphere disorder–order transition either occurs or is rheologically significant in these systems [404].

The restoring force for a dispersion to return to a random, isotropic situation at rest is either Brownian (thermal fluctuations) or osmotic [912]. The former is most important for submicrometer particles and the latter for larger particles. Changing the flow conditions changes the structure, and this leads to thixotropic effects, which are especially strong in flocculated systems.

Krieger and Dougherty [913] applied the theory of corresponding states to obtain the following expression for the viscosity of hard-sphere dispersions:

$$\frac{\eta}{\eta_m} = \left(1 - \frac{\phi}{\phi_{\max}}\right)^{-[\eta]\phi_{\max}} \quad (4.331)$$

where

$[\eta]$ is the dimensionless intrinsic viscosity, which has a theoretical value of 2.5 for monodisperse rigid spheres

ϕ_{\max} is the maximum packing volume fraction for which the viscosity η diverges

The value of ϕ_{\max} depends on the type of packing of the particles [636] (Table 4.8). The maximum packing fraction, ϕ_{\max} , is very sensitive to particle-size distribution and particle shape [914]. Broader particle-size distributions have greater values of ϕ_{\max} . On the other hand, nonspherical particles lead to poorer space-filling and hence lower ϕ_{\max} . Table 4.9 presents the values of $[\eta]$ and ϕ_{\max} obtained by fitting the results of a number of experiments on dispersions of asymmetric particles using Equation 4.331. The trend of $[\eta]$ to increase and of ϕ_{\max} to decrease with increasing asymmetry is clearly seen, but the product, $[\eta]\phi_{\max}$, is almost constant; $[\eta]\phi_{\max}$ is about 2 for spheres and about 1.4 for fibers. This fact can be utilized to estimate the viscosity of a wide variety of dispersions.

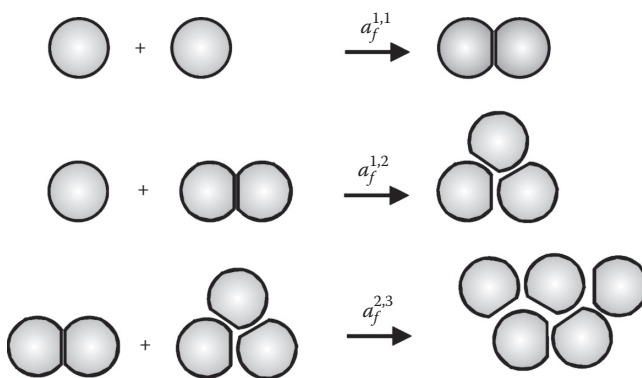


FIGURE 4.65 Elementary acts of flocculation according to the Smoluchowski scheme; $a_f^{i,j}$ ($i, j = 1, 2, 3, \dots$) are rate constants of flocculation.

A number of rheological experiments with foams and emulsions are summarized in the reviews by Prud'home and Khan [915] and Tadros [916]. These experiments demonstrate the influence of films between the droplets (or bubbles) on the shear viscosity of the dispersion as a whole. Unfortunately, there is no consistent theoretical explanation of this effect accounting for the different hydrodynamic resistance of the films between the deformed fluid particles as compared to the nondeformed spherical particles (see Sections 4.5.2 and 4.5.3). In the case of emulsions and foams, the deformed droplets or bubbles have a polyhedral shape, and maximum packing fraction can be $\phi_{\max} \approx 0.9$ and even higher. For this case, a special geometrical rheological theory has been developed [663,917,918].

Wessel and Ball [919] and Kanai et al. [920] studied in detail the effects of shear rate on the fractal structure of flocculated emulsion drops. They showed that the size of the flocs usually decreases with the increase of the shear stress; often the flocs are split to single particles at high shear rates. As a result, the viscosity decreases rapidly with the increase of shear rate.

Interesting effects are observed when dispersion contains both larger and smaller particles; the latter are usually polymer coils, spherical or cylindrical surfactant micelles, or microemulsion droplets. The presence of the smaller particles may induce clustering of the larger particles due to the depletion attraction (see Section 4.4.5.3.3); such effects are described in the works on surfactant-flocculated and polymer-flocculated emulsions [921–924]. Other effects can be observed in dispersions representing mixtures of liquid and solid particles. Yuhua et al. [925] have established that if the size of the solid particles is larger than three times the size of the emulsion drops, the emulsion can be treated as a continuous medium (of its own average viscosity), in which the solid particles are dispersed; such treatment is not possible when the solid particles are smaller.

Rheological properties of foams (elasticity, plasticity, and viscosity) play an important role in foam production, transportation, and applications. In the absence of external stress, the bubbles in foams are symmetrical and the tensions of the formed foam films are balanced inside the foam and close to the walls of the vessel [929]. At low external shear stresses, the bubbles deform and the deformations of the thin liquid films between them create elastic shear stresses. At a sufficiently large applied shear stress, the foam begins to flow. This stress is called the *yield stress*, τ_0 . Then, Equation 4.326 has to be replaced with the Bingham plastic model [930]:

$$\tau = \tau_0 + \eta \dot{\gamma} \quad (4.332)$$

Experiments show that in steadily sheared foams and concentrated emulsions, the viscosity coefficient η depends on the rate of shear strain, and in most cases the Herschel–Bulkley equation [931] is applicable:

$$\tau = \tau_0 + K \dot{\gamma}^n, \quad \eta = K \dot{\gamma}^{n-1} \quad (4.333)$$

Here

K is the consistency

n is the power-law index; $n < 1$ for shear thinning, whereas $n > 1$ for shear thickening

Systematic studies of the foam rheology [932–939] show that the power-law index varies between 0.25 and 0.5 depending on the elasticity of the individual air–solution surfaces. If the elasticity is lower than 10 mN/m, then n is close to 0.25, whereas for large surface elasticity (>100 mN/m) n increases to 0.5.

4.6 KINETICS OF COAGULATION

There are three scenarios for the occurrence of a two-particle collision in a dispersion depending on the type of particle–particle interactions. (1) If the repulsive forces are predominant, the two colliding particles will rebound and the colloidal dispersion will be stable. (2) When at a given separation the attractive and repulsive forces counterbalance each other (the film formed upon particle collision is stable), aggregates or flocs of attached particles can appear. (3) When the particles are fluid and the attractive interaction across the film is predominant, the film is unstable and ruptures; this leads to coalescence of the drops in emulsions or of the bubbles in foams.

To a great extent, the occurrence of coagulation is determined by the energy, U , of particle–particle interaction. U is related to the disjoining pressure, Π , by means of Equations 4.173 and 4.174. Qualitatively, the curves Π versus h (see Figure 4.17) and U versus h are similar. The coagulation is called fast or slow depending on whether the electrostatic barrier (see Figure 4.17) is less than kT or much higher than kT . In addition, the coagulation is termed *reversible* or *irreversible* depending on whether the depth of the primary minimum (see Figure 4.17) is comparable with kT or much greater than kT .

Three types of driving forces can lead to coagulation. (1) The body forces, such as gravity and centrifugal force, cause sedimentation of the heavier particles in suspensions or creaming of the lighter droplets in emulsions. (2) For the particles that are smaller than about 1 μm , the Brownian stochastic force dominates the body forces, and the Brownian collision of two particles becomes a prerequisite for their attachment and coagulation. (3) The temperature gradient in fluid dispersions causes thermocapillary migration of the particles driven by the Marangoni effect. The particles moving with different velocities can collide and form aggregates.

4.6.1 IRREVERSIBLE COAGULATION

The kinetic theory of fast irreversible coagulation was developed by von Smoluchowsky [940,941]. Later, the theory was extended to the case of slow and reversible coagulation. In any case of coagulation (flocculation), the general set of kinetic equations reads:

$$\frac{dn_k}{dt} = \frac{1}{2} \sum_{i=1}^{k-1} a_f^{i,k-i} n_i n_{k-i} - n_k \sum_{i=1}^{\infty} a_f^{k,i} n_i + q_k \quad (k = 1, 2, \dots) \quad (4.334)$$

Here

t is time

n_1 denotes the number of single particles per unit volume

n_k is the number of aggregates of k particles ($k = 2, 3, \dots$) per unit volume

$a_f^{i,j}$ ($i, j = 1, 2, 3, \dots$) are rate constants of flocculation (coagulation; see Figure 4.65)

q_k denotes the flux of aggregates of size k which are products of other processes, different from the flocculation itself (say, the reverse process of aggregate disassembly or the droplet coalescence in emulsions; see Equations 4.346 and 4.350)

In the special case of irreversible coagulation without coalescence, we have $q_k \equiv 0$. The first term in the right-hand side of Equation 4.334 is the rate of formation of k aggregates by the merging of two smaller aggregates, whereas the second term expresses the rate of loss of k aggregates due to their incorporation into larger aggregates. The total concentration of aggregates (as kinetically independent units), n , and the total concentration of the constituent particles (including those in aggregated form), n_{tot} , can be expressed as

$$n = \sum_{k=1}^{\infty} n_k, \quad n_{\text{tot}} = \sum_{k=1}^{\infty} kn_k \quad (4.335)$$

The rate constants can be expressed in the form:

$$a_{ij}^{i,j} = 4\pi D_{i,j}^{(0)}(R_i + R_j)E_{i,j} \quad (4.336)$$

where

$D_{i,j}^{(0)}$ is the relative diffusion coefficients for two flocks of radii R_i and R_j and aggregation number i and j , respectively

$E_{i,j}$ is the so-called collision efficiency [696,942]. We give expressions for $D_{i,j}^{(0)}$ and $E_{i,j}$ appropriate for various physical situations in the following section.

The Einstein approach (see Equation 4.320), combined with the Rybczynski–Hadamard equation (Equation 4.318), leads to the following expression for the relative diffusivity of two isolated Brownian droplets:

$$D_{i,j}^{(0)} = \frac{kT}{2\pi\eta} \frac{\eta_d + \eta}{3\eta_d + 2\eta} \left(\frac{1}{R_i} + \frac{1}{R_j} \right) \quad (\text{perikinetic coagulation}) \quad (4.337)$$

The limiting case $\eta_d \rightarrow 0$ corresponds to two bubbles, whereas in the other limit ($\eta_d \rightarrow \infty$) Equation 4.337 describes two solid particles or two fluid particles of tangentially immobile surfaces.

When the particle relative motion is driven by a body force or by the thermocapillary migration (rather than by self-diffusion), Equation 4.337 is no longer valid. Instead, in Equation 4.336 we have to formally substitute the following expression for $D_{i,j}^{(0)}$ (see Rogers and Davis [943]):

$$D_{i,j}^{(0)} = \frac{1}{4}(R_i + R_j)|\mathbf{v}_i - \mathbf{v}_j| \quad (\text{orthokinetic coagulation}) \quad (4.338)$$

Here \mathbf{v}_j denotes the velocity of a flock of aggregation number j . Physically, Equation 4.338 accounts for the fact that some particle (usually a larger one) moves faster than the remaining particles and can “capture” them upon collision. This type of coagulation is called *orthokinetic* to distinguish it from the self-diffusion-driven perikinetic coagulation described by Equation 4.337. In the case of gravity-driven flocculation, we can identify \mathbf{v}_j with the velocity U in Equation 4.318, where F is to be set equal to the gravitational force exerted on the particle; for a solid particle or a fluid particle of tangentially immobile surface, this yields $\mathbf{v}_j = 2g\Delta\rho R_j^2/(9\eta)$ with g the acceleration due to gravity and $\Delta\rho$ the density difference between the two phases.

In the case of orthokinetic coagulation of liquid drops driven by the thermocapillary migration, the particle velocity \mathbf{v}_j is given by the expression (see Young et al. [944]):

$$\mathbf{v}_j = \frac{2R_j E_T \lambda}{(3\eta_d + 2\eta)(\lambda_d + 2\lambda)} \nabla(\ln T) \quad (\text{thermocapillary velocity}) \quad (4.339)$$

where the thermal conductivity of the continuous and disperse phases are denoted by λ and λ_d , respectively. The interfacial thermal elasticity, E_T , is defined by Equation 4.293.

The collision efficiency, $E_{i,j}$, in Equation 4.336 accounts for the interactions (of both hydrodynamic and intermolecular origin) between two colliding particles. The inverse of $E_{i,j}$ is often called the *stability ratio* or the *Fuchs factor* [945] and can be expressed in the following general form [14,696]:

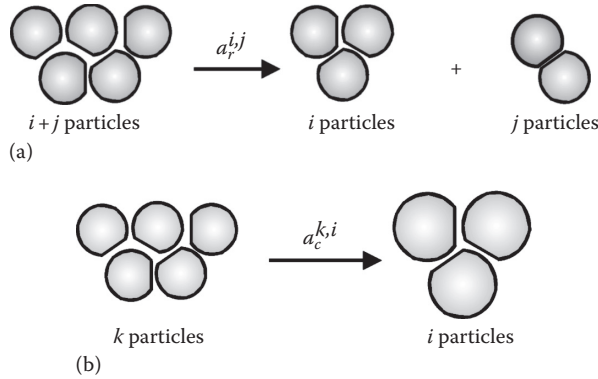


FIGURE 4.66 Elementary acts of aggregate splitting (a) and droplet coalescence within an aggregate (b); $a_r^{i,j}$ and $a_c^{k,i}$ ($i, j, k = 1, 2, 3, \dots$) are the rate constants of the respective processes.

$$W_{i,j} = \frac{1}{E_{i,j}} = 2 \int_0^\infty \frac{\beta(s)}{(s+2)^2} \exp\left[\frac{U_{i,j}(s)}{kT}\right] ds, \quad s \equiv \frac{2h}{R_i + R_j}$$

$$\beta \equiv \left(2\pi\eta R_* \frac{3\eta_d + 2\eta}{\eta_d + \eta}\right)^{-1} \frac{F_z}{V_z} \tag{4.340a}$$

where

- h is the closest surface-to-surface distance between the two particles
- R_* is defined by Equation 4.270
- $U_{i,j}(s)$ is the energy of (nonhydrodynamic) interactions between the particles (see Section 4.4)
- $\beta(s)$ accounts for the hydrodynamic interactions
- F_z/V_z is the particle friction coefficient

Thus, $\beta \rightarrow 1$ for $s \rightarrow \infty$, insofar as for large separations the particles obey the Rybczynski–Hadamard equation (Equation 4.318). In the opposite limit, $s \ll 1$, that is, close approach of the two particles, F_z/V_z can be calculated from Equations 4.271, 4.294 through 4.297, or 4.301, depending on the specific case. In particular, for $s \ll 1$ we have $\beta \propto 1/s$ for two solid particles (or fluid particles of tangentially immobile surfaces), $\beta \propto s^{-1/2}$ for two liquid droplets, and $\beta \propto \ln s$ for two gas bubbles. We see that for two solid particles ($\beta \propto 1/s$), the integral in Equation 4.340a may be divergent. To overcome this problem, one usually accepts that for the smallest separations $U_{i,j}$ is dominated by the van der Waals interaction, as given by Equation 4.185, that is, $U_{i,j} \rightarrow -\infty$, and, consequently, the integrand in Equation 4.340a tends to zero for $s \rightarrow 0$.

Note that the value of $W_{i,j}$ is determined mainly by the values of the integrand in the vicinity of the electrostatic maximum (barrier) of $U_{i,j}$ (see Figure 4.17), insofar as $U_{i,j}$ enters Equation 4.340a as an exponent. By using the method of the saddle point, Derjaguin [14] estimated the integral in Equation 4.340a:

$$W_{i,j} \equiv \frac{1}{E_{i,j}} \approx \left[\frac{8\pi kT}{-U_{i,j}''(s_m)} \right]^{1/2} \frac{\beta(s_m)}{(s_m + 2)^2} \exp\left[\frac{U_{i,j}(s_m)}{kT}\right] \tag{4.340b}$$

where s_m denotes the value of s corresponding to the maximum. We see that the larger the barrier, $U_{i,j}(s_m)$, the smaller the collision efficiency, $E_{i,j}$, and the slower the coagulation.

Note also that for imaginary particles, which experience neither long-range surface forces ($U_{i,j} = 0$) nor hydrodynamic interactions ($\beta = 1$), Equation 4.340a yields a collision efficiency $E_{i,j} = 1$

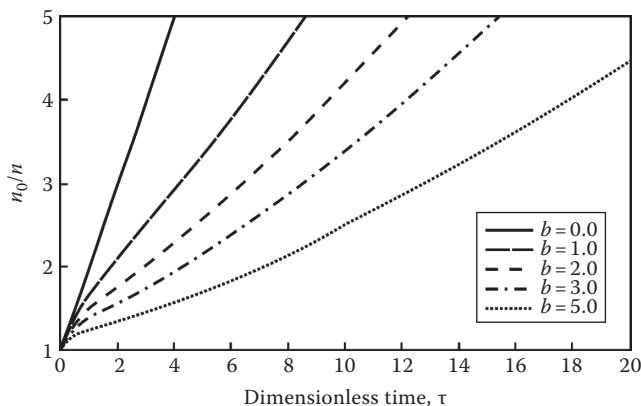


FIGURE 4.67 Reversible coagulation: theoretical plot of the inverse dimensionless aggregate concentration, n_0/n , vs. the dimensionless time, $\tau = a_f n_0 t / 2$, in the case of $M = 4$ and various values of the dimensionless ratio, $b = 2a_r / (n_0 a_p)$, of the rate constants of the reverse and straight process, a_r and a_p .

and Equation 4.336 reduces to the Smoluchowski [940,941] expression for the rate constant of the fast irreversible coagulation. In this particular case, Equation 4.334 represents an infinite set of nonlinear differential equations. If all flocculation rate constants are the same and equal to a_p , the problem has a unique exact solution [940,941]:

$$n = \frac{n_0}{1 + a_f n_0 t / 2}, \quad n_k = n_0 \frac{(a_f n_0 t / 2)^{k-1}}{(1 + a_f n_0 t / 2)^{k+1}} \quad (k = 1, 2, \dots) \quad (4.341)$$

It is supposed that the total average concentration of the constituent particles (in both singlet and aggregated form), n_{tot} , does not change and is equal to the initial number of particles, n_0 . Unlike n_{tot} , the concentration of the aggregates, n , decreases with time, while their size increases. Differentiating Equation 4.341 we obtain:

$$\frac{dn}{dt} = -\frac{a_f}{2} n^2, \quad \frac{d\bar{V}}{dt} = \frac{a_f}{2} \phi_0, \quad \bar{V} \equiv \frac{\phi_0}{n} \quad (4.342)$$

where

\bar{V} is the average volume per aggregate

ϕ_0 is the initial volume fraction of the constituent particles

Combining Equations 4.336 and 4.342, we obtain the following result for perikinetic (Brownian) coagulation:

$$\frac{\bar{V}}{V_0} = 1 + \frac{t}{t_{\text{Br}}}, \quad t_{\text{Br}} = \frac{R_0^2}{3\phi_0 D_0 E_0} \quad (4.343)$$

where

$V_0 = 4\pi R_0^3 / 3$ is the volume of a constituent particle

t_{Br} is the characteristic time of the coagulation process in this case

E_0 is an average collision efficiency

D_0 is an average diffusion coefficient

In contrast, \bar{V} is not a linear function of time for orthokinetic coagulation. When the flocculation is driven by a body force, that is, in case of sedimentation or centrifugation, we obtain [942]:

$$\frac{\bar{V}}{V_0} = \left(1 - \frac{t}{3t_{bf}}\right)^{-3}, \quad t_{bf} = \frac{2R_0}{3\phi_0 v_{bf} E_0} \tag{4.344}$$

where

- t_{bf} is the characteristic time in this case
- v_{bf} is an average velocity of aggregate motion

As discussed earlier, when the body force is gravitational, we have $v_{bf} = 2g\Delta\rho R_0^2 / (9\eta)$.

When the orthokinetic coagulation is driven by the thermocapillary migration, the counterpart of Equation 4.340 reads [942]

$$\frac{\bar{V}}{V_0} = \exp\left(\frac{t}{t_{tm}}\right), \quad t_{tm} = \frac{2R_0}{3\phi_0 v_{tm} E_0} \tag{4.345}$$

where

- v_{tm} is an average velocity of thermocapillary migration
- t_{tm} is the respective characteristic time

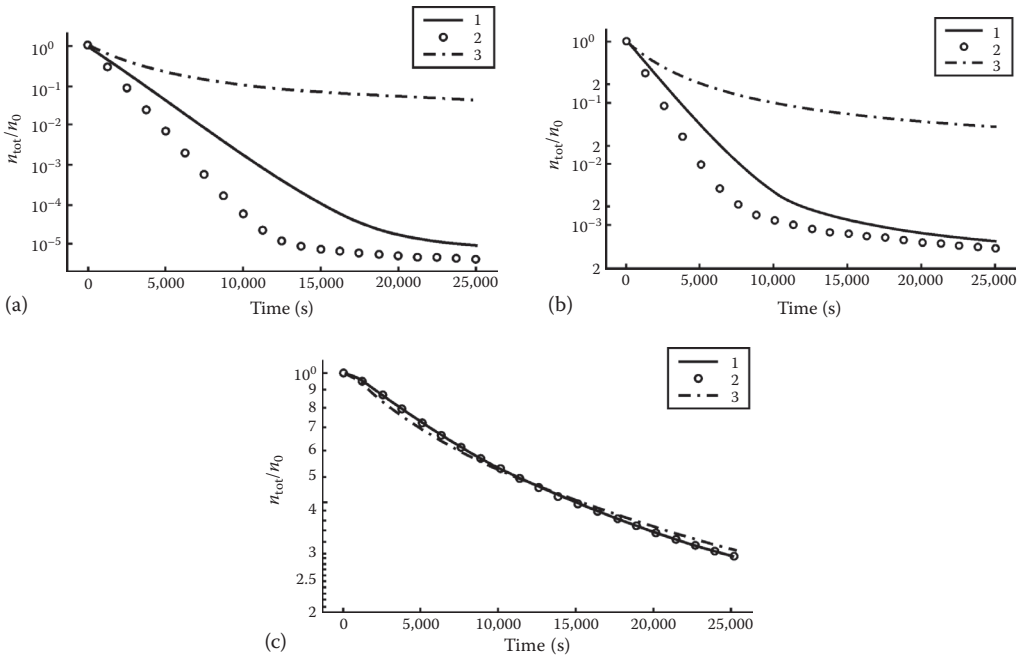


FIGURE 4.68 Relative change in the total number of drops, n_{tot} , vs. time, t ; initial number of primary drops $n_0 = 10^{12} \text{ cm}^{-3}$; coalescence rate constant $k_c^{2,1} \neq 10^{-3} \text{ s}^{-1}$. Curve 1: numerical solution of Equation 4.351. Curve 2: output of the model of Borwankar et al. [957]. Curve 3: output of the model of van den Tempel [956]. The values of the flocculation rate constant are (a) $a_f = 10^{-11} \text{ cm}^3/\text{s}$; (b) $a_f = 10^{-13} \text{ cm}^3/\text{s}$; (c) $a_f = 10^{-16} \text{ cm}^3/\text{s}$.

Note that $D_0 \propto R_0^{-1}$, $v_{\text{bf}} \propto R_0^2$, and $v_{\text{tm}} \propto R_0$ (see Equations 4.320 and 4.339). Then, from Equations 4.343 through 4.345, it follows that the three different characteristic times exhibit different dependencies on particle radius: $t_{\text{Br}} \propto R_0^3$, $t_{\text{bf}} \propto R_0^{-1}$, while t_{tm} is independent of R_0 . Thus, the Brownian coagulation is faster for the smaller particles, the body force-induced coagulation is more rapid for the larger particles, whereas the thermocapillary driven coagulation is not so sensitive to the particle size [946].

The Smoluchowski scheme based on Equations 4.341 and 4.342 has found numerous applications. An example for biochemical application is the study [947,948] of the kinetics of flocculation of latex particles caused by human gamma globulin in the presence of specific “key-lock” interactions. The infinite set of Smoluchowski equations (Equation 4.334) was solved by Bak and Heilmann [949] in the particular case when the aggregates cannot grow larger than a given size; an explicit analytical solution was obtained by these authors.

4.6.2 REVERSIBLE COAGULATION

In the case of reversible coagulation, the flocs can disaggregate because the primary minimum (Figure 4.17) is not deep enough [14]. For example, an aggregate composed of $i + j$ particles can be split on two aggregates containing i and j particles. We denote the rate constant of this reverse process by $a_r^{i,j}$ (Figure 4.66a). It is assumed that both the straight process of flocculation (Figure 4.65) and the reverse process (Figure 4.66a) take place. The kinetics of aggregation in this more general case is described by the Smoluchowski set of equations, Equation 4.334, where we have to substitute:

$$q_1 = \sum_{i=1}^{\infty} a_r^{1,i} n_{i+1}, \quad q_k = \sum_{i=1}^{\infty} a_r^{k,i} n_{i+k} - \frac{1}{2} n_k \sum_{i=1}^{k-1} a_r^{i,k-i} \quad (k = 2, 3, \dots) \quad (4.346)$$

In Equation 4.346 q_k equals the rate of formation of k aggregates in the process of disassembly of larger aggregates minus the rate of decay of the k aggregates. As before, the total number of constituent particles, n_{tot} , does not change. However, the total number of the aggregates, n , can either increase or decrease depending on whether the straight or the reverse process prevails. Summing up all Equations in 4.334 and using Equation 4.346, we derive the following equation for n :

$$\frac{dn}{dt} = \frac{1}{2} \sum_{i=1}^{\infty} \sum_{j=1}^{\infty} (a_r^{i,j} n_{i+j} - a_f^{i,j} n_i n_j) \quad (4.347)$$

Martinov and Muller [950] reported a general expression for the rate constants of the reverse process:

$$a_r^{i,j} = \frac{D_{i,j}^{(0)} E_{i,j}}{Z_{i,j}} \frac{1}{(R_i + R_j)^2} \quad (4.348)$$

where $Z_{i,j}$ is the so-called irreversible factor, which can be presented in the form

$$Z_{i,j} = \frac{1}{8} \int_{U_{i,j} < 0} (s+2)^2 \exp\left[-\frac{U_{i,j}(s)}{kT}\right] ds \quad (4.349)$$

The integration in Equation 4.349 is carried out over the region around the primary minimum, where $U_{i,j}$ takes negative values (see Figure 4.17). In other words, $Z_{i,j}$ is determined by the values

of $U_{i,j}$ in the region of the primary minimum, whereas $E_{i,j}$ is determined by the values of $U_{i,j}$ in the region of the electrostatic maximum (see Equations 4.340b and 4.349). When the minimum is deeper, $Z_{i,j}$ is larger and the rate constant in Equation 4.348 is smaller. In addition, as seen from Equations 4.340b and 4.348, the increase of the height of the barrier also decreases the rate of the reverse process. The physical interpretation of this fact is that to detach from an aggregate a particle has to first go out from the well and then to “jump” over the barrier (Figure 4.17).

To illustrate the effect of the reverse process on the rate of flocculation, we solved numerically the set of Equations 4.334, 4.346, and 4.347. To simplify the problem, we used the following assumptions: (1) the von Smoluchowski assumption that all rate constants of the straight process are equal to a_f ; (2) aggregates containing more than M particles cannot decay; (3) all rate constants of the reverse process are equal to a_r ; and (4) at the initial moment, only single constituent particles of concentration n_0 are available. In Figure 4.67, we plot the calculated curves of n_0/n versus the dimensionless time, $\tau = a_f n_0 t / 2$, for a fixed value, $M = 4$, and various values of the ratio of the rate constants of the straight and the reverse process, $b = 2a_r / (n_0 a_f)$. Note that n is defined by Equation 4.335. We see that in an initial time interval all curves in Figure 4.67 touch the von Smoluchowski distribution (corresponding to $b = 0$), but after this period we observe a reduction in the rate of flocculation, which is larger for the curves with larger values of b (larger rate constants of the reverse process). These S-shaped curves are typical for the case of reversible coagulation, which is also confirmed by the experiment [14,951].

4.6.3 KINETICS OF SIMULTANEOUS FLOCCULATION AND COALESCENCE IN EMULSIONS

When coalescence is present, in addition to the flocculation, the total number of constituent drops, n_{tot} (see Equation 4.335), does change, in contrast to the case of pure flocculation considered earlier [34]. Hartland and Gakis [952], and Hartland and Vohra [953] were the first to develop a model of coalescence that relates the lifetime of single films to the rate of phase separation in emulsions of fairly large drops (approximately 1 mm) in the absence of surfactant. Their analysis was further extended by Lobo et al. [954] to quantify the process of coalescence within an already creamed or settled emulsion (or foam) containing drops of size less than 100 μm ; these authors also took into account the effect of surfactants, which are commonly used as emulsifiers. Danov et al. [955] generalized the Smoluchowski scheme to account for the fact that the droplets within the flocs can coalesce to give larger droplets, as illustrated in Figure 4.66b. In this case, in the right-hand side of Equation 4.334 we have to substitute [955]

$$q_1 = \sum_{i=2}^{\infty} a_c^{i,1} n_i, \quad q_k = \sum_{i=k+1}^{\infty} a_c^{i,k} n_i - n_k \sum_{i=1}^{k-1} a_c^{k,i} \quad (k = 2, 3, \dots) \quad (4.350)$$

where $a_c^{k,i}$ is the rate constant of transformation (by coalescence) of an aggregate containing k droplets into an aggregate containing i droplets (see Figure 4.66b). The newly formed aggregate is further involved in the flocculation scheme, which thus accounts for the fact that the flocculation and coalescence processes are interdependent. In this scheme, the total coalescence rate, $a_{c,\text{tot}}^i$, and the total number of droplets, n_{tot} , obey the following equation [955]:

$$\frac{dn_{\text{tot}}}{dt} = - \sum_{i=2}^{\infty} a_{c,\text{tot}}^i n_i, \quad a_{c,\text{tot}}^i = \sum_{k=1}^{i-1} (i-k) a_c^{i,k} \quad (i = 2, 3, \dots) \quad (4.351)$$

To determine the rate constants of coalescence, $a_c^{k,i}$, Danov et al. [665] examined the effects of droplet interactions and Brownian motion on the coalescence rate in dilute emulsions of micrometer- and submicrometer-sized droplets. The processes of film formation, thinning, and rupture were included

as consecutive stages in the scheme of coalescence. Expressions for the interaction energy due to the various DLVO and non-DLVO surface forces between two deformed droplets were obtained [392] (see also Section 4.4).

Average models for the total number of droplets are also available [956,957]. The average model of van den Tempel [956] assumes linear structure of the aggregates. The coalescence rate is supposed to be proportional to the number of contacts within an aggregate. To simplify the problem, van den Tempel has used several assumptions, one of them is that the concentration of the single droplets, n_1 , obeys the Smoluchowski distribution (Equation 4.341) for $k = 1$. The average model of Borwankar et al. [957] is similar to that of van den Tempel but is physically more adequate. The assumptions used by the latter authors [957] make their solution more applicable to cases in which the flocculation (rather than the coalescence) is slow and is the rate determining stage. This is confirmed by the curves shown in Figure 4.68 which are calculated for the same rate of coalescence, but for three different rates of flocculation. For relatively high rates of flocculation (Figure 4.68a), the predictions of the three theories differ. For the intermediate rates of flocculation (Figure 4.68b), the prediction of the model by Borwankar et al. [957] is close to that of the more detailed model by Danov et al. [955]. For very low values of the flocculation rate constant, a_f , for which the coalescence is not the rate-determining stage, all three theories [955–957] give numerically close results (Figure 4.68c). Details about the coupling of coalescence and flocculation in dilute oil-in-water emulsions, experimental investigations, and numerical modeling can be found in Refs. [958–966].

ACKNOWLEDGMENTS

The authors gratefully acknowledge the support from the FP7 project Beyond-Everest, and from COST Action CM1101.

REFERENCES

1. Jungermann, E., *Cationic Surfactants*, Marcel Dekker, New York, 1970.
2. Lucassen-Reynders, E.H., *Anionic Surfactants—Physical Chemistry of Surfactant Action*, Marcel Dekker, New York, 1981.
3. Schick, M.J., *Nonionic Surfactants: Physical Chemistry*, Marcel Dekker, New York, 1986.
4. Gibbs, J.W., *The Scientific Papers of J.W. Gibbs*, Vol. 1, Dover, New York, 1961.
5. Ono, S. and Kondo, S., Molecular theory of surface tension in liquids, in *Handbuch der Physik*, Vol. 3/10, Flügge, S. (Ed.), Springer, Berlin, Germany, 1960, pp. 134–280.
6. Adamson, A.W. and Gast, A.P., *Physical Chemistry of Surfaces*, 6th edn., Wiley, New York, 1997.
7. Freundlich, H., *Colloid and Capillary Chemistry*, Methuen, London, U.K., 1926.
8. Langmuir, I., *J. Am. Chem. Soc.*, 40, 1361, 1918.
9. Volmer, M., *Z. Physikal. Chem.*, 115, 253, 1925.
10. Frumkin, A., *Z. Physikal. Chem.*, 116, 466, 1925.
11. Hill, T.L., *An Introduction to Statistical Thermodynamics*, Addison-Wesley, Reading, MA, 1962.
12. Lucassen-Reynders, E.H., *J. Phys. Chem.*, 70, 1777, 1966.
13. Borwankar, R.P. and Wasan, D.T., *Chem. Eng. Sci.*, 43, 1323, 1988.
14. Derjaguin, B.V., *Theory of Stability of Colloids and Thin Liquid Films*, Plenum Press, Consultants Bureau, New York, 1989.
15. Shchukin, E.D., Pertsov, A.V., and Amelina, E.A., *Colloid Chemistry*, Moscow University Press, Moscow, Russia, 1982 (Russian); Elsevier, 2001 (English).
16. Danov, K.D. and Kralchevsky, P.A., *Colloid J.*, 74, 172, 2012.
17. Rosen, M.J. and Aronson, S., *Colloids Surf.*, 3, 201, 1981.
18. Zeldowitch, J., *Acta Physicochim. (USSR)*, 1, 961, 1934.
19. Halsey, G. and Taylor, H.S., *J. Chem. Phys.*, 15, 624, 1947.
20. Gurkov, T.G., Kralchevsky, P.A., and Nagayama, K., *Colloid Polym. Sci.*, 274, 227, 1996.
21. Butler, J.A.V., *Proc. Roy. Soc. Ser. A*, 135, 348, 1932.

22. Fainerman, V.B. and Miller, R., *Langmuir*, 12, 6011, 1996.
23. Vaughn, M.W. and Slattery, J. C., *J. Colloid Interface Sci.*, 195, 1, 1997.
24. Makievski, A.V., Fainerman, V.B., Bree, M., Wüstneck, R., Krägel, J., and Miller, R., *J. Phys. Chem. B*, 102, 417, 1998.
25. Landau, L.D. and Lifshitz, E.M., *Statistical Physics*, Part 1, Pergamon, Oxford, U.K., 1980.
26. Kralchevsky, P.A., Danov, K.D., Broze, G., and Mehreteab, A., *Langmuir*, 15, 2351, 1999.
27. Hachisu, S., *J. Colloid Interface Sci.*, 33, 445, 1970.
28. Kalinin, V.V. and Radke, C.J., *Colloids Surf. A*, 114, 337, 1996.
29. Warszyński, P., Barzyk, W., Lunkenheimer, K., and Fruhner, H., *J. Phys. Chem. B*, 102, 10948, 1998.
30. Prosser, A.J. and Frances, E.I., *Colloids Surf. A*, 178, 1, 2001.
31. Kirkwood, J.G. and Oppenheim, I., *Chemical Thermodynamics*, McGraw-Hill, New York, 1961.
32. Robinson, R.A. and Stokes, R.H., *Electrolyte Solutions*, Butterworths, London, U.K., 1959.
33. Gouy, L.G., *J. Phys.*, 9, 457, 1910.
34. Davies, J. and Rideal, E., *Interfacial Phenomena*, Academic Press, New York, 1963.
35. Grahame, D.C., *Chem. Rev.*, 41, 441, 1947.
36. Israelachvili, J.N., *Intermolecular and Surface Forces*, Academic Press, London, U.K., 2011.
37. Kralchevsky, P.A. and Nagayama, K., *Particles at Fluid Interfaces and Membranes*, Elsevier, Amsterdam, the Netherlands, 2001.
38. Matijević, E. and Pethica, B.A., *Trans. Faraday Soc.*, 54, 1382, 1958.
39. van Voorst Vader, F., *Trans. Faraday Soc.*, 56, 1067, 1960.
40. Tajima, K., *Bull. Chem. Soc. Jpn.*, 44, 1767, 1971.
41. Stern, O., *Ztschr. Elektrochem.*, 30, 508, 1924.
42. Tajima, K., Muramatsu, M., and Sasaki, T., *Bull. Chem. Soc. Jpn.*, 43, 1991, 1970.
43. Tajima, K., *Bull. Chem. Soc. Jpn.*, 43, 3063, 1970.
44. Kolev, V.L., Danov, K.D., Kralchevsky, P.A., Broze, G., and Mehreteab, A., *Langmuir*, 18, 9106, 2002.
45. Cross, A.W. and Jayson, G.G., *J. Colloid Interface Sci.*, 162, 45, 1994.
46. Johnson, S.B., Drummond, C.J., Scales, P.J., and Nishimura, S., *Langmuir*, 11, 2367, 1995.
47. Alargova, R.G., Danov, K.D., Petkov, J.T., Kralchevsky, P.A., Broze, G., and Mehreteab, A., *Langmuir*, 13, 5544, 1997.
48. Rathman, J.F. and Scamehorn, J.F., *J. Phys. Chem.*, 88, 5807, 1984.
49. Berr, S.S., Coleman, M.J., Marriot, J., and Johnson Jr., J.S., *J. Phys. Chem.*, 90, 6492, 1986.
50. Rosen, M.J., *Surfactants and Interfacial Phenomena*, Wiley, New York, 1989.
51. Clint, J., *Surfactant Aggregation*, Chapman & Hall, London, U.K., 1992.
52. Alargova, R.G., Danov, K.D., Kralchevsky, P.A., Broze, G., and Mehreteab, A., *Langmuir*, 14, 4036, 1998.
53. Dimov, N.K., Kolev, V.L., Kralchevsky, P.A., Lyutov, L.G., Brose, G., and Mehreteab, A., *J. Colloid Interface Sci.*, 256, 23, 2002.
54. Kralchevsky, P.A., Danov, K.D., Kolev, V.L., Broze, G., and Mehreteab, A., *Langmuir*, 19, 5004, 2003.
55. Danov, K.D., Kralchevsky, P.A., Ananthapadmanabhan, K.P., and Lips, A., *J. Colloid Interface Sci.*, 300, 809, 2006.
56. Lunkenheimer, K., Barzyk, W., Hirte, R., and Rudert, R., *Langmuir*, 19, 6140, 2003.
57. Christov, N.C., Danov, K.D., Kralchevsky, P.A., Ananthapadmanabhan, K.P., and Lips, A., *Langmuir*, 22, 7528, 2006.
58. Danov, K.D., Kralchevska, S.D., Kralchevsky, P.A., Broze, G., and Mehreteab, A., *Langmuir*, 19, 5019, 2003.
59. Danov, K.D., Kralchevska, S.D., Kralchevsky, P.A., Ananthapadmanabhan, K.P., and Lips, A., *Langmuir*, 20, 5445, 2004.
60. Valkovska, D.S., Shearman, G.C., Bain, C.D., Darton, R.C., and Eastoe, J., *Langmuir*, 20, 4436, 2004.
61. Day, J.P.R., Campbell, R.A., Russell, O.P., and Bain, C.D., *J. Phys. Chem. C*, 111, 8757, 2007.
62. Valkovska, D.S., Danov, K.D., and Ivanov, I.B., *Colloids Surf. A*, 175, 179, 2000.
63. Danov, K.D., Kralchevsky, P.A., and Ivanov, I.B., Dynamic processes in surfactant stabilized emulsions, in *Encyclopedic Handbook of Emulsion Technology*, Sjöblom, J. (Ed.), Marcel Dekker, New York, 2001, Chapter 26 pp. 621–659.
64. Dukhin, S.S., Kretschmar, G., and Miller, R., *Dynamics of Adsorption at Liquid Interfaces*, Elsevier, Amsterdam, the Netherlands, 1995.
65. Eastoe, J. and Dalton, J.S., *Adv. Colloid Interface Sci.*, 85, 103, 2000.
66. Rayleigh, L., *Proc. Roy. Soc. (Lond.)*, 29, 71, 1879.
67. Bohr, N., *Philos. Trans. Roy. Soc. (Lond.) A*, 209, 281, 1909.

68. Defay, R. and Pétré, G., Dynamic surface tension, in *Surface and Colloid Science*, Vol. 3, Matijević, E. (Ed.), Wiley, New York, 1971, p. 27.
69. Miller, R. and Kretzschmar, G., *Adv. Colloid Interface Sci.*, 37, 97, 1991.
70. Wantke, K.-D., Lunkenheimer, K., and Hempt, C., *J. Colloid Interface Sci.*, 159, 28, 1993.
71. Chang, C.-H. and Franses, E.I., *J. Colloid Interface Sci.*, 164, 107, 1994.
72. Johnson, D.O. and Stebe, K.J., *J. Colloid Interface Sci.*, 182, 525, 1996.
73. Horozov, T. and Arnaudov, L., *J. Colloid Interface Sci.*, 219, 99, 1999.
74. Horozov, T. and Arnaudov, L., *J. Colloid Interface Sci.*, 222, 146, 2000.
75. van den Tempel, M. and Lucassen-Reynders, E.H., *Adv. Colloid Interface Sci.*, 18, 281, 1983.
76. Langevin, D., *Colloids Surf.*, 43, 121, 1990.
77. Lemaire, C. and Langevin, D., *Colloids Surf.*, 65, 101, 1992.
78. Grigorev, D.O., Krotov, V.V., and Noskov, B.A., *Colloid J.*, 56, 562, 1994.
79. Mysels, K.J., *Colloids Surf.*, 43, 241, 1990.
80. Kralchevsky, P.A., Radkov, Y.S., and Denkov, N.D., *J. Colloid Interface Sci.*, 161, 361, 1993.
81. Fainerman, V.B., Miller, R., and Joos, P., *Colloid Polym. Sci.*, 272, 731, 1994.
82. Fainerman, V.B. and Miller, R., *J. Colloid Interface Sci.*, 176, 118, 1995.
83. Horozov, T.S., Dushkin, C.D., Danov, K.D., Arnaudov, L.N., Velev, O.D., Mehreteab, A., and Broze, G., *Colloids Surf. A*, 113, 117, 1996.
84. Mishchuk, N.A., Dukhin, S.S., Fainerman, V.B., Kovalchuk, V.I., and Miller, R., *Colloids Surf. A*, 192, 157, 2001.
85. van den Bogaert, R. and Joos, P., *J. Phys. Chem.*, 83, 17, 1979.
86. Möbius, D. and Miller, R. (Eds.), *Drops and Bubbles in Interfacial Research*, Elsevier, Amsterdam, the Netherlands, 1998.
87. Jho, C. and Burke, R., *J. Colloid Interface Sci.*, 95, 61, 1983.
88. Joos, P. and van Hunsel, J., *Colloid Polym. Sci.*, 267, 1026, 1989.
89. Fainerman, V.B. and Miller, R., *Colloids Surf. A*, 97, 255, 1995.
90. Miller, R., Bree, M., and Fainerman, V.B., *Colloids Surf. A*, 142, 237, 1998.
91. Senkel, O., Miller, R., and Fainerman, V.B., *Colloids Surf. A*, 143, 517, 1998.
92. Bain, C.D., Manning-Benson, S., and Darton, R.C., *J. Colloid Interface Sci.*, 229, 247, 2000.
93. Rotenberg, Y., Boruvka, L., and Neumann, A.W., *J. Colloid Interface Sci.*, 37, 169, 1983.
94. Makievski, A.V., Loglio, G., Krägel, J., Miller, R., Fainerman, V.B., and Neumann, A.W., *J. Phys. Chem.*, 103, 9557, 1999.
95. Joos, P., *Dynamic Surface Phenomena*, VSP BV, AH Zeist, the Netherlands, 1999.
96. Ward, A.F.H. and Tordai, L., *J. Chem. Phys.*, 14, 453, 1946.
97. Miller, R., *Colloid Polym. Sci.*, 259, 375, 1981.
98. McCoy, B.J., *Colloid Polym. Sci.*, 261, 535, 1983.
99. Hansen, R.S., *J. Chem. Phys.*, 64, 637, 1960.
100. Filippov, L.K., *J. Colloid Interface Sci.*, 164, 471, 1994.
101. Daniel, R. and Berg, J.C., *J. Colloid Interface Sci.*, 237, 294, 2001.
102. Sutherland, K.L., *Aust. J. Sci. Res.*, A5, 683, 1952.
103. Arfken, G.B., Weber, H.J. and Harris, F.E., *Mathematical Methods for Physicists*, Elsevier, Amsterdam, 2013.
104. Korn, G.A. and Korn, T.M., *Mathematical Handbook*, McGraw-Hill, New York, 1968.
105. Danov, K.D., Kolev, V.L., Kralchevsky, P.A., Broze, G., and Mehreteab, A., *Langmuir*, 16, 2942, 2000.
106. Dukhin, S.S., Miller, R., and Kretzschmar, G., *Colloid Polym. Sci.*, 261, 335, 1983.
107. Dukhin, S.S. and Miller, R., *Colloid Polym. Sci.*, 272, 548, 1994.
108. MacLeod, C. and Radke, C.J., *Langmuir*, 10, 3555, 1994.
109. Vlahovska, P.M., Danov, K.D., Mehreteab, A., and Broze, G., *J. Colloid Interface Sci.*, 192, 194, 1997.
110. Danov, K.D., Vlahovska, P.M., Kralchevsky, P.A., Broze, G., and Mehreteab, A., *Colloids Surf. A*, 156, 389, 1999.
111. Diamant, H. and Andelman, D., *J. Phys. Chem.*, 100, 13732, 1996.
112. Diamant, H., Ariel, G., and Andelman, D., *Colloids Surf. A*, 183–185, 259, 2001.
113. Dattwani, S.S. and Stebe, K.J., *J. Colloid Interface Sci.*, 219, 282, 1999.
114. Danov, K.D., Kralchevsky, P.A., Ananthapadmanabhan, K.P., and Lips, A., *J. Colloid Interface Sci.*, 303, 56, 2006.
115. Nayfeh, A.H., *Perturbation Methods*, Wiley, New York, 1973.
116. Rillaerts, E. and Joos, P., *J. Colloid Interface Sci.*, 88, 1, 1982.

117. Durbut, P., Surface activity, in *Handbook of Detergents*, Part A, Broze, G. (Ed.), Marcel Dekker, New York, 1999, Chapter 3 pp. 47–98.
118. Bond, W.N. and Puls, H.O., *Philos. Mag.*, 24, 864, 1937.
119. Doss, K.S.G., *Koll. Z.*, 84, 138, 1938.
120. Blair, C.M., *J. Chem. Phys.*, 16, 113, 1948.
121. Ward, A.F.H., *Surface Chemistry*, Butterworths, London, U.K., 1949.
122. Dervichian, D.G., *Koll. Z.*, 146, 96, 1956.
123. Hansen, R.S. and Wallace, T., *J. Phys. Chem.*, 63, 1085, 1959.
124. Baret, J.F., *J. Phys. Chem.*, 72, 2755, 1968.
125. Baret, J.F., *J. Chem. Phys.*, 65, 895, 1968.
126. Baret, J.F., *J. Colloid Interface Sci.*, 30, 1, 1969.
127. Borwankar, R.P. and Wasan, D.T., *Chem. Eng. Sci.*, 38, 1637, 1983.
128. Alexandrov, N.A., Marinova, K.G., Gurkov, T.D., Danov, K.D., Kralchevsky, P.A., Stoyanov, S.D., Blijdenstein, T.B.J., Arnaudov, L.N., Pelan, E.G., and Lips, A., *J. Colloid Interface Sci.*, 376, 296, 2012.
129. Danov, K.D., Valkovska, D.S., and Kralchevsky, P.A., *J. Colloid Interface Sci.*, 251, 18, 2002.
130. Dong, C., Hsu, C.-T., Chin, C.-Y., and Lin, S.-Y., *Langmuir*, 16, 4573, 2000.
131. McBain, J.W., *Trans. Faraday Soc.*, 9, 99, 1913.
132. Vincent, B., *Adv. Colloid Interface Sci.*, 203, 51, 2014.
133. Missel, P.J., Mazer, N.A., Benedek, G.B., Young, C.Y., and Carey, M.C., *J. Phys. Chem.*, 84, 1044, 1980.
134. Anachkov, S.E., Kralchevsky, P.A., Danov, K.D., Georgieva, G.S., and Ananthapadmanabhan, K.P., *J. Colloid Interface Sci.*, 416, 258, 2014.
135. Kralchevsky, P.A., Danov, K.D., Anachkov, S.E., Georgieva, G.S., and Ananthapadmanabhan, K.P., *Curr. Opin. Colloid Interface Sci.*, 18, 524, 2013.
136. Danov, K.D., Kralchevsky, P.A., and Ananthapadmanabhan, K.P., *Adv. Colloid Interface Sci.*, 206, 17, 2014.
137. Mitchell, D.J. and Ninham, B.W., *J. Phys. Chem.*, 87, 2996, 1983.
138. Evans, E.A. and Skalak, R., *CRC Crit. Rev. Bioengin.*, 3, 181, 1979.
139. Kralchevsky, P.A., Danov, K.D., and Anachkov, S.E., *Colloid J.*, 76, 255, 2014.
140. Kresheck, G.C., Hamory, E., Davenport, G., and Scheraga, H.A., *J. Am. Chem. Soc.*, 88, 246, 1966.
141. Aniansson, E.A.G. and Wall, S.N., *J. Phys. Chem.*, 78, 1024, 1974.
142. Lucassen, J., *Faraday Discuss. Chem. Soc.*, 59, 76, 1975.
143. Noskov, B.A., *Kolloidn. Zh.*, 52, 509, 1990.
144. Johner, A. and Joanny, J.F., *Macromolecules*, 23, 5299, 1990.
145. Dushkin, C.D., Ivanov, I.B., and Kralchevsky, P.A., *Colloids Surf.*, 60, 235, 1991.
146. Joos, P. and van Hunsel, J., *Colloids Surf.*, 33, 99, 1988.
147. Li, B., Joos, P., and van Uffelen, M., *J. Colloid Interface Sci.*, 171, 270, 1995.
148. Geeraerts, G. and Joos, P., *Colloids Surf. A*, 90, 149, 1994.
149. Danov, K.D., Kralchevsky, P.A., Denkov, N.D., Ananthapadmanabhan, K.P., and Lips, A., *Adv. Colloid Interface Sci.*, 119, 1, 2006.
150. Danov, K.D., Kralchevsky, P.A., Denkov, N.D., Ananthapadmanabhan, K.P., and Lips, A., *Adv. Colloid Interface Sci.*, 119, 17, 2006.
151. Danov, K.D., Kralchevsky, P.A., Ananthapadmanabhan, K.P., and Lips, A., *Colloids Surf. A*, 282–283, 143, 2006.
152. McBain, J.W., *Colloidal Science*, D.C. Heat, Lexington, MA, 1950.
153. Christian, S.D. and Scamehorn, J.F., *Solubilization in Surfactant Aggregates*, Marcel Dekker, New York, 1995.
154. Miller, C.A., Micellar systems and microemulsions: solubilization aspects, in *Handbook of Surface and Colloid Chemistry*, 1st edn., Birdi, K.S. (Ed.), CRC Press, Boca Raton, FL, 1997, p. 157.
155. Vasilescu, M., Caragheorghopol, A., and Caldararu, H., *Adv. Colloid Interface Sci.*, 89–90, 169, 2001.
156. Carroll, B.J., *J. Colloid Interface Sci.*, 79, 126, 1981.
157. Kabalnov, A. and Weers, J., *Langmuir*, 12, 3442, 1996.
158. Weiss, J., Coupland, J.N., Brathwaite, D., and McClements, D.J., *Colloids Surf. A*, 121, 53, 1997.
159. Todorov, P.D., Kralchevsky, P.A., Denkov, N.D., Broze, G., and Mehreteab, A., *J. Colloid Interface Sci.*, 245, 371, 2002.
160. Kralchevsky, P.A. and Denkov, N.D., Triblock copolymers as promoters of solubilization of oils in aqueous surfactant solutions, in *Molecular Interfacial Phenomena of Polymers and Biopolymers*, Chen, P. (Ed.), Woodhead Publishing, Cambridge, U.K., 2005, Chapter 15, p. 538.
161. Sailaja, D., Suhasini, K.L., Kumar, S., and Gandhi, K.S., *Langmuir*, 19, 4014, 2003.

162. Chan, A.F., Fennel Evans, D., and Cussler, E.L., *AIChE J.*, 22, 1006, 1976.
163. Huang, C., Fennel Evans, D., and Cussler, E.L., *J. Colloid Interface Sci.*, 82, 499, 1981.
164. Shaeiwitz, J.A., Chan, A.F.-C., Cussler, E.L. and Fennel Evans, D., *J. Colloid Interface Sci.*, 84, 47, 1981.
165. Plucinski, P. and Nitsch, W., *J. Phys. Chem.*, 97, 8983, 1993.
166. Chen, B.-H., Miller, C.A., and Garrett, P.R., *Colloids Surf. A*, 128, 129, 1997.
167. Chen, B.-H., Miller, C.A., and Garrett, P.R., *Langmuir*, 14, 31, 1998.
168. Christov, N.C., Denkov, N.D., Kralchevsky, P.A., Broze, G., and Mehreteab, A., *Langmuir*, 18, 7880, 2002.
169. Kralchevsky, P.A., Denkov, N.D., Todorov, P.D., Marinov, G.S., Broze, G., and Mehreteab, A., *Langmuir*, 18, 7887, 2002.
170. Todorov, P.D., Marinov, G.S., Kralchevsky, P.A., Denkov, N.D., Durbut, P., Broze, G., and Mehreteab, A., *Langmuir*, 18, 7896, 2002.
171. Granek, R., *Langmuir*, 12, 5022, 1996.
172. Lawrence, A.S.C., *Discuss. Faraday Soc.*, 25, 51, 1958.
173. Lawrence, A.S.C., Bingham, A., Capper, C.B., and Hume, K., *J. Phys. Chem.*, 68, 3470, 1964.
174. Stowe, L.R. and Shaeiwitz, J.A., *J. Colloid Interface Sci.*, 90, 495, 1982.
175. Raterman, K.T. and Shaeiwitz, J.A., *J. Colloid Interface Sci.*, 98, 394, 1984.
176. Lim, J.-C. and Miller, C.A., *Langmuir*, 7, 2021, 1991.
177. Somasundaran, P. and Krishnakumar, S., *Colloids Surf. A*, 123–124, 491, 1997.
178. Ward, A.J., Kinetics of solubilization in surfactant-based systems, in *Solubilization in Surfactant Aggregates*, Christian, S.D. and Scamehorn, J.F. (Eds.), Marcel Dekker, New York, 1995, Chapter 7, pp. 237–272.
179. Nagarajan, R. and Ganesh, K., *J. Colloid Interface Sci.*, 184, 489, 1996.
180. Lebens, P.J.M. and Keurentjes, J.T.F., *Ind. Eng. Chem. Res.*, 35, 3415, 1996.
181. Xing, L. and Mattice, W.L., *Macromolecules*, 30, 1711, 1997.
182. Kříž, J., Masař, B., and Doskočilová, D., *Macromolecules*, 30, 4391, 1997.
183. Marinov, G., Michels, B., and Zana, R., *Langmuir*, 14, 2639, 1998.
184. Kositzka, M.J., Bohne, C., Alexandridis, P.T., Hatton, T.A., and Holzwarth, J.F., *Langmuir*, 15, 322, 1999.
185. Walderhaug, H., *J. Phys. Chem. B*, 103, 3352, 1999.
186. Paterson, I.F., Chowdhry, B.Z., Leharne, S.A., *Langmuir*, 15, 6178, 1999.
187. Bromberg, L. and Temchenko, M., *Langmuir*, 15, 8627, 1999.
188. Laplace, P.S., *Traité de mécanique céleste; Suppléments au Livre X*, 1805, 1806.
189. Bakker, G., Kapillartät und oberflächenspannung, in *Handbuch der Experimentalphysik*, Band 6, Akademische Verlagsgesellschaft, Leipzig, Germany, 1928.
190. Princen, H.M., The equilibrium shape of interfaces, drops, and bubbles, in *Surface and Colloid Science*, Vol. 2, Matijevic, E. (Ed.), Wiley, New York, 1969, p. 1.
191. Finn, R., *Equilibrium Capillary Surfaces*, Springer-Verlag, New York, 1986.
192. Weatherburn, C.E., *Differential Geometry in Three Dimensions*, Cambridge, U.K., 1930.
193. McConnell, A.J., *Application of Tensor Analysis*, Dover, New York, 1957.
194. Young, T., *Philos. Trans. Roy. Soc. (Lond.)*, 95, 55, 1805.
195. Jonson, R.E. and Dettre, Wettability and contact angles, in *Surface and Colloid Science*, Vol. 2, Matijevic, E. (Ed.), Wiley, New York, 1969, p. 85.
196. Starov, V.M., *Adv. Colloid Interface Sci.*, 39, 147, 1992.
197. Neumann, F., *Vorlesungen über die Theorie der Capillarität*, B.G. Teubner, Leipzig, Germany, 1894.
198. Ivanov, I.B., Kralchevsky, P.A., and Nikolov, A.D., *J. Colloid Interface Sci.*, 112, 97, 1986.
199. Hartland, S. and Hartley, R.W., *Axisymmetric Fluid-Liquid Interfaces*, Elsevier, Amsterdam, the Netherlands, 1976.
200. Kralchevsky, P.A., Eriksson, J.C., and Ljunggren, S., *Adv. Colloid Interface Sci.*, 48, 19, 1994.
201. Tachev, K.D., Angarska, J.K., Danov, K.D., and Kralchevsky, P.A., *Colloids Surf. B*, 19, 61, 2000.
202. Meunier, J. and Lee, L.T., *Langmuir*, 7, 1855, 1991.
203. Dan, N., Pincus, P., and Safran, S.A., *Langmuir*, 9, 2768, 1993.
204. Kralchevsky, P.A., Paunov, V.N. Denkov, N.D., and Nagayama, K., *J. Chem. Soc. Faraday Trans.*, 91, 3415, 1995.
205. Danov, K.D., Kralchevsky, P.A., and Stoyanov, S.D., *Langmuir*, 26, 143, 2010.
206. Basheva, E.S., Kralchevsky, P.A., Christov, N.C., Danov, K.D., Stoyanov, S.D., Blijdenstein, T.B.J., Kim, H.-J., Pelan, E.G., and Lips, A., *Langmuir*, 27, 2382, 2011.
207. Petsev, D.N., Denkov, N.D., and Kralchevsky, P.A., *J. Colloid Interface Sci.*, 176, 201, 1995.
208. De Gennes, P.G. and Taupin, C., *J. Phys. Chem.*, 86, 2294, 1982.

209. Concus, P., *J. Fluid Mech.*, 34, 481, 1968.
210. Kralchevsky, P.A., Ivanov, I.B., and Nikolov, A.D., *J. Colloid Interface Sci.*, 112, 108, 1986.
211. Abramowitz, M. and Stegun, I.A., *Handbook of Mathematical Functions*, Dover, New York, 1965.
212. Jahnke, E., Emde, F., and Lösch, F., *Tables of Higher Functions*, McGraw-Hill, New York, 1960.
213. Lo, L.L., *J. Fluid Mech.*, 132, 65, 1983.
214. Derjaguin, B.V., *Dokl. Akad. Nauk USSR*, 51, 517, 1946.
215. Scheludko, A. and Exerowa, D., *Comm. Dept. Chem. Bulg. Acad. Sci.*, 7, 123, 1959.
216. Sheludko, A., *Adv. Colloid Interface Sci.*, 1, 391, 1967.
217. Dimitrov, A.S., Kralchevsky, P.A., Nikolov, A.D., and Wasan, D.T., *Colloids Surf.*, 47, 299, 1990.
218. J. Plateau, Experimental and theoretical researches on the figures of equilibrium of a liquid mass withdrawn from the action of gravity, in *The Annual Report of the Smithsonian Institution*, Washington, DC, 1863, pp. 207–285.
219. J. Plateau, The figures of equilibrium of a liquid mass, in *The Annual Report of the Smithsonian Institution*, Washington, DC, 1864, pp. 338–369.
220. J. Plateau, *Statique Expérimentale et Théoretique des Liquides Soumis aux Seules Forces Moléculaires*, Gauthier-Villars, Paris, France, 1873.
221. Orr, F.M., Scriven, L.E., and Rivas, A.P., *J. Fluid Mech.*, 67, 723, 1975.
222. McFarlane, J.S. and Tabor, D., *Proc. R. Soc. Lond. A*, 202, 224, 1950.
223. Koos, E. and Willenbacher, N., *Science*, 331, 897, 2011.
224. Zettlemoyer, A.C., *Nucleation*, Marcel Dekker, New York, 1969.
225. Abraham, E.F., *Homogeneous Nucleation Theory*, Academic Press, New York, 1974.
226. Thomson, W. (Lord Kelvin), *Proc. Roy. Soc.*, 9, 225, 1858; Thomson, W., *Philos. Mag.*, 17, 61, 1859.
227. Lupis, C.H.P., *Chemical Thermodynamics of Materials*, North-Holland, New York, 1983.
228. Lifshitz, I.M. and Slyozov, V.V., *Zh. Exp. Teor. Fiz.*, 35, 479, 1958 (in Russian).
229. Wagner, C., *Z. Electrochem.*, 35, 581, 1961.
230. Kahlweit, M., *Faraday Discuss. Chem. Soc.*, 61, 48, 1976.
231. Parbhakar, K., Lewandowski, J., and Dao, L.H., *J. Colloid Interface Sci.*, 174, 142, 1995.
232. Kabalnov, A.S., Pertzov, A.V., and Shchukin, E.D., *Colloids Surf.*, 24, 19, 1987.
233. Kabalnov, A.S. and Shchukin, E.D., *Adv. Colloid Interface Sci.*, 38, 69, 1992.
234. McClements, D.J., Dungan, S.R., German, J.B., and Kinsela, J.E., *Food Hydrocolloids*, 6, 415, 1992.
235. Weiss, J., Coupland, J.N., and McClements, D.J., *J. Phys. Chem.*, 100, 1066, 1996.
236. Weiss, J., Cancelliere, C., and McClements, D.J., *Langmuir*, 16, 6833, 2000.
237. Kabalnov, A.S., *Langmuir*, 10, 680, 1994.
238. Ivanov, I.B. and Kralchevsky, P.A., Mechanics and thermodynamics of curved thin liquid films, in *Thin Liquid Films*, Ivanov, I.B. (Ed.), Marcel Dekker, New York, 1988, p. 49.
239. Kralchevsky, P.A. and Ivanov, I.B., *J. Colloid Interface Sci.*, 137, 234, 1990.
240. Kralchevsky, P.A., Danov, K.D., and Ivanov, I.B., Thin liquid film physics, in *Foams: Theory, Measurements and Applications*, Prud'homme, R.K. (Ed.), Marcel Dekker, New York, 1995, p. 1.
241. Rusanov, A.I., *Phase Equilibria and Surface Phenomena*, Khimia, Leningrad, Russia, 1967 (Russian); *Phasengleichgewichte und Grenzflächenerscheinungen*, Akademie Verlag, Berlin, Germany, 1978 (German).
242. Derjaguin, B.V. and Kussakov, M.M., *Acta Physicochem. USSR*, 10, 153, 1939.
243. Exerowa, D. and Scheludko, A., *Bull. Inst. Chim. Phys. Bulg. Acad. Sci.*, 4, 175, 1964.
244. Mysels, K.J., *J. Phys. Chem.*, 68, 3441, 1964.
245. Exerowa, D., *Commun. Dept. Chem. Bulg. Acad. Sci.*, 11, 739, 1978.
246. Kruglyakov, P.M., Equilibrium properties of free films and stability of foams and emulsions, in *Thin Liquid Films*, Ivanov, I.B. (Ed.), Marcel Dekker, New York, 1988, p. 767.
247. Martynov, G.A. and Derjaguin, B.V., *Kolloidn. Zh.*, 24, 480, 1962.
248. Toshev, B.V. and Ivanov, I.B., *Colloid Polym. Sci.*, 253, 558, 1975.
249. Ivanov, I.B. and Toshev, B.V., *Colloid Polym. Sci.*, 253, 593, 1975.
250. Frumkin, A., *Zh. Phys. Khim. USSR*, 12, 337, 1938.
251. de Feijter, J.A., Thermodynamics of thin liquid films, in *Thin Liquid Films*, Ivanov, I.B. (Ed.), Marcel Dekker, New York, 1988, p. 1.
252. Kralchevsky, P.A. and Ivanov, I.B., *Chem. Phys. Lett.*, 121, 111, 1985.
253. Nikolov, A.D., Kralchevsky, P.A., Ivanov, I.B., and Dimitrov, A.S., *AIChE Symp. Ser.*, 82(252), 82, 1986.
254. de Feijter, J.A. and Vrij, A., *J. Electroanal. Chem.*, 47, 9, 1972.
255. Kralchevsky, P.A. and Ivanov, I.B., *Chem. Phys. Lett.*, 121, 116, 1985.
256. Denkov, N.D., Petsev, D.N., and Danov, K.D., *J. Colloid Interface Sci.*, 176, 189, 1995.

257. Derjaguin, B.V., *Acta Physicochim. USSR*, 12, 181, 1940.
258. Princen, H.M. and Mason, S.G., *J. Colloid Sci.*, 20, 156, 1965.
259. Prins, A., *J. Colloid Interface Sci.*, 29, 177, 1969.
260. Clint, J.H., Clunie, J.S., Goodman, J.F., and Tate, J.R., *Nature (Lond.)*, 223, 291, 1969.
261. Yamanaka, T., *Bull. Chem. Soc. Jpn*, 48, 1755, 1975.
262. Princen, H.M., *J. Phys. Chem.*, 72, 3342, 1968.
263. Princen, H.M. and Frankel, S., *J. Colloid Interface Sci.*, 35, 186, 1971.
264. Scheludko, A., Radoev, B., and Kolarov, T., *Trans. Faraday Soc.*, 64, 2213, 1968.
265. Haydon, D.A. and Taylor, J.L., *Nature (Lond.)*, 217, 739, 1968.
266. Kolarov, T. and Zorin, Z.M., *Kolloidn. Zh.*, 42, 899, 1980.
267. Kruglyakov, P.M. and Rovin, Y.G., *Physical Chemistry of Black Hydrocarbon Films*, Nauka, Moscow, Russia, 1978 (in Russian).
268. Marinova, K.G., Gurkov, T.D., Velev, O.D., Ivanov, I.B., Campbell, B., and Borwankar, R.P., *Colloids Surf. A*, 123, 155, 1997.
269. Françon, M., *Progress in Microscopy*, Pergamon Press, London, U.K., 1961.
270. Beyer, H., *Theorie und Praxis der Interferenzmicroscopie*, Akademische Verlagsgesellschaft, Leipzig, Germany, 1974.
271. Zorin, Z.M., *Kolloidn. Zh.*, 39, 1158, 1977.
272. Zorin, Z., Platikanov, D., Rangelova, N., and Scheludko, A., Measurements of contact angles between bulk liquids and Newton black films for determining the line tension, in *Surface Forces and Liquid Interfaces*, Derjaguin, B.V. (Ed.), Nauka, Moscow, Russia, 1983, p. 200 (in Russian).
273. Nikolov, A.D., Kralchevsky, P.A., and Ivanov, I.B., *J. Colloid Interface Sci.*, 112, 122, 1986.
274. Lobo, L.A., Nikolov, A.D., Dimitrov, A.S., Kralchevsky, P.A., and Wasan, D.T., *Langmuir*, 6, 995, 1990.
275. Dimitrov, A.S., Nikolov, A.D., Kralchevsky, P.A., and Ivanov, I.B., *J. Colloid Interface Sci.*, 151, 462, 1992.
276. Picard, G., Schneider, J.E., and Fendler, J.H., *J. Phys. Chem.*, 94, 510, 1990.
277. Picard, G., Denicourt, N., and Fendler, J.H., *J. Phys. Chem.*, 95, 3705, 1991.
278. Skinner, F.K., Rotenberg, Y., and Neumann, A.W., *J. Colloid Interface Sci.*, 130, 25, 1989.
279. Dimitrov, A.S., Kralchevsky, P.A., Nikolov, A.D., Noshi, H., and Matsumoto, M., *J. Colloid Interface Sci.*, 145, 279, 1991.
280. Hadjiiski, A., Dimova, R., Denkov, N.D., Ivanov, I.B., and Borwankar, R., *Langmuir*, 12, 6665, 1996.
281. Ivanov, I.B., Hadjiiski, A., Denkov, N.D., Gurkov, T.D., Kralchevsky, P.A., and Koyasu, S., *Biophys. J.*, 75, 545, 1998.
282. Paunov, V.N., *Langmuir*, 19, 7970, 2003.
283. Cayre, O.J. and Paunov, V.N., *Langmuir*, 20, 9594, 2004.
284. Ikeda, S., Takahara, Y.K., Ishino, S., Matsumura, M., and Ohtani, B., *Chem. Lett.*, 34(10), 1386, 2005.
285. Paunov, V.N., Cayre, O.J., Noble, P.F., Stoyanov, S.D., Velikov, K.P., and Golding, M., *J. Colloid Interface Sci.*, 312, 381, 2007.
286. Park, B.J., Pantina, J.P., Furst, E.M., Oettel, M., Reynaert, S., and Vermant, J., *Langmuir*, 24, 1686, 2008.
287. Nicolson, M.M., *Proc. Camb. Philos. Soc.*, 45, 288, 1949.
288. Chan, D.Y.C., Henry, J.D., and White, L.R., *J. Colloid Interface Sci.*, 79, 410, 1981.
289. Paunov, V.N., Kralchevsky, P.A., Denkov, N.D., Ivanov, I.B., and Nagayama, K., *J. Colloid Interface Sci.*, 157, 100, 1993.
290. Kralchevsky, P.A., Paunov, V.N., Ivanov, I.B., and Nagayama, K., *J. Colloid Interface Sci.*, 151, 79, 1992.
291. Kralchevsky, P.A., Paunov, V.N., Denkov, N.D., Ivanov, I.B., and Nagayama, K., *J. Colloid Interface Sci.*, 155, 420, 1993.
292. Kralchevsky, P.A. and Nagayama, K., *Langmuir*, 10, 23, 1994.
293. Kralchevsky, P.A. and Nagayama, K., *Adv. Colloid Interface Sci.*, 85, 145, 2000.
294. Denkov, N.D., Velev, O.D., Kralchevsky, P.A., Ivanov, I.B., Nagayama, K., and Yoshimura, H., *Langmuir*, 8, 3183, 1992.
295. Dimitrov, A.S., Dushkin, C.D., Yoshimura, H., and Nagayama, K., *Langmuir*, 10, 432, 1994.
296. Sasaki, M. and Hane, K., *J. Appl. Phys.*, 80, 5427, 1996.
297. Du, H., Chen, P., Liu, F., Meng, F.-D., Li, T.-J., and Tang, X.-Y., *Mater. Chem. Phys.*, 51, 277, 1977.
298. Price, W.C., Williams, R.C., and Wyckoff, R.W.G., *Science*, 102, 277, 1945.
299. Cosslett, V.E. and Markham, R., *Nature*, 161, 250, 1948.
300. Home, R.W. and Pasquali-Ronchetti, I., *J. Ultrastruct. Res.*, 47, 361, 1974.
301. Harris, J.R., *Micron Microsc. Acta*, 22, 341, 1991.
302. Yoshimura, H., Matsumoto, M., Endo, S., and Nagayama, K., *Ultramicroscopy*, 32, 265, 1990.

303. Yamaki, M., Higo, J., and Nagayama, K., *Langmuir*, 11, 2975, 1995.
304. Nagayama, K., *Colloids Surf. A*, 109, 363, 1996.
305. Burmeister, F., Schäfle, C., Keilhofer, B., Bechinger, C., Boneberg, J., and Leiderer, P., *Adv. Mater.*, 10, 495, 1998.
306. Xia, Y., Tien, J., Qin, D., and Whitesides, G.M., *Langmuir*, 12, 4033, 1996.
307. Lindström, H., Rensmo, H., Sodergren, S., Solbrand, A., and Lindquist, S.E., *J. Phys. Chem.*, 100, 3084, 1996.
308. Matsushita, S., Miwa, T., and Fujishima, A., *Langmuir*, 13, 2582, 1997.
309. Murray, C.B., Kagan, C.R., and Bawendi, M.G., *Science*, 270, 1335, 1995.
310. Jap, B.K., Zulauf, M., Scheybani, T., Hefti, A., Baumeister, W., Aebi, U., and Engel, A., *Ultramicroscopy*, 46, 45, 1992.
311. De Rossi, D., Ahluwalia, A., and Mulè, M., *IEEE Eng. Med. Biol.*, 13, 103, 1994.
312. Kralchevsky, P.A. and Denkov, N.D., *Curr. Opin. Colloid Interface Sci.*, 6, 383, 2001.
313. Gil, T., Ipsen, J.H., Mouritsen, O.G., Sabra, M.C., Sperotto, M.M., and Zuckermann, M.J., *Biochim. Biophys. Acta*, 1376, 245, 1998.
314. Mansfield, S.L., Gotch, A.J., and Harms, G.S., *J. Phys. Chem., B*, 103, 2262, 1999.
315. Fisher, L.R. and Malloy, A.R., *Annu. Rep. Prog. Chem., Sect. C*, 95, 373, 1999.
316. Kralchevsky, P.A., Paunov, V.N., and Nagayama, K., *J. Fluid Mech.*, 299, 105, 1995.
317. Camoin, C., Roussel, J.F., Faure, R., and Blanc, R., *Europhys. Lett.*, 3, 449, 1987.
318. Velev, O.D., Denkov, N.D., Paunov, V.N., Kralchevsky, P.A., and Nagayama, K., *Langmuir*, 9, 3702, 1993.
319. Dushkin, C.D., Kralchevsky, P.A., Yoshimura, H., and Nagayama, K., *Phys. Rev. Lett.*, 75, 3454, 1995.
320. Lucassen, J., *Colloids Surf.*, 65, 131, 1992.
321. Stamou, D., Duschl, C., and Johannsmann, D., *Phys. Rev., E*, 62, 5263, 2000.
322. Kralchevsky, P.A., Denkov, N.D., and Danov, K.D., *Langmuir*, 17, 2001, 7694.
323. Danov, K.D., Kralchevsky, P.A., Naydenov, B.N., and Brenn, G., *J. Colloid Interface Sci.*, 287, 121, 2005.
324. Danov, K.D. and Kralchevsky, P.A., *Adv. Colloid Interface Sci.*, 154, 91, 2010.
325. Bowden, N., Terfort, A., Carbeck, J., and Whitesides, G.M., *Science*, 276, 233, 1997.
326. Bowden, N., Choi, I.S., Grzybowski, B.A., and Whitesides, G.M., *J. Am. Chem. Soc.*, 121, 5373, 1999.
327. Brown, A.B.D., Smith, C.G., and Rennie, A.R., *Phys. Rev. E*, 62, 951, 2000.
328. Loudet, J.C., Alsayed, A.M., Zhang, J., and Yodh, A.G., *Phys. Rev. Lett.*, 94, 018301, 2005.
329. Loudet, J.C., Yodh, A.G., and Pouligny, B., *Phys. Rev. Lett.*, 97, 018304, 2006.
330. Loudet, J.C. and Pouligny, B., *Europhys. Lett.*, 85, 28003, 2009.
331. van Nierop, E.A., Stijnman, M.A., and Hilgenfeldt, S., *Europhys. Lett.*, 72, 671, 2005.
332. Lehle, H., Noruzifar, E., and Oettel, M., *Eur. Phys. J. E*, 26, 151, 2008.
333. Lewandowski, E.P., Bernate, J.A., Searson, P.C., and Stebe, K.J., *Langmuir*, 24, 9302, 2008.
334. Lewandowski, E.P., Bernate, J.A., Tseng, A., Searson, P.C., and Stebe, K.J., *Soft Matter*, 5, 886, 2009.
335. Lewandowski, E.P., Cavallaro, M., Botto, L., Bernate, J.C., Garbin, V., and Stebe, K.J., *Langmuir*, 26, 15142, 2010.
336. Cavallaro, M., Botto, L., Lewandowski, E.P., Wang, M., and Stebe, K.J., *Proc. Natl. Acad. Sci. U.S.A.*, 108, 20923, 2011.
337. Botto, L., Lewandowski, E.P., Cavallaro, M., and Stebe, K.J., *Soft Matter*, 8, 9957, 2012.
338. Yunker, P.J., Still, T., Lohr, M.A., and Yodh, A.G., *Nature*, 476, 308, 2011.
339. Bleibel, J., Dominguez, A., and Oettel, M., *Eur. Phys. J.—Special Topics*, 222, 3071, 2013.
340. Velikov, K.P., Durst, F., and Velev, O.D. *Langmuir*, 14, 1148, 1998.
341. Sur, J. and Pak, H.K., *J. Korean Phys. Soc.*, 38, 582, 2001.
342. Danov, K.D., Pouligny, B., Angelova, M.I., and Kralchevsky, P.A., Strong capillary attraction between spherical inclusions in a multilayered lipid membrane, in *Studies in Surface Science and Catalysis*, Vol. 132, Iwasawa, Y., Oyama, N., and Kunieda, H. (Eds.), Elsevier, Amsterdam, the Netherlands, 2001, p. 519.
343. Danov, K.D., Pouligny, B., and Kralchevsky, P.A., *Langmuir*, 17, 2001, 6599.
344. Kralchevsky, P.A., Paunov, V.N., Denkov, N.D., and Nagayama, K., *J. Colloid Interface Sci.*, 167, 47, 1994.
345. Velev, O.D., Denkov, N.D., Paunov, V.N., Kralchevsky, P.A., and Nagayama, K., *J. Colloid Interface Sci.*, 167, 66, 1994.
346. Petkov, J.T., Denkov, N.D., Danov, K.D., Velev, O.D., Aust, R., and Durst, F., *J. Colloid Interface Sci.*, 172, 147, 1995.
347. Danov, K.D., Aust, R., Durst, F., and Lange, U., *J. Colloid Interface Sci.*, 175, 36, 1995.
348. Petkov, J.T., Danov, K.D., Denkov, N.D., Aust, R., and Durst, F., *Langmuir*, 12, 2650, 1996.

349. Petkov, J.T., Gurkov, T.D., and Campbell, B.E., *Langmuir*, 17, 4556, 2001.
350. Danov, K.D., Kralchevsky, P.A., Ananthapadmanabhan, K.P., and Lips, A., *Langmuir*, 22, 106, 2006.
351. Danov, K.D., Kralchevsky, P.A., and Boneva, M.P., *Langmuir*, 20, 6139, 2004.
352. Aveyard, R., Clint, J.H., Nees, D., and Paunov, V.N., *Langmuir*, 16, 1969, 2000.
353. Nikolaidis, M.G., Bausch, A.R., Hsu, M.F., Dinsmore, A.D., Brenner, M.P., Gay, C., and Weitz, D.A., *Nature*, 420, 299, 2002.
354. Danov, K.D., Kralchevsky, P.A., and Boneva, M.P., *Langmuir*, 22, 2653, 2006.
355. Danov, K.D. and Kralchevsky, P.A., *J. Colloid Interface Sci.*, 298, 213, 2006.
356. Aveyard, R., Binks, B.P., Clint, J.H., Fletcher, P.D.I., Horozov, T.S., Neumann, B., Paunov, V.N. et al., *Phys. Rev. Lett.*, 88, 246102, 2002.
357. Horozov, T.S., Aveyard, R., Clint, J.H., and Binks, B.P., *Langmuir*, 19, 2822, 2003.
358. Horozov, T.S., Aveyard, R., Binks, B.P., and Clint, J.H., *Langmuir*, 21, 7407, 2005.
359. Horozov, T.S. and Binks, B.P., *Colloids Surf. A*, 267, 64, 2005.
360. Ray, M.A. and Li, J., *Adv. Mater.*, 19, 2020, 2007.
361. Stancik, E.J., Kouhkan, M., and Fuller, G.G., *Langmuir*, 20, 90, 2004.
362. Reynaert, S., Moldenaers, P., and Vermant, J., *Langmuir*, 22, 4936, 2006.
363. Petkov, P.V., Danov, K.D., and Kralchevsky, P.A., *Langmuir*, 30, 2768, 2014.
364. Domínguez, A., Oettel, M., and Dietrich, S., *J. Chem. Phys.* 127, 204706, 2007.
365. Labib, M.E. and Williams, R., *J. Colloid Interface Sci.*, 115, 330, 1987.
366. Philipse, A.P. and Vrij, A., *J. Colloid Interface Sci.*, 128, 121, 1989.
367. Aubry, N. and Singh, P., *Phys. Rev. E*, 77, 056302, 2008.
368. Aubry, N., Singh, P., Janjua, M., and Nudurupati, S., *Proc. Natl. Acad. Sci. U.S.A.*, 105, 3711, 2008.
369. Janjua, M., Nudurupati, S., Singh, P., and Aubry, N., *Mech. Res. Commun.*, 36, 55, 2009.
370. Singh, P., Joseph, D.D., and Aubry, N., *Soft Matter*, 6, 4310, 2010.
371. Danov, K.D. and Kralchevsky, P.A., *J. Colloid Interface Sci.*, 405, 278, 2013.
372. Danov, K.D. and Kralchevsky, P.A., *J. Colloid Interface Sci.*, 405, 269, 2013.
373. Megens, M. and Aizenberg, J., *Nature*, 424, 1014, 2003.
374. Oettel, M., Domínguez, A., and Dietrich, S., *Phys. Rev. E*, 71, 051401, 2005.
375. Würger, A. and Foret, L., *J. Phys. Chem. B*, 109, 16435, 2005.
376. Danov, K.D. and Kralchevsky, P.A., *J. Colloid Interface Sci.*, 345, 505, 2010.
377. Boneva, M.P., Christov, N.C., Danov, K.D., and Kralchevsky, P.A., *Phys. Chem. Chem. Phys.*, 9, 6371, 2007.
378. Boneva, M.P., Danov, K.D., Christov, N.C., and Kralchevsky, P.A., *Langmuir*, 25, 9129, 2009.
379. Kralchevsky, P.A. and Danov, K.D., Interactions between particles at a fluid interface, in *Nanoscience: Colloidal and Interfacial Aspects*, Starov, V.M. (Ed.), CRC Press, New York, 2010, p. 397.
380. Derjaguin, B.V., Churaev, N.V., and Muller, V.M., *Surface Forces*, Plenum Press, Consultants Bureau, New York, 1987.
381. Derjaguin, B.V., *Kolloid Zeits.*, 69, 155, 1934.
382. Attard, P. and Parker, J.L., *J. Phys. Chem.*, 96, 5086, 1992.
383. Tabor, D. and Winterton, R.H.S., *Nature*, 219, 1120, 1968.
384. Keesom, W.H., *Proc. Amst.*, 15, 850, 1913.
385. Debye, P., *Physik*, 2, 178, 1920.
386. London, F., *Z. Physics*, 63, 245, 1930.
387. Hamaker, H.C., *Physics*, 4, 1058, 1937.
388. Usui, S., Sasaki, H., and Hasegawa, F., *Colloids Surf.*, 18, 53, 1986.
389. Lifshitz, E.M., *Soviet Phys. JETP (Engl. Transl.)*, 2, 73, 1956.
390. Dzyaloshinskii, I.E., Lifshitz, E.M., and Pitaevskii, L.P., *Adv. Phys.*, 10, 165, 1961.
391. Nir, S. and Vassiliev, C.S., Van der Waals interactions in thin films, in *Thin Liquid Films*, Ivanov, I.B. (Ed.), Marcel Dekker, New York, 1988, p. 207.
392. Danov, K.D., Petsev, D.N., Denkov, N.D., and Borwankar, R., *J. Chem. Phys.*, 99, 7179, 1993.
393. Casimir, H.R. and Polder, D., *Phys. Rev.*, 73, 360, 1948.
394. Mahanty, J. and Ninham, B.W., *Dispersion Forces*, Academic Press, New York, 1976.
395. Moelwyn-Hughes, E.A., *Physical Chemistry*, Pergamon Press, London, U.K., 1961, Chapter 21.
396. *Langmuir*, I., *J. Chem. Phys.*, 6, 873, 1938.
397. Tenchov, B.G. and Brankov, J.G., *J. Colloid Interface Sci.*, 109, 172, 1986.
398. Vassiliev, C.S., Tenchov, B.G., Grigorov, L.S., and Richmond, P., *J. Colloid Interface Sci.*, 93, 8, 1983.

399. Verwey, E.J.W. and Overbeek, J.Th.G., *The Theory of the Stability of Liophobic Colloids*, Elsevier, Amsterdam, the Netherlands, 1948.
400. Muller, V.M., *Kolloidn. Zh.*, 38, 704, 1976.
401. McCormack, D., Carnie, S.L., and Chan, D.Y.C., *J. Colloid Interface Sci.*, 169, 177, 1995.
402. Hogg, R., Healy, T.W., and Fuerstenau, D.W., *Trans. Faraday Soc.*, 62, 1638, 1966.
403. Usui, S., *J. Colloid Interface Sci.*, 44, 107, 1973.
404. Russel, W.B., Saville, D.A., and Schowalter, W.R., *Colloidal Dispersions*, University Press, Cambridge, U.K., 1989.
405. Debye, P. and Hückel, E., *Z. Phys.*, 24, 185, 1923.
406. McCartney, L.N. and Levine, S., *J. Colloid Interface Sci.*, 30, 345, 1969.
407. Derjaguin, B.V. and Landau, L.D., *Acta Physicochim. USSR*, 14, 633, 1941.
408. Efremov, I.F., Periodic colloidal structures, in *Colloid and Surface Science*, Vol. 8, Matijevic, E. (Ed.), Wiley, New York, 1976, p. 85.
409. Schulze, H., *J. Prakt. Chem.*, 25, 431, 1882.
410. Hardy, W.B., *Proc. Roy. Soc. (Lond.)*, 66, 110, 1900.
411. Guldbbrand, L., Jönsson, B., Wennerström, H., and Linse, P., *J. Chem. Phys.*, 80, 2221, 1984.
412. Kjellander, R. and Marčelja, S., *J. Phys. Chem.*, 90, 1230, 1986.
413. Attard, P., Mitchell, D.J., and Ninham, B.W., *J. Chem. Phys.*, 89, 4358, 1988.
414. Attard, P., Mitchell, D.J., and Ninham, B.W., *J. Chem. Phys.*, 88, 4987, 1988.
415. Kralchevsky, P.A. and Paunov, V.N., *Colloids Surf.*, 64, 245, 1992.
416. Marra, J., *J. Phys. Chem.*, 90, 2145, 1986.
417. Marra, J., *Biophys. J.*, 50, 815, 1986.
418. Kjellander, R., Marčelja, S., Pashley, R.M., and Quirk, J.P., *J. Phys. Chem.*, 92, 6489, 1988.
419. Kjellander, R., Marčelja, S., Pashley, R.M., and Quirk, J.P., *J. Chem. Phys.*, 92, 4399, 1990.
420. Khan, A., Jönsson, B., and Wennerström, H., *J. Phys. Chem.*, 89, 5180, 1985.
421. Naji, A., Jungblut, S., Moreira, A.G., and Netz, R.R., *Phys. A: Stat. Mech. Appl.*, 352, 131, 2005.
422. Paunov, V.N. and Kralchevsky, P.A., *Colloids Surf.*, 64, 265, 1992.
423. Tadros, Th.F., Steric interactions in thin liquid films, in *Thin Liquid Films*, Ivanov, I.B. (Ed.), Marcel Dekker, New York, 1988, p. 331.
424. Patel, S.S. and Tirel, M., *Ann. Rev. Phys. Chem.*, 40, 597, 1989.
425. Ploehn, H.J. and Russel, W.B., *Adv. Chem. Eng.*, 15, 137, 1990.
426. de Gennes, P.G., *Scaling Concepts in Polymer Physics*, Cornell University Press, Ithaca, NY, 1979, Chapter 3.
427. Dolan, A.K. and Edwards, S.F., *Proc. Roy. Soc. (Lond.) A*, 337, 509, 1974.
428. Dolan, A.K. and Edwards, S.F., *Proc. Roy. Soc. (Lond.) A*, 343, 427, 1975.
429. de Gennes, P.G., *C. R. Acad. Sci. (Paris)*, 300, 839, 1985.
430. de Gennes, P.G., *Adv. Colloid Interface Sci.*, 27, 189, 1987.
431. Alexander, S.J., *Physique*, 38, 983, 1977.
432. Taunton, H.J., Toprakcioglu, C., Fetters, L.J., and Klein, J., *Macromolecules*, 23, 571, 1990.
433. Klein, J. and Luckham, P., *Nature*, 300, 429, 1982; Klein, J. and Luckham, P., *Macromolecules*, 17, 1041, 1984.
434. Luckham, P.F. and Klein, J., *J. Chem. Soc. Faraday Trans.*, 86, 1363, 1990.
435. Sonntag, H., Ehmka, B., Miller, R., and Knapschinski, L., *Adv. Colloid Interface Sci.*, 16, 381, 1982.
436. Horn, R.G. and Israelachvili, J.N., *Chem. Phys. Lett.*, 71, 192, 1980.
437. Nikolov, A.D., Wasan, D.T., Kralchevsky, P.A., and Ivanov, I.B., Ordered structures in thinning micellar foam and latex films, in *Ordering and Organisation in Ionic Solutions*, Ise, N. and Sogami, I. (Eds.), World Scientific, Singapore, 1988.
438. Nikolov, A.D. and Wasan, D.T., *J. Colloid Interface Sci.*, 133, 1, 1989.
439. Nikolov, A.D., Kralchevsky, P.A., Ivanov, I.B., and Wasan, D.T., *J. Colloid Interface Sci.*, 133, 13, 1989.
440. Nikolov, A.D., Wasan, D.T., Denkov, N.D., Kralchevsky, P.A., and Ivanov, I.B., *Prog. Colloid Polym. Sci.*, 82, 87, 1990.
441. Wasan, D.T., Nikolov, A.D., Kralchevsky, P.A., and Ivanov, I.B., *Colloids Surf.*, 67, 139, 1992.
442. Asakura, S. and Oosawa, F., *J. Chem. Phys.*, 22, 1255, 1954; Asakura, S. and Oosawa, F., *J. Polym. Sci.*, 33, 183, 1958.
443. de Hek, H. and Vrij, A., *J. Colloid Interface Sci.*, 84, 409, 1981.
444. Snook, I.K. and van Megen, W., *J. Chem. Phys.*, 72, 2907, 1980.
445. Kjellander, R. and Marčelja, S., *Chem. Phys. Lett.*, 120, 393, 1985.
446. Tarazona, P. and Vicente, L., *Mol. Phys.*, 56, 557, 1985.

447. Evans, R., and Parry, A.O., *J. Phys. Condens. Matter*, 2, SA15, 1990.
448. Henderson, J.R., *Mol. Phys.*, 59, 89, 1986.
449. Mitchell, D.J., Ninham, B.W., and Pailthorpe, B.A., *J. Chem. Soc. Faraday Trans. 2*, 74, 1116, 1978.
450. Henderson, D., *J. Colloid Interface Sci.*, 121, 486, 1988.
451. Kjellander, R. and Sarman, S., *Chem. Phys. Lett.*, 149, 102, 1988.
452. Trokhymchuk, A. and Henderson, D., *Curr. Opin. Colloid Interface Sci.*, 20, 33, 2015.
453. Pollard, M.L. and Radke, C.J., *J. Chem. Phys.*, 101, 6979, 1994.
454. Chu, X.L., Nikolov, A.D., and Wasan, D.T., *Langmuir*, 10, 4403, 1994.
455. Chu, X.L., Nikolov, A.D., and Wasan, D.T., *J. Chem. Phys.*, 103, 6653, 1995.
456. Trokhymchuk, A., Henderson, D., Nikolov, A., and Wasan, D.T., *J. Phys. Chem. B*, 107, 3927, 2003.
457. Blawdziewicz, J. and Wajnryb, E., *Europhys. Lett.*, 71, 269, 2005.
458. Kralchevsky, P.A. and Denkov, N.D., *Chem. Phys. Lett.*, 240, 385, 1995.
459. Trokhymchuk, A., Henderson, D., Nikolov, A., and Wasan, D.T., *Langmuir*, 17, 4940, 2001.
460. Carnahan, N.F. and Starling, K.E., *J. Chem. Phys.*, 51, 635, 1969.
461. Basheva, E.S., Kralchevsky, P.A., Danov, K.D., Ananthapadmanabhan, K.P., and Lips, A., *Phys. Chem. Chem. Phys.*, 9, 5183, 2007.
462. Mysels, K.J. and Jones, M.N., *Discuss. Faraday Soc.*, 42, 42, 1966.
463. Christov, N.C., Danov, K.D., Zeng, Y., Kralchevsky, P.A., and von Klitzing, R., *Langmuir*, 26, 915, 2010.
464. Bondy, C., *Trans. Faraday Soc.*, 35, 1093, 1939.
465. Patel, P.D. and Russel, W.B., *J. Colloid Interface Sci.*, 131, 192, 1989.
466. Aronson, M.P., *Langmuir*, 5, 494, 1989.
467. van Lent, B., Israels, R., Scheutjens, J.M.H.M., and Fleer, G.J., *J. Colloid Interface Sci.*, 137, 380, 1990.
468. Joanny, J.F., Leibler, L., and de Gennes, P.G., *J. Polym. Sci.*, 17, 1073, 1979.
469. Evans, E. and Needham, D., *Macromolecules*, 21, 1822, 1988.
470. Yang, S., Tan, H., Yan, D., Nies, E., and Shi, A.-C., *Phys. Rev. E*, 75, 061803, 2007.
471. Melby, P., Prevost, A., Egolf, D.A., and Urbach, J.S., *Phys. Rev. E*, 76, 051307, 2007.
472. Lang, P.R., *J. Chem. Phys.*, 127, 124906, 2007.
473. July, C., Kleshchanok, D., and Lang, P.R., *Eur. Phys. J. E*, 35, 60, 2012.
474. Tulpar, A., Tilton, R.D., and Walz, J.Y., *Langmuir*, 23, 4351, 2007.
475. Lekkerkerker, H.N.W. and Tuinier, R., *Colloids and the Depletion Interaction*, Springer, Berlin, Germany, 2011.
476. Johannott, E.S., *Philos. Mag.*, 11, 746, 1906.
477. Perrin, J., *Ann. Phys. (Paris)*, 10, 160, 1918.
478. Bruil, H.G. and Lyklema, J., *Nature*, 233, 19, 1971.
479. Friberg, S., Linden, St.E., and Saito, H., *Nature*, 251, 494, 1974.
480. Keuskamp, J.W. and Lyklema, J., *ACS Symp. Ser.*, 8, 191, 1975.
481. Kruglyakov, P.M., *Kolloidn. Zh.*, 36, 160, 1974.
482. Kruglyakov, P.M. and Rovin, Yu.G., *Physical Chemistry of Black Hydrocarbon Films*, Nauka, Moscow, Russia, 1978 (in Russian).
483. Denkov, N.D., Yoshimura, H., Nagayama, K., and Kouyama, T., *Phys. Rev. Lett.*, 76, 2354, 1996.
484. Denkov, N.D., Yoshimura, H., and Nagayama, K., *Ultramicroscopy*, 65, 147, 1996.
485. Kralchevsky, P.A., Nikolov, A.D., Wasan, D.T., and Ivanov, I.B., *Langmuir*, 6, 1180, 1990.
486. Bergeron, V. and Radke, C.J., *Langmuir*, 8, 3020, 1992.
487. Bergeron, V., Jimenez-Laguna, A.I., and Radke, C.J., *Langmuir*, 8, 3027, 1992.
488. Richetti, P. and Kékicheff, P., *Phys. Rev. Lett.*, 68, 1951, 1992.
489. Parker, J.L., Richetti, P., and Kékicheff, P., *Phys. Rev. Lett.*, 68, 1955, 1992.
490. McNamee, C.E., Tsujii, Y., Ohshima, H., and Matsumoto, M., *Langmuir*, 20, 1953, 2004.
491. Kralchevsky, P. and Stavans, J., *Phys. Rev. Lett.*, 74, 2752, 1995.
492. Bergeron, V. and Radke, C.J., *Colloid Polym. Sci.*, 273, 165, 1995.
493. Marinova, K.G., Gurkov, T.D., Dimitrova, T.D., Alargova, R.G., and Smith, D., *Langmuir*, 14, 2011, 1998.
494. Basheva, E.S., Nikolov, A.D., Kralchevsky, P.A., Ivanov, I.B., and Wasan, D.T., Multi-stepwise drainage and viscosity of macroscopic films formed from latex suspensions, in *Surfactants in Solution*, Vol. 12, Mittal, K.L. and Shah, D.O. (Eds.), Plenum Press, New York, 1991, p. 467.
495. Basheva, E.S., Danov, K.D., and Kralchevsky, P.A., *Langmuir*, 13, 4342, 1997.
496. Dushkin, C.D., Nagayama, K., Miwa, T., and Kralchevsky, P.A., *Langmuir*, 9, 3695, 1993.
497. Sethumadhavan, G.N., Nikolov, A.D., and Wasan, D.T., *J. Colloid Interface Sci.*, 240, 105, 2001.
498. Piech, M. and Walz, J.Y., *J. Phys. Chem. B*, 108, 9177, 2004.

499. Klapp, S.H.L., Zeng, Y., Qu, D., and von Klitzing, R., *Phys. Rev. Lett.*, 100, 118303, 2008.
500. Klapp, S.H.L., Grandner, S., Zeng, Y., and von Klitzing, R., *J. Phys.: Condens. Matter*, 20, 494232, 2008.
501. Klapp, S.H.L., Grandner, S., Zeng, Y., and von Klitzing, R., *Soft Matter*, 6, 2330, 2010.
502. Zeng, Y., Grandner, S., Oliveira, C.L.P., Thünemann, A.F., Paris, O., Pedersen, J.S., Klapp, S.H.L., and von Klitzing, R., *Soft Matter*, 7, 10899, 2011.
503. Koczo, K., Nikolov, A.D., Wasan, D.T., Borwankar, R.P., and Gonsalves, A., *J. Colloid Interface Sci.*, 178, 694, 1996.
504. Asnacios, A., Espert, A., Colin, A., and Langevin, D., *Phys. Rev. Lett.*, 78, 4974, 1997.
505. Bergeron, V. and Claesson, P.M., *Adv. Colloid Interface Sci.*, 96, 1, 2002.
506. Kolaric, B., Förster, S., and von Klitzing, R., *Progr. Colloid Polym. Sci.*, 117, 195, 2001.
507. von Klitzing, R. and Kolaric, B., *Tenside Surfactants Deterg.*, 39, 247, 2002.
508. Stubenrauch, C. and von Klitzing, R., *J. Phys.: Condens. Matter*, 15, R1197, 2003.
509. Beltran, C.M., Guillot, S., and Langevin, D., *Macromolecules*, 36, 8506, 2003.
510. Beltran, C.M. and Langevin, D., *Phys. Rev. Lett.*, 94, 217803, 2005.
511. Heinig, P., Beltran, C.M., and Langevin, D., *Phys. Rev. E*, 73, 051607, 2006.
512. Jönsson, B., Broukhno, A., Forsman, J., and Åkesson, T., *Langmuir*, 19, 9914, 2003.
513. Danov, K.D., Basheva, E.S., Kralchevsky, P.A., Ananthapadmanabhan, K.P., and Lips, A., *Adv. Colloid Interface Sci.*, 168, 50, 2011.
514. Anachkov, S.E., Danov, K.D., Basheva, E.S., Kralchevsky, P.A., and Ananthapadmanabhan, K.P., *Adv. Colloid Interface Sci.*, 183–184, 55, 2012.
515. Bales, B.L. and Almgren, M., *J. Phys. Chem.*, 99, 15153, 1995.
516. Turro, N.J. and Yekta, A., *J. Am. Chem. Soc.*, 100, 5951, 1978.
517. Quina, F.H., Nassar, P.M., Bonilha, J.B.S., and Bales, B.L., *J. Phys. Chem.*, 99, 17028, 1995.
518. Gehlen, M.H. and De Schryver, F.C., *J. Phys. Chem.*, 97, 11242, 1993.
519. Mukerjee, P. and Mysels, K.J., Critical micelle concentration of aqueous surfactant systems, National Standard Reference Data Series 36, National Bureau of Standards, Washington, DC, 1971.
520. Shah, S.S., Saeed, A., and Sharif, Q.M., *Colloids Surf. A*, 155, 405, 1999.
521. Benrraou, M., Bales, B.L., and Zana, R., *J. Phys. Chem. B*, 107, 13432, 2003.
522. Weidemaier, K., Tavernier, H.L., and Fayer, M.D., *J. Phys. Chem. B*, 101, 9352, 1997.
523. Hansson, P., Jönsson, B., Ström, C., and Söderman, O., *J. Phys. Chem. B*, 104, 3496, 2000.
524. Van Stam, J., Depaemelaere, S., and De Schryver, F.C., *J. Chem. Educ.*, 75, 93, 1998.
525. Mata, J., Varade, D., and Bahadur, P., *Thermochim. Acta*, 428, 147, 2005.
526. Hassan, P.A., Hodgdon, T.K., Sagasaki, M., Fritz-Popovski, G., and Kaler, E.W., *Comp. Rend. Chim.*, 12, 18, 2009.
527. Mukhim, T. and Ismail, K., *J. Surf. Sci. Technol.*, 21, 113, 2005.
528. Bhat, M.A., Dar, A.A., Amin, A., Rashid, P.I., and Rather, G.M., *J. Chem. Thermodyn.*, 39, 1500, 2007.
529. Amos, D.A., Lynn, S., and Radke, C.J., *Langmuir*, 14, 2297, 1998.
530. Stanley, H.E. and Teixeira, J., *J. Chem. Phys.*, 73, 3404, 1980.
531. Norrish, K., *Discuss. Faraday Soc.*, 18, 120, 1954.
532. Van Olphen, H., *Clays Clay Miner.*, 2, 418, 1954.
533. Clunie, J.S., Goodman, J.F., and Symons, P.C., *Nature (Lond.)*, 216, 1203, 1967.
534. Jordine, E.St.A., *J. Colloid Interface Sci.*, 45, 435, 1973.
535. Derjaguin, B.V., Churaev, N.V., *Croatica Chem. Acta*, 50, 187, 1977.
536. LeNeveu, D.M., Rand, R.P., Parsegian, V.A., and Gingell, D., *Biophys. J.*, 18, 209, 1977.
537. Lis, L.J., McAlister, M., Fuller, N., Rand, R.P., and Parsegian, V.A., *Biophys. J.*, 37, 657, 1982.
538. Israelachvili, J.N. and Adams, G.E., *J. Chem. Soc. Faraday Trans. 1*, 74, 975, 1978.
539. Pashley, R.M. and Israelachvili, J.N., *Colloids Surf.*, 2, 169, 1981.
540. Pashley, R.M. and Israelachvili, J.N., *J. Colloid Interface Sci.*, 101, 511, 1984.
541. Pashley, R.M., *J. Colloid Interface Sci.*, 80, 153, 1981.
542. Pashley, R.M., *J. Colloid Interface Sci.*, 83, 531, 1981.
543. Pashley, R.M., *Adv. Colloid Interface Sci.*, 16, 57, 1982.
544. Peschel, G., Belouschek, P., Müller, M.M., Müller, M.R., and König, R., *Colloid Polym. Sci.*, 260, 444, 1982.
545. Horn, R.G., Smith, D.T., and Haller, W., *Chem. Phys. Lett.*, 162, 404, 1989.
546. Claesson, P., Carmona-Ribeiro, A.M., Kurihara, K., *J. Phys. Chem.*, 93, 917, 1989.
547. Petsev, D.N. and Vekilov, P.G., *Phys. Rev. Lett.*, 84, 1339, 2000.
548. Petsev, D.N., Thomas, B.R., Yau, S.-T., and Vekilov, P.G., *Biophys. J.*, 78, 2060, 2000.

549. Valle-Delgado, J.J., Molina-Bolívar, J.A., Galisteo-González, F., Gálvez-Ruiz, M.J., Feiler, A., and Rutland, M.W., *Langmuir*, 21, 9544, 2005.
550. Valle-Delgado, J.J., Molina-Bolívar, J.A., Galisteo-González, F., and Gálvez-Ruiz, M.J., *Curr. Opin. Colloid Interface Sci.*, 16, 572, 2011.
551. Stanley, C. and Rau, D.C., *Curr. Opin. Colloid Interface Sci.*, 16, 551, 2011.
552. Zhang, N.H., Tan, Z.Q., Li, J.J., Meng, W.L., and Xu, L.W., *Curr. Opin. Colloid Interface Sci.*, 16, 592, 2011.
553. Aroti, A., Leontidis, E., Dubios, M., and Zemb, T., *Biophys. J.*, 93, 1580, 2007.
554. Leontidis, E., Aroti, A., Belloni, L., Dubios, M., and Zemb, T., *Biophys. J.*, 93, 1591, 2007.
555. Sparr, E. and Wennerström, H., *Curr. Opin. Colloid Interface Sci.*, 16, 561, 2011.
556. Demé, B. and Zemb, T., *Curr. Opin. Colloid Interface Sci.*, 16, 584, 2011.
557. Sanfeld, A. and Steinchen, A., *Adv. Colloid Interface Sci.*, 140, 1, 2008.
558. Kaldasch, J., Senge, B., and Laven, J., *Rheol. Acta*, 48, 665, 2009.
559. Bongrand, P., Intermolecular forces, in *Physical Basis of Cell–Cell Adhesion*, Bongrand, P. (Ed.), CRC Press, Boca Raton, FL, 1987, p. 1.
560. Binder, B., Goede, A., Berndt, N., and Holzhütter, H.-G., *PLoS One*, 4, 1, 2009.
561. Rand, R. and Parsegian, V., *Biochim. Biophys. Acta*, 988, 351, 1989.
562. Cevc, G., *J. Chem. Soc. Faraday Trans.*, 87, 2733, 1991.
563. Leikin, S., Parsegian, V.A., Rau, D.C., Rand, R.P., *Annu. Rev. Phys. Chem.*, 44, 369, 1993.
564. Israelachvili, J. and Wennerström, H., *Nature*, 379, 219, 1996.
565. Butt, H.-J., Capella, B., and Kappl, M., *Surf. Sci. Rep.*, 59, 1, 2005.
566. Leite, F.L., Bueno, C.C., Da Róz, A.L., Ziemath, E.C., and Oliveira Jr., O.N., *Int. J. Mol. Sci.*, 13, 12773, 2012.
567. Healy, T.W., Homola, A., James, R.O., and Hunter, R.J., *Faraday Discuss. Chem. Soc.*, 65, 156, 1978.
568. Marčelja, S. and Radič, N., *Chem. Phys. Lett.*, 42, 129, 1976.
569. Besseling, N.A.M., *Langmuir*, 13, 2113, 1997.
570. Forsman, J., Woodward, C.E., and Jönsson, B., *Langmuir*, 13, 5459, 1997.
571. Attard, P. and Batchelor, M.T., *Chem. Phys. Lett.*, 149, 206, 1988.
572. Faraudo, J., *Curr. Opin. Colloid Interface Sci.*, 16, 557, 2011.
573. Schneck, E. and Netz, R.R., *Curr. Opin. Colloid Interface Sci.*, 16, 607, 2011.
574. Jönsson, B. and Wennerström, H., *J. Chem. Soc. Faraday Trans. 2*, 79, 19, 1983.
575. Kjelländer, R., *J. Chem. Soc. Faraday Trans. 2*, 80, 1323, 1984.
576. Bratko, D. and Jönsson, B., *Chem. Phys. Lett.*, 128, 449, 1986.
577. Trokhymchuk, A., Henderson, D., and Wasan, D.T., *J. Colloid Interface Sci.*, 210, 320, 1999.
578. Simon, S.A. and McIntosh, T.J., *Proc. Natl. Acad. Sci. U.S.A.*, 86, 9263, 1989.
579. Richmond, P., *J. Chem. Soc. Faraday Trans. 2*, 70, 1066, 1974.
580. Dzhavakhidze, P.G., Kornyshev, A.A., and Levadny, V.G., *Nuovo Cimento*, 10D, 627, 1988.
581. Kornyshev, A.A. and Leikin, S., *Phys. Rev. A*, 40, 6431, 1989.
582. Leikin, S. and Kornyshev, A.A., *J. Chem. Phys.*, 92, 6890, 1990.
583. Attard, P. and Patey, G.N., *Phys. Rev. A*, 43, 2953, 1991.
584. Henderson, D. and Lozada-Cassou, M., *J. Colloid Interface Sci.*, 114, 180, 1986.
585. Henderson, D. and Lozada-Cassou, M., *J. Colloid Interface Sci.*, 162, 508, 1994.
586. Basu, S. and Sharma, M.M., *J. Colloid Interface Sci.*, 165, 355, 1994.
587. Paunov, V.N., Dimova, R.I., Kralchevsky, P.A., Broze, G., and Mehreteab, A., *J. Colloid Interface Sci.*, 182, 239, 1996.
588. Paunov, V.N. and Binks, B.P., *Langmuir*, 15, 2015, 1999.
589. Kralchevsky, P.A., Danov, K.D., and Basheva, E.S., *Curr. Opin. Colloid Interface Sci.*, 16, 517, 2011.
590. Tchaliowska, S., Herder, P., Pugh, R., Stenius, P., and Eriksson, J.C., *Langmuir*, 6, 1535, 1990.
591. Pashley, R.M., McGuiggan, P.M., Ninham, B.W., and Evans, D.F., *Science*, 229, 1088, 1985.
592. Rabinovich, Y.I. and Derjaguin, B.V., *Colloids Surf.*, 30, 243, 1988.
593. Parker, J.L., Cho, D.L., and Claesson, P.M., *J. Phys. Chem.*, 93, 6121, 1989.
594. Christenson, H.K., Claesson, P.M., Berg, J., and Herder, P.C., *J. Phys. Chem.*, 93, 1472, 1989.
595. Christenson, H.K., Fang, J., Ninham, B.W., and Parker, J.L., *J. Phys. Chem.*, 94, 8004, 1990.
596. Ducker, W.A., Xu, Z., and Israelachvili, J.N., *Langmuir*, 10, 3279, 1994.
597. Eriksson, J.C., Ljunggren, S., and Claesson, P.M., *J. Chem. Soc. Faraday Trans. 2*, 85, 163, 1989.
598. Joesten, M.D. and Schaad, L.J., *Hydrogen Bonding*, Marcel Dekker, New York, 1974.
599. Stillinger, F.H. and Ben-Naim, A., *J. Chem. Phys.*, 47, 4431, 1967.
600. Conway, B.E., *Adv. Colloid Interface Sci.*, 8, 91, 1977.

601. Kuzmin, V.L. and Rusanov, A.I., *Kolloidn. Z.*, 39, 455, 1977.
602. Dubrovich, N.A., *Kolloidn. Z.*, 57, 275, 1995.
603. Eriksson, J.C., Henriksson, U., and Kumpulainen, A., *Colloids Surf. A*, 282–283, 79, 2006.
604. Paunov, V.N., Sandler, S.I., and Kaler, E.W., *Langmuir*, 17, 4126, 2001.
605. Angarska, J.K., Dimitrova, B.S., Danov, K.D., Kralchevsky, P.A., Ananthapadmanabhan, K.P., and Lips, A., *Langmuir*, 20, 1799, 2004.
606. Christenson, H.K. and Claesson, P.M., *Science*, 239, 390, 1988.
607. Parker, J.L., Claesson, P.M., and Attard, P., *J. Phys. Chem.*, 98, 8468, 1994.
608. Carambassis, A., Jonker, L.C., Attard, P., and Rutland, M.W., *Phys. Rev. Lett.*, 80, 5357, 1998.
609. Mahnke, J., Stearnes, J., Hayes, R.A., Fornasiero, D., and Ralston, J., *Phys. Chem. Chem. Phys.*, 1, 2793, 1999.
610. Considine, R.F., Hayes, R.A., and Horn, R.G., *Langmuir*, 15, 1657, 1999.
611. Considine, R.F. and Drummond, C., *Langmuir*, 16, 631, 2000.
612. Attard, P., *Langmuir*, 16, 4455, 2000.
613. Yakubov, G.E., Butt, H.-J., and Vinogradova, O., *J. Phys. Chem. B*, 104, 3407, 2000.
614. Ederth, T., *J. Phys. Chem. B*, 104, 9704, 2000.
615. Ishida, N., Sakamoto, M., Miyahara, M., and Higashitani, K., *Langmuir*, 16, 5681, 2000.
616. Ishida, N., Inoue, T., Miyahara, M., and Higashitani, K., *Langmuir*, 16, 6377, 2000.
617. Hammer, M.U., Anderson, T.H., Chaimovich, A., Shell, M.S., and Israelachvili, J., *Faraday Discuss.*, 146, 299, 2010.
618. Popa, I., Gillies, G., Papastavrou, G., and Borkovec, M., *J. Phys. Chem. B*, 113, 8458, 2009.
619. Helfrich, W., *Z. Naturforsch.*, 33a, 305, 1978.
620. Servuss, R.M. and Helfrich, W., *J. Phys. (France)*, 50, 809, 1989.
621. Fernandez-Puente, L., Bivas, I., Mitov, M.D., and Méléard, P., *Europhys. Lett.*, 28, 181, 1994.
622. Safinya, C.R., Roux, D., Smith, G.S., Sinha, S.K., Dimon, P., Clark, N.A., and Bellocq, A.M., *Phys. Rev. Lett.*, 57, 2718, 1986.
623. McIntosh, T.J., Magid, A.D., and Simon, S.A., *Biochemistry*, 28, 7904, 1989.
624. Abillon, O. and Perez, E., *J. Phys. (France)*, 51, 2543, 1990.
625. Israelachvili, J.N. and Wennerström, H., *J. Phys. Chem.*, 96, 520, 1992.
626. Evans, E.A. and Skalak, R., *Mechanics and Thermodynamics of Biomembranes*, CRC Press, Boca Raton, FL, 1980.
627. Aniansson, G.A.E., Wall, S.N., Almgren, M., Hoffman, H., Kielmann, I., Ulbricht, W., Zana, R., Lang, J., and Tondre, C., *J. Phys. Chem.*, 80, 905, 1976.
628. Aniansson, G.A.E., *J. Phys. Chem.*, 82, 2805, 1978.
629. Dimitrova, T.D., Leal-Calderon, F., Gurkov, T.D., and Campbell, B., *Langmuir*, 17, 8069, 2001.
630. Danov, K.D., Ivanov, I.B., Ananthapadmanabhan, K.P., Lips, A., *Adv. Colloid Interface Sci.*, 128–130, 185, 2006.
631. Bird, R.B., Stewart, W.E., and Lightfoot, E.N., *Transport Phenomena*, Wiley, New York, 1960.
632. Germain, P., *Mécanique des Milieux Continus*, Masson et Cie, Paris, France, 1962.
633. Batchelor, G.K., *An Introduction of Fluid Mechanics*, Cambridge University Press, London, U.K., 1967.
634. Slattery, J.C., *Momentum, Energy, and Mass Transfer in Continua*, R.E. Krieger, Huntington, New York, 1978.
635. Landau, L.D. and Lifshitz, E.M., *Fluid Mechanics*, Pergamon Press, Oxford, U.K., 1984.
636. Barnes, H.A., Hutton, J.F., and Walters, K., *An Introduction to Rheology*, Elsevier, Amsterdam, the Netherlands, 1989.
637. Walters, K., Overview of macroscopic viscoelastic flow, in *Viscoelasticity and Rheology*, Lodge, A.S., Renardy, M., and Nohel, J.A. (Eds.), Academic Press, London, U.K., 1985, p. 47.
638. Boger, D.V., *Ann. Rev. Fluid Mech.*, 19, 157, 1987.
639. Barnes, H.A., *J. Rheol.*, 33, 329, 1989.
640. Barnes, H.A., *A Handbook of Elementary Rheology*, University of Wales, Institute of Non-Newtonian Fluid Mechanics, Aberystwyth, U.K., 2000.
641. Sagis, L.M.C., *Rev. Modern Phys.*, 83, 1367, 2011.
642. Navier, M., *Mém. de l'Acad. d. Sci.*, 6, 389, 1827.
643. Stokes, G.G., *Trans. Camb. Philos. Soc.*, 8, 287, 1845.
644. Happel, J. and Brenner, H., *Low Reynolds Number Hydrodynamics with Special Applications to Particulate Media*, Prentice-Hall, Englewood Cliffs, New York, 1965.
645. Kim, S. and Karrila, S.J., *Microhydrodynamics: Principles and Selected Applications*, Butterworth-Heinemann, Boston, MA, 1991.

646. Reynolds, O., *Philos. Trans. Roy. Soc. (Lond.)*, A177, 157, 1886.
647. Lamb, H., *Hydrodynamics*, Cambridge University Press, London, U.K., 1963.
648. Felderhof, B.U., *J. Chem. Phys.*, 49, 44, 1968.
649. Sche, S. and Fijnaut, H.M., *Surf. Sci.*, 76, 186, 1976.
650. Maldarelli, Ch. and Jain, R.K., The hydrodynamic stability of thin films, in *Thin Liquid Films*, Ivanov, I.B. (Ed.), Marcel Dekker, New York, 1988, p. 497.
651. Valkovska, D.S. and Danov, K.D., *J. Colloid Interface Sci.*, 241, 400, 2001.
652. Danov, K.D., Effect of surfactants on drop stability and thin film drainage, in *Fluid Mechanics of Surfactant and Polymer Solutions*, Starov, V. and Ivanov, I.B. (Eds.), Springer, New York, 2004, p. 1.
653. Hardy, W. and Bircumshaw, I., *Proc. Roy. Soc. (Lond.)*, A108, 1, 1925.
654. Horn, R.G., Vinogradova, O.I., Mackay, M.E. and Phan-Thien, N., *J. Chem. Phys.*, 112, 6424, 2000.
655. Dimitrov, D.S. and Ivanov, I.B., *J. Colloid Interface Sci.*, 64, 97, 1978.
656. Ivanov, I.B., Dimitrov, D.S., Somasundaran, P., and Jain, R.K., *Chem. Eng. Sci.*, 40, 137, 1985.
657. Ivanov, I.B. and Dimitrov, D.S., Thin film drainage, in *Thin Liquid Films*, Ivanov, I.B. (Ed.), Marcel Dekker, New York, 1988, p. 379.
658. Danov, K.D., Kralchevsky, P.A. and Ivanov, I.B., in *Handbook of Detergents, Part A: Properties*, Broze, G. (Ed.), Marcel Dekker, New York, 1999, p. 303.
659. O'Neill, M.E. and Stewartson, K., *J. Fluid Mech.*, 27, 705, 1967.
660. Goldman, A.J., Cox, R.G., and Brenner, H., *Chem. Eng. Sci.*, 22, 637, 1967.
661. Goldman, A.J., Cox, R.G., and Brenner, H., *Chem. Eng. Sci.*, 22, 653, 1967.
662. Levich, V.G., *Physicochemical Hydrodynamics*, Prentice-Hall, Englewood Cliffs, NJ, 1962.
663. Edwards, D.A., Brenner, H., and Wasan, D.T., *Interfacial Transport Processes and Rheology*, Butterworth-Heinemann, Boston, MA, 1991.
664. Charles, G.E. and Mason, S.G., *J. Colloid Sci.*, 15, 236, 1960.
665. Danov, K.D., Denkov, N.D., Petsev, D.N., Ivanov, I.B., and Borwankar, R., *Langmuir*, 9, 1731, 1993.
666. Danov, K.D., Valkovska, D.S., and Ivanov, I.B., *J. Colloid Interface Sci.*, 211, 291, 1999.
667. Hartland, S., Coalescence in dense-packed dispersions, in *Thin Liquid Films*, Ivanov, I.B. (Ed.), Marcel Dekker, New York, 1988, p. 663.
668. Hetsroni, G. (Ed.), *Handbook of Multiphase System*, Hemisphere Publishing, New York, 1982, pp. 1–96.
669. Davis, A.M.J., Kezirian, M.T., and Brenner, H., *J. Colloid Interface Sci.*, 165, 129, 1994.
670. Brenner, H., *Chem. Eng. Sci.*, 18, 1, 1963.
671. Brenner, H., *Chem. Eng. Sci.*, 19, 599, 1964; Brenner, H., *Chem. Eng. Sci.*, 19, 631, 1964.
672. Brenner, H. and O'Neill, M.E., *Chem. Eng. Sci.*, 27, 1421, 1972.
673. Van de Ven, T.G.M., *Colloidal Hydrodynamics*, Academic Press, London, U.K., 1988.
674. Jeffery, G.B., *Proc. Lond. Math. Soc.*, 14, 327, 1915.
675. Stimson, M. and Jeffery, G.B., *Proc. Roy. Soc. (Lond.)*, A111, 110, 1926.
676. Cooley, M.D.A. and O'Neill, M.E., *Mathematika*, 16, 37, 1969.
677. Cooley, M.D.A. and O'Neill, M.E., *Proc. Camb. Philos. Soc.*, 66, 407, 1969.
678. Davis, M.H., *Chem. Eng. Sci.*, 24, 1769, 1969.
679. O'Neill, M.E. and Majumdar, S.R., *Z. Angew. Math. Phys.*, 21, 164, 1970; O'Neill, M.E. and Majumdar, S.R., *Z. Angew. Math. Phys.*, 21, 180, 1970.
680. Davis, M.H., *Two Unequal Spheres in a Slow Linear Shear Flow*, Report NCAR-TN/STR-64, National Center for Atmospheric Research, Boulder, CO, 1971.
681. Batchelor, G.K., *J. Fluid Mech.*, 74, 1, 1976.
682. Davis, R.H. and Hill, N.A., *J. Fluid Mech.*, 236, 513, 1992.
683. Batchelor, G.K., *J. Fluid Mech.*, 119, 379, 1982.
684. Batchelor, G.K. and Wen, C.-S., *J. Fluid Mech.*, 124, 495, 1982.
685. Jeffrey, D.J. and Onishi, Y., *J. Fluid Mech.*, 139, 261, 1984.
686. Fuentes, Y.O., Kim, S., and Jeffrey, D.J., *Phys. Fluids*, 31, 2445, 1988; Fuentes, Y.O., Kim, S., and Jeffrey, D.J., *Phys. Fluids*, A1, 61, 1989.
687. Stokes, G.G., *Trans. Camb. Philos. Soc.*, 1, 104, 1851.
688. Exerowa, D. and Kruglyakov, P. M., *Foam and Foam Films: Theory, Experiment, Application*, Elsevier, New York, 1998.
689. Ivanov, I.B., Radoev, B.P., Traykov, T.T., Dimitrov, D.S., Manev, E.D., and Vassilieff, C.S., in *Proceedings of the International Conference on Colloid Surface Science*, Wolfram, E. (Ed.), Akademia Kiado, Budapest, Hungary, 1975, p. 583.
690. Denkov, N.D., Petsev, D.N., and Danov, K.D., *Phys. Rev. Lett.*, 71, 3226, 1993.
691. Valkovska, D.S., Danov, K.D., and Ivanov, I.B., *Colloid Surf. A*, 156, 547, 1999.

692. Davis, R.H., Schonberg, J.A., and Rallison, J.M., *Phys. Fluids*, A1, 77, 1989.
693. Chi, B.K. and Leal, L.G., *J. Fluid Mech.*, 201, 123, 1989.
694. Ascoli, E.P., Dandy, D.S., and Leal, L.G., *J. Fluid Mech.*, 213, 287, 1990.
695. Yiantsios, S.G. and Davis, R.H., *J. Fluid Mech.*, 217, 547, 1990.
696. Zhang, X. and Davis, R.H., *J. Fluid Mech.*, 230, 479, 1991.
697. Chesters, A.K., *Trans. Inst. Chem. Eng. A*, 69, 259, 1991.
698. Yiantsios, S.G. and Davis, R.H., *J. Colloid Interface Sci.*, 144, 412, 1991.
699. Yiantsios, S.G. and Higgins, B.G., *J. Colloid Interface Sci.*, 147, 341, 1991.
700. Joye, J.-L., Hirasaki, G.J., and Miller, C.A., *Langmuir*, 8, 3083, 1992.
701. Joye, J.-L., Hirasaki, G.J., and Miller, C.A., *Langmuir*, 10, 3174, 1994.
702. Abid, S. and Chesters, A.K., *Int. J. Multiphase Flow*, 20, 613, 1994.
703. Li, D., *J. Colloid Interface Sci.*, 163, 108, 1994.
704. Saboni, A., Gourdon, C., and Chesters, A.K., *J. Colloid Interface Sci.*, 175, 27, 1995.
705. Rother, M.A., Zinchenko, A.Z., and Davis, R.H., *J. Fluid Mech.*, 346, 117, 1997.
706. Singh, G., Miller, C.A., and Hirasaki, G.J., *J. Colloid Interface Sci.*, 187, 334, 1997.
707. Cristini, V., Blawdziewicz, J., and Loewenberg, M., *J. Fluid Mech.*, 366, 259, 1998.
708. Bazhlekov, I.B., Chesters, A.K., and van de Vosse, F.N., *Int. J. Multiphase Flow*, 26, 445, 2000.
709. Bazhlekov, I.B., van de Vosse, F.N., and Chesters, A.K., *J. Non-Newtonian Fluid Mech.*, 93, 181, 2000.
710. Chesters, A.K. and Bazhlekov, I.B., *J. Colloid Interface Sci.*, 230, 229–243, 2000.
711. Boulton-Stone, J.M. and Blake, J.R., *J. Fluid Mech.*, 254, 437, 1993.
712. Frankel, S. and Mysels, K., *J. Phys. Chem.*, 66, 190, 1962.
713. Tabakova, S.S. and Danov, K.D., *J. Colloid Interface Sci.*, 336, 273, 2009.
714. Velev, O.D., Constantinides, G.N., Avraam, D.G., Payatakes, A.C., and Borwankar, R.P., *J. Colloid Interface Sci.*, 175, 68, 1995.
715. Exerowa, D., Nikolov, A., and Zacharieva, M., *J. Colloid Interface Sci.*, 81, 419, 1981.
716. de Vries, A.J., *Rec. Trav. Chim. Pays-Bas.*, 77, 441, 1958.
717. Vrij, A., *Discuss. Faraday Soc.*, 42, 23, 1966.
718. Ivanov, I.B., Radoev, B.P., Manev, E.D., and Sheludko, A.D., *Trans. Faraday Soc.*, 66, 1262, 1970.
719. Gumerman, R.J. and Homsy, G.M., *Chem. Eng. Commun.*, 2, 27, 1975.
720. Malhotra, A.K. and Wasan, D.T., *Chem. Eng. Commun.*, 48 35, 1986.
721. Valkovska, D. S., Danov, K.D., and Ivanov, I.B., *Adv. Colloid Interface Sci.*, 96, 101, 2002.
722. Manev, E.D., Sazdanova, S.V., and Wasan, D.T., *J. Colloid Interface Sci.*, 97, 591, 1984.
723. Ivanov, I.B., *Pure Appl. Chem.*, 52, 1241, 1980.
724. Aveyard, R., Binks, B.P., Fletcher, P.D.I., and Ye, X., *Prog. Colloid Polymer Sci.*, 89, 114, 1992.
725. Velev, O.D., Gurkov, T.D., Chakarova, Sv.K., Dimitrova, B.I., and Ivanov, I.B., *Colloids Surf. A*, 83, 43, 1994.
726. Dickinson, E., Murray, B.S., and Stainsby, G., *J. Chem. Soc. Faraday Trans.*, 84, 871, 1988.
727. Ivanov, I.B., Lectures at INTEVEP, Petroleos de Venezuela, Caracas, Venezuela, June 1995.
728. Ivanov, I.B. and Kralchevsky, P.A., *Colloid Surf. A*, 128, 155, 1997.
729. Basheva, E.S., Gurkov, T.D., Ivanov, I.B., Bantchev, G.B., Campbell, B., and Borwankar, R.P., *Langmuir*, 15, 6764, 1999.
730. Gurkov, T.D. and Basheva, E.S., Hydrodynamic behavior and stability of approaching deformable drops, in *Encyclopedia of Surface & Colloid Science*, Hubbard, A.T. (Ed.), Marcel Dekker, New York, 2002.
731. Gurkov, T.D., Angarska, J.K., Tahcev, K.D., and Gaschler, W., *Colloids Surf. A*, 382, 174, 2011.
732. Boussinesq, M.J., *Ann. Chim. Phys.*, 29, 349, 1913; Boussinesq, M.J., *Ann. Chim. Phys.*, 29, 357, 1913.
733. Aris, R., *Vectors, Tensors, and the Basic Equations of Fluid Mechanics*, Prentice Hall, Englewood Cliffs, NJ, 1962.
734. Brenner, H. and Leal, L.G., *J. Colloid Interface Sci.*, 62, 238, 1977.
735. Brenner, H. and Leal, L.G., *J. Colloid Interface Sci.*, 65, 191, 1978.
736. Brenner, H. and Leal, L.G., *AIChE J.*, 24, 246, 1978.
737. Brenner, H. and Leal, L.G., *J. Colloid Interface Sci.*, 88, 136, 1982.
738. Stone, H.A., *Phys. Fluids*, A2, 111, 1990.
739. Valkovska, D.S. and Danov, K.D., *J. Colloid Interface Sci.*, 223, 314, 2000.
740. Stoyanov, S.D. and Denkov, N.D., *Langmuir*, 17, 1150, 2001.
741. Feng, S.-S., *J. Colloid Interface Sci.*, 160, 449, 1993.
742. Stebe, K.J. and Maldarelli, Ch., *Phys. Fluids*, A3, 3, 1991.
743. Stebe, K.J. and Maldarelli, Ch., *J. Colloid Interface Sci.*, 163, 177, 1994.
744. Scriven, L.E., *Chem. Eng. Sci.*, 12, 98, 1960.

745. Scriven, L.E. and Sterling, C.V., *J. Fluid Mech.*, 19, 321, 1964.
746. Slattery, J.C., *Chem. Eng. Sci.*, 19, 379, 1964; *Chem. Eng. Sci.*, 19, 453, 1964.
747. Slattery, J.C., *I&EC Fundam.*, 6, 108, 1967.
748. Slattery, J.C., *Interfacial Transport Phenomena*, Springer-Verlag, New York, 1990.
749. Barton, K.D. and Subramanian, R.S., *J. Colloid Interface Sci.*, 133, 214, 1989.
750. Feuillebois, F., *J. Colloid Interface Sci.*, 131, 267, 1989.
751. Merritt, R.M. and Subramanian, R.S., *J. Colloid Interface Sci.*, 131, 514, 1989.
752. Mannheimer, R.J. and Schechter, R.S., *J. Colloid Interface Sci.*, 12, 98, 1969.
753. Pintar, A.J., Israel, A.B., and Wasan, D.T., *J. Colloid Interface Sci.*, 37, 52, 1971.
754. Gardner, J.W. and Schechter, R.S., *Colloid Interface Sci.*, 4, 98, 1976.
755. Li, D. and Slattery, J.C., *J. Colloid Interface Sci.*, 125, 190, 1988.
756. Tambe, D.E. and Sharma, M.M., *J. Colloid Interface Sci.*, 147, 137, 1991.
757. Tambe, D.E. and Sharma, M.M., *J. Colloid Interface Sci.*, 157, 244, 1993.
758. Tambe, D.E. and Sharma, M.M., *J. Colloid Interface Sci.*, 162, 1, 1994.
759. Horozov, T., Danov, K., Kralchevsky, P., Ivanov, I., and Borwankar, R., A local approach in interfacial rheology: Theory and experiment, in *First World Congress on Emulsion*, Paris, France, 3-20, 137, 1993.
760. Danov, K. D., Ivanov, I. B., and Kralchevsky, P. A., Interfacial rheology and emulsion stability, in *Second World Congress on Emulsion*, Paris, France, 2-2, 152, 1997.
761. Ivanov, I.B., Danov, K.D., Ananthapadmanabhan, K.P. and Lips, A. *Adv. Colloid Interface Sci.*, 114–115, 61, 2005.
762. Murray, B.S. and Dickinson, E., *Food Sci. Technol.*, 2, 131, 1996.
763. Miller, R., Wüstneck, R., Kärger, J., and Kretzschmar, G., *Colloids Surf. A*, 111, 75, 1996.
764. Dickinson, E., *Colloids Surf. B*, 20, 197, 2001.
765. Bos, M.A. and van Vliet, T., *Adv. Colloid Interface Sci.*, 91, 437, 2001.
766. Kärger, J. and Derkatch, S.R., *Curr. Opin. Colloid Interface Sci.*, 15, 246, 2010.
767. Miller, R., Ferri, J.K., Javadi, A., Kärger, J., Mucic, N., and Wüstneck, R., *Colloid Polym. Sci.*, 288, 937, 2010.
768. Kärger, J., Derkatch, S.R., and Miller, R., *Adv. Colloid Interface Sci.*, 144, 38, 2008.
769. Murray, B.S., *Curr. Opin. Colloid Interface Sci.*, 16, 27, 2011.
770. Radulova, G.M., Danov, K.D., Kralchevsky, P.A., Petkov, J.T., and Stoyanov, S.D., *Soft Matter*, 10, 5777, 2014.
771. Danov, K.D., Radulova, G.M., Kralchevsky, P.A., Golemanov, K., and Stoyanov, S.D., *Faraday Discuss.*, 158,195, 2012.
772. Danov, K.D., Kralchevsky, P.A., Radulova, G.M., Basheva, E.S., Stoyanov, S.D., and Pelan, E.G., *Adv. Colloid Interface Sci.*, 2015, doi: 10.1016/j.cis.2014.04.009.
773. Stanimirova, R., Marinova, K., Tcholakova, S., Denkov, N.D., Stoyanov, S., and Pelan, E., *Langmuir*, 27, 12486, 2011.
774. de Groot, S.R. and Mazur, P., *Non-Equilibrium Thermodynamics*, Interscience, New York, 1962.
775. Sagis, L.M.C and Öttinger, H.C., *Phys. Rev. E*, 88, 022149, 2013.
776. Moeckel, G.P., *Arch. Rat. Mech. Anal.*, 57, 255, 1975.
777. Rushton, E. and Davies, G.A., *Appl. Sci. Res.*, 28, 37, 1973.
778. Haber, S., Hetsroni, G., and Solan, A., *Int. J. Multiphase Flow*, 1, 57, 1973.
779. Reed, L.D. and Morrison, F.A., *Int. J. Multiphase Flow*, 1, 573, 1974.
780. Hetsroni, G. and Haber, S., *Int. J. Multiphase Flow*, 4, 1, 1978.
781. Morrison, F.A. and Reed, L.D., *Int. J. Multiphase Flow*, 4, 433, 1978.
782. Beshkov, V.N., Radoev, B.P., and Ivanov, I.B., *Int. J. Multiphase Flow*, 4, 563, 1978.
783. Danov, K.D., Stoyanov, S.D., Vitanov, N.K., and Ivanov, I.B., *J. Colloid Interface Sci.*, 368, 342, 2012.
784. Murdoch, P.G. and Leng, D.E., *Chem. Eng. Sci.*, 26, 1881, 1971.
785. Reed, X.B., Riolo, E., and Hartland, S., *Int. J. Multiphase Flow*, 1, 411, 1974; Reed, X.B., Riolo, E., and Hartland, S., *Int. J. Multiphase Flow*, 1, 437, 1974.
786. Ivanov, I.B. and Traykov, T.T., *Int. J. Multiphase Flow*, 2, 397, 1976.
787. Traykov, T.T. and Ivanov, I.B., *Int. J. Multiphase Flow*, 3, 471, 1977.
788. Lu, C.-Y.D. and Cates, M.E., *Langmuir*, 11, 4225, 1995.
789. Jeelani, S.A.K. and Hartland, S., *J. Colloid Interface Sci.*, 164, 296, 1994.
790. Zapryanov, Z., Malhotra, A.K., Aderangi, N., and Wasan, D.T., *Int. J. Multiphase Flow*, 9, 105, 1983.
791. Malhotra, A.K. and Wasan, D.T., *Chem. Eng. Commun.*, 55, 95, 1987.

792. Malhotra, A.K. and Wasan, D.T., Interfacial rheological properties of adsorbed surfactant films with applications to emulsion and foam stability, in *Thin Liquid Films*, Ivanov, I.B. (Ed.), Marcel Dekker, New York, 1988, p. 829.
793. Singh, G., Hirasaki, G.J., and Miller, C.A., *J. Colloid Interface Sci.*, 184, 92, 1996.
794. Traykov, T.T., Manev, E.D., and Ivanov, I.B., *Int. J. Multiphase Flow*, 3, 485, 1977.
795. Bancroft, W.D., *J. Phys. Chem.*, 17, 514, 1913.
796. Griffin, J., *Soc. Cosmet. Chem.*, 5, 4, 1954.
797. Davies, J.T., in *Proceedings of the Second International Congress on Surface Activity*, Vol. 1, Butterworths, London, U.K., 1957, p. 426.
798. Shinoda, K. and Friberg, S., *Emulsion and Solubilization*, Wiley, New York, 1986.
799. Davis, H.T., Factors determining emulsion type: HLB and beyond, in *Proceedings of First World Congress on Emulsion*, October 19–22, Paris, France, 1993, p. 69.
800. Israelachvili, J., The history, applications and science of emulsion, in *Proceedings of First World Congress on Emulsion*, October 19–22, Paris, France, 1993, p. 53.
801. Kralchevsky, P.A., *J. Colloid Interface Sci.*, 137, 217, 1990.
802. Gompper, G. and Schick, M., *Phys. Rev.*, B41, 9148, 1990.
803. Lerczak, J., Schick, M., and Gompper, G., *Phys. Rev.*, 46, 985, 1992.
804. Andelman, D., Cates, M.E., Roux, D., and Safran, S., *J. Chem. Phys.*, 87, 7229, 1987.
805. Chandra, P. and Safran, S., *Europhys. Lett.*, 17, 691, 1992.
806. Danov, K.D., Velev, O.D., Ivanov, I.B., and Borwankar, R.P., Bancroft rule and hydrodynamic stability of thin films and emulsions, in *First World Congress on Emulsion*, October 19–22, Paris, France, 1993, p. 125.
807. Kunieda, H., Evans, D.F., Solans, C., and Yoshida, *Colloids Surf.*, 47, 35, 1990.
808. Koper, G.J.M., Sager, W.F.C., Smeets, J., and Bedeaux, D., *J. Phys. Chem.*, 99, 13291, 1995.
809. Ivanov, I.B., Danov, K.D., and Kralchevsky, P.A., *Colloids Surf. A*, 152, 161, 1999.
810. Velev, O.D., Gurkov, T.D., and Borwankar, R.P., *J. Colloid Interface Sci.*, 159, 497, 1993.
811. Velev, O.D., Gurkov, T.D., Ivanov, I.B., and Borwankar, R.P., *Phys. Rev. Lett.*, 75, 264, 1995.
812. Danov, K., Ivanov, I., Zapryanov, Z., Nakache, E., and Raharimalala, S., Marginal stability of emulsion thin film, in *Proceedings of the Conference of Synergetics, Order and Chaos*, Velarde, M. (Ed.), World Scientific, Singapore, 1988, p. 178.
813. Valkovska, D.S., Kralchevsky, P.A., Danov, K.D., Broze, G., and Mehreteab, A., *Langmuir*, 16, 8892, 2000.
814. Danov, K.D., Gurkov, T.D., Dimitrova, T.D., and Smith, D., *J. Colloid Interface Sci.*, 188, 313, 1997.
815. Chevaillier, J.P., Klaseboer, E., Masbernat, O., and Gourdon, C., *J. Colloid Interface Sci.*, 299, 472, 2006.
816. Chan, D.Y.C., Klaseboer, E., and Manica, R., *Soft Matter*, 7, 2235, 2011.
817. Chan, D.Y.C., Klaseboer, E., and Manica, R., *Adv. Colloid Interface Sci.*, 165, 70, 2011.
818. Ivanov, I.B., Chakarova, S.K., and Dimitrova, B.I., *Colloids Surf.*, 22, 311, 1987.
819. Dimitrova, B.I., Ivanov, I.B., and Nakache, E., *J. Dispersion Sci. Technol.*, 9, 321, 1988.
820. Sternling, C.V. and Scriven, L.E., *AIChE J.*, 5, 514, 1959.
821. Lin, S.P. and Brenner, H.J., *J. Colloid Interface Sci.*, 85, 59, 1982.
822. Holly, F.J., On the wetting and drying of epithelial surfaces, in *Wetting, Spreading and Adhesion*, Padday, J.F. (Ed.), Academic Press, New York, 1978, p. 439.
823. Castillo, J.L. and Velarde, M.G., *J. Colloid Interface Sci.*, 108, 264, 1985.
824. Davis, R.H., *Adv. Colloid Interface Sci.*, 43, 17, 1993.
825. Uijttewaal, W.S.J., Nijhof, E.-J., and Heethaar, R.M., *Phys. Fluids*, A5, 819, 1993.
826. Zapryanov, Z. and Tabakova, S., *Dynamics of Bubbles, Drops and Rigid Particles*, Kluwer Academic Publishers, London, U.K., 1999.
827. Lorentz, H.A., *Abhandl. Theoret. Phys.*, 1, 23, 1906.
828. Faxen, H., *Arkiv. Mat. Astron. Fys.*, 17, 27, 1923.
829. Wakiya, S., *J. Phys. Soc. Jpn*, 12, 1130, 1957.
830. Dean, W.R. and O'Neill, M.E., *Mathematika*, 10, 13, 1963.
831. O'Neill, M.E., *Mathematika*, 11, 67, 1964.
832. Cooley, M.D.A. and O'Neill, M.E., *J. Inst. Math. Appl.*, 4, 163, 1968.
833. Keh, H.J. and Tseng, C.H., *Int. J. Multiphase Flow*, 1, 185, 1994.
834. Schonberg, J. and Hinch, E.J., *J. Fluid Mech.*, 203, 517, 1989.
835. Ryskin, G. and Leal, L.G., *J. Fluid Mech.*, 148, 1, 1984; Ryskin, G. and Leal, L.G., *J. Fluid Mech.*, 148, 19, 1984; Ryskin, G. and Leal, L.G., *J. Fluid Mech.*, 148, 37, 1984.
836. Liron, N. and Barta, E., *J. Fluid Mech.*, 238, 579, 1992.

837. Shapira, M. and Haber, S., *Int. J. Multiphase Flow*, 14, 483, 1988.
838. Shapira, M. and Haber, S., *Int. J. Multiphase Flow*, 16, 305, 1990.
839. Yang, S.-M. and Leal, L.G., *J. Fluid Mech.*, 149, 275, 1984.
840. Yang, S.-M. and Leal, L.G., *Int. J. Multiphase Flow*, 16, 597, 1990.
841. Lebedev, A.A., *Zhur. Russ. Fiz. Khim.*, 48, 1916.
842. Silvey, A., *Phys. Rev.*, 7, 106, 1916.
843. Hadamar, J.S., *Comp. Rend. Acad. Sci. (Paris)*, 152, 1735, 1911.
844. Rybczynski, W., *Bull. Intern. Acad. Sci. (Cracovie)*, A, 1911.
845. He, Z., Dagan, Z., and Maldarelli, Ch., *J. Fluid Mech.*, 222, 1, 1991.
846. Malysa, K., Krasowska, M., and Krzan, M., *Adv. Colloid Interface Sci.*, 114–115, 205, 2005.
847. Krzan, M., Zawala, J., and Malysa, K., *Colloids Surf. A*, 298, 42, 2007.
848. Krzan, M. and Malysa, K., *Physicochem. Problems Mineral Process.*, 43, 43, 2009.
849. Krzan, M. and Malysa, K., *Physicochem. Problems Mineral Process.*, 48, 49, 2012.
850. Zawala, J., Malysa, E., Krzan, M., and Malysa, K., *Physicochem. Problems Mineral Process.*, 50, 143, 2014.
851. Danov, K.D., Aust, R., Durst, F., and Lange, U., *Chem. Eng. Sci.*, 50, 263, 1995.
852. Danov, K.D., Aust, R., Durst, F., and Lange, U., *Chem. Eng. Sci.*, 50, 2943, 1995.
853. Danov, K.D., Aust, R., Durst, F., and Lange, U., *Int. J. Multiphase Flow*, 21, 1169, 1995.
854. Danov, K.D., Gurkov, T.D., Raszillier, H., and Durst, F., *Chem. Eng. Sci.*, 53, 3413, 1998.
855. Stoos, J.A. and Leal, L.G., *J. Fluid Mech.*, 217, 263, 1990.
856. Danov, K.D., Dimova, R.I., and Pouligny, B., *Phys. Fluids*, 12, 2711, 2000.
857. Dimova, R.I., Danov, K.D., Pouligny, B., and Ivanov, I.B., *J. Colloid Interface Sci.*, 226, 35, 2000.
858. Angelova, M.I. and Pouligny, B., *Pure Appl. Optics*, 2, 261, 1993.
859. Pouligny, B., Martinot-Lagarde, G., and Angelova, M.I., *Progr. Colloid Polym. Sci.*, 98, 280, 1995.
860. Dietrich, C., Angelova, M., and Pouligny, B., *J. Phys. II France*, 7, 1651, 1997.
861. Velikov, K., Dietrich, C., Hadjiski, A., Danov, K., and Pouligny, B., *Europhys. Lett.*, 40(4), 405, 1997.
862. Velikov, K., Danov, K., Angelova, M., Dietrich, C., and Pouligny, B., *Colloids Surf. A*, 149, 245, 1999.
863. Dimova, R., Dietrich, C., Hadjiisky, A., Danov, K., and Pouligny, B., *Eur. Phys. J. B*, 12, 589, 1999.
864. Danov, K.D., Pouligny, B., Angelova, M.I., and Kralchevsky, P.A., *Studies in Surface Science and Catalysis*, Vol. 132, Elsevier, Amsterdam, the Netherlands, 2001.
865. Barentin, C., Ybert, C., di Meglio, J.M., and Joanny, J.F., *J. Fluid Mech.*, 397, 331, 1999.
866. Maenosono, S., Dushkin, C.D., and Yamaguchi, Y., *Colloid Polym. Sci.*, 227, 993, 1999.
867. Barentin, C., Muller, P., and Ybert, C., *Eur. Phys. J. E*, 2, 153, 2000.
868. Dimova, R., Pouligny, B., and Dietrich, C., *Biophys. J.*, 79, 340, 2000.
869. Joseph, D.D., Wang, J., Bai, R., Yang, B.H., and Hu, H.H., *J. Fluid Mech.*, 496, 139, 2003.
870. Sickert, M. and Rondelez, F., *Phys. Rev. Lett.*, 90, 126104, 2003.
871. Fischer, T.M., *Phys. Rev. Lett.*, 92, 139603, 2004.
872. Sickert, M. and Rondelez, F., *Phys. Rev. Lett.*, 92, 139604, 2004.
873. Haris, S.S. and Giorgio, T.D., *Gene Therapy*, 12, 512, 2005.
874. Khattari, Z., Ruschel, Y., Wen, H.Z., Fischer, A. and Fischer, T.M., *J. Phys. Chem. B*, 109, 3402, 2005.
875. Singh, P. and Joseph, D.D., *J. Fluid Mech.*, 530, 31, 2005.
876. Fischer, T.M., Dhar, P., and Heinig, P., *J. Fluid Mech.*, 558, 451, 2006.
877. Sickert, M., Rondelez, F., and Stone, H.A., *Europhys. Lett.*, 79, 66005, 2007.
878. Chen, W. and Tong, P., *Europhys. Lett.*, 84, 28003, 2008.
879. Peng, Y., Chen, W., Fisher, T.M., Weitz, D.A., and Tong, P., *J. Fluid Mech.*, 618, 243, 2009.
880. Lee, M.H., Reich, D.H., Stebe, K.J., and Leheny, R.L., *Langmuir*, 26, 2650, 2010.
881. Wilke, N., Vega Merkado, F., and Maggio, B., *Langmuir*, 26, 11050, 2010.
882. Singh, P., Joseph, D.D., and Aubry, N., *Soft Matter*, 6, 4310, 2010.
883. Ally, J. and Amirfazli, A., *AIP Conf. Proc.*, 1311, 307, 2010.
884. Abras, D., Pranami, G., and Abbott, N.L., *Soft Matter*, 8, 2026, 2012.
885. Koynov, K. and Butt, H.-J., *AIP Conf. Proc.*, 1518, 357, 2013.
886. Morse, J., Huang, A., Li, G., Maxey, M.R., and Tang, J.X., *Biophys. J.*, 105, 21, 2013.
887. Memdoza, A.J., Guzman, E., Martinez-Pedrero, F., Ritacco, H., Rubio, R.G., Ortega, F., Starov, V.M. and Miller, R., *Adv. Colloid Interface Sci.*, 206, 303, 2014.
888. Hunter, R.J., *Foundation of Colloid Science*, Vol. 1, Clarendon Press, Oxford, U.K., 1987.
889. Hunter, R.J., *Foundation of Colloid Science*, Vol. 2, Clarendon Press, Oxford, U.K., 1989.
890. Einstein, A., *Ann. Phys.*, 19, 289, 1906.
891. Kubo, R., *Rep. Prog. Phys.*, 29, 255, 1966.
892. Einstein, A., *Ann. Phys.*, 34, 591, 1911.

893. Taylor, G.I., *Proc. Roy. Soc. A*, 138, 41, 1932.
894. Oldroyd, J.G., *Proc. Roy. Soc. A*, 232, 567, 1955.
895. Taylor, G.I., *Proc. Roy. Soc. A*, 146, 501, 1934.
896. Fröhlich, H. and Sack, R., *Proc. Roy. Soc. A*, 185, 415, 1946.
897. Oldroyd, J.G., *Proc. Roy. Soc. A*, 218, 122, 1953.
898. Batchelor, G.K., *J. Fluid Mech.*, 83, 97, 1977.
899. De Kruijff, C.G., Van Iersel, E.M.F., Vrij, A., and Russel, W.B., *J. Chem. Phys.*, 83, 4717, 1985.
900. Loewenberg, M. and Hinch, E.J., *J. Fluid Mech.*, 321, 395, 1996.
901. Da Cunha, F.R. and Hinch, E.J., *J. Fluid Mech.*, 309, 211, 1996.
902. Li, X. and Pozrikidis, C., *J. Fluid Mech.*, 341, 165, 1997.
903. Loewenberg, M., *J. Fluids Eng.*, 120, 824, 1998.
904. Blawdziewicz, J., Vajnryb, E., and Loewenberg, M., *J. Fluid Mech.*, 395, 29, 1999.
905. Ramirez, J.A., Zinchenko, A., Loewenberg, M., and Davis, R.H., *Chem. Eng. Sci.*, 54, 149, 1999.
906. Blawdziewicz, J., Vlahovska, P., and Loewenberg, M., *Physica A*, 276, 50, 2000.
907. Breyannis, G. and Pozrikidis, C., *Theor. Comp. Fluid Dynam.*, 13, 327, 2000.
908. Li, X. and Pozrikidis, C., *Int. J. Multiphase Flow*, 26, 1247, 2000.
909. Rednikov, A.Y., Ryazantsev, Y.S., and Velarde, M.G., *Phys. Fluids*, 6, 451, 1994.
910. Velarde, M.G., *Phil. Trans. Roy. Soc., Math. Phys. Eng. Sci.*, 356, 829, 1998.
911. Danov K.D., *J. Colloid Interface Sci.*, 235, 144, 2001.
912. Barnes, H.A., Rheology of emulsions - a review, in Proc. First World Congress on Emulsion 19-22 Oct. 1993, Paris, 1993, p. 267.
913. Krieger, L.M. and Dougherty, T.J., *Trans. Soc. Rheol.*, 3, 137, 1959.
914. Wakeman, R., *Powder Tech.*, 11, 297, 1975.
915. Prud'home, R.K. and Khan, S.A., Experimental results on foam rheology, in *Foams: Theory, Measurements, and Applications*, Prud'home, R.K. and Khan, S.A., Eds., Marcel Dekker, New York, 1996, p. 217.
916. Tadros, T.F., Fundamental principles of emulsion rheology and their applications, in Proc. First World Congress on Emulsion 19-22 Oct. 1993, Paris, 1993, p. 237.
917. Pal, R., Bhattacharya, S.N., and Rhodes, E., *Can. J. Chem. Eng.*, 64, 3, 1986.
918. Edwards, D.A. and Wasan, D.T., Foam rheology: the theory and role of interfacial rheological properties, in *Foams: Theory, Measurements, and Applications*, Prud'home, R.K. and Khan, S.A., Eds., Marcel Dekker, New York, 1996, p. 189.
919. Wessel, R. and Ball, R.C., *Phys. Rev.*, A46, 3009, 1992.
920. Kanai, H., Navarrete, R.C., Macosko, C.W., and Scriven, L.E., *Rheol. Acta*, 31, 333, 1992.
921. Pal, R., *Chem. Eng. Comm.*, 98, 211, 1990.
922. Pal, R., *Colloids Surf. A*, 71, 173, 1993.
923. Prins, A., Liquid flow in foams as affected by rheological surface properties: a contribution to a better understanding of the foaming behaviour of liquids, in *Hydrodynamics of Dispersed Media*, Hulin, J.P., Cazabat, A.M., Guyon, E., and Carmona, F., Eds., Elsevier/North-Holland, Amsterdam, 1990, p. 5.
924. Babak, V.G., *Colloids Surf. A*, 85, 279, 1994.
925. Yuhua, Y., Pal, R., and Masliyah, J., *Chem Eng. Sci.*, 46, 985, 1991.
926. Giesekus, H., Disperse systems: dependence of rheological properties on the type of flow with implications for food rheology, in *Physical Properties of Foods*, Jowitt, R. et al., Eds., Appl. Sci. Publishers, London, 1983, ch. 13.
927. Turian, R. and Yuan, T.-F., *AIChE J.*, 23, 232, 1977.
928. Clarke, B., *Trans. Inst. Chem. Eng.*, 45, 251, 1967.
929. Denkov, N.D., Tcholakova, S., Höhler, R., and Cohen-Addad, S., Foam Rheology, in *Foam Engineering. Fundamentals and Applications*, Stevenson, P., Ed., John Wiley & Sons, UK, 2012, p. 91.
930. Bingham, E.C., *U. S. Bureau of Standards Bulletin*, 13, 309, 1916.
931. Herschel, W.K. and Bulkley, R., *Kolloid Z.*, 39, 291, 1926.

932. Denkov, N.D., Tcholakova, S., Golemanov, K., Ananthapadmanabhan, K.P., and Lips, A., *Phys. Rev. Lett.*, 100, 138301, 2008.
933. Tcholakova, S., Denkov, N.D., Golemanov, K., Ananthapadmanabhan, K.P., and Lips, A., *Phys. Rev. E*, 78, 011405, 2008.
934. Golemanov, K., Denkov, N.D., Tcholakova, S., Vethamunthu, M., and Lips, A., *Langmuir*, 24, 9956, 2008.
935. Denkov, N.D., Tcholakova, S., Golemanov, K., Hu, T., Lips, A., *Amer. Inst. Physics Conference Proceedings*, 1027, 902, 2008.
936. Denkov, N.D., Tcholakova, S., Golemanov, K., Ananthapadmanabhan, K.P., and Lips, A., *Soft Matter*, 5, 3389, 2009.
937. Politova, N., Tcholakova, S., Golemanov, K., Denkov, N.D., Vethamunthu, M., and Ananthapadmanabhan, K.P., *Langmuir*, 28, 1115, 2012.
938. Mitrinova, Z., Tcholakova, S., Golemanov, K., Denkov, N.D., Vethamunthu, M., and Ananthapadmanabhan, K.P., *Colloids Surf. A*, 438, 186, 2013.
939. Mitrinova, Z., Tcholakova, S., Popova, Z., Denkov, N., Dasgupta, B.R., and Ananthapadmanabhan, K.P., *Langmuir*, 29, 8255, 2013.
940. von Smoluchowsky, M., *Phys. Z.*, 17, 557, 1916.
941. von Smoluchowsky, M., *Z. Phys. Chem.*, 92, 129, 1917.
942. Wang, H. and Davis, R.H., *J. Colloid Interface Sci.*, 159, 108, 1993.
943. Rogers, J.R. and Davis, R.H., *Mettal. Trans.*, A21, 59, 1990.
944. Young, N.O., Goldstein, J.S., and Block, M.J., *J. Fluid Mech.*, 6, 350, 1959.
945. Fuchs, N.A., *Z. Phys.*, 89, 736, 1934.
946. Friedlander, S.K., *Smoke, Dust and Haze: Fundamentals of Aerosol Behaviour*, Wiley-Interscience, New York, 1977.
947. Singer, J.M., Vekemans, F.C.A., Lichtenbelt, J.W.Th., Hesselink, F.Th., and Wiersema, P.H., *J. Colloid Interface Sci.*, 45, 608, 1973.
948. Leckband, D.E., Schmitt, F.-J., Israelachvili, J.N., and Knoll, W., *Biochemistry*, 33, 4611, 1994.
949. Bak, T.A. and Heilmann, O., *J. Phys. A: Math. Gen.*, 24, 4889, 1991.
950. Martinov, G.A. and Muller, V.M., in *Research in Surface Forces*, Vol. 4, Plenum Press, Consultants Bureau, New York, 1975, p. 3.
951. Elminyawi, I.M., Gangopadhyay, S., and Sorensen, C.M., *J. Colloid Interface Sci.*, 144, 315, 1991.
952. Hartland, S. and Gakis, N., *Proc. Roy. Soc. (Lond.)*, A369, 137, 1979.
953. Hartland, S. and Vohra, D.K., *J. Colloid Interface Sci.*, 77, 295, 1980.
954. Lobo, L., Ivanov, I.B., and Wasan, D.T., *AIChE J.*, 39, 322, 1993.
955. Danov, K.D., Ivanov, I.B., Gurkov, T.D., and Borwankar, R.P., *J. Colloid Interface Sci.*, 167, 8, 1994.
956. van den Tempel, M., *Recueil*, 72, 433, 1953.
957. Borwankar, R.P., Lobo, L.A., and Wasan, D.T., *Colloid Surf.*, 69, 135, 1992.
958. Dukhin, S., Sæther, Ø., and Sjöblom, J., Coupling of coalescence and flocculation in dilute O/W emulsions, in *Encyclopedia Handbook of Emulsion Technology*, Sjöblom, J., Ed., Marcel Dekker, New York, 2001, p. 71.
959. Urbina-Villalba, G. and Garcia-Sucre, M., *Mol. Simulat.*, 27, 75, 2001.
960. Madras, G. and McCoy, B.J., *J. Colloid Interface Sci.*, 246, 356, 2002.
961. Barthelmes, G., Pratsinis, S.E., and Buggisch, H., *Chem. Eng. Sci.*, 58, 2893, 2003.
962. Han, B.B., Akeprathumchai, S., Wickramasinghe, S.R., and Qian, X., *AIChE J.*, 49, 1687, 2003.
963. Urbina-Villalba, G., Garcia-Sucre, M., and Toro-Mendoza, J., *Phys. Rev. E*, 68, 061408, 2003.
964. *Emulsions: Structure, Stability and Interactions*, Petsev D.N., Ed., Elsevier, London, 2004.
965. Urbina-Villalba, G., *Int. J. Mol. Sci.*, 10, 761, 2009.
966. Rahn-Chique, K., Puertas, A.M., Rumero-Cano, M.S., Rojas, C., and Urbina-Villalba, G., *Adv. Colloid Interface Sci.*, 178, 1, 2012.